Numerical Simulations of Anelastic and Boussinesq Rotating Convection with Radial Entropy Gradient Boundary Conditions

By

Benjamin Rurik Syquia Ocampo

A thesis submitted in partial fulfillment of the requirements for the degree of

Master of Science

in

Geophysics

Department of Physics

University of Alberta

Abstract

Observations from the gas giants Jupiter or Saturn allow for researchers to construct geophysical fluid dynamical numerical models in an attempt to replicate the observed features. Most models aim at replicating the zonal jets and the eddies observed on these gas giants to understand how they are driven. Two dominant theories have arisen as a result of the controversy of the generation of these features: the weather layer hypothesis and the deep winds hypothesis. The weather layer hypothesis assumes that the zonal jets are driven by cloud physics in the troposphere while the deep winds hypothesis states that these jets are driven by convection in the deep interior. Some success has been seen in the weather layer models as some were able to generate eddies or even great storms. Whereas some success has been seen in the deep winds models as some were able to generate equatorial and high latitude zonal jets.

Most deep winds models are based on Boussinesq or anelastic convection in a rotating spherical shell. Convection is implemented by using either constant entropy boundary conditions or constant radial entropy gradient boundary conditions. This allows for the generation of zonal jets for a strong enough thermal forcing since the secondary flow comes from the interaction between the convection cells and the outer boundary. However, based off measurements from the Galileo space probe, they imply that Jupiter has a stably stratified fluid layer near the top of its atmosphere. Typically, these models that replicate the zonal jets do not include the stably stratified fluid layer near the top boundary.

Due to developments in general circulation model software, regional models can be used to simulate local fluid dynamics in a rotating spherical shell. However, if models focus on either poles of the planet, conventional spherical coordinate system is not optimal since singularities exist at the poles. Instead, a cubed-sphere curvilinear grid system can be used to successfully resolve these models. This should allow for emphasis of fluid dynamics at the region with a reduced computational cost compared to full spherical shell models.

In this thesis, we implement rotating convection models in both full and regional rotating

spherical shell models. The full spherical shell model implements the constant conductive radial entropy gradient boundary conditions to allow for anelastic convection in the models and to add the stably stratified fluid layer at the outer boundary. For the regional convection simulation, we model a Boussinesq fluid at the North polar region of a rotating spherical shell using a cubed-sphere curvilinear grid system. The results from the rotating anelastic convective spherical shell models without the stably stratified fluid layer near the outer boundary show zonal flow oscillations for a high enough thermal forcing, where they indicate that the fluid is in a relaxation oscillation regime. Implementing the stratified fluid layer leads to a tendency towards suppression in these oscillations via decrease in their amplitude. However, for a thick enough layer, these oscillations become suppressed such that the model does not evolve into the relaxation oscillation state. The retrograde jets from models with no stratified fluid layer also became smoother when the stably stratified fluid layer is implemented.

Long-lived eddies have also been generated for the near-Boussinesq case of the rotating anelastic spherical shell models with the stably stratified fluid layer. These eddies are generated for a large enough thermal forcing and drift around the tangent cylinder. However, increasing the thermal forcing leads to a merging of these long-lived eddies, leading to the generation of anticyclonic great eddies. Other models with a higher density stratification in this thesis did not generate any long-lived eddies.

Based on the results from the regional model with horizontal periodic boundary conditions, the fluid motion associated with convective mixing is strong enough to interact with the corners of the geometry. Different open horizontal boundary conditions were implemented in an attempt to eliminate the interaction. However, the results using these conditions lead to either interactions with the corners or numerical problems.

Preface

This thesis is an original work by Benjamin Rurik Syquia Ocampo. No part of this thesis has been previously published.

Acknowledgments

I would like to express my gratitude towards everyone who have made contributions to the work described in this thesis. First and foremost, I express my gratitude to my supervisor, Dr. Moritz Heimpel, for taking me as his student. With his encouragement of high quality work, his advice on how to improve my knowledge and methodology, and his guidance that allowed me to grow as a research scientist, my experience as a graduate student has been very rich and rewarding. I also express my thanks to my committee members, Dr. Mathieu Dumberry, Dr. Paul Lu, and Dr. Claire Currie, for their interest in my work.

My work would not have been made possible without the help of Compute Canada. They have given me the computational resources needed to carry out my numerical work. Thus, they have my gratitude. Westgrid, Calcul Quebec, and SciNet also have my thanks as they have provided me access to their powerful computer clusters, which allowed me to conduct my research with efficiency.

I will also give my thanks to the Department of Physics at the University of Alberta. The courses and seminars that they offered and I attended have greatly benefitted me.

Last but not least, I would like to thank my family and friends for supporting me. I express my gratitude to my Mom, Dad, and my Brother for their constant love and support. I am also indebted to my fiancee, Adriana Faciu, for her love and unyielding support. I also express my gratitude towards my friends, Keith Cuff, Colin More, and Olivia Henderson, for offering their support, help, and advice that allowed me improve both my fluid dynamics knowledge and my presentation skills.

Contents

List of Tables

List of Figures

Symbol	Description	Page
T	Temperature	6
z_d	Depth	6
dT/dz_d	Pressure Dependent Temperature Gradient	6
$\hat{\boldsymbol{z}}$	Axis of Rotation	9
r_i	Inner radius of the Spherical Shell	14
r_o	Outer radius of the Spherical Shell	14
$\boldsymbol{\Omega}$	Rate of Rotation	14
ρ	Density	14
$\boldsymbol{r}$	Spherical Position Vector	14
t	Time	14
$\boldsymbol{u}$	Velocity Field	14
P	Pressure	14
ν	Kinematic Viscosity	14
α	Thermal Expansion Coefficient	14
g	Gravity	14
κ	Thermal Diffusivity	15
d	Length Scale	16
ΔT	Temperature Scale	16
Pr	Prandtl Number	17
E	Ekman Number	17
Ra	Rayleigh Number	17
η	Radius Ratio	19
m_p	Polytropic Index	19
N_ρ	Density Stratification	19
S	Rate of Strain Tensor	19
δ_{ij}	Kronecker Delta	19
s	Entropy	19
Δs	Entropy Scale	19
c_p	Specific heat at Constant Pressure	20
Di	Dissipation Number	20
Ra^*	Modified Rayleigh Number	20
Ra_f^*	Modified Flux-Based Rayleigh Number	20
s_c	Conductive Entropy	21
Nu^*	Modified Nusselt Number	21
Q_f	Heat Flux	21
U_γ	Poloidal Potential	21
U_ζ	Toroidal Potential	21

∇_H	Horizontal Gradient	21
Δ_H	Horizontal Laplacian	21
$Y_l^m(\theta, \phi)$	Spherical Harmonics Function	23
m	Spherical Harmonic Order / Azimuthal Wavenumber	23
l	Spherical Harmonic Degree	23
P_m^l	Associated Legendre Function	23
P_l	Legendre Function	23
$W_{lm}(r)$	Spherical Coefficient Function	23
$C_n(x)$	Chebyshev Polynomials of Order n	24
Q_E	Explicit Time Stepping Scheme	26
Q_I	Implicit Time Stepping Scheme	26
$Re(u_i)$	Reynolds Number	27
$Ro(u_i)$	Rossby Number	27
KE	Total Kinetic Energy	27
KE_ζ	Toroidal Kinetic Energy	27
KE_γ	Poloidal Kinetic Energy	27
$\boldsymbol{G}$	Dissipation and Metric Terms	29
ι	Elevation of Fluid Relative to Mean Elevation	29
Θ	Potential Temperature	30
A	Eddy Viscosity	30
χ	Arbitrary Dynamic Variable	30
G_χ^{sponge}	Sponge Dissipation Term	31
τ_i	Relaxation Time Scale at Base of Sponge Layer	31
τ_b	Relaxation Time Scale at Boundary Layer	31
C_χ	Phase Speed of χ	31
λ	Latitude	32
τ	Viscous Diffusion Time	34
L	Vertical Length Scale (MITgcm)	34
R_i	Regional Spherical Shell Inner radius	36
R_o	Regional Spherical Shell Outer radius	36
δx_{3j}	Depth Grid Spacing	36
K_T	Thermal Diffusivity (MITgcm)	37
δ_E	Ekman Layer	38
Γ	White Noise Perturbation Function	39
Ta	Taylor Number	42
$\mathscr{R}(r)$	Depth-Dependent Rayleigh Number	48
H	Heat Sink	48
$\beta(r)$	Radial Conductive Entropy Gradient	48
r_{nb}	Radial Point of Neutral Buoyancy	48

η_{nb}	r_{nb} Scaled by the Outer Radius	48
Ri	Richardson Number	135

Chapter 1

Introduction

Before discussing numerical experiments on gas giants, we first present key features of the atmospheric fluid dynamics observed on gas giants in our solar system. The replication of these features is the primary goal of these numerical experiments as they provide us with further understanding in the fluid dynamical process involved in their formation. In this chapter, we will focus on presenting key features that Jupiter and Saturn exhibit on their atmosphere and two theories that attempt to explain the mechanism that drives the observed zonal jets.

1.1 Observations of Jupiter and Saturn

Many observations of Jupiter come from unmanned spacecraft and ground-based telescopes with spacecraft observations dating back to the Pioneer 10 flyby mission in 1973 and ground-based observations dating back to Cassini in the 17th century (Anderson et al., 2002; Hide, 1968). In addition to Pioneer 10, other flyby spacecrafts, such as the Cassini-Huygens space probe, were launched to further collect observational data on Jupiter (Porco et al., 2003). However, the Galileo spacecraft is the first to conduct an orbiter mission, which was launched in 1989 (Vasavada & Showman, 2005). This mission provided measurements on the deep wind and thermal structures of Jupiter near the equator (Atkinson, Pollack, & Seiff, 1998; Magalhaes, Seiff, & Young, 2002). The current orbiter mission to provide further observational data on Jupiter is Juno, where the spacecraft was launched in 2011 and has been in orbit since July 5, 2017 (Nybakken, 2011).

One noticeable feature observed on Jupiter's atmosphere is its banded structure, which is highly correlated with strong zonal winds and can be seen in Figure 1.1. There are two types of bands: the dark bands (or belts) and the light bands (or zones). The dark bands

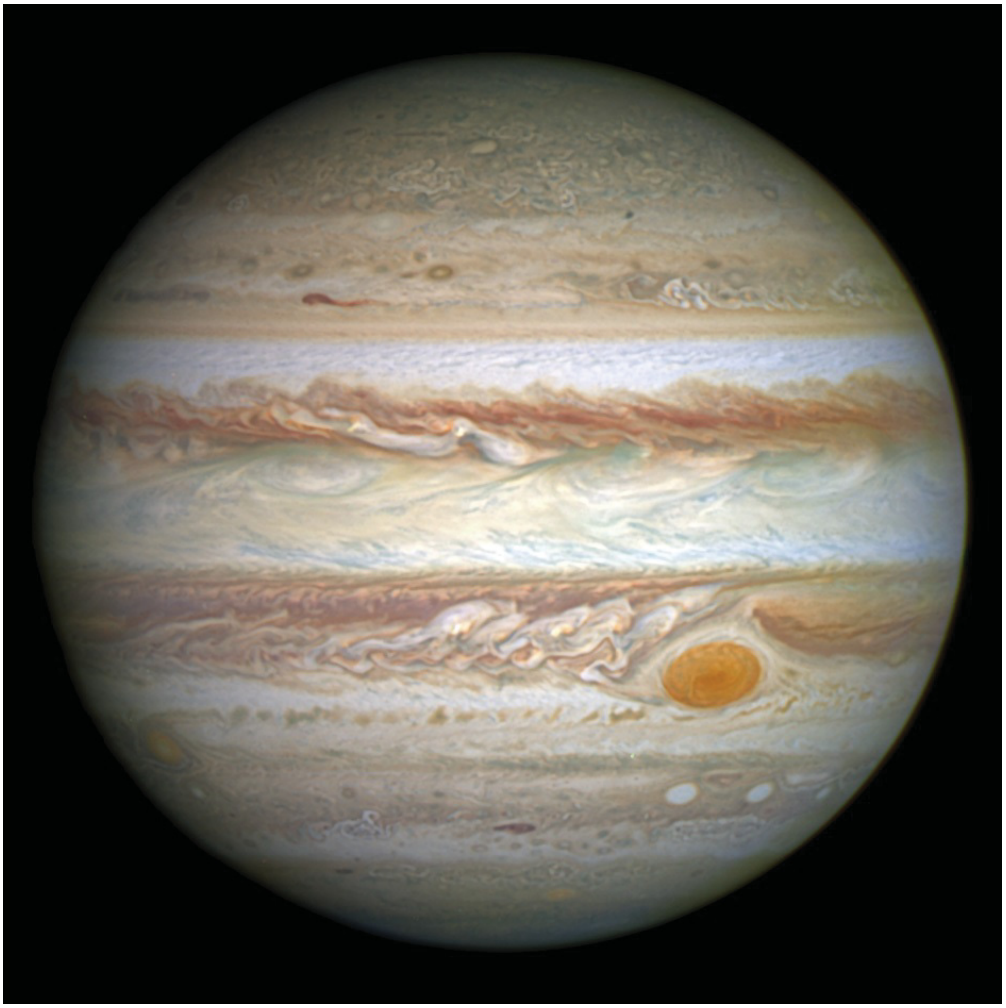

Figure 1.1: This image of Jupiter captured by Cassini in 2000 (NASA, 2009).

are anticyclonic while the light bands are cyclonic. The banded structure is caused by the shearing action between two adjacent zonal jets flowing in opposite directions (Smith & Hunt, 2004). Figure 1.2 shows that Jupiter exhibits high latitudinal prograde jets and a strong equatorial prograde jet. The retrograde jets are generally weaker than the prograde jets.

Besides the the zonal wind structure, Jupiter also exhibits vortices on its atmosphere. One of the most remarkable features that corresponds to Jupiter's vorticity structure is the Great Red Spot (Smith & Hunt, 1976). This spot is a large, oval shaped anticyclonic storm that resides around the planetographic latitude of 22^oS (Hide, 1961; Smith & Hunt, 1976). From Smith and Hunt (2004), the Great Red Spot is measured to be 39,000km in East-West length and 12,500 in North-South width. This spot is rather long-lived with observations tracing back to roughly 300 years ago (Smith & Hunt, 1976). However, this Great Red

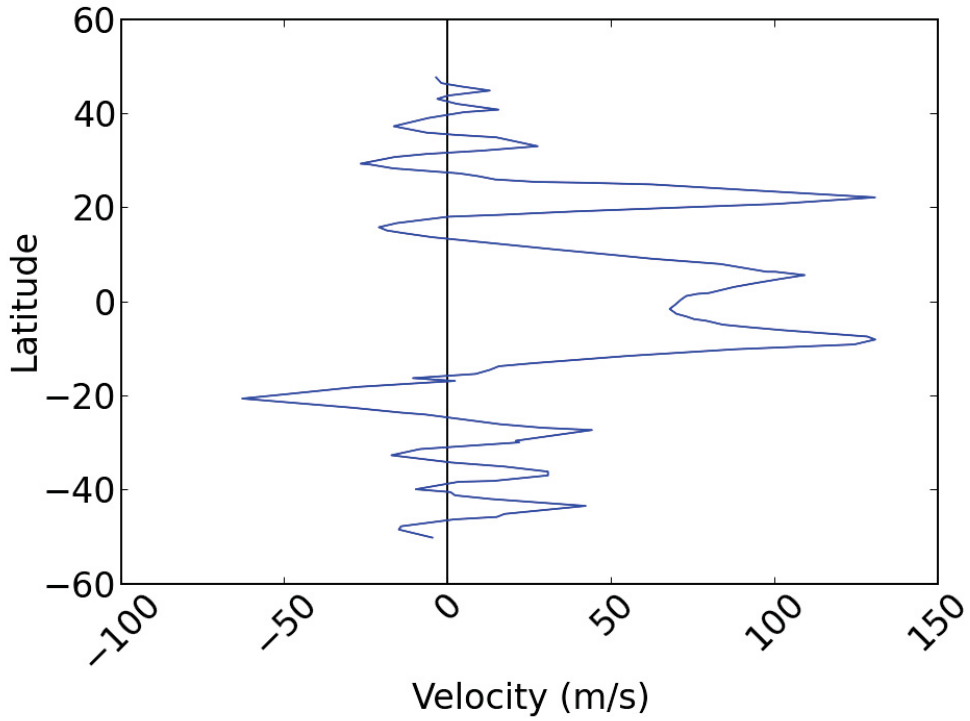

Figure 1.2: The zonal wind profile of Jupiter based on observations from Cassini. Note that the prograde flow is represented by positive values of the velocity while the retrograde flow is represented by the negative values. The data used to produced this graph is from Simon et al. (2015).

Spot is confined within the South Tropical Zone, which is flanked in the North by the South Equatorial Belt and to the South by the South Temperate Belt. It also has a mean westward drift speed of 3 m s^{-1} and a maximum velocity of 120 m s^{-1} (Smith & Hunt, 1976). The Great Red Spot also has a maximum relative vorticity of roughly $6 \cdot 10^{-5}$ s^{-1}, which is roughly 1/3 of the local planetary vorticity (Smith & Hunt, 2004).

The vorticity structure on Jupiter's atmosphere also consists of smaller white oval storms and instabilities in the North and South poles. Several white oval storms can be seen at planetographic latitudes 33^oS and 41^oS on Figure 1.1 (Smith & Hunt, 2004). From Smith and Hunt (2004), smaller white ovals can also be seen near planetographic latitudes 17^oN, 34^oN and 40^oN. These white ovals can have their major diameter range between 1000 km to 5000 km. Recent observations made by the Juno spacecraft also show eddies at the North and South poles, as seen on Figures 1.3 and 1.4, respectively.

Apart from atmospheric observations, measurements made by satellites and telescopes along with theoretical models provide inferences of the interior structure of Jupiter. The

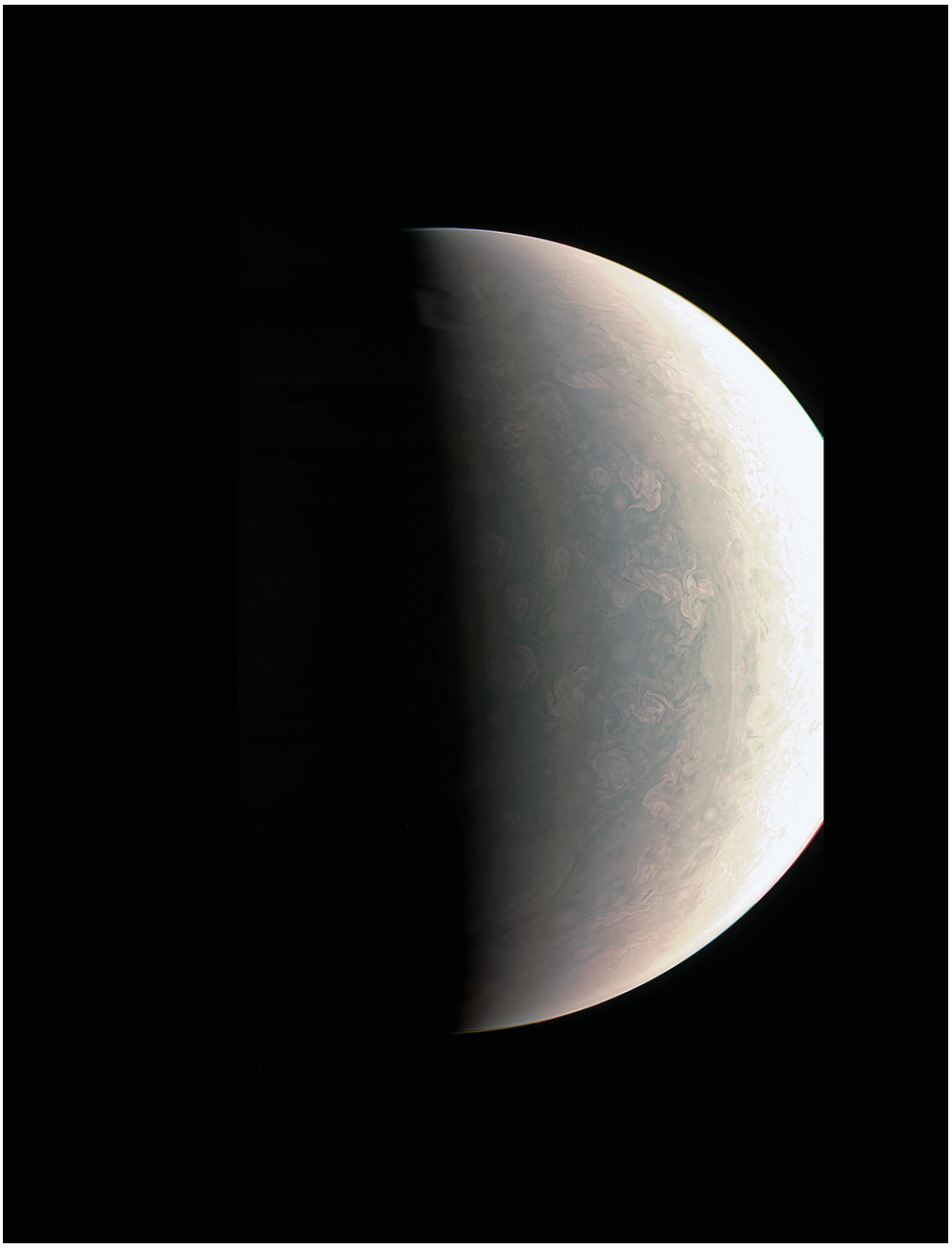

Figure 1.3: Image of Jupiter's North pole captured by the Juno spacecraft in August 27, 2016 (NASA, 2016c).

interior structure of Jupiter has three unique, quasi-homogeneous regions that can be classified from the interior to the surface as the solid inner core, the fluid metallic envelope, and the fluid molecular layer (Guillot, 1999; Nellis, Weir, & Mitchell, 1996). The molecular layer consists primarily of molecular (or non-conductive) hydrogen and helium, which indicates that this region is not significantly affected by Lorentz forces. The metallic region on the

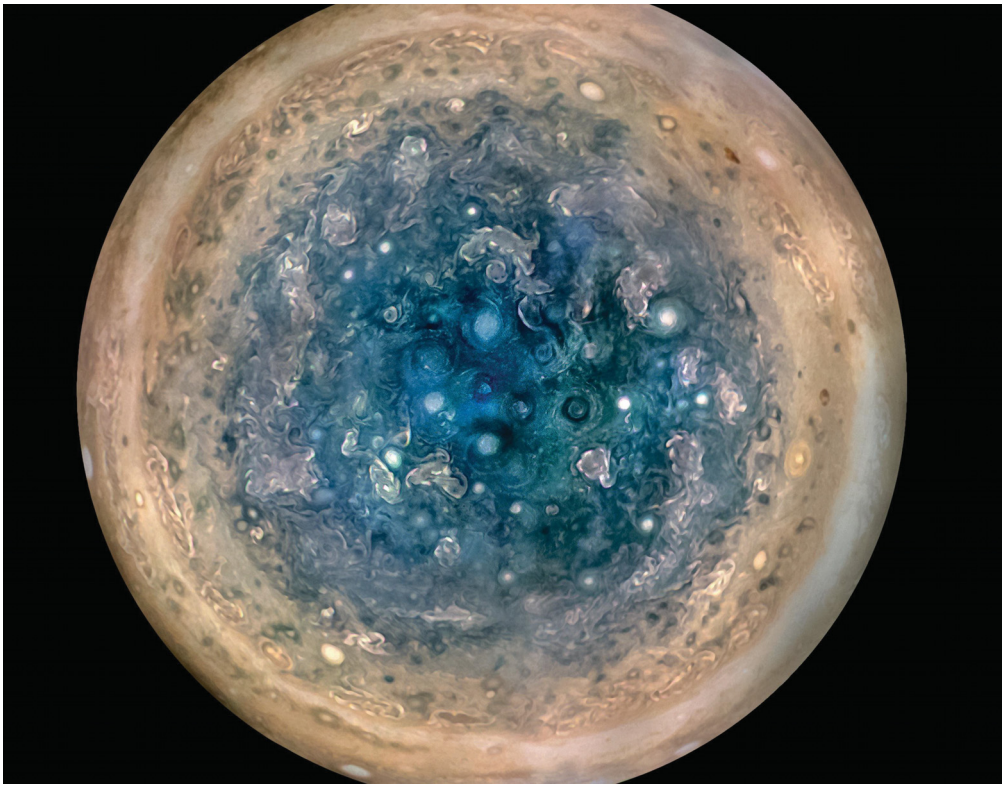

Figure 1.4: Image of Jupiter's South pole captured by the Juno spacecraft in 2017 at an altitude of 52,000 km (NASA, 2017).

other hand consists primarily of metallic (or conductive) hydrogen and helium, which implies that the regional fluid behaviour is significantly affected by Lorentz forces. From Gastine, Wicht, Duarte, Heimpel, and Becker (2014) and French et al. (2012), the molecular envelope in Jupiter extends from the surface to 0.9 of Jupiter's radius.

Saturn's atmosphere exhibits features similar to Jupiter's atmosphere. One feature that Saturn shares with Jupiter is that it exhibits a banded structure on its atmosphere, which can be seen in Figure 1.5. Similar to Jupiter, Saturn's banded structure is correlated with its zonal wind jets (Garcia-Melendo, Perez-Hoyos, Sanchez-Lavega, & Hueso, 2011; Smith et al., 1981). Due to observations collected from the Cassini spacecraft, Saturn also exhibits high latitude zonal jets (Garcia-Melendo et al., 2011). Eddies at both the North and South poles of Saturn are also observed, which can be seen in Figures 1.6 and 1.7, respectively. However, the molecular envelope has been estimated to be 0.6 of Saturn's radius from the surface (Liu, Goldreich, & Stevenson, 2008).

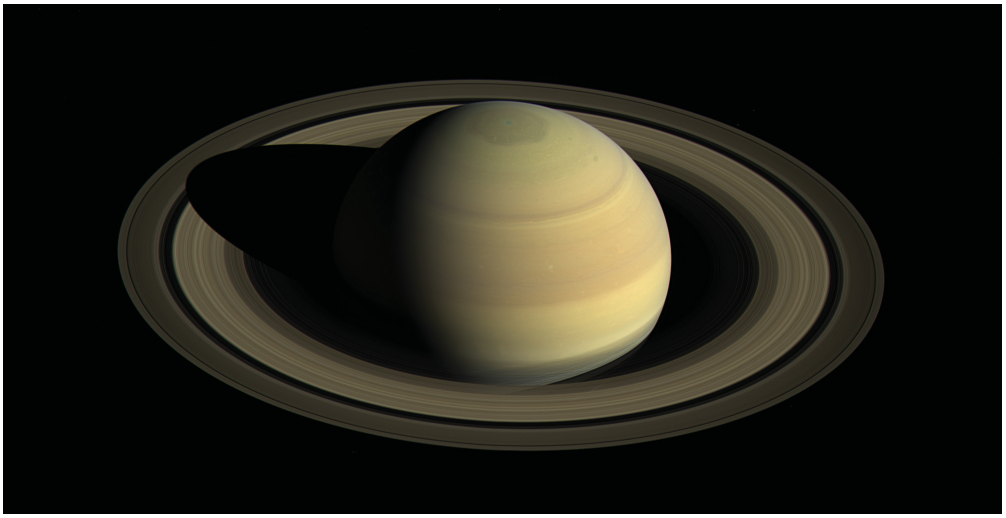

Figure 1.5: Image of Saturn captured by the Cassini spacecraft in 2016 (NASA, 2016d).

1.1.1 Galileo Mission

In 1989, the Galileo spacecraft was launched from the Atlantis space shuttle orbiting Earth towards Jupiter, with its mission to collect observational data on Jupiter and its moons over the course of two years (Fischer, 2001). Unlike the Voyager missions, Galileo was an orbiter one. The spacecraft released the Galileo probe in 1995, which was capable of collecting extensive data at Jupiter's atmosphere between the surface and 22 bars (D'Amario, Bright, & Wolf, 1992; Vasavada & Showman, 2005). Along with the data collected from Jupiter's moons, the Galileo mission was considered a success. At September 21, 2003, the Galileo probe was scuttled via direct plummet into Jupiter near the equator, thus marking the end of the Galileo mission (Vasavada & Showman, 2005).

Data collected by the atmospheric structure investigation instruments attached to the probe provides some information on the temperature structure of Jupiter's atmosphere between 0 and 22 bars at a planetographic latitude of roughly 7.3^oN (Atkinson et al., 1998; Magalhaes et al., 2002). From data collected by the instruments, Magalhaes et al. (2002) were able to derive the pressure dependant temperature gradient ($\mathrm{d}T/\mathrm{d}z_d$) profile of Jupiter's atmosphere with depth z_d. Based on the temperature data from the T_1 temperature sensor alone (see FIG. 7 of Magalhaes et al. (2002)), the pressure dependant temperature gradient profile varies between a minimum of roughly -0.10 K km^{-1} and a maximum of roughly 0.25 K km^{-1}. Based on Magalhaes et al. (2002), any value of $\mathrm{d}T/\mathrm{d}z_d > 0$ implies static stability. Strong stratification exists between 0 and 9 bars. However, the atmospheric region past 9 bars appears to be weakly stratified since $\mathrm{d}T/\mathrm{d}z_d$ fluctuates between that static stability and instability regions.

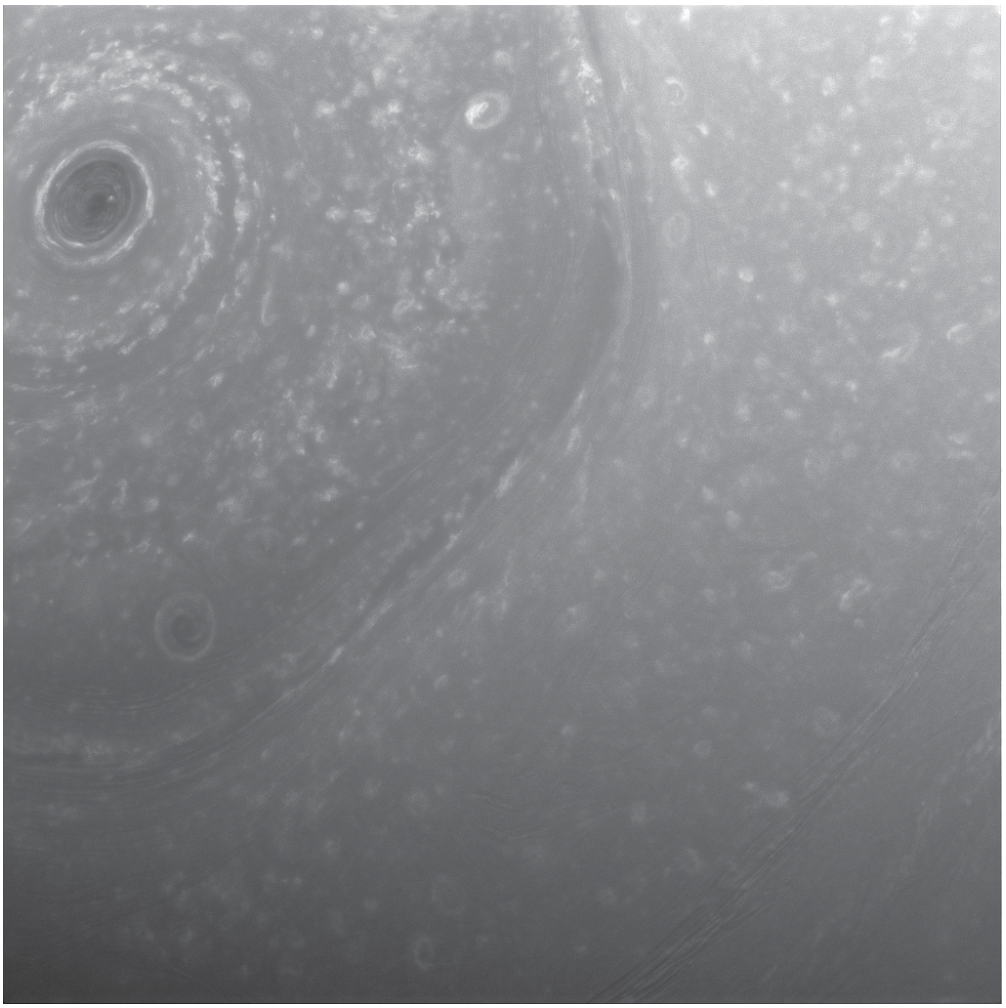

Figure 1.6: Image of Saturn's North pole captured by the Cassini spacecraft in December 3, 2016 (NASA, 2016a).

Along with the atmospheric structure investigation measurements, the Doppler winds experiment instruments attached to the Galileo probe has allowed it to collect zonal wind data up to and including 22 bars (Atkinson et al., 1998). The analysis of the zonal wind structure data (see Figure 4 of Atkinson et al. (1998)) indicates that these winds plateau at around 170 m s^{-1} past 10 bars up to and including 22 bars, and reaches a maximum of around 180m/s near 5 bars. This data suggest that the zonal wind structure could be constant beyond 22 bars. However, this is uncertain until more data can be collected beyond 22 bars in Jupiter's atmosphere.

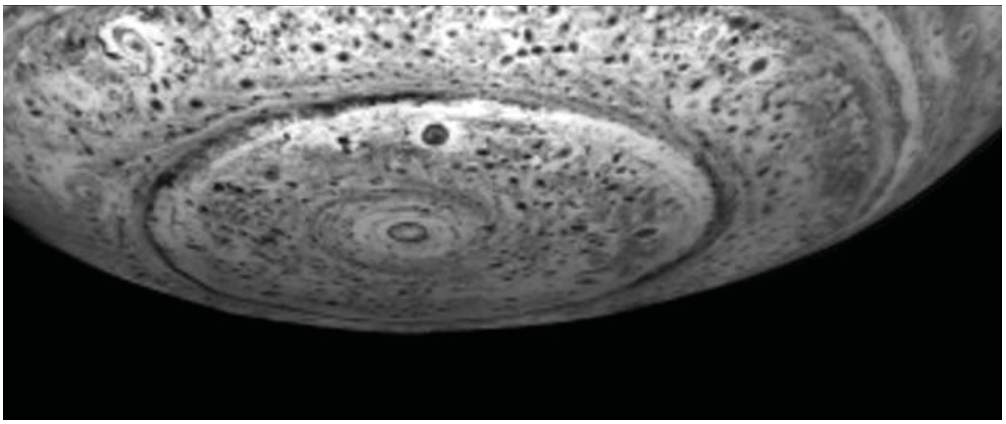

Figure 1.7: Image of Saturn's South pole captured by the Cassini spacecraft in May 11, 2007 (NASA, 2016b).

1.2 Two Models on Zonal Flow Driving Mechanism

The data provided by both the atmospheric structure investigation and Doppler winds experiment has sparked some controversy about how Jupiter is able to maintain such a strong zonal wind structure. One hypothesis called the shallow or weather layer hypothesis claims that the winds are restricted within the cloud layer, where these winds are driven by cloud physics. The other is the deep winds hypothesis, which claims that the winds are driven within the deep convective region of the planet.

1.2.1 Weather Layer Hypothesis

The weather layer hypothesis claims that these wind jets are driven by mechanisms within the cloud layer at the troposphere (Vasavada & Showman, 2005). From Irwin, Weir, Taylor, Calcutt, and Carlson (2001), belts from Jupiter's banded structure have high thermal emissions while zones have low thermal emissions, in which this variability is mainly driven by the cloud layer at around the 1.4 bar region. The likely mechanism for this thermal emissions contrast is the condensation in the cloud layer. This leads to latitudinal thermal contrasts that may result in vertical shear according to the thermal wind equations (Vasavada & Showman, 2005). From both the cloud layer and the thermal contrasts, this leads to the possibility that these flows are quasi-barotropic and are driven by baroclinic instabilities on a rapidly rotating planet (Williams, 1978).

1.2.2 Deep Winds Hypothesis

Based on the zonal wind profile from Atkinson et al. (1998), it suggests that these zonal flows are adiabatic. This could be due to a strong convection region in the deep interior that extends downward from the base of the stably stratified region to the base of Jupiter's molecular envelope (Vasavada & Showman, 2005). Assuming a convective rotating gas giant with a molecular layer, convection cells will form around the tangent cylinder as a result, where the tangent cylinder is a surface that is parallel to the planetary axis of rotation $\hat{\boldsymbol{z}}$ and is tangent to the inner boundary as seen in Figure 1.8 (Busse, 1976). The fluid in these convection cells moves in the form of Taylor columns that extend across the molecular layer (Busse, 1976; Pedlosky, 1987).

From the deep winds hypothesis, the zonal winds observed in Jupiter are driven from an interaction between the Taylor columns and the outer boundary within the molecular envelope (Busse, 1976). The interaction between the Taylor columns and the outer boundary leads to the generation of secondary zonal flow (Zhang, 1992). The curvature of the outer boundary also leads to a tilt in the convection cells (Zhang, 1992). This results in a positive feedback loop such that the generation of the secondary zonal flow will continue to tilt of the convection cells until the Reynolds stresses balances out the internal viscous stresses (Vasavada & Showman, 2005; Zhang, 1992). The zonal flow saturation and the energy cascade cessation can be scaled by the Rhines Scale, which is inversely proportional to the boundary curvature effect described by the β-parameter (Heimpel, Aurnou, & Wicht, 2005; Rhines, 1975). Note that previous deep winds models typically only consider the molecular layer. This is because the Lorentz forces associated with the metallic envelope act as a restoring force such that the fluid motion in this envelope is much less than the motion in the molecular layer.

1.2.3 Computational Models

Computational models that follow the weather layer hypothesis have seen success in generating some atmospheric properties as seen on Jupiter. A recent study by Morales-Juberias and Dowling (2013) was able to replicate a great storm similar to that of the Great Red Spot on Jupiter. However, their model does not include any cloud physics. Another study by Scott and Polvani (2007) was able to generate a banded structure on an anelastic rotating gas giant. Unfortunately, their model was unable to get the strong equatorial prograde jet observed on Jupiter. However, most computational models that follow the Weather Layer hypothesis are effectively 2.5-dimensional as radial or vertical velocity components are typ-

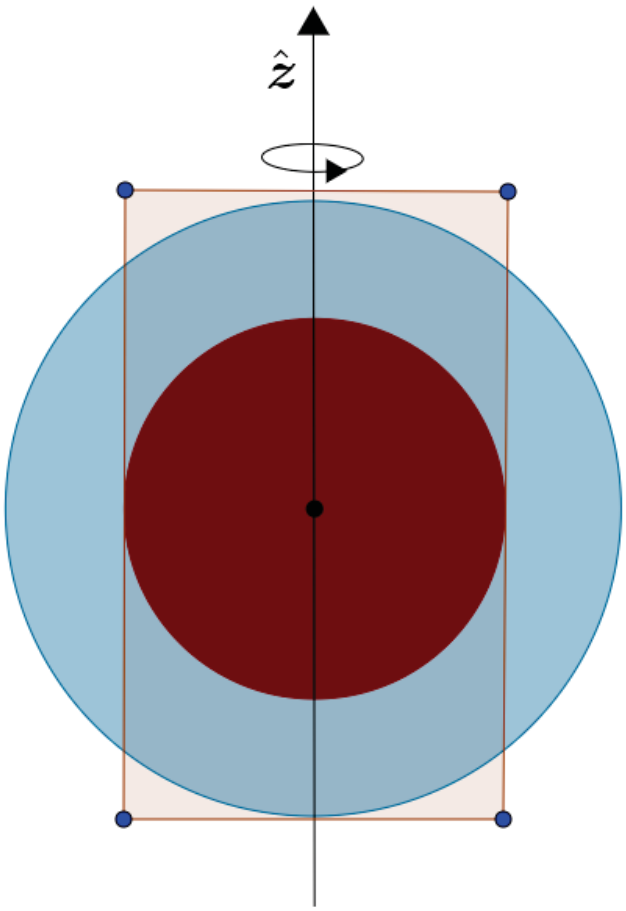

Figure 1.8: An azimuthal slice of a spherical shell rotating around $\hat{z}$ with the conductive layer shaded by red representing the inner boundary and the non-conductive layer shaded by blue. The tangent cylinder is represented by the orange translucent rectangle that is tangent to the inner boundary and parallel to $\hat{z}$. Note that the conductive layer has a radius of 0.6 of the spherical shell's radius.

ically solved from the mass conservation equation after numerically solving the horizontal velocity components assuming hydrostatic balance (Dowling et al., 1998; Rivier, Loft, & Polvani, 2002).

Numerical simulations following the deep winds hypothesis on gas giants have seen some success in generating zonal jets with properties equivalent to Jovian zonal jets. One of the first computational studies to generate zonal jets on a rotating Boussinesq convective spherical shell is from Heimpel et al. (2005). This experiment was able to generate a strong prograde equatorial jet and weaker high latitude alternating jets. Implementation of the

anelastic approximation has only occurred in recent studies. Both studies from Gastine and Wicht (2012) and Jones and Kuzanyan (2009) implemented rotating anelastic convective spherical shell models with constant entropy boundary conditions. Their results show that increasing the density stratification will cause the convection cells to form around the outer boundary instead of the inner boundary. The explanation for this behaviour is that the larger buoyancy terms become more confined near the outer boundary, while the fluid density increases at the inner boundary for increasing density stratification (Gastine & Wicht, 2012). The introduction of a stably stratified thin layer near the outer boundary have only been found in recent studies. For example, Takehiro and Lister (2001) implemented the stably stratified fluid layer near the outer boundary using constant temperature boundary conditions at the inner and outer radii for rotating convective Boussinesq spherical shell models. They showed that stably stratified fluid layer acts as a low pass filter, such that it attenuates the large wavenumber horizontal components of the convection cells. This means that the large wavenumber horizontal components can penetrate the stably stratified fluid layer while the small scale components remains within the convectively unstable layer. Thus, the implication is that the large scale horizontal components contributes to the zonal flow near the outer boundary. Another study from Heimpel, Gastine, and Wicht (2016) use constant entropy gradient boundary conditions to implement a stably stratified thin layer near the outer boundary of a rotating anelastic convective spherical shell. Since an inward radial entropy gradient is set at both boundaries, a volumetric entropy sink was used to ensure that the overall heat of the system does not increase to infinity over time. Their model exhibits a strong equatorial prograde jet, weaker higher latitude alternating jets and long-lived eddies at the poles.

1.3 Objectives

In this thesis, we use numerical models to explore the effects that the stratified layer near the top boundary have on the fluid dynamics of rotating anelastic spherical shells with convection, and the fluid dynamics of North polar regional models on a rotating Boussinesq spherical shell with convection. For our models with the stratified fluid layer, we conduct a parameter study by varying the thermal forcing, the density stratification, and the stratified fluid layer thickness of different models to see what dependancies the fluid motion exhibits. We find that the the stably stratified fluid layer has a tendency to suppress zonal flow oscillations. We also find that zonal jets become smoother as the stably stratified fluid layer increases. However, for near-Boussinesq models with the stratified fluid layer thickness that

extends from the outer boundary to half of the spherical shell, we are able to generate long-lived eddies and even great eddies, where these great eddies are comparable to the Great Red Spot on Jupiter. For the regional models, we apply the cubed-sphere coordinate system onto our North polar regional models to avoid the avoid the polar singularities that the conventional spherical Laplacian has. We also use various horizontal boundary conditions, such as periodic and open, to account for the strong fluid motion associated with convection. The results from these models are either unrealistic or numerically unstable.

Chapter one of describes the atmospheric dynamics of the gas giants based on observational data of Jupiter and Saturn. Chapter two introduces the numerical methods and software used in these models. Chapter three discusses the results and feasibility of using regional modelling of Boussinesq convection on the North pole of the rotating spherical shell. Chapter four discusses the implementation of the stably stratified fluid layer using the constant conductive radial entropy gradient boundary conditions and its effect on the fluid dynamics of the rotating anelastic convection on a spherical shell with varying density stratification and thermal forcing. Chapter five analyzes eddy generation of a near-Boussinesq model with an implemented stably stratified fluid layer.

Chapter 2

Numerical Methods

Two sets of numerical models were used to simulate atmospheric behaviour of gas giants. The first set of models use the global circulation model (GCM) software MITgcm. This software is versatile such that it allows the use of non-linear orthogonal coordinate systems. MITgcm was used to simulate fluid motion near the North pole of a rotating Boussinesq spherical shell using cubed-sphere coordinate system but with a maximum latitudinal extent with origin at 90^oN. The second set of models use a dynamo modelling software called MagIC, which allows for numerical simulations of the fluid motion of rotating anelastic spherical shells with convection.

2.1 MagIC

The pseudo-spectral software, MagIC, solves the magnetohydrodynamic (MHD) conservation equations for an anelastic fluid model in a spherical shell. This software is publicly available at `https://github.com/magic-sph/magic` under the GNU GPL v3 licence. This software was originally an anelastic solar dynamo code made by Glatzmaier (1984), which was later used for the geodynamo by Glatzmaier and Roberts (1995). Wicht (2002) modified the software to include an electrically conducting inner core. The Boussinesq version of the code called MAG was developed by U. Christensen, Olson, and Glatzmaier (1999), which uses temperature as its primary thermal variable. Further modifications by Gastine and Wicht (2012) implemented the anelastic approximation which replaced temperature with entropy. Recently, the spherical harmonics library called SHTns was implemented in MagIC (Schaeffer, 2013). MagIC allows for implementation of constant entropy and constant radial entropy gradient boundary conditions. This software was also tested and benchmarked against other dynamo models (Breuer et al., 2010; U. R. Christensen et al., 2001; Jones

et al., 2011). For this thesis, the non-magnetic form of the MHD equations are used with constant radial entropy gradient boundary conditions.

2.1.1 Rotating Boussinesq Convection Equations

A fluid that flows in response to heating below and cooling above undergoes the process of thermal convection (Chandrasekhar, 1981). Conservation of mass, momentum and energy are needed to provide a complete mathematical description of the fluid motion, in which the formulation of these equations can be seen in literature such as Chandrasekhar (1981), Pedlosky (1987), and Tritton (1988). In order to obtain a unique solution, boundary conditions need to be specified. For the case of a convective Boussinesq fluid, thermal boundary conditions across the top and bottom are defined with either constant temperature or constant radial temperature gradient.

For a convective fluid inside a spherical shell with an inner radius r_i and an outer radius r_o with a rotation rate of $\boldsymbol{\Omega} = \Omega\hat{\boldsymbol{z}}$ along the axis of rotation $\hat{\boldsymbol{z}}$, the mass conservation equation is given by

$$\frac{\partial \rho}{\partial t} + \nabla \cdot \rho \boldsymbol{u} = 0, \tag{2.1}$$

where $\rho = \rho(\boldsymbol{r}, t)$ is the density with spherical position vector $\boldsymbol{r} = (r, \theta, \phi)$ and time t, and $\boldsymbol{u} = \boldsymbol{u}(u_r(\boldsymbol{r}, t), u_\phi(\boldsymbol{r}, t), u_\theta(\boldsymbol{r}, t))$ is the velocity field that includes the r, ϕ, and θ velocity components defined as u_r, u_ϕ, and u_θ, respectively.

The momentum conservation equation with rotation and convection is given by

$$\frac{\partial \boldsymbol{u}}{\partial t} + \boldsymbol{u} \cdot \nabla \boldsymbol{u} = -\frac{1}{\rho}\nabla P - 2\Omega(\hat{\boldsymbol{z}} \times \boldsymbol{u}) + \nu\nabla^2 \boldsymbol{u} + \alpha g T \hat{\boldsymbol{r}} - g\hat{\boldsymbol{r}}, \tag{2.2}$$

where $P = P(\boldsymbol{r}, t)$ is the pressure, $T = T(\boldsymbol{r}, t)$ is the temperature, ν is the kinematic viscosity, α is the thermal expansion coefficient, and g is the gravitational acceleration along the $\hat{\boldsymbol{r}}$ direction. However, we can rewrite the pressure as

$$P = P + P', \tag{2.3}$$

where P_0 is the hydrostatic pressure and P' is the perturbation pressure. Since $\nabla \bar{P} = -g\rho\hat{\boldsymbol{r}}$, we can rewrite the momentum conservation equation as

$$\frac{\partial \boldsymbol{u}}{\partial t} + \boldsymbol{u} \cdot \nabla \boldsymbol{u} = -\frac{1}{\rho}\nabla P' - 2\Omega(\hat{\boldsymbol{z}} \times \boldsymbol{u}) + \nu\nabla^2 \boldsymbol{u} + \alpha g T \hat{\boldsymbol{r}}. \tag{2.4}$$

The energy conservation equation with no internal heat generation is defined by

$$\frac{\partial T}{\partial t} + \boldsymbol{u} \cdot \nabla T = \kappa \nabla^2 T, \tag{2.5}$$

where κ is the thermal diffusivity.

Under the Boussinesq approximation, a fluid that can be treated as incompressible from the flow can simplify the governing equations by making $\rho = \rho_0$ homogeneous in all but the energy conservation equation. This simplifies equation (2.1) to

$$\nabla \cdot \boldsymbol{u} = 0, \tag{2.6}$$

which changes equation (2.4) to

$$\frac{\partial \boldsymbol{u}}{\partial t} + \boldsymbol{u} \cdot \nabla \boldsymbol{u} = -\frac{1}{\rho_0} \nabla P' - 2\Omega(\hat{\boldsymbol{z}} \times \boldsymbol{u}) + \nu \nabla^2 \boldsymbol{u} + \alpha g T \hat{\boldsymbol{r}}. \tag{2.7}$$

This approximation is valid when modelling thermal convection in oceans, mantles and inner cores, where the fluid experiences negligible density changes due to compression (Glatzmaier, 2014).

2.1.1.1 Dynamic Similarity

If the non-dimensional governing parameters of two similar fluid systems match each other equally, then their fluid motion are dynamically similar to each other (Tritton, 1988). In the case for rotating convection, these governing parameters can be obtained by first determining the non-dimensional form of the governing equations. In order to convert the governing equations represented by equations (2.5) to (2.7) into their non-dimensional form, the variables $\boldsymbol{z}$, $\boldsymbol{u}$, t, T, and P must first be expressed in terms of their dimensionless counterparts

denoted by the * notation represented by the following equations:

$$\begin{aligned}
\boldsymbol{r} &= (d)\,\boldsymbol{r}^*, \\
\boldsymbol{u} &= \left(\frac{\kappa}{d}\right)\boldsymbol{u}^*, \\
t &= \left(\frac{d^2}{\kappa}\right)t^*, \\
T &= (\Delta T)T^*, \\
P' &= \left(\frac{\rho\kappa\nu}{d^2}\right)P^*.
\end{aligned} \tag{2.8}$$

Note that $d = r_o - r_i$ represents the length scale, d^2/κ represents the thermal diffusion time scale, and ΔT represents the temperature difference between the top and bottom boundaries.

Substituting equation (2.8) into the momentum conservation equation (2.4) turns it into

$$\begin{aligned}
\left(\frac{\kappa^2}{d^3}\right)\left(\frac{\partial \boldsymbol{u}^*}{\partial t^*} + \boldsymbol{u}^*\cdot\nabla^*\boldsymbol{u}^*\right) = &-\left(\frac{\rho\kappa\nu}{d^3}\right)\frac{1}{\rho}\nabla^* P^* - \left(\frac{\kappa}{d}\right)2\Omega(\hat{\boldsymbol{z}}\times\boldsymbol{u}^*) + \\
&+\left(\frac{\kappa}{d^3}\right)\nu\nabla^{*2}\boldsymbol{u}^* + (\Delta T)\alpha g T^*\hat{r},
\end{aligned} \tag{2.9}$$

where $\nabla = (1/d)\nabla^*$.

Dividing both sides of equation (2.9) by κ^2/d^3 leads to

$$\begin{aligned}
\left(\frac{\partial \boldsymbol{u}^*}{\partial t^*} + \boldsymbol{u}^*\cdot\nabla^*\boldsymbol{u}^*\right) = &-\left(\frac{\nu}{\kappa}\right)\nabla^* P^* - \left(\frac{d^2}{\kappa}\right)2\Omega(\hat{\boldsymbol{z}}\times\boldsymbol{u}^*) + \\
&+\left(\frac{1}{\kappa}\right)\nu\nabla^{*2}\boldsymbol{u}^* + \left(\frac{\Delta T d^3}{\kappa^2}\right)\alpha g T^*\hat{r}.
\end{aligned} \tag{2.10}$$

However, dividing both sides of equation (2.10) by ν/κ leads to

$$\left(\frac{\kappa}{\nu}\right)\left(\frac{\partial \boldsymbol{u}^*}{\partial t^*} + \boldsymbol{u}^* \cdot \nabla^* \boldsymbol{u}^*\right) = -\nabla^* P^* - 2\left(\frac{\Omega d^2}{\nu}\right)(\hat{\boldsymbol{z}} \times \boldsymbol{u}^*) + \nabla^{*2}\boldsymbol{u}^* + \left(\frac{g\alpha \Delta T d^3}{\kappa\nu}\right) T^* \hat{r}. \tag{2.11}$$

The coefficients in equation (2.11) form the non-dimensional parameters that classify and govern the fluid motion present in the system. Rewriting equation (2.11) as

$$\frac{1}{Pr}\left(\frac{\partial \boldsymbol{u}^*}{\partial t^*} + \boldsymbol{u}^* \cdot \nabla^* \boldsymbol{u}^*\right) = -\nabla^* P^* - \frac{2}{E}(\hat{\boldsymbol{z}} \times \boldsymbol{u}^*) + \nabla^{*2}\boldsymbol{u}^* + RaT^* \hat{r}, \tag{2.12}$$

these parameters are called the Prandtl Number Pr, the Ekman Number E, and the Rayleigh number Ra, which are represented by

$$Pr = \frac{\nu}{\kappa}, \tag{2.13}$$

$$E = \frac{\nu}{\Omega d^2}, \tag{2.14}$$

and

$$Ra = \frac{g\alpha d^3 \Delta T}{\kappa\nu}. \tag{2.15}$$

The Prandtl number Pr is defined as the ratio between kinematic viscosity and thermal diffusivity. The Ekman number E represents the ratio between kinematic viscosity and the Coriolis term. The Rayleigh number Ra represents the ratio between buoyancy term and the diffusivity term (Wicht, 2002). Note that each convective model has a critical Rayleigh number Ra_c. If $Ra > Ra_c$, then instabilities occur in the fluid model due to convection (Chandrasekhar, 1981). Otherwise, the fluid remains stable with a dominant conductive heat transport.

Equation (2.8) is substituted into the energy conservation equation (2.5), becoming

$$\left(\frac{\kappa \Delta T}{d^2}\right)\left(\frac{\partial T^*}{\partial t^*} + \boldsymbol{u^*} \cdot \nabla^* T^*\right) = \left(\frac{\kappa \Delta T}{d^2}\right)\nabla^{*2} T^*. \tag{2.16}$$

Since the coefficients on both sides of equation (2.16) are the same, the conservation equation remains relatively unchanged as seen by the following equation:

$$\frac{\partial T^*}{\partial t^*} + \boldsymbol{u}^* \cdot \nabla^* T^* = \nabla^{*2} T^*. \tag{2.17}$$

Likewise, the conservation of mass equation represented by equation (2.6) is simply

$$\nabla^* \cdot \boldsymbol{u}^* = 0. \tag{2.18}$$

2.1.2 Rotating Anelastic Convection Equations

For fluid models that undergo non-negligible density variations under mechanical forcing, the Boussinesq approximation would not be appropriate to use. However, solving the fully compressible rotating convection equations would also include sound waves in the model. Unfortunately, sound waves would make resolving the model computationally costly because the timescales of them are much smaller than the timescales of the convective fluid motion (Jones et al., 2011). Therefore, an appropriate approximation to use that would allow for non-negligible density variations and eliminate sound waves is be the anelastic approximation.

Based on Jones et al. (2011) and Gastine and Wicht (2012), the rotating anelastic convection equations are derived by separating the thermodynamic variables (density ρ, temperature T and pressure P) into their adiabatic background state (denoted by the bar notation) and perturbation term (denoted by the $'$ notation). These variable turn into the following equations:

$$\begin{aligned} \rho &= \bar{\rho} + \rho', \\ T &= \bar{T} + T', \\ P &= \bar{P} + P'. \end{aligned} \tag{2.19}$$

Assuming that gravity $g(r) \sim r^{-2}$ for a fluid in a spherical shell with inner radius r_i and an outer radius r_o, $\bar{\rho}$ is defined as

$$\bar{\rho}(r) = \bar{T}^{m_p}, \tag{2.20}$$

where $\bar{T}$ is represented by

$$\bar{T}(r) = \frac{c_0}{(1-\eta)r} + 1 - c_0. \tag{2.21}$$

The coefficient c_0 is defined as

$$c_0 = \frac{\eta}{1-\eta}\left(\exp\left[\frac{N_\rho}{m}\right] - 1\right), \tag{2.22}$$

where N_ρ is defined by

$$N_\rho = \ln\left[\frac{\bar{\rho}(r_i)}{\bar{\rho}(r_o)}\right]. \tag{2.23}$$

Note that $\eta = r_i/r_o$ represents the radius ratio and N_ρ represents the number of density scale heights or density stratification (Gastine & Wicht, 2012). The fluid in the spherical shell is modelled as an ideal gas with background density $\bar{\rho}$, background temperature $\bar{T}$, and polytropic index m_p (Gastine & Wicht, 2012).

From Gastine and Wicht (2012), this leads to the dimensionless conservation equations for mass, momentum and energy defined as

$$\nabla \cdot \bar{\rho}\boldsymbol{u} = 0, \tag{2.24}$$

$$E\left(\frac{\partial \boldsymbol{u}}{\partial t} + \boldsymbol{u}\cdot\nabla\boldsymbol{u}\right) = \frac{1}{\bar{\rho}}\nabla P' - 2\hat{\boldsymbol{z}}\times\boldsymbol{u} + \frac{RaE}{Pr}\frac{r_o^2}{r^2}s\hat{\boldsymbol{r}} + \frac{E}{\bar{\rho}}\nabla\cdot S, \tag{2.25}$$

and

$$\bar{\rho}\bar{T}\left(\frac{\partial s}{\partial t} + \boldsymbol{u}\cdot\nabla s\right) = \frac{1}{Pr}\nabla\cdot\bar{\rho}\bar{T}\nabla s + Di\bar{\rho}S^2, \tag{2.26}$$

respectively, where the traceless rate-of-strain tensor S is represented by

$$S = \bar{\rho}\left(\frac{\partial u_i}{\partial x_j} + \frac{\partial u_j}{\partial x_i} - \frac{2}{3}\delta_{ij}\frac{\partial u_k}{\partial x_k}\right). \tag{2.27}$$

Equation (2.27) is in indicial notation using the Kronecker delta δ_{ij}. Note that these equations are applied onto a fluid in a spherical shell of shell thickness $d = r_o - r_i$ with a rotation rate of Ω around an axis of rotation $\hat{\boldsymbol{z}}$ with an entropy difference of Δs across the inner and outer radii. The fluid properties used in these equations are thermal diffusivity κ, kinematic

viscosity ν and specific heat at constant pressure c_p.

Similar to the non-dimensional form for the Boussinesq rotating convection equations, the anelastic rotating convection equations also have governing non-dimensional parameters. For the anelastic version, the Prandtl number Pr, Ekman number E and Rayleigh number defined by the following equations:

$$Pr = \frac{\nu}{\kappa}, \tag{2.28}$$

$$E = \frac{\nu}{\Omega d^2}, \tag{2.29}$$

$$Ra = \frac{g_o \alpha d^3 \Delta s}{c_p \kappa \nu}. \tag{2.30}$$

Note that $g_o = g(r = r_o)$. The dissipation number Di is defined by

$$Di = \frac{\eta Pr}{Ra}\left(\exp\left[\frac{N_\rho}{m}\right] - 1\right). \tag{2.31}$$

Another non-dimensional parameter that can also be applied to equation (2.24) is the modified Rayleigh number Ra^* defined by

$$Ra^* = \frac{RaE^2}{Pr} = \frac{g_o \Delta s}{c_p \Omega d}, \tag{2.32}$$

which turns equation (2.25) into

$$E\left(\frac{\partial \boldsymbol{u}}{\partial t} + \boldsymbol{u}\cdot\nabla\boldsymbol{u}\right) = \frac{1}{\bar{\rho}}\nabla P' - 2\hat{\boldsymbol{z}}\times\boldsymbol{u} + \frac{Ra^*}{E}\frac{r_o^2}{r^2}s\hat{\boldsymbol{r}} + \frac{E}{\bar{\rho}}\nabla\cdot S. \tag{2.33}$$

However, to obtain unique solutions in solving these governing equations, boundary conditions need to be defined at r_i and r_o. For the case of an anelastic fluid, constant conductive entropy or constant conductive entropy gradient boundary conditions can be implemented. As such, the modified flux-based Rayleigh number Ra_f^* is introduced and defined by

$$Ra_f^* = \frac{g}{c_p \Omega^2}\left|\frac{\partial s_c}{\partial r}\right| Nu^*, \tag{2.34}$$

where s_c is the conductive entropy and Nu^* is the modified Nusselt number represented by

$$Nu^* = \frac{Q_f}{\rho T \Omega d^2 (\mathrm{d}s_c/\mathrm{d}r))}. \tag{2.35}$$

Note that Q_f represents the heat flux.

2.1.3 Poloidal and Toroidal Decomposition

Before discussing the numerical methods used in the pseudo-spectral code MagIC, a description of poloidal and toroidal decomposition is needed. The following sections detailing the poloidal and toroidal decomposition, the spherical harmonic representation, the radial representation, and the time stepping are based on the MagIC documentation.

Any vector field, $\boldsymbol{a}$, that satisfies

$$\nabla \cdot \boldsymbol{a} = 0 \tag{2.36}$$

is called a solenoidal field. Since $\bar{\rho}\boldsymbol{u}$ in the mass conservation equation for the anelastic approximation defined by equation (2.24) satisfies (2.36), it can be separated into poloidal and toroidal components defined by

$$\bar{\rho}\boldsymbol{u} = \nabla \times (\nabla \times U_\gamma \hat{\boldsymbol{r}}) + \nabla \times U_\zeta \hat{\boldsymbol{r}}, \tag{2.37}$$

where U_γ is the poloidal potential and U_ζ is the toroidal potential.

In spherical coordinates, the horizontal gradient operator $\nabla_H b$, the horizontal divergence operator $\nabla_H \cdot \boldsymbol{a}$, and the horizontal curl operator $\nabla_H \times \boldsymbol{a}$ are defined by

$$\nabla_H b = \frac{1}{r}\frac{\partial b}{\partial \theta}\hat{\boldsymbol{\theta}} + \frac{1}{r\sin\theta}\frac{\partial b}{\partial \phi}\hat{\boldsymbol{\phi}}, \tag{2.38}$$

$$\nabla_H \cdot \boldsymbol{a} = \frac{1}{r\sin\theta}\frac{\partial}{\partial \theta}\left(\sin\theta \boldsymbol{a}\cdot\hat{\boldsymbol{\theta}}\right) + \frac{1}{r\sin\theta}\frac{\partial}{\partial \phi}\left(\boldsymbol{a}\cdot\hat{\boldsymbol{\phi}}\right), \tag{2.39}$$

and

$$\nabla_H \times \boldsymbol{a} = \frac{1}{r}\left[\frac{1}{\sin\theta}\frac{\partial}{\partial \phi}(\boldsymbol{a}\cdot\hat{\boldsymbol{r}}) - \frac{\partial}{\partial r}(r\boldsymbol{a}\cdot\hat{\boldsymbol{\phi}})\right]\hat{\boldsymbol{\theta}} + \frac{1}{r}\left[\frac{\partial}{\partial r}(r\boldsymbol{a}\cdot\hat{\boldsymbol{\theta}}) - \frac{\partial}{\partial \theta}(\boldsymbol{a}\cdot\hat{\boldsymbol{r}})\right]\hat{\boldsymbol{\phi}}, \tag{2.40}$$

where b is any given scalar field (e.g., Griffiths, 1999). The horizontal Laplacian Δ_H is a

combination of both the horizontal gradient and the horizontal divergence and is defined by

$$\Delta_H = \nabla_H \cdot \nabla_H = \frac{1}{r^2 \sin\theta} \frac{\partial}{\partial\theta} \left(\sin\theta \frac{\partial}{\partial\theta} \right) + \frac{1}{r^2 \sin^2\theta} \frac{\partial^2}{\partial\phi^2}, \tag{2.41}$$

which can operate on any scalar field.

Expanding equation (2.37) turns $\bar{\rho}\boldsymbol{u}$ into

$$\begin{aligned} \bar{\rho}\boldsymbol{u} = & \frac{1}{r} \left[-\frac{1}{r\sin\theta} \left(\frac{\partial}{\partial\theta} \left(\sin\theta \frac{\partial U_\gamma}{\partial\theta} \right) + \frac{1}{\sin\theta} \frac{\partial^2 U_\gamma}{\partial\phi^2} \right) \hat{\boldsymbol{r}} + \left(\frac{\partial}{\partial r} \frac{\partial U_\gamma}{\partial\theta} \right) \hat{\boldsymbol{\theta}} + \right. \\ & \left. + \frac{1}{\sin\theta} \left(\frac{\partial}{\partial r} \frac{\partial U_\gamma}{\partial\phi} \right) \hat{\boldsymbol{\phi}} \right] + \frac{1}{r} \left[\frac{1}{\sin\theta} \left(\frac{\partial U_\zeta}{\partial\phi} \right) \hat{\boldsymbol{\theta}} - \left(\frac{\partial U_\zeta}{\partial\theta} \right) \hat{\boldsymbol{\phi}} \right], \end{aligned} \tag{2.42}$$

which can be simplified into

$$\bar{\rho}\boldsymbol{u} = -\Delta_H U_\gamma \hat{\boldsymbol{r}} + \nabla_H \frac{\partial}{\partial r} U_\gamma + \nabla_H \times (U_\zeta \hat{\boldsymbol{r}}). \tag{2.43}$$

Taking the curl of $\bar{\rho}\boldsymbol{u}$ turns equation (2.43) into

$$\begin{aligned} \nabla \times \bar{\rho}\boldsymbol{u} = & \left[-\frac{1}{r\sin\theta} \frac{\partial}{\partial\phi} \left(\Delta_H + \frac{\partial^2}{\partial r^2} \right) U_\gamma \hat{\boldsymbol{\theta}} + \frac{1}{r} \frac{\partial}{\partial\theta} \left(\Delta_H + \frac{\partial^2}{\partial r^2} \right) U_\gamma \hat{\boldsymbol{\phi}} \right] + \\ & + \left[\frac{1}{r^2\sin\theta} \left(\frac{\partial}{\partial\theta} \left(\sin\theta \frac{\partial U_\zeta}{\partial\theta} \right) + \frac{1}{\sin\theta} \left(\frac{\partial^2 U_\zeta}{\partial\phi^2} \right) \right) \hat{\boldsymbol{r}} + \right. \\ & \left. + \frac{1}{r} \left(\frac{\partial}{\partial r} \frac{\partial U_\zeta}{\partial\theta} \right) \hat{\boldsymbol{\theta}} + \frac{1}{r\sin\theta} \left(\frac{\partial}{\partial r} \frac{\partial U_\zeta}{\partial\phi} \right) \hat{\boldsymbol{\phi}} \right], \end{aligned} \tag{2.44}$$

which can be simplified into

$$\nabla \times \bar{\rho}\boldsymbol{u} = \frac{1}{r} \left[\left(\frac{\partial}{\partial\theta} \hat{\boldsymbol{\phi}} - \frac{1}{\sin\theta} \frac{\partial}{\partial\phi} \hat{\boldsymbol{\theta}} \right) \left(\Delta_H + \frac{\partial^2}{\partial r^2} \right) U_\gamma \right] + \nabla_H \frac{\partial}{\partial r} U_\zeta - \Delta_H U_\zeta \hat{\boldsymbol{r}}. \tag{2.45}$$

2.1.4 Spherical Harmonic Representation

A natural choice for expanding the θ and ϕ terms is the spherical harmonics function $Y_l^m(\theta,\phi)$ defined by

$$Y_l^m(\theta,\phi) = P_l^m(\cos\theta)e^{im\phi}, \tag{2.46}$$

where l and m represent the degree and order, respectively. The function P_l^m is the associated Legendre function defined by

$$P_l^m(x) = (1-x^2)^{|m|/2}\left(\frac{\mathrm{d}}{\mathrm{d}x}\right)^{|m|} P_l(x), \tag{2.47}$$

where P_l represents the Legendre polynomial defined by

$$P^l(x) = \frac{1}{2^l l!}\left(\frac{\mathrm{d}}{\mathrm{d}x}\right)^l (x^2-1)^l, \tag{2.48}$$

(e.g., Griffiths, 2005).

MagIC normalizes equation (2.46) using the orthogonality relation represented by

$$\int_0^{2\pi}\int_0^{\pi} Y_l^m(\theta,\phi)\bar{Y}_{l'}^{m'}(\theta,\phi)\sin\theta\mathrm{d}\theta\mathrm{d}\phi = \delta_{ll'}\delta^{mm'}, \tag{2.49}$$

leading to

$$Y_l^m(\theta,\phi) = \sqrt{\frac{1}{4\pi}\frac{(2l+1)(l-|m|)!}{2(l+|m|)!}}P_l^m(\cos\theta)e^{im\phi}(-1)^m. \tag{2.50}$$

Note that $\bar{Y}_l^m$ represents the complex conjugate of Y_l^m. Thus, the poloidal potential $U_\gamma(r,\theta,\phi)$ can be represented in terms of the normalized spherical harmonics. This means that $U_\gamma(r,\theta,\phi)$ can be defined as

$$U_\gamma(r,\theta,\phi) = \sum_{l=0}^{l_{max}}\sum_{m=-l}^{l} W_{lm}(r)Y_l^m(\theta,\phi). \tag{2.51}$$

In order to transform $U_\gamma(r,\theta,\phi)$ from grid space into spherical harmonic space, a two step process is needed. The spherical coefficient function $W_{lm}(r)$, represented by

$$W_{lm}(r) = \frac{1}{\pi}\int_0^{\pi} W_m(r,\theta)P_l^m(\cos\theta)\sin\theta\mathrm{d}\theta, \tag{2.52}$$

needs to be solved, where $W_m(r,\theta)$ is defined by

$$W_m(r,\theta) = \frac{1}{2\pi}\int_0^{\pi} U_\gamma(r,\theta,\phi)e^{-im\phi}\mathrm{d}\phi. \tag{2.53}$$

Note that $U_\gamma(r,\theta,\phi)$ is a real function such that the complex conjugate of $W_{lm}(r)$ can be rewritten as $W^*_{lm}(r) = W_{l,-m}$ due to the symmetry of spherical harmonics. As a result, $m \geq 0$ is only considered when solving for $W_{lm}(r)$.

MagIC solves the coefficient function by first discretizing the grid space in θ and ϕ. The latitudinal points are defined as $\theta = \theta_j$, which are set by the Gaussian quadrature with N_θ number of points while $\phi = \phi_i$ are the longitudinal points defined evenly with a minimum $N_\phi = l_{max} + 1$ number of points. MagIC numerically solves (2.52) using

$$g_{lm}(r) = \frac{1}{N_\theta}\sum_{j=1}^{N_\theta} w_j g_m(r,\theta_j)P_l^m(\cos\theta_j), \tag{2.54}$$

where fast Fourier transforms are applied in the longitudinal direction where w_j represents the weights. Note that l_{max} is chosen such that $l_{max} = (N_\theta - 1)/3$ in order to prevent aliasing.

2.1.5 Radial Representation

The radial dependencies are expanded into Chebyshev polynomials $C_n(x)$, which is defined by

$$C_n(x) = \cos(n\arccos(x)) \tag{2.55}$$

of order n for $-1 \leq x \leq 1$ in MagIC. However, $-1 \leq x \leq 1$ is mapped onto the radial direction of range $r_i \leq r \leq r_o$. Expanding $W_{lm}(r)$ in terms of $C_n(r)$ leads to

$$W_{lm}(r) = \sum_{n=0}^{N} W_{lmn}C_n(r), \tag{2.56}$$

which is truncated to order N.

To transform $W_{lr}(r)$ into spectral space from grid space, W_{lmn} must be solved by

$$W_{lmn} = \frac{2-\delta_{n0}}{\pi}\int_{-1}^{1}\frac{W_{lm}(r(x))C_n(x)}{\sqrt{1-x^2}}\mathrm{d}x, \tag{2.57}$$

where $x(r)$ is defined as

$$x(r) = 2\frac{r - r_i}{r_o - r_i} - 1. \tag{2.58}$$

For C_{Nr-1} with N_r number of Chebyshev radial grid points, the radial grid points with index $k = 1, 2, ..., N_r$ can be determined by first discretizing x using

$$x_k = \cos\left(\pi\frac{k-1}{N_r - 1}\right). \tag{2.59}$$

Then, the Chebyshev radial grid points are chosen using the Chebyshev polynomials defined by

$$C_n(x_k) = \cos\left(\pi\frac{n(k-1)}{N_r - 1}\right) \tag{2.60}$$

The advantage of using the Chebyshev polynomials for defining the radial grid points is that it increases the grid point density towards the inner and outer boundaries where thermal and viscous boundary layers are defined, allowing the program to better resolve the fluid behaviour near the boundaries. To prevent aliasing, $N > N_r$ must be chosen where N represents the total number of radial grid points and is typically chosen as $N = N_r + 2$.

2.1.6 Time Stepping

MagIC uses a combination of both implicit and explicit approaches for time stepping. Explicit time stepping schemes are typically accurate but are computationally expensive due to the rather low time step δt required to satisfy the stability criterion of the given numerical model (Press, Teukolsky, Vetterling, & Flannery, 2007). On the other hand, implicit time stepping schemes are typically stable for larger time steps, which can be more computationally efficient compared to explicit schemes. However, when choosing the appropriate scheme for solving the governing equations, a purely implicit scheme will not be computationally efficient since all of the spherical harmonic terms are coupled by the non-linear terms. This results in a loss in computational efficiency at higher resolution, which outweighs the gain from purely implicit schemes due to the involvement of a large matrix rather than a series of smaller matrices. Another foreseeable problem is the Coriolis term because it has the (l, m, n) modes that couple with the $(l-1, m, n)$ and $(l+1, m, n)$ modes. The Coriolis term also couples with both the toroidal and poloidal flow potentials. Thus, combining both implicit and explicit schemes would lead to a more computationally efficient method compared

to either fully implicit or fully explicit schemes.

To describe the explicit and implicit time stepping scheme that MagIC uses, the general differential equation in time needs to be considered and is defined as

$$\frac{\partial x}{\partial t} = -Q_I(x,t) + Q_E(x,t), \tag{2.61}$$

where Q_I represents the implicit time stepping scheme and Q_E represents the explicit time stepping scheme. Note that $Q_I^k = Q_I(x,t_k)$ and $x^k = x(t_k)$ where t_k represents the k^{th} time step. Using the recursive time stepping equation, $t_{k+1} = t_k + \delta t$, the implicit time stepping scheme can be defined as

$$\left(\frac{x^{k+1}-x^k}{\delta t}\right)_{Q_I} = -\left(wQ_I^{k+1} + (1-w)Q_I^k\right), \tag{2.62}$$

where the weight of t_{k+1} is defined as w. Note that if $w = 0.5$, then (2.62) resembles that of the implicit Crank-Nicholson scheme (Press et al., 2007).

The explicit time stepping scheme is defined as

$$\left(\frac{x^{k+1}-x^k}{\delta t}\right)_{Q_E} = \frac{3}{2}Q_E^k - \frac{1}{2}Q_E^{k-1}, \tag{2.63}$$

which is known as the Adams-Bashforth scheme.

The combination of equations (2.62) and (2.63) leads to

$$\left(\frac{x^{k+1}-x^k}{\delta t}\right) + wQ_I^{k+1} + (1-w)Q_I^k = \frac{3}{2}Q_E^k - \frac{1}{2}Q_E^{k-1}, \tag{2.64}$$

which is the mixed implicit and explicit time stepping scheme that MagIC uses.

2.1.7 Diagnostics and Output

MagIC has built-in functions that allows for output of diagnostic ascii files and visualization binary files. The diagnostics files are typically time series files, with emphasis on the kinetic energy time series. This kinetic energy time series file contains both the toroidal and poloidal volume averaged energy components, providing information on the thermal forcing strength and the zonal flow development of the fluid system. Another useful diagnostic file is the background entropy, density, and gravity radial profiles of the fluid system. The binary files on the other hand provide information on the entropy and velocity profiles of the fluid flow at a given timestep. The r, ϕ, and θ components of both the fluid velocity are available

for visualization along any surface of constant ϕ, θ, or r. The entropy profiles can also be visualized along any surface of constant ϕ, θ, or r. The fluid velocity is typically scaled by the Reynolds number $Re = Re(u_i)$ defined by

$$Re(u_i) = \frac{u_i d}{\nu}, \tag{2.65}$$

where it uses the i^{th} component of velocity field $\boldsymbol{u}$. The Reynolds number represents a ratio between the inertial forces and the momentum diffusivity. However, another non-dimensional number to scale the velocity field to is the Rossby number, which is defined by

$$Ro(u_i) = \frac{u_i}{\Omega d}. \tag{2.66}$$

For rotating fluid models, the Rossby number is preferred over the Reynolds number since it shows the strength of the fluid speed relative to the Coriolis term. To convert the Rossby number from the Reynolds number,

$$Ro = ReE \tag{2.67}$$

must be used, where E is the Ekman number. The kinetic energy is solved using a volume (V) integration given by

$$KE = \frac{1}{2}\int_V \bar{\rho}\boldsymbol{u}\cdot\boldsymbol{u}\mathrm{d}V, \tag{2.68}$$

which is separated into the toroidal and poloidal components KE_ζ and KE_γ, respectively, such that $KE = KE_\zeta + KE_\gamma$. However, to keep KE consistent with Gastine and Wicht (2012), the velocity $\boldsymbol{u}$ in equation (2.68) will not be scaled to Ro.

2.2 MITgcm

MITgcm is a global circulation model that can solve both the Boussinesq and anelastic governing equations of either ocean or atmospheric systems. This software is public, which is available at `http://mitgcm.org/public/source_code.html` under the copyright of Massachusetts Institute of Technology. This software uses the the finite-volume method to solve the Boussinesq non-hydrostatic governing equations using an Arakawa-C grid (Adcroft, Hill, & Marshall, 1997; Marshall, Adcroft, Hill, Perelman, & Heisey, 1997; Marshall, Hill, Perelman, & Adcroft, 1997). Due to the use of the finite-volume method, MITgcm allows for

implementation of flexible topography models systems from small scales (such as lakes or rivers) to larger scales (such as oceans or planets) (Adcroft, Campin, Hill, & Marshall, 2004). MITgcm also implements the forward quasi-second order Adams-Bashford time-stepping scheme for the momentum conservation equations (Adcroft et al., 1997). MITgcm boasts automatic maintenance for generated adjoint and allows for serial or parallel jobs across multiple computer technologies (Heimbach, Hill, & Giering, 2002; Hill, Adcroft, Jamous, & Marshall, 1999; Hill & Marshall, 1996). Furthermore, this program allows implementation of Cartesian, cylindrical, spherical, or any well defined orthogonal grid system such as the cubed-sphere grid, which was benchmarked against the cubed-sphere model by Held and Suarez (1994) (Adcroft et al., 2004). Another key feature for MITgcm is the implementation of horizontal open boundary conditions (Gopalakrishnan, Cornuelle, Hoteit, Rudnick, & Owens, 2013). For this thesis, the linear free-surface non-hydrostatic Boussinesq equations are used on a regional cubed-sphere oceanic model with several different horizontal boundary conditions implemented. The descriptions of the governing equations and open boundary conditions are based on the MITgcm documentation.

2.2.1 Governing Equations

Global circulation model's simulate fluid dynamical behaviour on atmospheric or oceanic systems that are typically associated with Earth. They do this by solving the conservation equations for mass, momentum and potential temperature equations. For oceanic models, the salinity conservation equation is used if salinity is included in the model. However, GCM's also require the density of states to solve these equations, which are normally based off an ocean or atmospheric system. For regional numerical models, horizontal and vertical boundary conditions must be set such that solving the governing equations converge to a unique solution.

The Boussinesq momentum conservation for the non-hydrostatic formulation is separated into both the horizontal and vertical components defined by

$$\frac{\partial \boldsymbol{u}_h}{\partial t} + \boldsymbol{u} \cdot \nabla \boldsymbol{u}_h + \frac{1}{\rho_0} \nabla_h P' + (2\boldsymbol{\Omega} \times \boldsymbol{u})_h = \boldsymbol{G}_h \tag{2.69}$$

and

$$\frac{\partial u_3}{\partial t} + \boldsymbol{u} \cdot \nabla u_3 + \frac{1}{\rho_0} \frac{\partial P'}{\partial x_3} + \hat{\boldsymbol{k}} \cdot (2\boldsymbol{\Omega} \times \boldsymbol{u}) - \frac{\rho'}{\rho_0} g = \hat{\boldsymbol{k}} \cdot \boldsymbol{G}, \tag{2.70}$$

respectively, under any given orthogonal coordinate system $\boldsymbol{x} = x_1 \hat{\boldsymbol{i}} + x_2 \hat{\boldsymbol{j}} + x_3 \hat{\boldsymbol{k}}$, where

$\hat{\boldsymbol{u}} = u_1(\boldsymbol{x})\hat{\boldsymbol{i}} + u_2(\boldsymbol{x})\hat{\boldsymbol{j}} + u_3(\boldsymbol{x})\hat{\boldsymbol{k}}$ is the velocity field, $_h$ notation denotes horizontal components $\hat{\boldsymbol{i}}$ and $\hat{\boldsymbol{j}}$, pressure P, density ρ, planetary vorticity $\boldsymbol{\Omega}$, and the dissipation and metric terms $\boldsymbol{G}$. Note that in order to derive equations (2.69) and (2.70), ρ and P are separated into their reference and perturbation terms denoted by $_0$ and $'$ notation, respectively, represented by

$$\rho = \rho_0 + \rho' \tag{2.71}$$

and

$$P = P_0 + P'. \tag{2.72}$$

Density ρ is typically associated with the equation of state, which in this case is the linear approximation for an ocean body defined by the empirical equation

$$\rho(T, \mathscr{S}, P) = \rho_0(1 - \alpha_T(T - T_0) - \beta_{\mathscr{S}}(\mathscr{S} - \mathscr{S}_0) + \beta_P(P - P_0)), \tag{2.73}$$

where $\mathscr{S}$ is salinity and T is temperature. The parameters α_T, $\beta_{\mathscr{S}}$ and β_P are defined as the thermal expansion coefficient, saline contraction coefficient and the compressibility coefficient, respectively. For an ocean system, these parameters are conventionally set to $\alpha_T \approx 2(\pm 1.5) \cdot 10^{-4}\mathrm{K}^{-1}$, $\beta_{\mathscr{S}} \approx 7.6(\pm 0.2) \cdot 10^{-4}\mathrm{ppt}^{-1}$ and $\beta_P \approx 4.1(\pm 0.5) \cdot 10^{-10}\mathrm{Pa}^{-1}$ (Vallis, 2006). Note that the reference or hydrostatic pressure P_0 is absent in the momentum conservation equation since it provides no contribution to the fluid dynamics.

Implementation of the free surface can also be included. Since the models of interest are convective fluid regional models on a rotating spherical shell, no precipitation, evaporation, or run-offs are needed. Therefore, the linear approximation for the free surface is given by

$$\frac{\partial \iota}{\partial t} + u_1|_{x_3=\iota-\iota_0}\frac{\partial \iota}{\partial x_2} + u_2|_{x_3=\iota-\iota_0}\frac{\partial \iota}{\partial x_2} + u_3|_{x_3=\iota-\iota_0} = 0, \tag{2.74}$$

where ι is the elevation of the fluid relative to the mean fluid elevation ι_0 (Roullet & Madec, 2000). Note that depth coordinate at ι_0 is set to $x_3 = 0$. Under the Boussinesq approximation, equation (2.74) can be rewritten as

$$\frac{\partial \iota}{\partial t} + u_1|_{x_3=\iota-\iota_0}\left[1 - \frac{\partial \iota}{\partial x_2}\right] + u_2|_{x_3=\iota-\iota_0}\left[1 - \frac{\partial \iota}{\partial x_2}\right] = 0. \tag{2.75}$$

Note that the linear free surface approximation is needed if the non-rigid lid and free-slip top boundary conditions are implemented in MITgcm. For rotating convective fluid dynamics, the rigid lid approximation would be detrimental as it filters out external gravity waves,

altering the nature of the barotropic Rossby waves (Roullet & Madec, 2000). Free-slip is also needed as the no-slip boundary conditions suppresses zonal flow at the boundaries (Gastine & Wicht, 2012).

Under the Boussinesq approximation, the conservation of mass equation is defined by

$$\nabla_h \cdot \boldsymbol{u}_h + \frac{\partial u_3}{\partial x_3} = 0. \tag{2.76}$$

The potential temperature (Θ) conservation equation is defined by

$$\frac{\partial \Theta}{\partial t} + \boldsymbol{u} \cdot \nabla \Theta = G_\Theta, \tag{2.77}$$

where G_Θ represents the forcing and dissipation of Θ. To describe potential temperature, let us consider a fluid parcel at some pressure P and temperature T. If we take the fluid parcel and adiabatically brought it to P_0, then the temperature of the fluid at P_0 is called potential temperature, which is a conserved quantity (Pedlosky, 1987).

In this thesis, the fluid in the regional models do not have salinity. Thus, the salinity conservation equation will not be used.

MITgcm uses the constant horizontal eddy viscosity A_h instead of kinematic viscosity where $_h$ represents the horizontal component. By definition, horizontal eddy viscosity represents the the damping term due to stresses from the vertical plane and is defined by

$$A_h = \left(\frac{v_C}{\pi}\right)^2 \delta s^2 |\bar{D}|, \tag{2.78}$$

which is based on formulation from Smagorinsky (1963), where v_C represents a dimensionless scaling factor, δs represents the local grid spacing and $|\bar{D}|$ representing the the horizontal velocity deformation rate. Eddy viscosity is somewhat similar to the kinematic viscosity because they both can be thought of as the diffusivity of momentum and vorticity (Tritton, 1988).

2.2.2 Open Boundary Conditions

The typical horizontal boundary conditions implemented in regional models are periodic. Periodic boundary conditions are defined by

$$\chi(x = BL_1) = \chi(x = BL_2), \tag{2.79}$$

where χ is any dynamic variable and x can be any horizontal coordinate (x_1 or x_2) with

$x = BL_1$ and $x = BL_2$ indicating the location of both boundaries along x. However, the use of periodic horizontal boundary conditions is unrealistic for some models, such as North or South pole regional models or models with strong thermal forcing at the bottom boundary. Thus, open boundary conditions were implemented in MITgcm to allow for more realistic fluid behaviour in regional models, which are defined such that the boundary in the model can appear as though it extends to infinity (Camerlengo & O'Brien, 1980).

One example of dampening the fluid motion at the horizontal open boundary is the sponge layer. In MITgcm, it is represented by

$$G_\chi^{\text{sponge}} = \frac{(1-l^*)(\chi - \chi_{BL})}{(1-l^*)\tau_b - l^*\tau_i}. \tag{2.80}$$

The dissipation term applied to any dynamic variable χ in their respective conservation equation is called G_χ^{sponge}, where $0 < l < L_s$ with sponge layer thickness L_s and $l^* = l/L_s$, χ_{BL} represents χ located at any horizontal boundary, and τ_b and τ_i represents the relaxation time scales at the boundary and at $l = 0$, respectively. The problem with the open boundary conditions with a sponge layer is that it potentially requires a large number of grid points to be set up as the sponge layer for the model to converge to a realistic solution.

Another way of damping the fluid at the horizontal open boundary is the radiative condition, in which MITgcm implements the Orlanski boundary conditions from Orlanski (1976). The Orlanski condition are a modification of the Sommerfield radiative condition, which solves the radiation condition, represented by

$$\frac{\partial \chi}{\partial t} + C_\chi \frac{\partial \chi}{\partial x} = 0, \tag{2.81}$$

at the boundaries, where C_χ is the wave phase velocity. Orlanski (1976) numerically determines C_χ using

$$C_\chi = -\frac{\chi_{B-1}^k - \chi_{B-1}^{k-2}}{\chi_{B-1}^k + \chi_{B-1}^{k-2} - \chi_{B-1}^{k-1}} \frac{\delta x}{2\delta t}, \tag{2.82}$$

where $\chi_B^k = \chi(t_k, x_B)$ with time $t_k = t_0 + k\delta t$ for some initial time t_0 and x_B representing the location of the boundary with index B. To determine χ_B^{k+1}, the recursive equation given by

$$\chi_B^{k+1} = \frac{1 - \frac{\delta t}{\delta x} C_\chi}{1 - \frac{\delta t}{\delta x} C_\chi} \chi_B^{k-1} + \frac{2\frac{\delta t}{\delta x} C_\chi}{1 + \frac{\delta t}{\delta x} c_\chi} \chi_{B-1}^k \tag{2.83}$$

must be used. Equation (2.83) must also satisfy the following condition:

$$0 \leq C_\chi < \delta x/\delta t. \tag{2.84}$$

2.2.3 Cubed-Sphere Coordinate System

Ideally, using the conventional spherical coordinate system should suffice for simulating the fluid dynamics of a rotating spherical fluid model. However, let's consider the full spherical gradient term as seen in the momentum conservation equations (2.69) and (2.70) given by

$$\Delta b = \hat{\boldsymbol{r}}\frac{\partial b}{\partial r} + \hat{\boldsymbol{\theta}}\frac{1}{r}\frac{\partial b}{\partial \theta} + \hat{\boldsymbol{\phi}}\frac{1}{r\sin\theta}\frac{\partial}{\partial \phi}, \tag{2.85}$$

where b is any scalar field. Due to the presence of the $1/\cos\lambda = 1/\sin\theta$ term in the spherical gradient operator with latitude λ, a singularity exists at $\lambda = 90^o$N or S (Adcroft et al., 2004). Another problem with using the conventional spherical convention is the spacing near the poles. Defining the spacing between two points along a line of constant latitude as δx with constant longitudinal spacing defined as $\delta\phi$, δx decreases as λ increases northward or southward from the equator as seen by

$$\delta x = R\delta\phi\cos\lambda, \tag{2.86}$$

where R is the mean planetary radius and ϕ is the longitude (Adcroft et al., 2004).

One way to get around this is the cubed-sphere coordinate system. It projects a sphere onto a cube of length a by partitioning the sphere into six equal faces labelled P_n for $n = 1, 2, 3, 4, 5, 6$. The faces P_5 and P_6 are the North and South faces respectively as seen in Figure 2.1 (Nair, Thomas, & Loft, 2005). Each face has their own local Cartesian coordinate system defined as (x_n, y_n) and centred on their respective face such that $|x_n| \leq a/2$ and $|y_n| \leq a/2$. An example of the cubed-sphere coordinate system on a full sphere can be seen on Figure 2.2. MITgcm implements the conformal grid from Rancic, Purser, and Mesinger (1996) and the use of finite volume scheme to solve the momentum equations (Adcroft et al., 2004). Studies such as Kwok, Hunke, Maslowski, Menemenlis, and Zhang (2008) and Kataria et al. (2016) use MITgcm with implementation of the cubed-sphere coordinate system to allow more uniform spacing and avoid polar singularities.

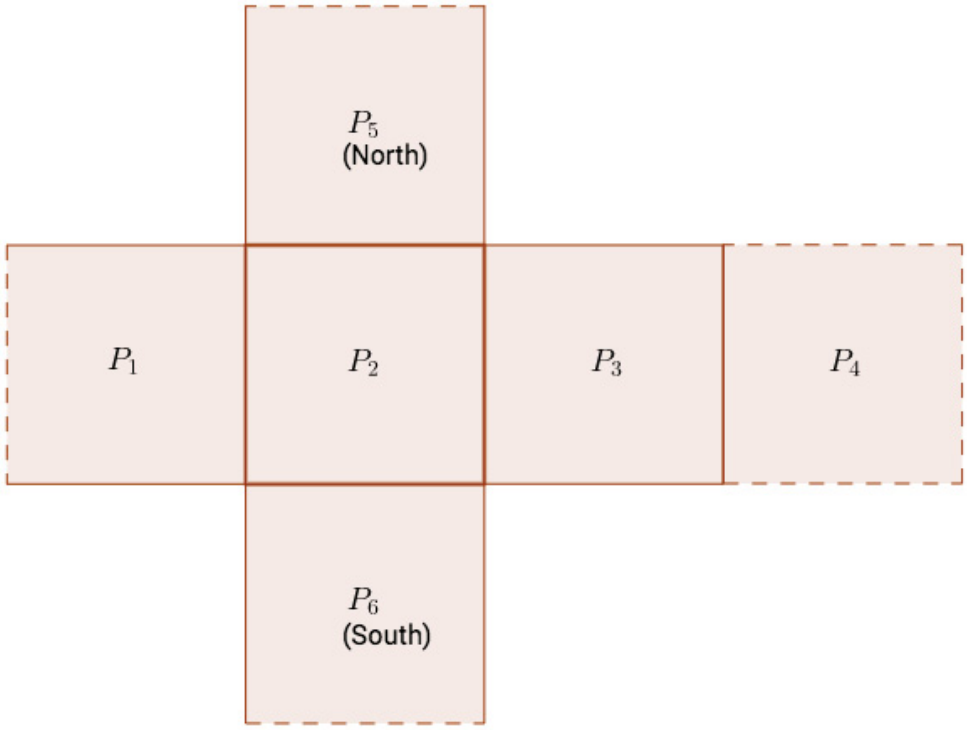

Figure 2.1: A schematic showing all of the faces of a cube labelled P_n for $n = 1, 2, 3, 4, 5, 6$. Note that the dashed lines represents the respective P_n's connection with other faces such as P_5's connection with P_3.

2.2.4 Diagnostics and Output Files

Just like MagIC, MITgcm outputs both ascii diagnostic and binary visualization files. However, the diagnostic files must be implemented by an external package and only outputs the diagnostic value horizontally averaged per vertical level per time step. To simplify the diagnostic output, the code was modified such that the diagnostic values are volumetrically averaged per time step instead. The diagnostic variable used is the squared velocity component value ${u_i}^2$, which is proportional to the kinetic energy of the system. The visualization binary files are outputted per time step. These binary files output the velocity components, temperature, and surface height in a three-dimensional array per time step. All dynamic and diagnostic outputs are in dimensional units. The velocity and energy variables will be scaled in terms of the Rossby number defined by

$$Ro(u_i) = \frac{u_i}{L\Omega}, \tag{2.87}$$

where L is the vertical length scale of the model. Time will also be scaled to the viscous

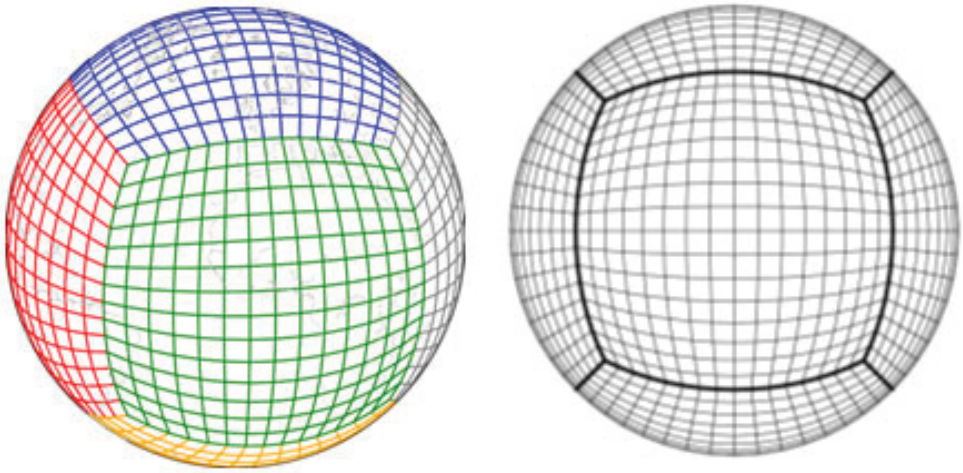

Figure 2.2: A schematic of a 16x16 cubed-sphere coordinate system using the Gnomic grid. The figure on the left uses a spherical representation of the earth with different colours indicating different faces. The figure on the right provides another view of the cubed-sphere coordinate system centred on one of the faces (GFDL, 2016).

diffusion time defined by

$$\tau = \frac{L^2}{A}. \tag{2.88}$$

The volume averaged temperature time series data are also scaled into a non-dimensional quantity (T^*) defined by

$$T^* = \frac{1}{\Delta T}\left(T - \frac{\Delta T}{2}\right), \tag{2.89}$$

where ΔT represents the temperature difference between the top and bottom boundaries.

Chapter 3

Regional Rotating Boussinesq Non-Hydrostatic Simulations using Cubed-Sphere Curvilinear Grid System

Depending on the topography and coordinate system, regional modelling provides more focus on the fluid dynamics of smaller fluid bodies or a small region of fluid planets. The focus of this regional model will be on the polar region of a rotating convective Boussinesq fluid planet in an attempt to replicate the high latitude jets as observed on Jupiter and Saturn by various space probes and ground-based telescopes. Appropriate top and bottom thermal boundary conditions are implemented to force the fluid into a convective state.

To ensure that the fluid is forced into a convective regime, the thermal forcing must be strong enough such that the Rayleigh number is larger than the system's critical Rayleigh number. This is done by implementing a constant hot temperature boundary condition at the lower boundary and a constant cold temperature boundary condition at the upper boundary such that the temperature difference across the upper and lower boundaries leads to a Rayleigh number greater than the critical Rayleigh number. The thermodynamic properties of the model, such as the thermal diffusivity and thermal expansivity, are also modified such that the Rayleigh number is past critical.

Since this is a regional model focusing on a polar region of a rotating convective Boussinesq planet, the cubed-sphere coordinate system is more appropriate to use. This eliminates the complication of the singularity located at 90^oN when using the spherical coordinate system. However, the addition of a regional cubed-sphere model adds another complication in

deciding the appropriate horizontal boundary conditions for this model. Thus, the periodic, sponge, and the radiative horizontal boundary conditions have been selected to determine if such conditions are adequate for the regional model.

In this chapter, the horizontal and open boundary conditions are applied onto a convective polar regional model of a rotating Boussinesq planet to understand the fluid dynamics at the region.

3.1 Coordinate System

For all regional models in this chapter, the horizontal coordinates are represented by a cubed-sphere coordinate system with a Chebyshev polynomial equivalent representation for the depth coordinate system centred. Note that the models are centred at the North pole of the planet (90^oN). The horizontal geometry looks similar to a square as seen on Figure 3.1. The implementation of the cubed-sphere coordinate system is needed to eliminate polar singularities and small volume spacing near the poles exhibited by conventional spherical coordinate system (Adcroft et al., 2004). Along the radial axis, the model geometry can be thought of as a region of a spherical shell with an outer radius R_o km and inner radius R_i km. The depth grid spacing (δx_{3j}) is selected by using the Chebyshev equivalent polynomials given by

$$\delta x_{3j} = C \cos\left(\frac{j\pi}{N}\right) \tag{3.1}$$

for N points and some constant $C \approx R_o - R_i$. Note that N does not necessarily represent the true number of radial grid points as the radial grid points near $j = 1$ and $j = N$ for $j = 1, 2, ..., N-1, N$, can reach small values of δx_{3j}, which can be difficult to resolve and unnecessary to the model. As such, values near $j = 1$ and $j = N$ can be ignored by choosing a cut off value N_{cut}. This leads to a modified indexing system given by $j = N_{cut}+1, N_{cut}+2, ..., N-N_{cut}-2, N-N_{cut}-1$. The inner radius R_i can be determined by summing all values of δz_j and subtracting the known R_o by that sum.

3.2 Model Parameters

The modelling of planetary fluid convection depends on the non-dimensional parameters, the governing equations and the boundary conditions. For the non-dimensional parameters, the Rayleigh number Ra, the Ekman E and the Prandtl number Pr are needed, which are

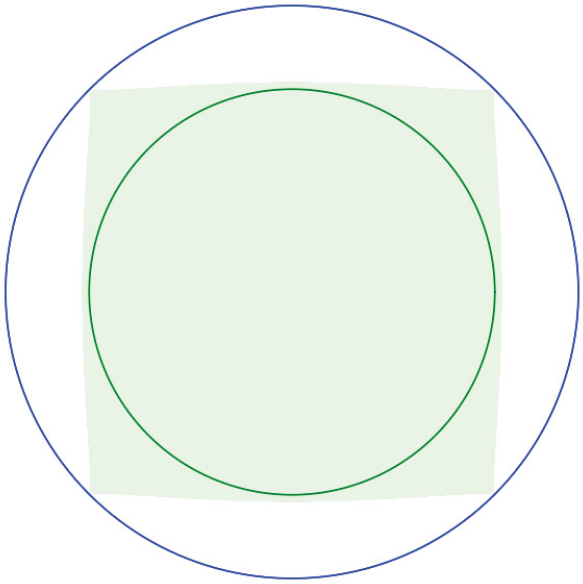

Figure 3.1: The horizontal geometry of the regional model represented by the blue shaded region. The solid green line represents the 55^oN line of latitude, which also represents the minimum latitudinal extent of the region. The maximum extent of the model is represented by the 42^oN line of latitude (blue line).

defined by the following equations:

$$Ra = \frac{g\alpha_T \Delta T L^3}{AK_T}, \tag{3.2}$$

$$E = \frac{A}{L^2\Omega}, \tag{3.3}$$

$$Pr = \frac{A}{K_T}. \tag{3.4}$$

The modified Rayleigh number $Ra^* = RaE^2/Pr$ is typically used since it represents the thermal forcing to rotational constraint ratio. Note that these parameters use the eddy viscosity A, thermal diffusivity K_T, the volumetric thermal expansivity coefficient α_T, gravity

g, planetary rotation rate Ω, total depth L, and the temperature difference across the top and bottom boundaries ΔT. Note that L is determined by summing all values of δz_j used in the model. The governing equations used are the non-hydrostatic equations for a rotating Boussinesq fluid with the equation of state represented by the linear approximation for the ocean.

The implementation of the resolution is dependent on the E and the Courant-Freidrichs-Lewy (CFL) condition. For the numerical model to resolve correctly, the CFL condition, given defined by

$$A < \frac{\min[\delta x_h]^2}{4\delta t}, \tag{3.5}$$

must be satisfied, where $\min[\delta x_h]$ represents the minimum value of the horizontal grid spacing δx_h and δt represents the time step (Griffies & Hallberg, 2000). In addition to the CFL condition, the Ekman layer (δ_E) must also be resolved, implying that the inequality

$$\max[\delta x_3] < \delta_E = L\sqrt{E} \tag{3.6}$$

must be satisfied, where $\max[\delta x_3]$ represents the maximum value of the vertical grid spacing δx_3 (Tritton, 1988). In terms of gas giants, E is estimated at $\sim 10^{-16}$ for Jupiter and $\sim 10^{-17}$ for Saturn (Gastine, Heimpel, & Wicht, 2014). However, a model with $E \sim 10^{-16}$ would make it nearly impossible to resolve the fluid dynamics using numerical software because the computational resources required would be too costly relative to the resources currently available. Thus, a much larger E is required.

The regional models presented in this chapter all use the same model parameters, initial conditions and vertical boundary conditions. For this study, $E = 10^{-4}$ and $Pr = 1$ are used based on rotating convective spherical shell models from Gastine and Wicht (2012) and Gastine, Heimpel, and Wicht (2014). All regional models are thermally forced to a convective state with $Ra^* \approx 0.08802$, which is past critical where $Ra_c^* \approx 0.04700$. Constant temperature and free-slip boundary conditions are implemented at the top and bottom boundaries with a temperature difference of $\Delta T = 30^o$C and linear free surface at the top. In terms of the fluid property, the Boussinesq fluid is salinity-free with an eddy viscosity of $A = 1.22647 \cdot 10^4$ m^2 s^{-1} and thermal diffusivity of $K_T = 1.22647 \cdot 10^4$ m^2 s^{-1}. The volumetric thermal expansivity coefficient is also set to $\alpha_T = 2.10029 \cdot 10^{-6}$ ^{o}C^{-1} with a reference density of 1000kg m^{-3}. The spherical shell itself has a rotation period of $8.64 \cdot 10^4$ s with a radius ratio of $R_i/R_o \approx 0.80$ and constant gravitational acceleration of 9.81 m s^{-2}. The regional model itself is roughly square in the latitude-longitude axes centred at 90^oN. The resolution is $180 \times 180 \times 135$ where

135 represents the number of depth grid points.

3.3 Initial Conditions

When a fluid starting at rest is heated at the lower boundary, it can reach different equilibrium regimes, depending on Ra^*. When $Ra^* < Ra_c^*$, the fluid is in the conductive state. The depth dependent temperature profile of a conductive fluid is defined by

$$T(x_3) = T_t + \frac{T_b - T_t}{L} x_3 \tag{3.7}$$

with temperature T and depth x_3, where $x_3 = 0$ defines the surface such that $T_t = T(x_3 = 0)$ and $T_b(x_3 = L)$. When $Ra^* > Ra_c^*$, the fluid reaches a convective state. In order to save computational resources, the initial condition of all regional models is set such that the fluid is at rest with a temperature profile similar to that of a conductive state defined by

$$T_(x_1, x_2, x_3) = T_t + \frac{T_b - T_t}{L} x_3 + \epsilon \Delta T \Gamma(x_1, x_2, x_3) \tag{3.8}$$

with horizontal coordinates x_1 and x_2, vertical coordinate x_3, and white noise perturbation function $\Gamma(x_1, x_2, x_3)$ defined as a random number generated from a uniform probability distribution function with maximum amplitude 1. Note that ϵ is a coefficient that determines the maximum amplitude of the white noise generated. In our models, we use $\epsilon = 0.4$.

3.4 Results of North Pole Regional Models

In this study, MITgcm was used to generate the results of three regional models with different horizontal boundary conditions. The first horizontal boundary condition tested is periodic. The other two are horizontal open boundary conditions with the sponge and the Orlanski conditions.

3.4.1 Horizontal Periodic Boundary Conditions

In this regional model, the periodic boundary conditions on both horizontal coordinates were implemented. Mathematically, this is defined by

$$\chi(x = BL_1) = \chi(x = BL_2) \tag{3.9}$$

for any dynamic variable χ along a horizontal coordinate $BL_1 \leq x \leq BL_2$. Note that x can

be either horizontal coordinate, x_1 or x_2, with location of the boundary layer denoted as BL along x. As seen in Figure 3.1, there are four horizontal boundaries.

The time series data for the radial kinetic energy can be seen on Figure 3.2 where the kinetic energy is represented by $Ro^2(u_3)$ for vertical velocity u_3 and time is scaled to the viscous diffusion time given by

$$\tau = \frac{L^2}{A} \tag{3.10}$$

with vertical length scale $L = R_o - R_i$. This leads to $\tau \approx 1.355 \cdot 10^8$ s. The fluid motion in the regional model reached a steady state past $t \approx 0.011\tau$.

Examining the radial velocity at the bottom boundary scaled by the Rossby number $Ro(u_3)$ presented in Figure 3.3(a), the image provides some unrealistic results that are most likely due to numerical errors. Focusing on the diagonal line associated with the local maximum and minimum areas, the magnitude of u_3 appears to be relatively high compared to other parts of the Figure 3.3(a). This implies that despite the implementation of the periodic boundary conditions, the fluid is somehow interacting with the corners of the topography.

3.4.2 Horizontal Sponge Condition

In this model, the horizontal sponge condition is implemented. Recall that the damping term for any dynamic variable χ of a fluid in a sponge layer of thickness L_s is represented by

$$G_\chi^{\text{sponge}} = \frac{(1 - l^*)(\chi - \chi_{BL})}{(1 - l^*)\tau_b - l^*\tau_i}, \tag{3.11}$$

where G_χ^{sponge} is the dissipation term due to the sponge layer for any dynamic variable χ in their respective conservation equation with $0 < l < L_s$ with sponge layer thickness L_s and $l^* = l/L_s$, χ_{BL} represents χ located at any horizontal boundary, and τ_b and τ_i represents the relaxation time scales at the boundary and at $l = 0$, respectively. We choose the number of grid points for the sponge layer to be $N_s = 40$, which sets L_s. Since the horizontal resolution for this model is 180×180, this implies that along any horizontal coordinate, 80 out of 180 grid points are set as the sponge layer at both boundaries. The relaxation time scales are set to $\tau_b = 49.4$ s and $\tau_i = \tau = 4.94 \cdot 10^9$ s. With an exponent difference of $\log_{10}[\tau_b/\tau_i] = 8$, this should be sufficient to dampen the fluid to zero motion at the sponge layer.

The kinetic energy time series data u_3 scaled to the squared Rossby number $Ro^2(u_3)$ for this model is presented in Figure 3.2. Based on Figure 3.2, the model has reached a steady

convective state past $t \approx 0.010\tau$.

Examining the radial velocity along the horizontal coordinates at the lower boundary given by Figure 3.3(b) at $t \approx 0.0207\tau$ indicates some numerical problems, which similar to the model with horizontal periodic boundary conditions. The diagonal line associated with the local maximum and minimum areas exhibit high magnitude radial velocity behaviour. This indicates that the fluid is interacting with the corners causing a reflective behaviour along those lines of longitude. Figure 3.3(b) also shows that there is fluid motion along within the sponge layer. This implies that the fluid motion driven by the thermal forcing is strong enough to overcome the damping term within the sponge layer.

3.4.3 Horizontal Orlanski Condition

To set up the Orlanski conditions along the horizontal open boundaries, estimations of the maximum phase velocity and the average time period are needed. Recall that the Orlanski conditions are a modification of the Sommerfield radiative conditions which solves the radiation condition represented by

$$\frac{\partial \chi}{\partial t} + C_\chi \frac{\partial \chi}{\partial x} = 0 \tag{3.12}$$

at the boundaries, where C_χ is the wave phase velocity of any dynamic variable χ (Orlanski, 1976). Orlanski (1976) numerically determines C_χ with

$$C_\chi = -\frac{\chi^k_{B-1} - \chi^{k-2}_{B-1}}{\chi^k_{B-1} + \chi^{k-2}_{B-1} - \chi^{k-1}_{B-1}} \frac{\delta x}{2\delta t}, \tag{3.13}$$

where $\chi^k_B = \chi(t_k, x_B)$ with time $t_k = t_0 + k\delta t$ for some initial time t_0, and x_B representing a boundary point with index B. To determine χ^{k+1}_B, the recursive equation given by

$$\chi^{k+1}_B = \frac{1 - \frac{\delta t}{\delta x} C_\chi}{1 - \frac{\delta t}{\delta x} C_\chi} \chi^{k-1}_B + \frac{2\frac{\delta t}{\delta x} C_\chi}{1 + \frac{\delta t}{\delta x} C_\chi} \chi^k_{B-1} \tag{3.14}$$

must be used, where C_χ must satisfy $0 \leq C_\chi < \delta x/\delta t$.

Based on Zhang (1992), the non-dimensional angular frequency and wavenumber of a rotating convecting Boussinesq spherical fluid shell are in the order of ~ 100 and ~ 30 respectively. Note that models they use are near critical runs where $(Ra^* - Ra^*_c)/Ra^*_c$ are of order 0.1. They determine both the non-dimensional angular frequency and wavenumber based on the number of convection cells their models exhibit and the time it takes for one of the cells to make a full rotation, respectively, where the time is scaled by the viscous

diffusion time. Since the Taylor columns rotate around the tangent cylinder, the length scale of $L_\omega = c_S 2\pi R_i$ is used where c_S is a scaling factor and ω is the angular frequency associated with the rotation of these columns around the tangent cylinder. From Zhang (1992), they use a Taylor number of $Ta = 10^{10}$, where Ta is defined as

$$Ta = \left(\frac{2\Omega}{\nu}\right)^2 \left(\frac{1}{1-\eta}\right)^4. \tag{3.15}$$

Using $\eta = 0.4$ from Zhang (1992), $\omega/\Omega = 1/180$. With the non-dimensional wavenumber, the dimensional wavelength can be approximated with $L_\omega \approx (2\pi R_i)/30$. Thus, if we choose $C_\chi = \Omega L_s$, then $c_S = (1/30)(1/2\pi)(1/80) \approx 2.95 * 10^{-5}$. In this model, we test c_S between $2.0 \cdot 10^{-5}$ and 1.0.

However, the resulting models using the Orlanski conditions became numerically unstable. The Orlanski condition uses the radiation condition defined by equation (3.12) and solves for the phase speed C_χ with equation (3.12). Unfortunately, if there exist waves of different phase velocities or non-wave behaviour such as Taylor columns or eddies, then the Orlanski conditions will not be able to resolve the model correctly since they can only account for waves of one phase speed (Gallacher, Hebert, & Schaferkotter, 2011). Considering that this model is rotating with $E = 10^{-4}$ and thermally forced with $Ra^* \approx 0.088 \approx 1.544 Ra_c^*$, there will exist waves of different wave speeds throughout the model. Due to the convective fluid action, this has led to numerically unstable models using the Orlanski condition.

3.4.4 Discussion

Models that use both the horizontal periodic and open boundary conditions either output unrealistic results or become numerically unstable. The model that uses the horizontal periodic boundary conditions results in strong fluid behaviour at the diagonal line associated with the local maximum and minimum areas. This implies that there is some interaction along the corners of the model's topography. Likewise, this behaviour can also be observed at the model using the horizontal sponge layer. Another issue is that the sponge layer does not fully dampen the fluid motion near the outer boundary. The model using the Orlanski condition, on the other hand, is numerically unstable. The most likely cause of such unrealistic fluid motion in all three models is due to the strong fluid motion driven by convection such that the Orlanski conditions are unable to appropriately resolve the motion near the boundaries.

Regional models that attempt to understand and focus on the fluid dynamics of polar regional models of a rotating spherical shell using convection must either test other horizontal

boundary conditions not accounted for in the models in this chapter or modify the parameters governing the sponge or Orlanski conditions to account for the strong fluid motion associated with convection.

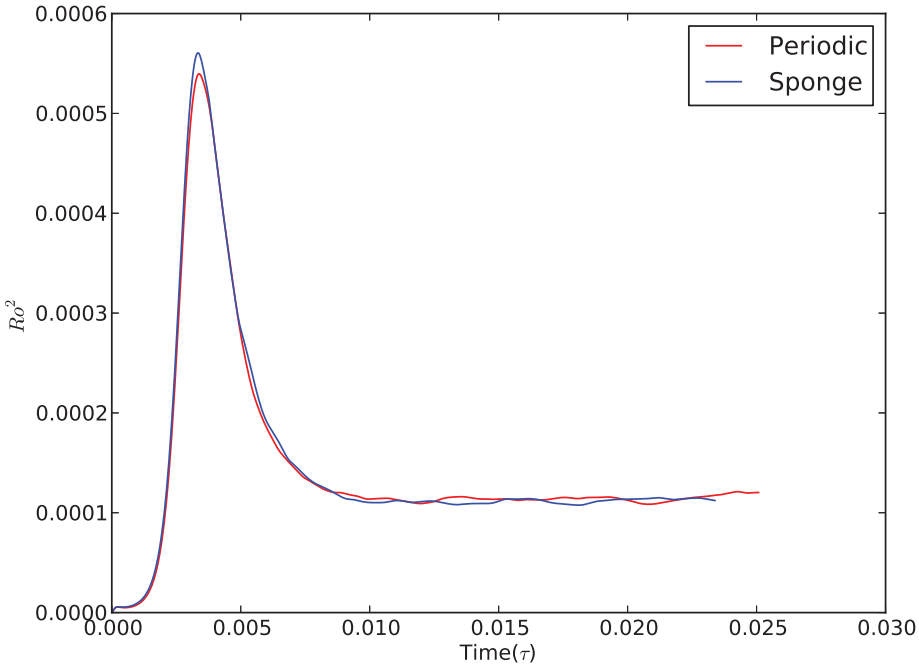

Figure 3.2: The vertical velocity kinetic energy time series data of the regional models using the viscous diffusion time scale τ and with u_3^2 scaled to $Ro^2(u_3)$.

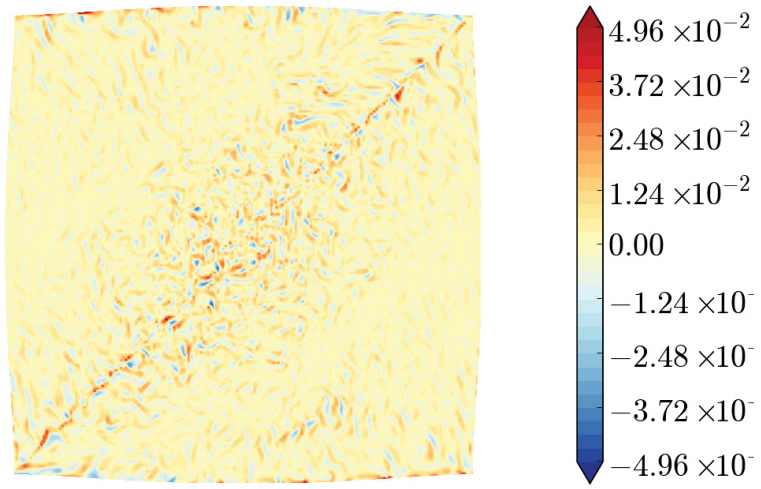

(a) Periodic

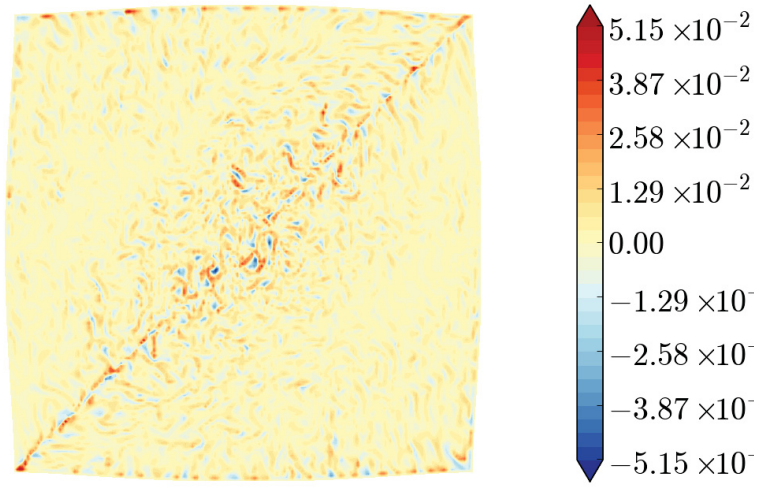

(b) Sponge

Figure 3.3: The radial velocity of the regional models at the bottom boundary scaled to the Rossby number. These images are taken at $\tau \approx 0.0207$, which is at their respective stable state. Note that the positive direction for the vertical velocity is the radially inward direction.

Chapter 4

Parametric Study of Rotating Anelastic Spherical Shell Convection with a Stratified Layer

Based on the Galileo space probe's measurements on Jupiter's atmosphere, stable stratification at the outer boundary could play a role in the fluid dynamics of the planet's atmosphere (e.g., Magalhaes et al., 2002). For our models that use the rotating anelastic convective spherical shell, implementing the constant conductive radial entropy gradient boundary conditions at the inner and outer radii will allow a layer of stable stratification to occur near outer boundary of the shell. The stably stratified fluid layer thickness could be modified by changing the difference of the conductive radial entropy gradient across the boundaries. Since the outward entropy flux from the inner boundary represents the heat contribution from the inner radius and the inward entropy flux from the outer boundary represents the heat contribution from the outer radius, a volumetric entropy sink is needed to ensure the overall thermal energy of the model does not increase over time.

To bring the fluid into a convective state, the model's Rayleigh number must be greater than its critical Rayleigh number. Determining the system's critical Rayleigh depends on the stably stratified fluid layer thickness, the rotational constraint, and the density stratification of the system.

Since very few studies explored the effects that the stably stratified fluid layer near the top boundary have on the fluid dynamics of rotating anelastic spherical shells with convection, we conduct a parameter study in an attempt to understand it. This chapter explores the effects that the Rayleigh number, the density stratification and the stably stratified fluid layer thickness have on the fluid dynamics of the models. These results will be compared to

benchmark studies from Gastine and Wicht (2012) and Cuff (2016), which focus on numerical models with no stratified fluid layer.

4.1 Model Parameters

Rotating anelastic convective spherical shell models are controlled by non-dimensional parameters and boundary conditions. Typically, the Rayleigh number Ra controls the thermal forcing of these models, which is defined as

$$Ra = \frac{g_o \alpha d^3 \Delta s}{c_p \kappa \nu} \tag{4.1}$$

for the rotating anelastic convective spherical shell models. Note that κ is the thermal diffusivity, ν is the kinematic viscosity, c_p is the specific heat at constant pressure, and s is the entropy. However, the modified Rayleigh number Ra^* will be used instead and is defined by

$$Ra^* = \frac{RaE^2}{Pr}, \tag{4.2}$$

where the Ekman number E controls the rotational state and the Prandtl number Pr controls the kinematic viscosity to thermal diffusivity ratio. In terms of the background state (denoted by the bar notation) of the density $\bar{\rho}(r)$, the fluid is modelled as an ideal gas with a polytropic index m_p and density stratification (or number of density scale heights) N_ρ where $\bar{\rho}(r)$ is defined as

$$\bar{\rho}(r) = \bar{T}^{m_p}. \tag{4.3}$$

Note that $\bar{T}(r)$ is defined by

$$\bar{T}(r) = \frac{c_0}{(1-\eta)r} + 1 - c_0, \tag{4.4}$$

where c_0 is defined as

$$c_0 = \frac{\eta}{1-\eta}\left(\exp\left[\frac{N_\rho}{m_p}\right] - 1\right) \tag{4.5}$$

and N_ρ is given by

$$N_\rho = \ln\left[\frac{\bar{\rho}(r_i)}{\bar{\rho}(r_o)}\right]. \tag{4.6}$$

Note that $\eta = r_i/r_o$ represents the radius ratio where r_i represents the inner radius of the spherical shell and r_o represents the outer radius. The thermal boundary conditions for these models are either constant conductive entropy or constant conductive radial entropy gradient across the inner and outer radii. The mechanical boundary conditions on the other hand can be either free-slip or no-slip at the inner and outer radii.

Resolution for these numerical models are based on the Ekman layer. For the numerical model to resolve, the inequality given by

$$\max[\delta r] < \delta_E = d\sqrt{E} \tag{4.7}$$

must be satisfied, where $\max[\delta r]$ represents the maximum grid point spacing along the radial direction δr and δ_E represents the Ekman layer with length scale $d = r_o - r_i$, which is normalized to $d = 1.0$. To keep the models consistent with Gastine and Wicht (2012), a radius ratio of $\eta = 0.60$ will be used, which also avoids numerical problems and a high computational cost associated in using models of higher η. Estimated values of E for Jupiter and Saturn are $E \sim 10^{-16}$ and $E \sim 10^{-17}$, respectively (Gastine, Heimpel, & Wicht, 2014). However, resolving models with $E \sim 10^{-16}$ or lower requires a huge amount of computational resources. Thus, a constant value of $E = 10^{-4}$ is set for the numerical models in this chapter, which is consistent with Gastine and Wicht (2012). Based on both Gastine and Wicht (2012) and Gastine, Heimpel, and Wicht (2014), a Prandtl number of $Pr = 1$ is used. Free-slip boundary conditions at the top and bottom are used since they do not suppress zonal flow at the outer boundary (Gastine & Wicht, 2012). As for the background density, we use $m_p = 2$ to keep it consistent with Gastine and Wicht (2012). However, all models in this chapter use constant conductive radial entropy gradient boundary conditions to vary the stably stratified fluid layer thickness near the outer boundary. MagIC software was used to generate all the results of their respective models presented in this chapter.

4.2 Onset of Convection for Variations in the Stably Stratified Fluid Layer Thickness

To ensure that a model reaches a convective state, the model's Rayleigh number Ra must be greater than the critical Rayleigh number Ra_c. This leads to the formation of M number of linear convection cells around the inner boundary, where m is also the wavenumber in the convective system. If $Ra < Ra_c$, then heat transport is dominated by conduction, where all modes are suppressed. Since the models are anelastic, the density stratification will affect the dynamics of the convection cells. Implementation of stably stratified fluid layer will also affect the dynamics.

Gastine and Wicht (2012) studies the changes that the convection cells in anelastic models experience for varying N_ρ. For their models, they use the depth-dependent Rayleigh number $\mathscr{R}(r)$. However, we define $\mathscr{R}(r)$ with

$$\mathscr{R}(r) = \frac{g(r)\beta(r)}{g_o\beta_i} Ra^*, \tag{4.8}$$

which is based on Heimpel et al. (2016), where r is the radius constrained between $\eta \leq r/r_o \leq 1.00$. Gravity g is define by

$$g(r) = g_o \left(\frac{r_o}{r}\right)^2, \tag{4.9}$$

where gravity at the outer boundary is set to $g_o = g(r_o) = 1$. The conductive radial entropy gradient is defined as $\beta(r) = \mathrm{d}s_c/\mathrm{d}r$, where $\beta_i = \beta(r_i)$. Note that if a region of fluid has $\mathscr{R}(r) < 0$, then it is stably stratified, while a fluid with $\mathscr{R}(r) > 0$ is convectively unstable. A fluid that has $\mathscr{R}(r) = 0$ is neutrally buoyant. The conductive entropy s_c is solved using

$$\nabla \cdot (\bar{\rho}\bar{T}\nabla s_c) = -H, \tag{4.10}$$

where H is the volumetric entropy sink that ensures heat conservation (Heimpel et al., 2016). The radial point of neutral buoyancy is denoted as $r_{nb} = r_o\eta_{n_b}$. It is defined such that $\mathscr{R}(r = r_{nb}) = 0$, which means that the thickness of the stably stratified fluid layer is defined as $r_o - r_{nb} = r_o(1 - \eta_{nb})$.

Figure 4.1 shows the $g\partial s_c/\partial r$ profile for various N_ρ with various stably stratified fluid layer thicknesses. For $N_\rho = 10^{-2}, 1, 3, 5$ models, the values of η_{nb} chosen are 0.70, 0.76, 0.80, 0.90, 0.96, 0.98 and 1.00. Starting from $N_\rho = 10^{-2}$ that exhibits concave up $g\partial s_c/\partial r$ curvature, for increasing N_ρ, the curvature of $g\partial s_c/\partial r$ gradually changes from concave up to

concave down, specifically from $N_\rho = 1$ to $N_\rho = 3$. The stability also increases for increasing N_ρ, which is denoted by the value of $|ds_c/dr|$ at $r/r_o = 1.00$.

The results of determining the modified critical Rayleigh number $Ra_c^* = Ra_c E^2/Pr$ can be seen in Table 4.1 along with M for various N_ρ and η_{nb}. For decreasing η_{nb}, Ra_c^* increases, as seen in Table 4.1. The time series data, presented in Figure 4.2 for $N_\rho = 3$ for $\eta_{nb} = 1.00$, 0.90, 0.80, and 0.70, also shows that the near critical models remains in the linear regime or the time independent kinetic energy state. Kinetic energy is defined as $KE = KE_\zeta + KE_\gamma$, where KE_ζ is the toroidal component of the kinetic energy and KE_γ is the poloidal component. Since convection cells form at areas of high buoyancy, the thermal forcing at the inner boundary must be strong enough to overcome the stably stratified fluid layer at the outer boundary. This results in an increasing Ra_c^* for decreasing η_{nb} to thermally force the fluid into a convective state, which can be seen in Table 4.1. Another effect for decreasing η_{nb} is that it decreases the thickness of the convection cells, which can be seen in Figure 4.3, where it presents images of the radial velocity at the equator for $N_\rho = 3$ with various η_{nb} at $Ra^* = Ra_c^*$. Similar to the results of Gastine and Wicht (2012), Table 4.1 also shows that Ra_c^* increases for increasing N_ρ. Increasing N_ρ also decreases the thickness of the convection cells as seen in Figure 4.4 for $\eta_{nb} = 1.00$, where this figure shows the radial velocity at an equatorial slice for the $N_\rho = 5$, 3, 1, and 10^{-2} models at $Ra^* = Ra_c^*$. The wave number m also increases as N_ρ increases, which is determined by counting the number of convection cells around the inner radius. Note that a pair of minimum and maximum areas denoted by the red and blue colours, respectively, represents a convection cell.

N_ρ	η_{nb}	Ra_c^*	m
10^{-2}	0.70	0.0081	14
10^{-2}	0.76	0.0050	18
10^{-2}	0.80	0.0044	20
10^{-2}	0.90	0.0038	20
10^{-2}	0.96	0.0034	20
10^{-2}	0.98	0.0034	20
10^{-2}	1.00	0.0033	20
1	0.70	0.0136	31
1	0.76	0.0086	32
1	0.80	0.0074	33
1	0.90	0.0060	33
1	0.96	0.0056	33
1	0.98	0.0055	33

1	1.00	0.0054	33
3	0.70	0.0183	41
3	0.76	0.0129	41
3	0.80	0.0116	41
3	0.90	0.0096	43
3	0.96	0.0091	43
3	0.98	0.0090	43
3	1.00	0.0088	43
5	0.70	0.0201	43
5	0.76	0.0148	44
5	0.80	0.0132	44
5	0.90	0.0116	45
5	0.96	0.0112	46
5	0.98	0.0111	46
5	1.00	0.0111	46

Table 4.1: Results of finding Ra_c^* for each η_{nb} model for $N_\rho = 10^{-2}$, 1, 3 and 5. The normalized neutral buoyancy point η_{nb} is set by using the constant entropy gradient boundary conditions at the inner and outer radii. Note that m represents the wavenumber of each model.

4.3 Convective Regimes for Variations in the Stably Stratified Fluid Layer Thickness

When the thermal forcing of the model dominated by Ra^* increases, fluid flow becomes more turbulent and time dependent. The convection cells also become less regular and more time dependent due to the turbulent motion of the fluid. The result of the irregular convection cells leads to the generation of zonal winds as a manifestation of the convection cells extending up to the outer boundary. However, this is dependent on both the thermal forcing and the stable stratification layer thickness of the model.

Models for $N_\rho = 10^{-2}$, 1, 3, 5 and $\eta_{nb} = 0.80$, 0.90, 0.96, 0.98, 1.00 have been used to show the effects increasing Ra^*. Table 4.2 shows N_ρ, η_{nb}, Ra^* and resolution of the respective models tested, where the resolution is in the form of $N_r \times N_\phi$ for N_r number of radial grid points and N_ϕ number of ϕ grid points. Note that the number of θ grid points is $N_\theta = N_\phi/2$. As seen in Table 4.2, we increase the resolution for increasing Ra^*, which implies that the computational cost increases. This is expected since we must satisfy the CFL conditions

defined by

$$\max\left[\frac{|u_1|}{\delta x_1}+\frac{|u_2|}{\delta x_2}+\frac{|u_3|}{\delta x_3}\right]\delta t<1 \tag{4.11}$$

to resolve the models. Note that $\max[F]$ represents the maximum value of any given function F, u_i for $i=1,2,3$ represents the velocity components, δx_i represents the grid spacing, and δt represents the time step. If Ra^* increases, then the magnitude of the fluid speed will increase and thus require a thinner grid spacing to satisfy the CFL conditions (Zang, Street, & Koseff, 1994).

Table 4.2 also shows each model's root mean square of the Rossby number at their steady state, which denoted as RMS(Ro). As Ra^* increases for constant η_{nb} and N_ρ, RMS(Ro) increases. However, RMS(Ro) generally increases if η_{nb} increases for constant N_ρ and Ra^*. The same also goes for increasing N_{nb} with constant η_{nb} and Ra^*.

N_ρ	η_{nb}	Ra_*/Ra_c^*	Resolution ($N_r\times N_\phi$)	RMS(Ro)
10^{-2}	0.80	1.0	97×256	$1.5030\cdot10^{-4}$
10^{-2}	0.80	11.4	97×256	$9.3878\cdot10^{-3}$
10^{-2}	0.80	22.7	97×256	$1.6855\cdot10^{-2}$
10^{-2}	0.80	45.4	97×256	$2.3620\cdot10^{-2}$
10^{-2}	0.80	68.2	97×256	$2.8731\cdot10^{-2}$
10^{-2}	0.80	90.9	97×256	$3.1266\cdot10^{-2}$
10^{-2}	0.80	113.6	97×256	$3.3116\cdot10^{-2}$
10^{-2}	0.80	227.3	193×384	$3.4674\cdot10^{-2}$
10^{-2}	0.80	454.5	193×384	$5.0210\cdot10^{-2}$
10^{-2}	0.80	681.8	193×384	$6.4141\cdot10^{-2}$
10^{-2}	0.80	1136.4	385×384	$6.3007\cdot10^{-2}$
10^{-2}	0.90	1.0	97×256	$2.4495\cdot10^{-4}$
10^{-2}	0.90	13.2	97×256	$1.3177\cdot10^{-2}$
10^{-2}	0.90	26.3	97×256	$2.3338\cdot10^{-2}$
10^{-2}	0.90	52.6	97×256	$3.5173\cdot10^{-2}$
10^{-2}	0.90	78.9	97×256	$4.3739\cdot10^{-2}$
10^{-2}	0.90	105.3	97×256	$5.1472\cdot10^{-2}$
10^{-2}	0.90	131.6	97×256	$6.3678\cdot10^{-2}$
10^{-2}	0.90	263.2	193×384	$6.6616\cdot10^{-2}$
10^{-2}	0.90	526.3	193×384	0.11701
10^{-2}	0.90	789.5	193×384	0.13233
10^{-2}	0.96	1.0	97×256	$2.5463\cdot10^{-4}$

10^{-2}	0.96	13.9	97×256	$1.4718 \cdot 10^{-2}$
10^{-2}	0.96	27.8	97×256	$2.5668 \cdot 10^{-2}$
10^{-2}	0.96	55.6	97×256	$3.7596 \cdot 10^{-2}$
10^{-2}	0.96	83.3	97×256	$4.9710 \cdot 10^{-2}$
10^{-2}	0.96	111.1	97×256	$6.0590 \cdot 10^{-2}$
10^{-2}	0.96	138.9	97×256	$7.8850 \cdot 10^{-2}$
10^{-2}	0.96	277.8	193×384	$9.2890 \cdot 10^{-2}$
10^{-2}	0.96	555.6	193×384	0.10496
10^{-2}	0.96	833.3	193×384	0.13306
10^{-2}	0.96	1470.6	385×384	0.16675
10^{-2}	0.98	1.0	97×256	$1.1955 \cdot 10^{-4}$
10^{-2}	0.98	13.9	97×256	$1.5160 \cdot 10^{-2}$
10^{-2}	0.98	27.8	97×256	$2.6280 \cdot 10^{-2}$
10^{-2}	0.98	55.6	97×256	$3.9060 \cdot 10^{-2}$
10^{-2}	0.98	83.3	97×256	$5.1710 \cdot 10^{-2}$
10^{-2}	0.98	111.1	97×256	$6.0870 \cdot 10^{-2}$
10^{-2}	0.98	138.9	97×256	$7.7270 \cdot 10^{-2}$
10^{-2}	0.98	277.8	193×384	0.10552
10^{-2}	0.98	555.6	193×384	0.13200
10^{-2}	0.98	833.3	193×384	0.15375
10^{-2}	0.98	1470.6	385×384	0.17113
10^{-2}	1.00	1.0	97×256	$1.6769 \cdot 10^{-4}$
10^{-2}	1.00	13.9	97×256	$1.5580 \cdot 10^{-2}$
10^{-2}	1.00	27.8	97×256	$2.7700 \cdot 10^{-2}$
10^{-2}	1.00	55.6	97×256	$4.0360 \cdot 10^{-2}$
10^{-2}	1.00	83.3	97×256	$5.1910 \cdot 10^{-2}$
10^{-2}	1.00	111.1	97×256	$6.4240 \cdot 10^{-2}$
10^{-2}	1.00	138.9	97×256	$7.4370 \cdot 10^{-2}$
10^{-2}	1.00	277.8	193×384	0.10546
10^{-2}	1.00	555.6	193×384	0.14083
10^{-2}	1.00	833.3	193×384	0.15636
10^{-2}	1.00	1515.2	385×384	0.17552
1	0.80	1.0	97×256	$1.2075 \cdot 10^{-4}$
1	0.80	6.8	193×256	$1.2210 \cdot 10^{-2}$
1	0.80	13.5	193×256	$2.1940 \cdot 10^{-2}$
1	0.80	27.0	193×256	$3.2640 \cdot 10^{-2}$
1	0.80	40.5	193×256	$4.1330 \cdot 10^{-2}$
1	0.80	54.1	193×256	$4.8940 \cdot 10^{-2}$
1	0.80	67.6	193×256	$9.0680 \cdot 10^{-2}$

1	0.80	135.1	481×384	$8.0990 \cdot 10^{-2}$
1	0.80	270.3	481×384	$9.5680 \cdot 10^{-2}$
1	0.80	405.4	481×384	0.10428
1	0.80	675.7	481×384	0.10428
1	0.90	1.0	97×256	$1.0765 \cdot 10^{-4}$
1	0.90	8.3	193×256	$1.9700 \cdot 10^{-2}$
1	0.90	16.7	193×256	$3.3520 \cdot 10^{-2}$
1	0.90	33.3	193×256	$5.1670 \cdot 10^{-2}$
1	0.90	50.0	193×256	$6.7690 \cdot 10^{-2}$
1	0.90	66.7	193×256	$8.1680 \cdot 10^{-2}$
1	0.90	83.3	193×256	$9.1230 \cdot 10^{-2}$
1	0.90	166.7	481×384	0.10538
1	0.90	333.3	481×384	0.12277
1	0.90	500.0	481×384	0.15776
1	0.90	833.3	481×384	0.10562
1	0.96	1.0	97×256	$1.3754 \cdot 10^{-4}$
1	0.96	8.9	193×256	$2.3990 \cdot 10^{-2}$
1	0.96	17.9	193×256	$3.9100 \cdot 10^{-2}$
1	0.96	35.7	193×256	$6.2600 \cdot 10^{-2}$
1	0.96	53.6	193×256	$8.1830 \cdot 10^{-2}$
1	0.96	71.4	193×256	$9.4350 \cdot 10^{-2}$
1	0.96	89.3	193×256	0.10541
1	0.96	178.6	481×384	0.11076
1	0.96	357.1	481×384	0.10856
1	0.96	535.7	481×384	0.11168
1	0.96	892.9	481×384	0.11134
1	0.98	1.0	97×256	$1.2641 \cdot 10^{-4}$
1	0.98	9.1	193×256	$2.5030 \cdot 10^{-2}$
1	0.98	18.2	193×256	$4.0580 \cdot 10^{-2}$
1	0.98	36.4	193×256	$6.3930 \cdot 10^{-2}$
1	0.98	54.5	193×256	$8.5560 \cdot 10^{-2}$
1	0.98	72.7	193×256	$9.9040 \cdot 10^{-2}$
1	0.98	90.9	193×256	0.10966
1	0.98	181.8	481×384	0.11467
1	0.98	363.6	481×384	0.10933
1	0.98	545.5	481×384	0.11443
1	0.98	909.1	481×384	0.12995
1	1.00	1.0	97×256	$1.1794 \cdot 10^{-4}$
1	1.00	9.3	193×256	$2.6100 \cdot 10^{-2}$

1	1.00	18.5	193×256	$4.1710 \cdot 10^{-2}$
1	1.00	37.0	193×256	$6.5660 \cdot 10^{-2}$
1	1.00	55.6	193×256	$8.6420 \cdot 10^{-2}$
1	1.00	74.1	193×256	0.10258
1	1.00	92.6	193×256	0.11403
1	1.00	185.2	481×384	0.11783
1	1.00	370.4	481×384	0.11441
1	1.00	555.6	481×384	0.11777
1	1.00	925.9	481×384	0.12174
3	0.80	1.0	97×256	$2.1330 \cdot 10^{-4}$
3	0.80	4.3	289×256	$1.5580 \cdot 10^{-2}$
3	0.80	8.6	289×256	$3.5500 \cdot 10^{-2}$
3	0.80	17.2	289×256	$5.3330 \cdot 10^{-2}$
3	0.80	25.9	289×256	$6.8890 \cdot 10^{-2}$
3	0.80	34.5	289×256	$8.1460 \cdot 10^{-2}$
3	0.80	43.1	289×256	$9.0680 \cdot 10^{-2}$
3	0.80	86.2	577×384	0.10891
3	0.80	172.4	577×384	0.11214
3	0.80	431.0	577×384	0.12520
3	0.90	1.0	97×256	$1.6812 \cdot 10^{-4}$
3	0.90	5.2	289×256	$2.7890 \cdot 10^{-2}$
3	0.90	10.4	289×256	$5.1570 \cdot 10^{-2}$
3	0.90	20.8	289×256	$8.0430 \cdot 10^{-2}$
3	0.90	31.2	289×256	0.10565
3	0.90	41.7	289×256	0.12172
3	0.90	52.1	289×256	0.13177
3	0.90	104.2	577×384	0.14271
3	0.90	208.3	577×384	0.16152
3	0.90	312.5	577×384	$0.16132 \cdot 10^{-2}$
3	0.90	520.8	577×384	0.16251
3	0.96	1.0	97×256	$1.4931 \cdot 10^{-4}$
3	0.96	5.5	289×256	$3.2260 \cdot 10^{-2}$
3	0.96	11.0	289×256	$5.9220 \cdot 10^{-2}$
3	0.96	22.0	289×256	$9.1830 \cdot 10^{-2}$
3	0.96	33.0	289×256	0.11312
3	0.96	44.0	289×256	0.13983
3	0.96	54.9	289×256	0.14359
3	0.96	109.9	577×384	0.17578
3	0.96	219.8	577×384	0.18636

3	0.96	329.7	577×384	0.13575
3	0.96	549.5	577×384	0.20668
3	0.98	1.0	97×256	$1.7243 \cdot 10^{-4}$
3	0.98	5.6	289×256	$4.2900 \cdot 10^{-2}$
3	0.98	11.1	289×256	$6.5890 \cdot 10^{-2}$
3	0.98	22.2	289×256	$9.8950 \cdot 10^{-2}$
3	0.98	33.3	289×256	0.12569
3	0.98	44.4	289×256	0.13415
3	0.98	55.6	289×256	0.14486
3	0.98	111.1	577×384	0.18329
3	0.98	222.2	577×384	0.19671
3	0.98	333.3	577×384	0.13870
3	0.98	555.6	577×384	0.21319
3	1.00	1.0	97×256	$1.8444 \cdot 10^{-4}$
3	1.00	5.7	289×256	$4.2280 \cdot 10^{-2}$
3	1.00	11.4	289×256	$6.1980 \cdot 10^{-2}$
3	1.00	22.7	289×256	$9.7410 \cdot 10^{-2}$
3	1.00	34.1	289×256	0.12336
3	1.00	45.5	289×256	0.13606
3	1.00	56.8	289×256	0.15008
3	1.00	113.6	577×384	0.18415
3	1.00	227.3	577×384	0.15832
3	1.00	340.9	577×384	0.13713
3	1.00	568.2	577×384	0.16393
5	0.80	1.0	97×256	$1.8294 \cdot 10^{-4}$
5	0.80	3.8	289×256	$1.5260 \cdot 10^{-2}$
5	0.80	7.6	289×256	$3.8900 \cdot 10^{-2}$
5	0.80	15.2	289×256	$7.5480 \cdot 10^{-2}$
5	0.80	22.7	289×256	$9.5630 \cdot 10^{-2}$
5	0.80	30.3	289×256	$9.1080 \cdot 10^{-2}$
5	0.80	37.9	289×256	0.10216
5	0.80	75.8	1921×640	0.10492
5	0.90	1.0	97×256	$1.7562 \cdot 10^{-4}$
5	0.90	4.3	289×256	$2.7770 \cdot 10^{-2}$
5	0.90	8.6	289×256	$6.3320 \cdot 10^{-2}$
5	0.90	17.2	289×256	0.10701
5	0.90	25.9	385×384	0.13681
5	0.90	34.5	385×384	0.15586
5	0.90	43.1	385×384	0.16634

5	0.90	86.2	1537×640	0.10398
5	0.96	1.0	97×256	$1.4158 \cdot 10^{-4}$
5	0.96	4.5	289×256	$3.4040 \cdot 10^{-2}$
5	0.96	8.9	289×256	$6.9580 \cdot 10^{-2}$
5	0.96	17.9	289×256	0.11724
5	0.96	26.8	385×384	0.13942
5	0.96	35.7	385×384	0.15555
5	0.96	44.6	385×384	0.16990
5	0.96	89.3	769×640	0.20411
5	0.98	1.0	97×256	$8.7000 \cdot 10^{-5}$
5	0.98	4.5	289×256	$3.3670 \cdot 10^{-2}$
5	0.98	9.0	289×256	$7.0790 \cdot 10^{-2}$
5	0.98	18.0	385×384	1.1566
5	0.98	27.0	385×384	1.1299
5	0.98	36.0	385×384	1.3614
5	0.98	45.0	385×384	1.5387
5	0.98	90.1	1537×640	1.7114
5	1.00	1.0	97×256	$1.2607 \cdot 10^{-4}$
5	1.00	4.5	289×256	$3.5420 \cdot 10^{-2}$
5	1.00	9.0	289×256	$7.3870 \cdot 10^{-2}$
5	1.00	18.0	385×384	1.0943
5	1.00	27.0	385×384	1.4761
5	1.00	36.0	385×384	1.6205
5	1.00	45.0	385×384	1.8520
5	1.00	90.1	1537×640	1.9995

Table 4.2: The resolution used to run each model with their respective N_ρ, Ra^*, and η_{nb} inputs at $E = 10^{-4}$. The RMS(Ro) output at their respective model's steady state is also presented. Note that $N_\theta = N_\phi/2$ and the maximum spherical harmonic degree is set to $l_{max} = (N_\theta - 1)/3$.

The study conducted by Gastine and Wicht (2012) determined the convections regimes that exist amongst the rotating anelastic convective spherical shell models for various N_ρ and Ra^* values tested using constant conductive entropy boundary conditions. Cuff (2016) also presents the convection regimes they found but with models using the constant conductive radial entropy gradient boundary conditions, but with $\eta_{nb} = 1.00$ only. The first regime is associated with fluids near the onset of convection, which is called the linear state. The fluid in this state generates linear convection cells with time independent kinetic energy.

Examples of this can be seen in the time series data of $N_\rho = 3$ models with $\eta_{nb} = 1.00$, 0.90, 0.80 and 0.70 at $Ra^* = Ra_c^*$ shown in Figure 4.2. Slightly increasing Ra^* leads to the next regime where both the poloidal and the toroidal kinetic energies oscillate at the same period with similar amplitudes denoted as the quasi-perioidic regime while the toroidal component dominates the poloidal component. Despite the oscillations in the fluid flow, the convection cells are maintained. However, increasing Ra^* even more changes the regime from the quasi-perioidic state to the first chaotic state. In this state, the toroidal kinetic energy dominates the poloidal component, implying that the zonal flow dominates the kinetic energy. The next regime is another oscillatory one after increasing Ra^* called the relaxation oscillation state. In this state, the toroidal kinetic energy is still dominant but both the toroidal and poloidal components oscillate at the same frequency. The amplitude of the toroidal kinetic energy oscillations tends to be much greater than the poloidal kinetic energy oscillations. The final regime is the second chaotic regime, where the toroidal energy dominates the poloidal energy after increasing Ra but with fluid motion similar to that of the first chaotic state. The order of these regimes are given by

$$\text{Linear} \rightarrow \text{Quasi-periodic} \rightarrow \text{Chaotic(1)} \rightarrow \text{Relaxation Oscillation} \rightarrow \text{Chaotic(2)}, \quad (4.12)$$

where Chaotic(1) represents the first chaotic regime and Chaotic(2) represents the second chaotic regime.

Figures 4.5 to 4.9 shows the kinetic energy time series data for $N_\rho = 10^{-2}$ and $\eta_{nb} = 1.00$, 0.98, 0.96, 0.90, 0.80 models of various Ra^* values. Models with $Ra^* = Ra_c^*$ exhibit linear convective regime, which can be seen in (a) of Figures 4.5 to 4.9. Increasing Ra^* to $\sim 4.5 Ra_c^*$ exhibits the time dependent quasi-periodic convective regime, which can be seen in (b) of Figures 4.5 to 4.9. Increasing Ra^* even more leads to the first chaotic regime, where no discernible pattern is observed in the kinetic energy time series data, which can be seen in (c) to (f) of Figures 4.5 to 4.9. The $N_\rho = 10^{-2}$ does not exhibit the relaxation oscillation regime for increasing Ra^*. In all $N_\rho = 10^{-2}$ models that exhibit the quasi-periodic or the first chaotic state, the toroidal kinetic energy component dominates the poloidal component.

The kinetic energy time series data for higher stratification models ($N_\rho = 1$, 3 and 5) with $\eta_{nb} = 1.00$, 0.98, 0.96, 0.90, 0.80 are shown in Figures 4.10 to 4.24. These models exhibit the linear convective regime at $Ra^* = Ra_c^*$. Increasing Ra^* changes the regime from linear to quasi-periodic. Further increases to Ra^* lead to the first chaotic regime. However, some of the higher stratification models exhibit the relaxation oscillation regime for increasing Ra^*, which is absent in the $N_\rho = 10^{-2}$ models. Lower values of η_{nb} appear to inhibit the formation of the relaxation oscillation regime. Examples of this can be seen in the $N_\rho = 3$ models with

$\eta_{nb} = 0.80$, which are shown in Figures 4.19. None of these models exhibit the relaxation oscillation regime. They can be compared with the $\eta_{nb} = 1.00$ models, in which higher Ra^* models exhibit the relaxation oscillation regime, where they are shown in Figures 4.15(c) to 4.15(f). The second chaotic regime is only exhibited in the $N_\rho = 5$ models with $\eta_{nb} = 0.80$, which can be seen in Figures 4.24(e) and 4.24(f). The relaxation oscillation regime for the $N_\rho = 5$ model with $\eta_{nb} = 0.80$ is presented in Figure 4.24(d).

Figure 4.25 shows the convection regime diagram for $N_\rho = 10^{-2}$ for various Ra^*/Ra_c^* and η_{nb} values with Ra_c^* dependent on η_{nb} and N_ρ. The convection regimes exhibited by the $N_\rho = 10^{-2}$ models only exhibits the first three regimes. The Ra^* range for the models that exhibit the linear and the quasi-periodic regimes lengthens as η_{nb} decreases. For increasing N_ρ from $N_\rho = 10^{-2}$, models with $N_\rho = 1$ start exhibiting the relaxation oscillation regime at $\eta_{nb} = 0.98$ and 1.00 for $Ra^*/Ra_c^* > 25$, which can be seen in Figure 4.26. The relaxation oscillation regime is exhibited for all η_{nb} models except for $\eta_{nb} = 0.80$ for increasing N_ρ to $N_\rho = 3$, which can be seen in Figure 4.27. However, the second chaotic regime is present for $N_\rho = 5$ models with $\eta_{nb} = 0.80$ only, which is shown in Figure 4.28.

Note that the $N_\rho = 10^{-2}$ with $Ra^* = 0.5000$ models with $\eta_{nb} = 1.00$, 0.98, and 0.96 reach numerical instability. These models are still used since they are relatively stable up to but not including the point of instability. Thus, the time series data for these models will only include the numerically stable state only.

4.4 Development of Zonal Flow

Since convection drives the zonal flow of a fluid inside a rapidly rotating spherical shell and the stably stratified fluid layer has a tendency to restrict three-dimensional flow near the outer boundary to two-dimensional horizontal flow, both the Taylor-Proudman theorem and the thermal winds phenomenon should play a role in the zonal flow development of these models. In order to mathematically introduce both the Taylor-Proudman theorem and the thermal winds phenomenon, the anelastic Navier Stokes equation represented by

$$E\left(\frac{\partial \boldsymbol{u}}{\partial t} + \boldsymbol{u}\cdot\nabla\boldsymbol{u}\right) = \frac{1}{\bar{\rho}}\nabla P' - 2\hat{\boldsymbol{z}}\times\boldsymbol{u} + \frac{RaE}{Pr}\frac{r_o^2}{r^2}s\hat{\boldsymbol{r}} + \frac{E}{\bar{\rho}}\nabla\cdot S \tag{4.13}$$

needs to be revisited, where S is the traceless rate-of-strain tensor defined by

$$S = \bar{\rho}\left(\frac{\partial u_i}{\partial x_j} + \frac{\partial u_j}{\partial x_i} - \frac{2}{3}\delta_{ij}\frac{\partial u_k}{\partial x_k}\right), \tag{4.14}$$

in which S is in summation notation with Kronecker delta δ_{ik}. Note that P' is the perturbation pressure and r is the radius, where r_o is the outer radius of the spherical shell rotating around the axis of rotation $\hat{z}$ with rotation rate Ω and entropy s. By applying the curl on both sides of equation (4.13), we get the vorticity equation, which is given by

$$E\left(\frac{\partial \boldsymbol{\omega}}{\partial t} + \boldsymbol{\omega}\cdot\nabla\boldsymbol{u}\right) = 2\left(\frac{\partial \boldsymbol{u}}{\partial z} - \hat{\boldsymbol{z}}\nabla\cdot\boldsymbol{u}\right) + \nabla\times\left(\frac{RaE}{Pr}\frac{r_o^2}{r^2}s\hat{\boldsymbol{r}}\right), \tag{4.15}$$

where vorticity $\boldsymbol{\omega} = \nabla\times\boldsymbol{u}$. For a small enough Rossby number such that $\boldsymbol{\omega} << 2\Omega\hat{z}$, equation (4.15) converts to

$$2\left(\hat{\boldsymbol{z}}\nabla\cdot\boldsymbol{u} - \frac{\partial \boldsymbol{u}}{\partial z}\right) = \nabla\times\left(\frac{RaE}{Pr}\frac{r_o^2}{r^2}s\hat{\boldsymbol{r}}\right). \tag{4.16}$$

4.4.1 Thermal Wind Equations

Based on (Pedlosky, 1987), the thermal wind equations are determined from the q and ϕ components of the vorticity equation (4.16), where q is the cylindrical radius.

Solving the curl of the right hand side of equation (4.16) using the spherical coordinate system while maintaining the cylindrical coordinates on the left hand side, the ϕ component can be written as

$$\frac{\partial u_\phi}{\partial z} = \frac{RaE}{2Pr}\frac{r_o^2}{r^3}\frac{\partial s}{\partial \theta}. \tag{4.17}$$

Note that we obtained the azimuthally averaged profiles of both the left and right hand sides of equation (4.17) for several different numerical models. Both profiles are highly correlated with each other. Therefore, the results that are presented are with respect to the right hand side, which will still be denoted as $\partial u_\phi/\partial z$.

The other component of the thermal wind equations is the q component is defined by

$$\frac{\partial u_q}{\partial z} = \frac{RaE}{2Pr}\frac{1}{q}\frac{\partial}{\partial q}\left(\frac{r_o^2}{r^2}s\right). \tag{4.18}$$

4.4.2 Modified Taylor-Proudman Theory

If s undergoes small variations or viscosity is negligible such that $E = 0$, then the right hand side of (4.16) goes to zero and thus the thermal wind phenomenon will not occur, which is

represented by

$$\left(\hat{\boldsymbol{z}}\nabla\cdot\boldsymbol{u}-\frac{\partial\boldsymbol{u}}{\partial z}\right)=0. \tag{4.19}$$

We expand equation (4.19) to get

$$\hat{\boldsymbol{z}}\left(\frac{1}{q}\frac{\partial}{\partial q}(qu_q)+\frac{1}{q}\frac{\partial u_\phi}{\partial\phi}\right)-\hat{\boldsymbol{q}}\frac{\partial u_q}{\partial z}-\hat{\boldsymbol{\phi}}\frac{\partial u_\phi}{\partial z}=0. \tag{4.20}$$

From equation (4.20), we get

$$\frac{\partial}{\partial q}(qu_q)+\frac{\partial u_\phi}{\partial\phi}=\frac{\partial u_q}{\partial z}=\frac{\partial u_\phi}{\partial z}=0, \tag{4.21}$$

which show that the horizontal velocity components are z independent. Expanding the z component of equation (4.20) leads to

$$q\frac{\partial u_q}{\partial q}+u_q+\frac{\partial u_\phi}{\partial\phi}=0. \tag{4.22}$$

If we rewrite equation (4.22) as

$$\frac{\partial u_\phi}{\partial\phi}=-q\frac{\partial u_q}{\partial q}-u_q, \tag{4.23}$$

it implies that $\partial u_\phi/\partial\phi$ must change to counteract any variations of either u_q or $q\partial u_q/\partial q$. If u_q remains constant in q, then $\partial u_\phi/\partial\phi=-u_q$ to ensure that equation (4.21) is satisfied. This implies that u_ϕ will never be constant in ϕ unless $u_q=0$ and $\partial u_q/\partial q=0$. Even then, $\partial u_\phi/\partial\phi=0$ does not guarantee that $u_\phi=0$. This shows that u_ϕ is the dominant horizontal velocity component.

Substituting the z component of equation (4.20) into the anelastic continuity equation, given by

$$\nabla\cdot\bar{\rho}\boldsymbol{u}=\bar{\rho}\nabla\cdot\boldsymbol{u}+\boldsymbol{u}\cdot\nabla\bar{\rho}=0, \tag{4.24}$$

leads to

$$\bar{\rho}\frac{\partial u_z}{\partial z}=-\boldsymbol{u}\cdot\nabla\bar{\rho}. \tag{4.25}$$

Equation (4.25) can also be written as

$$\frac{\partial u_z}{\partial z} = -\frac{1}{\bar{\rho}}\left(\frac{u_q}{q}\frac{\partial}{\partial q}(q\bar{\rho}) + u_z\frac{\partial \bar{\rho}}{\partial z}\right). \tag{4.26}$$

From Pedlosky (1987) and Zhang and Schubert (2000), equations (4.21) and (4.26) are consistent with the Taylor-Proudman theorem, but modified for the rotating convective anelastic spherical shell models. These equations show that for infinitesimally steady fluid motion, it is nearly two dimensional and dominated by u_ϕ (Zhang & Schubert, 2000). This would imply that $\partial u_z/\partial z \approx 0$, meaning that fluid motion will be in the form of columnar convection cells, which is parallel to the axis of rotation. However, if the model follows the Boussinesq approximation, then $\partial u_z/\partial z = 0$ can be obtained trivially. This implies that

$$2\boldsymbol{\Omega} \cdot \nabla \boldsymbol{u} = 0. \tag{4.27}$$

However, the theorem breaks down when the columns interact with the outer boundary. This interaction causes secondary motion to occur in the form of zonal flow. The interaction between the outer boundary curvature and the convection cells leads to a tilt in these cells. The generation of the zonal secondary flow further tilts the cells until the Reynolds stresses balance the internal viscous stresses (Vasavada & Showman, 2005; Zhang, 1992). The scale to describe the zonal flow saturation and its energy cascade cessation is called the Rhines scale, which is inversely proportional to the β-parameter (Rhines, 1975). The β-parameter is associated with the β effect, which defines the effect that the global rotation of the model has on the fluid as it travels towards either the North or South pole from the equator (Pedlosky, 1987). In shallow models, the β-paramater is associated with an approximation of the planetary vorticity f given by

$$f \approx 2\Omega \sin\lambda \sim f_0 + \beta_0 y, \tag{4.28}$$

where f_0 is defined as

$$f_0 = 2\Omega \sin\lambda_0 \tag{4.29}$$

with latitude λ and distance from the equator y. The parameter β_0 is defined as

$$\beta_0 = \frac{2\Omega \cos\lambda_0}{r_o} \tag{4.30}$$

(e.g., Pedlosky, 1987). For spherical shells, the β-parameter is a topographical one defined

as β_h, which is given by

$$\beta_h = -2\Omega \frac{dh/dq}{h}, \tag{4.31}$$

where $h = 2r_o \sin\lambda$ (Heimpel et al., 2005).

4.4.3 Comparing Thermal Wind Equations and Modified Taylor-Proudman Theory

To recap, the thermal wind equations are defined as

$$\frac{\partial u_\phi}{\partial z} = \frac{RaE}{2Pr}\frac{r_o^2}{r^3}\frac{\partial s}{\partial \theta} \tag{4.32}$$

and

$$\frac{\partial u_q}{\partial z} = \frac{RaE}{2Pr}\frac{1}{q}\frac{\partial}{\partial q}\left(\frac{r_o^2}{r^2}s\right), \tag{4.33}$$

while the modified Taylor-Proudman theorem involves

$$\frac{\partial}{\partial q}(qu_q) + \frac{\partial u_\phi}{\partial \phi} = \frac{\partial u_q}{\partial z} = \frac{\partial u_\phi}{\partial z} = 0 \tag{4.34}$$

and

$$\frac{\partial u_z}{\partial z} = -\frac{1}{\bar{\rho}}\left(\frac{u_q}{q}\frac{\partial}{\partial q}(q\bar{\rho}) + u_z\frac{\partial \bar{\rho}}{\partial z}\right). \tag{4.35}$$

The derivation for both the thermal wind equations and the modified Taylor-Proudman theorem relies on the vorticity equation (4.15), assuming that $\boldsymbol{\omega} << 2\Omega\hat{z}$. However, the differences between them can be seen in terms of how the horizontal velocity components, u_ϕ and u_q, are used. For the thermal wind equations, the horizontal velocity components are three-dimensional such that they will change in z if the entropy changes in θ or q. The thermal wind equations also show that the zonal jets are governed by changes in entropy along θ. The modified Taylor-Proudman theorem, on the other hand, states that the motion is nearly two-dimensional and that the horizontal velocity components are z independent. However, the $\partial u_z/\partial z$ depends on u_z, u_q and $\bar{\rho}$. In terms of the zonal jets, the modified Taylor-Proudman theorem and from Zhang (1992) indicate that they are generated from the interaction between the convection cells and curvature of the outer boundary.

4.4.4 Results

Figures 4.29 to 4.36 show the axisymmetric (or azimuthally averaged) $\partial s/\partial r$ profile for $N_\rho = 10^{-2}$, 1, 3, and 5 with $\eta_{nb} = 1.00$ and 0.80. For the $N_\rho = 1.00$ and $\eta_{nb} = 1.00$ models presented in Figure 4.31, the axisymmetric radial entropy gradient starts out roughly θ independent for $Ra^* = Ra_c^*$. As Ra^* increases, the axisymmetric radial entropy gradient becomes more θ dependent at the equatorial area, which is represented by the large magnitude axisymmetric radial entropy at the equatorial region parallel to the tangent cylinder. However, the stability throughout the spherical shell increases as Ra^* increases. This leads to the strong convectively unstable fluid becoming constrained near inner boundary as Ra^* increases. This can be seen in $N_\rho = 1.00$ models with $\eta_{nb} = 1.00$ with $Ra^* = 0.5000$ and 0.7500, which are shown in Figures 4.31(e) to 4.31(f). This behaviour is somewhat similar when η_{nb} decreases to $\eta_{nb} = 0.80$ while maintaining $N_\rho = 1$, as seen in Figure 4.32. Due to the presence of the stably stratified fluid layer, the major differences can be seen for increasing Ra^*. As Ra^* increases, the stability in both the stably stratified fluid layer and the convectively unstable layer increases, where the stability increase means that $\partial s/\partial r$ decreases. An example of this can be seen in the $N_\rho = 1.00$ models with $\eta_{nb} = 0.80$, which are shown in Figure 4.30. The behaviour of increasing stability for increasing Ra^* throughout the spherical shell have been seen in $N_\rho = 10^{-2}$, 1, 3, and 5 models with $\eta_{nb} = 1.00$, 0.98, 0.96, 0.90, and 0.80.

In terms of the thermal winds phenomenon, Figures 4.37 to 4.44 show the axisymmetric $\partial u_\phi/\partial z$ profile for $N_\rho = 10^{-2}$, 1, 3, and 5 with $\eta_{nb} = 1.00$ and 0.80. For $N_\rho = 1.00$ models with $\eta_{nb} = 1.00$, the magnitude of $\partial u_\phi/\partial z$ is the largest near the tangent cylinder near the inner boundary at $Ra^* = Ra_c^*$, which can be seen in Figure 4.39. However, the non-zero $\partial u_\phi/\partial z$ areas near the tangent cylinder expand around the spherical shell as Ra^* increases. This results in dominance of $\partial u_\phi/\partial z > 0$ in the Southern hemisphere and $\partial u_\phi/\partial z < 0$ in the Northern hemisphere. These dominant areas want to force the fluid near the tangent cylinder to rotate in the retrograde direction. Since these dominant areas span throughout the spherical shell, they do not greatly affect the zonal jets. As η_{nb} decreases, both hemispheres exhibit a mix of $\partial u_\phi/\partial z > 0$ and $\partial u_\phi/\partial z < 0$ areas near the outer boundary near the tangent cylinder. However, dominance of $\partial u_\phi/\partial z > 0$ in the Southern hemisphere and $\partial u_\phi/\partial z < 0$ in the Northern hemisphere is still exhibited in these models, which are similar to the $\eta_{nb} = 1.00$ ones. An example of this can be seen in the $N_\rho = 1$ models for $\eta_{nb} = 0.80$, which can be seen in Figure 4.40. For the $N_\rho = 3$ and 5 models with $\eta_{nb} = 1.00$ and $\eta_{nb} = 0.80$ and the $N_\rho = 10^{-2}$ models with $\eta_{nb} = 1.00$, which can be seen in Figures 4.41 to 4.44 and Figure 4.37, they follow a similar behaviour to the $N_\rho = 1$ models. However, the

$N_\rho = 10^{-2}$ models with $\eta_{nb} = 0.80$ is a unique case with all the numerical models tested as it exhibits a mix $\partial u_\phi/\partial z > 0$ and $\partial u_\phi/\partial z < 0$ areas throughout the entire shell, which can be seen in Figure 4.38.

Figures 4.45 to 4.56 show the axisymmetric zonal velocity (u_ϕ) profile for $N_\rho = 10^{-2}$, 1, 3 and 5 models with $\eta_{nb} = 1.00$, 0.90 and 0.80 and various Ra^* values. For $N_\rho = 10^{-2}$ models, which can be seen in Figures 4.45 to 4.47, their axisymmetric zonal flow velocity profiles show that the strong retrograde jets represented by the blue area near the tangent cylinder has a larger thickness and magnitude compared to the strong prograde jet represented by the red area for for Ra_c^*. As Ra^* increases for $\eta_{nb} = 1.00$ and 0.90, which can be seen in Figures 4.45 and 4.46, both the retrograde and prograde jets decrease in thickness and increase in magnitude. However, the $N_\rho = 10^{-2}$ models with $\eta_{nb} = 0.80$ are different from the other models, which are seen in Figure 4.47. While the models with $Ra^* < 0.50000$ behave similarly compared to the $\eta_{nb} = 1.00$ and 0.90 models for small Ra^*, the $Ra^* = 0.5000$ and $Ra^* = 1.0000$ models do not, which are seen by Figures 4.47(e) to 4.47(f). While the retrograde jet thickness decreases from $Ra^* = 0.5000$ to $Ra^* = 1.0000$, the prograde jet also decreases in thickness but retracts from the outer boundary. The magnitude of the prograde jet also decreases with increasing Ra^* starting from $Ra^* = 0.1000$, which can be seen in Figures 4.47(d) to 4.47(f).

The behaviour exhibited by $N_\rho = 10^{-2}$ models and $\eta_{nb} = 1.00$, 0.98, 0.96 and 0.90 are also exhibited by $N_\rho = 1$, 3 and 5 models with $\eta_{nb} = 1.00$, 0.98, 0.96, 0.90 and 0.80, which are presented by Figures 4.48 to 4.56. However, with higher density stratification ($N_\rho \geq 1$) and $Ra^* \geq 0.0500$ models, a tilting behaviour with the origin point at the equator can be noticed, which can be seen in (c) to (f) of Figures 4.48 to 4.56. The tilt angle increases for increasing N_ρ, which an example can be seen for $\eta_{nb} = 1.00$ and $Ra^* = 0.5000$ models with $N_\rho = 1$, 3, and 5 presented in Figures 4.48(e), 4.51(f), and 4.54(f), respectively. Decreasing η_{nb} also increases the tilt, which, for example, can be seen for $N_\rho = 1$ models with $Ra^* = 0.5000$ and $\eta_{nb} = 1.00$, 0.90, and 0.80 presented in Figures 4.48(f), 4.52(f), and 4.53(f), respectively. Increasing Ra^* also increases the tilt angle for all $\eta_{nb} = 1.00$, 0.98, 0.96, 0.90 and 0.80 and for $N_\rho = 1$, 3, and 5 models.

Besides using the axisymmetric zonal velocity profile of the model, analyzing the zonal velocity at the outer boundary using a hammer projection allows us to observe the zonal flow development of the models. For the $N_\rho = 1$ models with $\eta_{nb} = 1.00$, increasing Ra^* turns the zonal flow from a smooth form to a more rough form, which can be seen in Figure 4.57. This leads to the dissipation of the structured convection cells at the outer boundary, which leads to the formation of both the prograde and retrograde jets. Decreasing η_{nb} to $\eta_{nb} = 0.80$ also leads to a similar behaviour for increasing Ra^*. However, the strong retrograde jets for

the $\eta_{nb} = 0.80$, which are seen in Figure 4.58, are smoother compared to the $\eta_{nb} = 1.00$ models. Increasing N_ρ to $N_\rho = 3$ exhibits similar behaviour as mentioned for $N_\rho = 1$ for both $\eta_{nb} = 1.00$ and 0.80, which can be seen in Figures 4.59 and 4.60.

4.5 Discussion

A benchmark study from Gastine and Wicht (2012) conducted numerical simulations using rotating convective anelastic spherical shell models with constant conductive entropy boundary conditions. They were able to generate strong polar prograde jets for $N_\rho = 10^{-2}$, 1, 2, and 3 with $Ra^* \sim 0.1$. Weak polar prograde jets, however, were generated from high Ra^* models with $N_\rho = 4$, whereas none were generated for $N_\rho = 5$. They also show that their near critical ($Ra^* \sim Ra_c^*$) models generate convection cells near the inner boundary for models with $N_\rho = 10^{-2}$. However, as N_ρ increases, the convection cells move towards the outer boundary and becomes more constrained. The explanation for this behaviour is based on the depth dependent Rayleigh number $\mathscr{R}$ defined by equation (4.8), which is associated with buoyancy. Their models with $N_\rho = 10^{-2}$ show that when $\mathscr{R}(r = r_i) > \mathscr{R}(r = r_o)$, the fluid near the inner boundary is more buoyant than the fluid at the outer boundary. As N_ρ increases, $\mathscr{R}(r = r_i)$ started to decrease while $\mathscr{R}(r = r_i)$ started to increase. At $N_\rho = 2$, $\mathscr{R}(r = r_i) < \mathscr{R}(r = r_o)$, which is when the convection cells start to move towards the outer boundary. They were also able to show five convective regimes for increasing Ra^*, which are similar to the convective regimes shown in equation (4.12). However, none of their $N_\rho = 4$ and 5 models exhibit the relaxation oscillation regime.

A later benchmark study by Cuff (2016) used the constant conductive radial entropy gradient boundary conditions for their rotating convective anelastic spherical shell models. Specifically, they use the neutral buoyancy condition at the outer radius (or $\eta_{nb} = 1.00$) with $E = 10^{-4}$ and $N_\rho = 10^{-2}$, 3, 5, and 7. While none of their models were able to generate strong polar prograde jets, they were able to generate weaker, alternating high latitudinal zonal jets near the outer radius for high Ra^* models with $N_\rho \geq 1$. Unlike models from Gastine and Wicht (2012), their models exhibit a tilt in the strong prograde and retrograde jets for $N_\rho \geq 3$ models. The tilt angle increases for increasing Ra^* and increasing N_ρ. Their near critical models show that the convection cells always formed near the inner boundary. The explanation for this is that $\mathscr{R}(r = r_i) > \mathscr{R}(r = r_o) = 0$ for all their models that use the neutral buoyancy condition at the outer radius. They also used their models to identify the convective regimes they observed. Their $N_\rho = 10^{-2}$ models were unable to exhibit the relaxation oscillation regime, whereas their $N_\rho = 3$, 5 and 7 models exhibit it at higher Ra^*.

However, none of their models were able to go into the the second chaotic state.

From our convective regime diagrams shown in Figures 4.25 to 4.28, the models with $\eta_{nb} = 1.00$ show results that are similar to the results from Cuff (2016). Comparing our results to Cuff (2016), they both show that the $N_\rho \geq 1$ models exhibit the relaxation oscillation regime for higher Ra^* while the $N_\rho = 10^{-2}$ models do not. However, when we decrease η_{nb}, we found the second chaotic regime, which can be seen in the $N_\rho = 5$ models with $\eta_{nb} = 0.80$ shown in Figure 4.28. While the second chaotic regime is absent in the study Cuff (2016), models from Gastine and Wicht (2012) exhibit it. However, they were able to get this regime with their lower stratification ($N_\rho \leq 3$) models, whereas we were only able to get it at $N_\rho = 5$ with $\eta_{nb} = 0.80$. Decreasing η_{nb} also leads to an inhibition of the relaxation oscillation regime, while the Ra^* range in the first chaotic regime increases. The quasi-periodic regime increases in the Ra^* range when η_{nb} decreases.

For our models, none of the $N_\rho \geq 1$ models generated any high latitudinal jets, which are jets with latitudes greater than the strong retrograde jets near the tangent cylinder. However, these models exhibit a tilt in both the strong prograde and retrograde jets, similar to models from Cuff (2016). The tilting angle also increases with increasing Ra^* and N_ρ. Unlike the $N_\rho = 10^{-2}$ models from Cuff (2016), we were able to replicate strong prograde jets at the poles for $Ra^* \geq 1.0000$ and $\eta_{nb} = 1.00$, 0.98, 0.96, and 0.90, which can be seen in (f) of Figures 4.45 to 4.46. Our near critical models also show that the convection cells are constrained near the inner boundary, which are consistent with the near critical models from Cuff (2016).

The axisymmetric $\partial u_\phi / \partial z$ profiles from the $N_\rho = 1$ and 3 models with $\eta_{nb} = 1.00$ and 0.80, as shown in Figures 4.39 to 4.42, have dominance of $\partial u_\phi / \partial z > 0$ in the Southern hemisphere and $\partial u_\phi / \partial z < 0$ in the Northern hemisphere. However, the introduction of a stably stratified fluid layer leads to a generation of $\partial u_\phi / \partial z < 0$ areas in the Northern hemisphere and $\partial u_\phi / \partial z > 0$ areas in the Southern hemisphere near the tangent cylinder near the outer boundary for a large enough Ra^*. This implies that with a large enough Ra^* and a low enough η_{nb}, the thermal winds phenomenon should affect the zonal flow near the outer boundary. However, both the $\eta_{nb} = 0.80$ and the $\eta_{nb} = 1.00$ models appear to be similar, which makes it difficult to determine the effect the thermal winds phenomenon on the $\eta_{nb} = 0.80$ models with $N_\rho \geq 1$. The exception lies with the $N_\rho = 10^{-2}$ models with $\eta_{nb} = 0.80$, in which they have mixture of $\partial u_\phi / \partial z < 0$ and $\partial u_\phi / \partial z > 0$ in both hemispheres with no dominance of either one.

One of the effects that the stably stratified fluid layer has on the fluid dynamics is that it has a tendency towards suppression of the zonal flow oscillations. This can be inferred from its interaction with the kinetic energy oscillations at higher Ra^*. From the convective

regime diagrams shown in Figures 4.25 to 4.28, as η_{nb} decreases, the Ra^* needed to reach the relaxation oscillation regime also increases. However, if a fluid is in the relaxation oscillation regime, the amplitudes of the oscillations decrease as η_{nb} decreases. An example of this phenomenon can be seen in a comparison of the time series data for $N_\rho = 3$ models with $\eta_{nb} = 1.00$, 0.90, and 0.80 for $Ra^* \geq 0.300$. Starting with $\eta_{nb} = 1.00$, the models that exhibit the relaxation oscillation regime are with $Ra^* \geq 0.1000$, which are shown in Figures 4.15(d) to 4.15(f). These models can be compared with the $N_\rho = 3$ models with $\eta_{nb} = 0.90$ for $Ra^* \geq 0.1000$, which are shown in Figures 4.18(d) to 4.18(f). The oscillation amplitudes from the $N_\rho = 3$ models with $\eta_{nb} = 0.90$ for $Ra^* \geq 0.1000$ are smaller than the $\eta_{nb} = 1.00$ models for $Ra^* \geq 0.1000$. However, the relaxation oscillation regime does not appear in the $\eta_{nb} = 0.80$ models for $Ra^* \geq 0.1000$, which can be seen in Figures 4.19(d) to 4.19(f). This further shows that the stably stratified fluid layer has a tendency towards suppression of zonal flow oscillations.

The zonal velocity at $r = r_o$ for $N_\rho = 1$ and 3 models with $\eta_{nb} = 0.80$ also show that the stably stratified fluid layer restricts the fluid flow to two dimensions, which can be seen in Figures 4.58 and 4.60. This can be seen in comparing the strong prograde and retrograde jets generated in the $\eta_{nb} = 0.80$ models with their $\eta_{nb} = 1.00$ counterparts, which are presented in Figures 4.57 and 4.59. The strong prograde and retrograde jets generated in the $\eta_{nb} = 1.00$ models are less smooth compared to their $\eta_{nb} = 0.80$ counterparts.

Another effect that the stably stratified fluid layer has on the fluid dynamics can be inferred from the convective regime diagram for the $N_\rho = 5$ models, which are shown in Figure 4.28. For the $\eta_{nb} = 0.8$ models, they exhibit the relaxation oscillation regime at $7.5 \leq Ra^*/Ra_c^* \leq 22.5$. However, when $Ra^*/Ra_c^* > 22.5$, then the oscillations become suppressed and thus reach the second chaotic regime. This implies that as Ra^* increases, the stability in the stably stratified fluid layer also increases. This could mean that for a large enough Ra^*, any models that exhibit the relaxation oscillation regime for $\eta_{nb} \neq 1.00$ could force the fluid into the second chaotic state and thus, further constrain the fluid motion along r.

However, $N_\rho = 10^{-2}$ models with $\eta_{nb} = 0.80$ are special cases, especially for $Ra^* \geq 0.4000$. These models will be discussed with great detail in the next chapter.

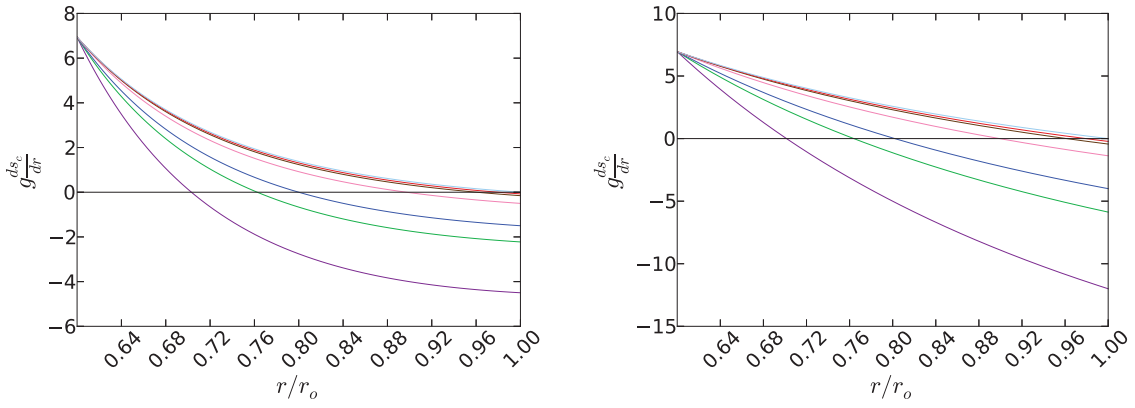

(a) $N_\rho = 10^{-2}$

(b) $N_\rho = 1$

(c) $N_\rho = 3$

(d) $N_\rho = 5$

Figure 4.1: $g\partial s_c/\partial r$ profile for models with various N_ρ and η_{nb} values. The normalized neutral buoyancy point η_{nb} used in these models are 0.70, 0.76, 0.80, 0.90, 0.96, 0.98, and 1.00, which are represented by the purple, green, dark blue, pink, brown, red, and light blue lines, respectively.

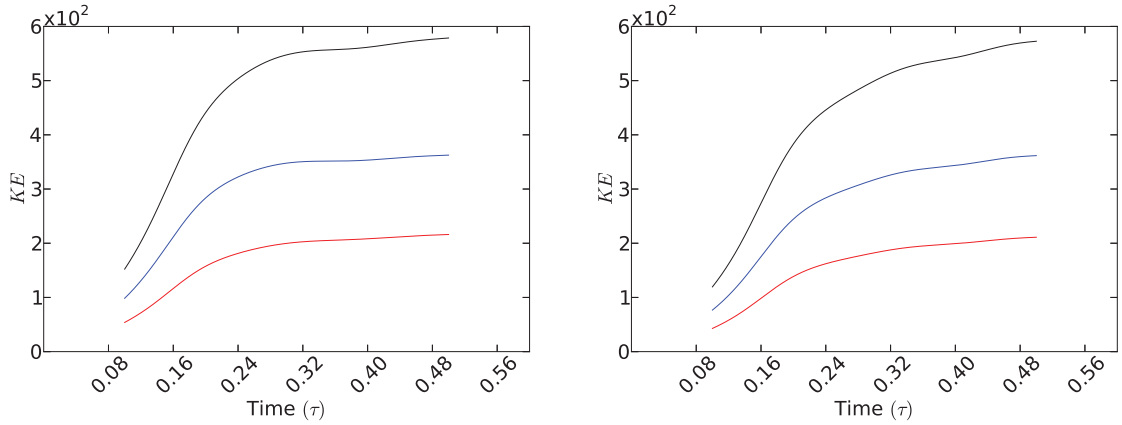

(a) $\eta_{nb} = 1.000$ at $Ra_c^* = 0.0088$

(b) $\eta_{nb} = 0.900$ at $Ra_c^* = 0.0096$

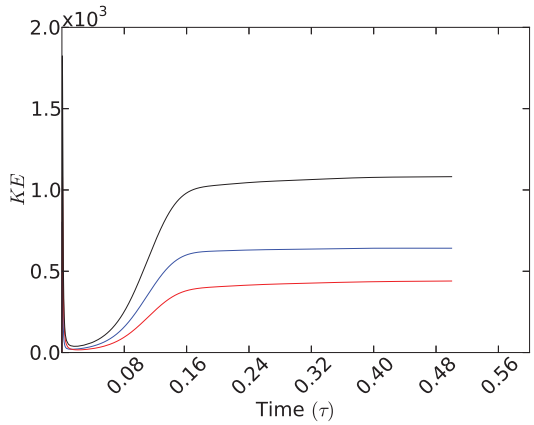

(c) $\eta_{nb} = 0.800$ at $Ra_c^* = 0.0116$

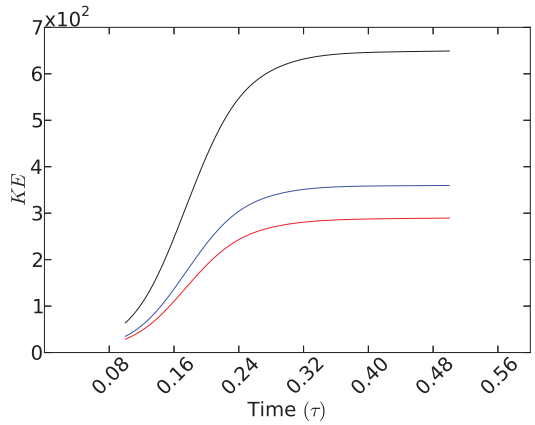

(d) $\eta_{nb} = 0.700$ at $Ra_c^* = 0.0183$

Figure 4.2: Time Series of the radial velocity for $\eta_{nb} = 1.00$, 0.90, 0.80 and 0.70 of $N_\rho = 3$ at steady state. The black line represents the total kinetic energy $KE = KE_\zeta + KE_\gamma$, where KE_ζ is the toroidal component of the kinetic energy and KE_γ is the poloidal component. Note that KE_ζ is represented by the red line and KE_γ is represented by the blue line.

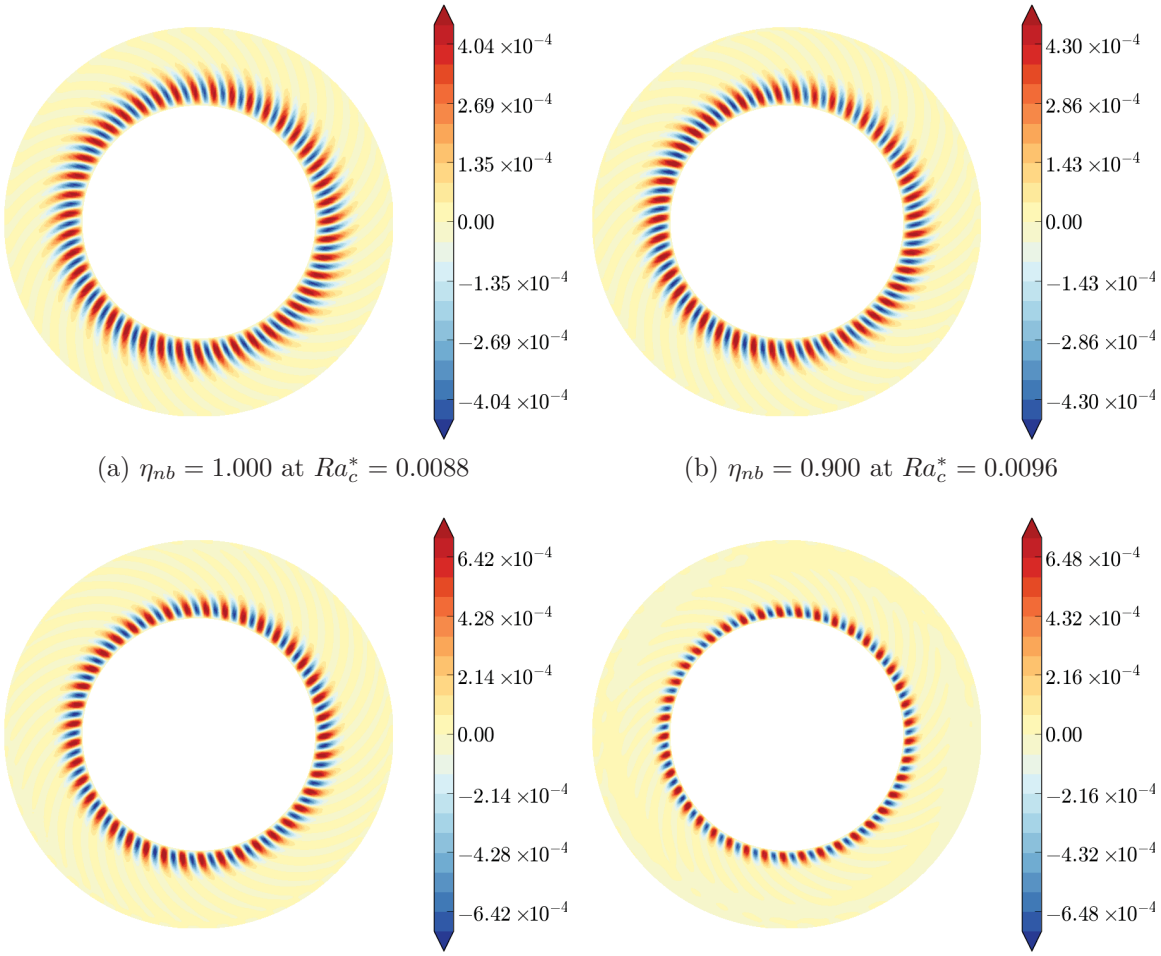

(a) $\eta_{nb} = 1.000$ at $Ra_c^* = 0.0088$

(b) $\eta_{nb} = 0.900$ at $Ra_c^* = 0.0096$

(c) $\eta_{nb} = 0.800$ at $Ra_c^* = 0.0116$

(d) $\eta_{nb} = 0.700$ at $Ra_c^* = 0.0183$

Figure 4.3: Equatorial slice images of the radial velocity for $\eta_{nb} = 1.00$, 0.90, 0.80 and 0.70 of $N_\rho = 3$ at steady state for their respective value of Ra_c^*. A convection cell is represented by a pair of maximum and minimum areas near the inner boundary.

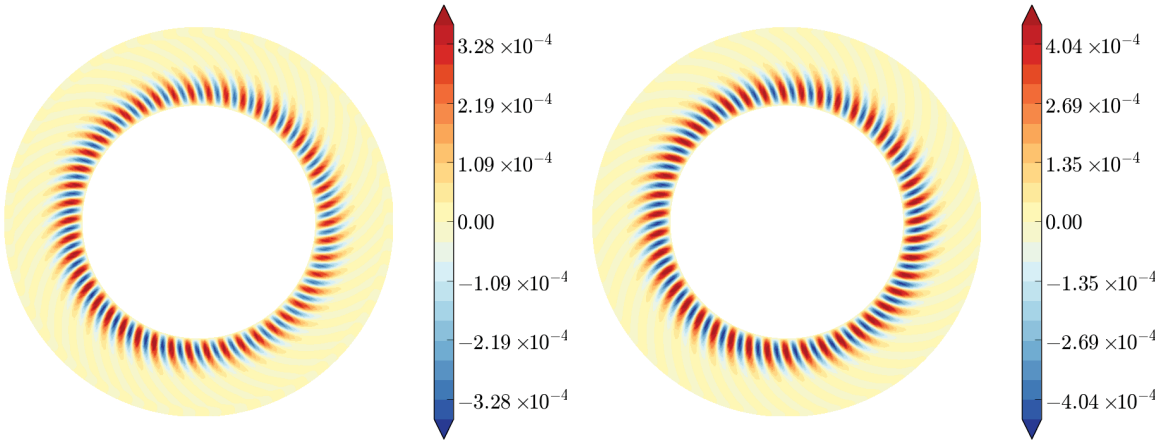

(a) $N_\rho = 5$ at $Ra_c^* = 0.0111$

(b) $N_\rho = 3$ at $Ra_c^* = 0.0088$

(c) $N_\rho = 1$ at $Ra_c^* = 0.0054$

(d) $N_\rho = 10^{-2}$ at $Ra_c^* = 0.0033$

Figure 4.4: Equatorial slice images of the radial velocity for $N_\rho = 5$, 3, 1, and 10^{-2} for $\eta_{nb} = 1.00$ at steady state for their respective value of Ra_c^*. A convection cell is represented by a pair of maximum and minimum areas near the inner boundary.

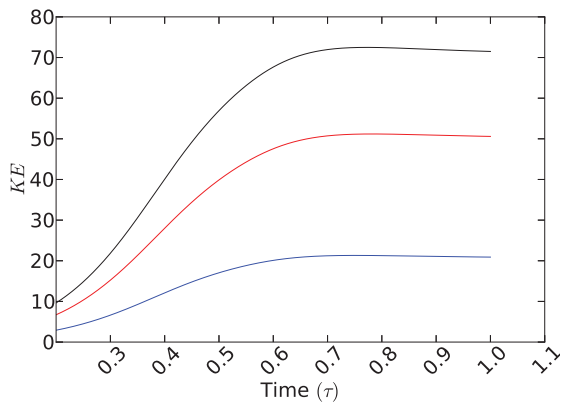

(a) $Ra^* = Ra_c^* = 0.0034$

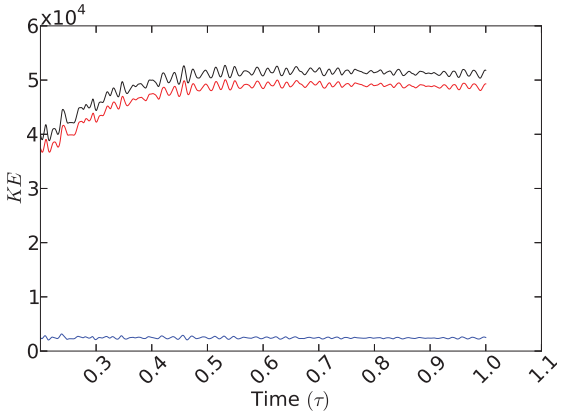

(b) $Ra^* = 4.4Ra_c^* = 0.0150$

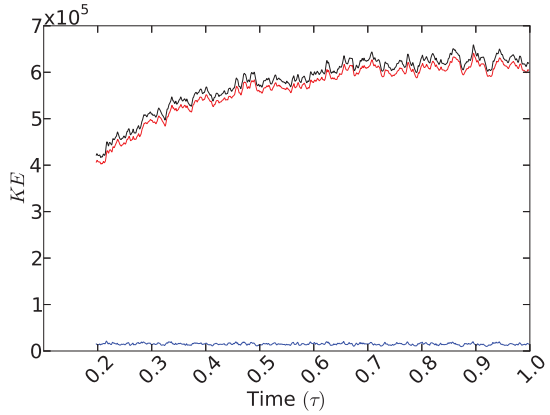

(c) $Ra^* = 14.7Ra_c^* = 0.0500$

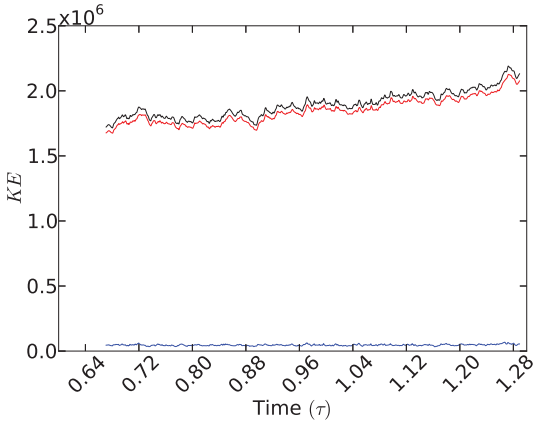

(d) $Ra^* = 29.4Ra_c^* = 0.1000$

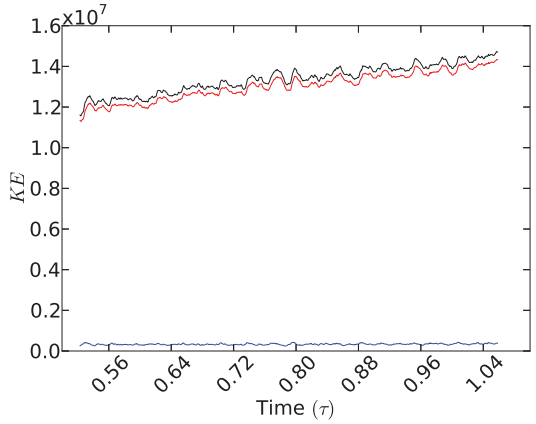

(e) $Ra^* = 147.1Ra_c^* = 0.5000$

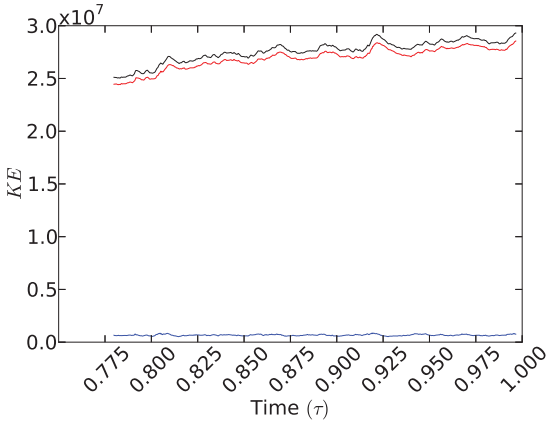

(f) $Ra^* = 294.1Ra_c^* = 1.0000$

Figure 4.5: Kinetic energy time series data for $N_\rho = 10^{-2}$ at $\eta_{nb} = 1.00$. The black line represents the total kinetic energy $KE = KE_\zeta + KE_\gamma$, where KE_ζ is represented by the red line and KE_γ is represented by the blue line.

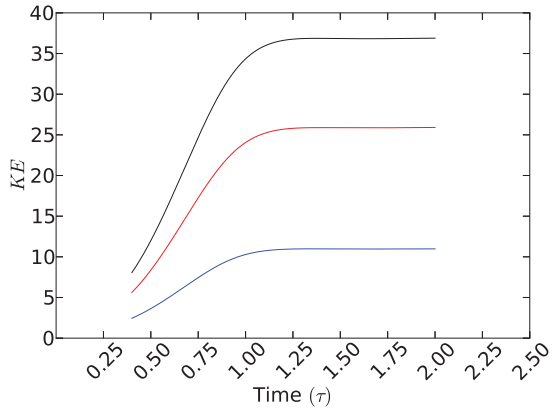

(a) $Ra^* = Ra_c^* = 0.0034$

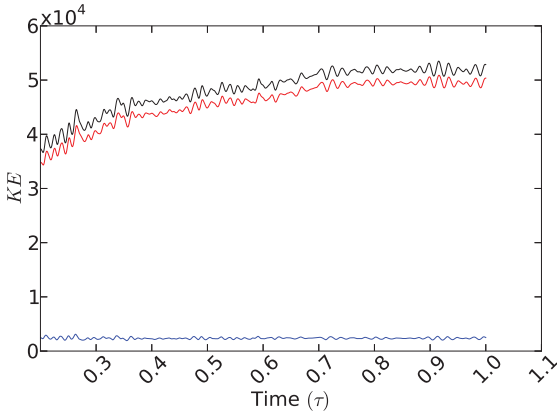

(b) $Ra^* = 4.4Ra_c^* = 0.0150$

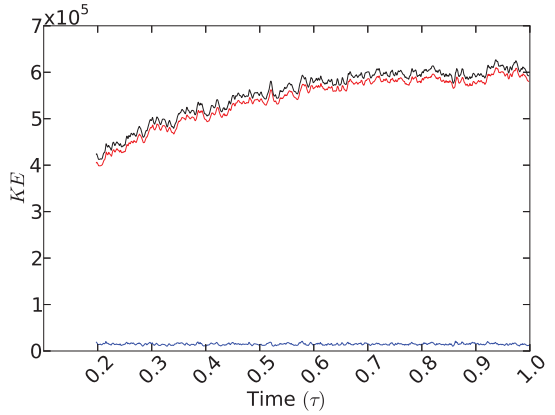

(c) $Ra^* = 14.7Ra_c^* = 0.0500$

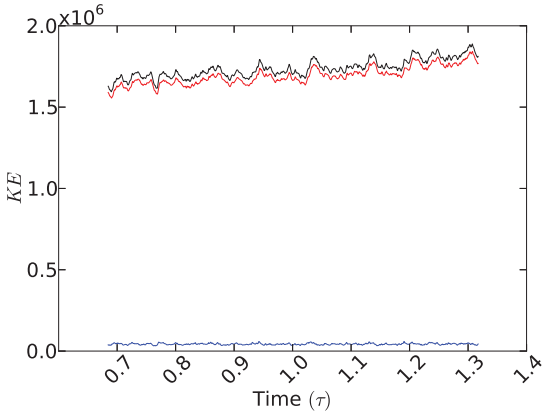

(d) $Ra^* = 29.4Ra_c^* = 0.1000$

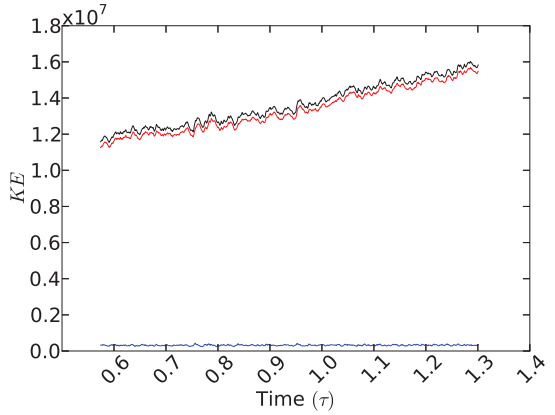

(e) $Ra^* = 147.1Ra_c^* = 0.5000$

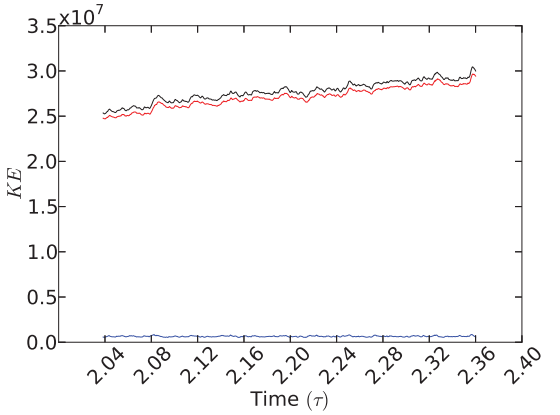

(f) $Ra^* = 294.1Ra_c^* = 1.0000$

Figure 4.6: Kinetic energy time series data for $N_\rho = 10^{-2}$ at $\eta_{nb} = 0.98$. The black line represents the total kinetic energy $KE = KE_\zeta + KE_\gamma$, where KE_ζ is represented by the red line and KE_γ is represented by the blue line.

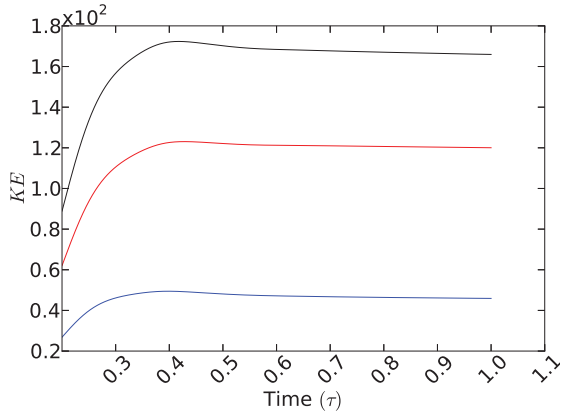

(a) $Ra^* = Ra_c^* = 0.0036$

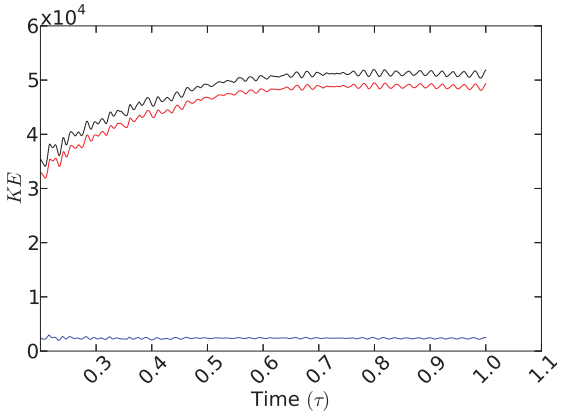

(b) $Ra^* = 4.2Ra_c^* = 0.0150$

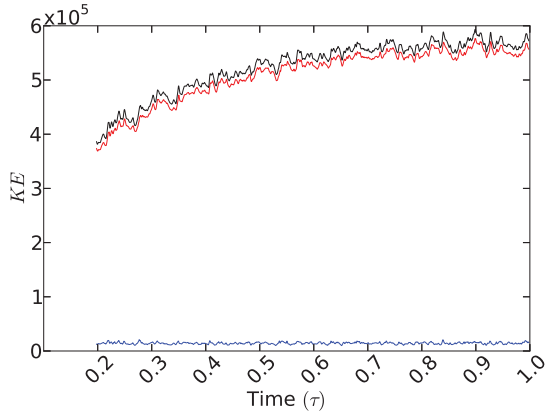

(c) $Ra^* = 13.9Ra_c^* = 0.0500$

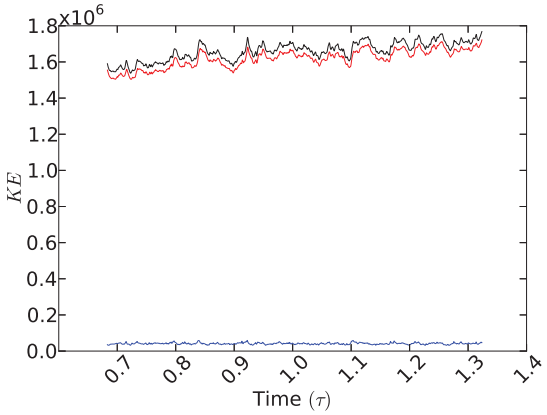

(d) $Ra^* = 27.8Ra_c^* = 0.1000$

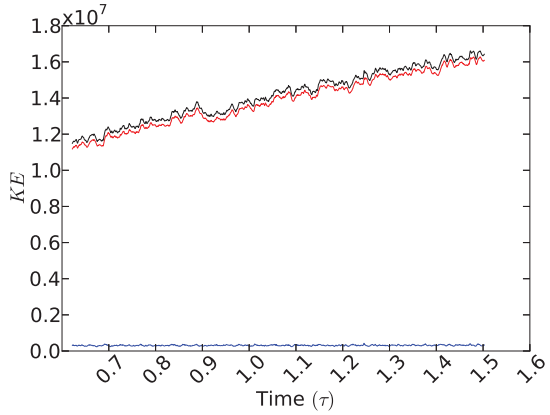

(e) $Ra^* = 138.9Ra_c^* = 0.5000$

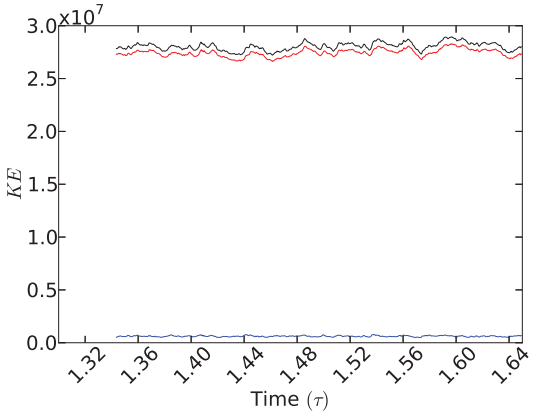

(f) $Ra^* = 277.8Ra_c^* = 1.0000$

Figure 4.7: Kinetic energy time series data for $N_\rho = 10^{-2}$ at $\eta_{nb} = 0.96$. The black line represents the total kinetic energy $KE = KE_\zeta + KE_\gamma$, where KE_ζ is represented by the red line and KE_γ is represented by the blue line.

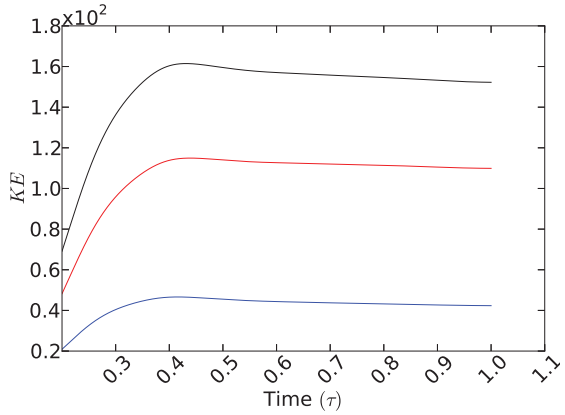

(a) $Ra^* = Ra_c^* = 0.0038$

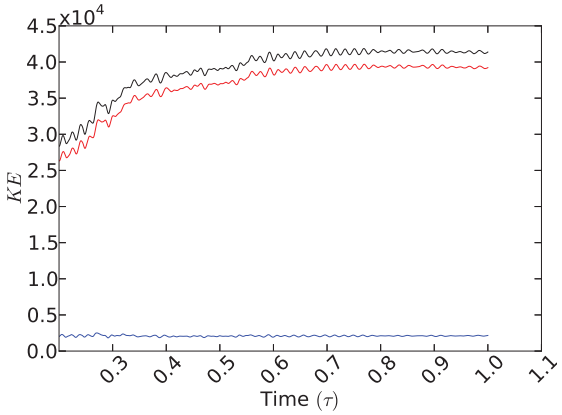

(b) $Ra^* = 3.9Ra_c^* = 0.0150$

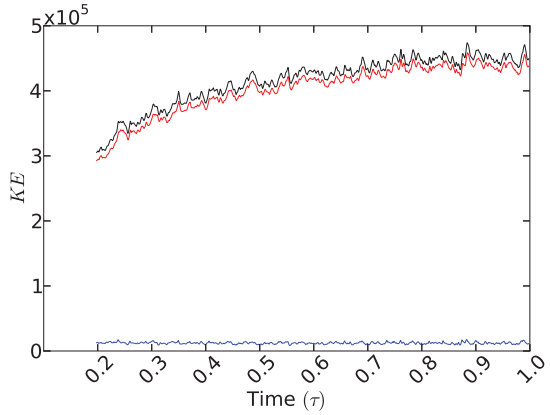

(c) $Ra^* = 13.2Ra_c^* = 0.0500$

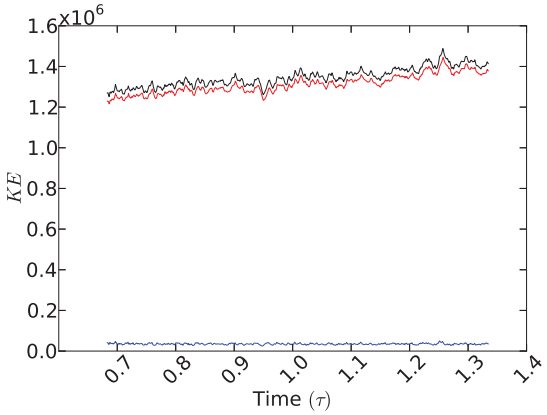

(d) $Ra^* = 26.3Ra_c^* = 0.1000$

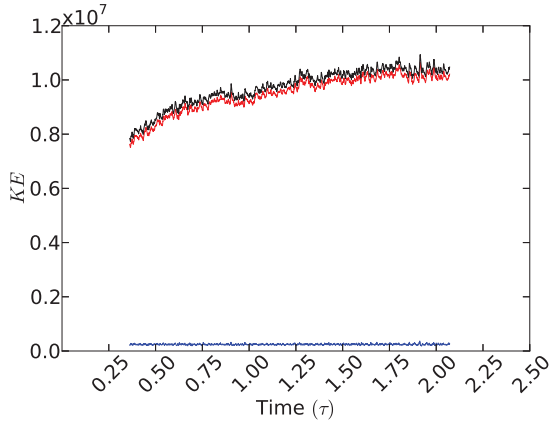

(e) $Ra^* = 131.6Ra_c^* = 0.5000$

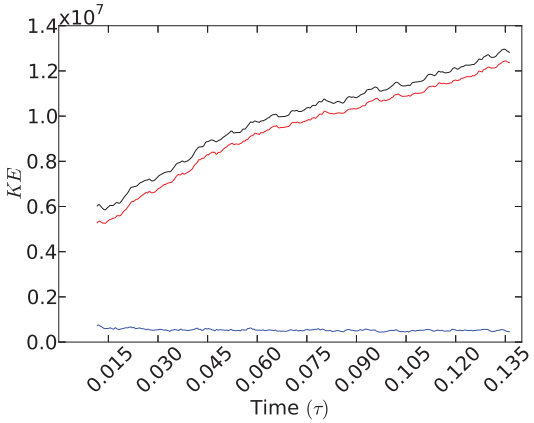

(f) $Ra^* = 263.2Ra_c^* = 1.0000$

Figure 4.8: Kinetic energy time series data for $N_\rho = 10^{-2}$ at $\eta_{nb} = 0.90$. The black line represents the total kinetic energy $KE = KE_\zeta + KE_\gamma$, where KE_ζ is represented by the red line and KE_γ is represented by the blue line.

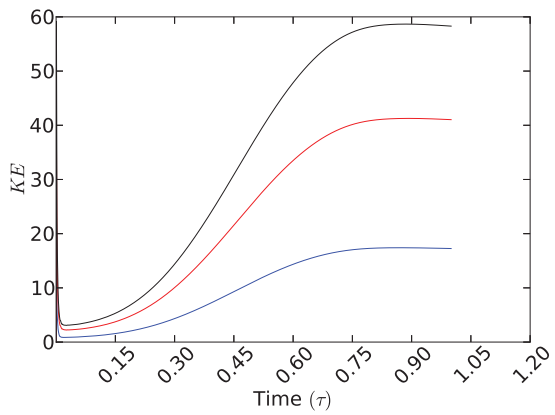

(a) $Ra^* = Ra_c^* = 0.0044$

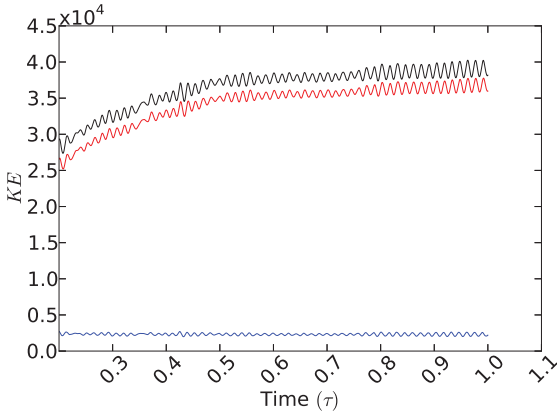

(b) $Ra^* = 4.5Ra_c^* = 0.0200$

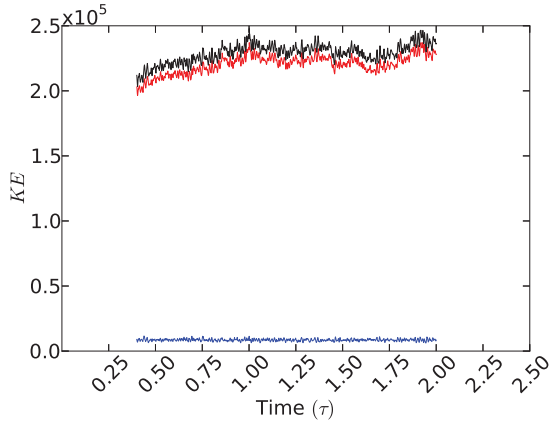

(c) $Ra^* = 11.4Ra_c^* = 0.0500$

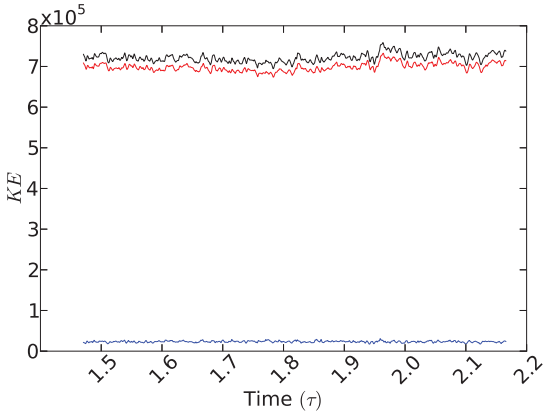

(d) $Ra^* = 22.7Ra_c^* = 0.1000$

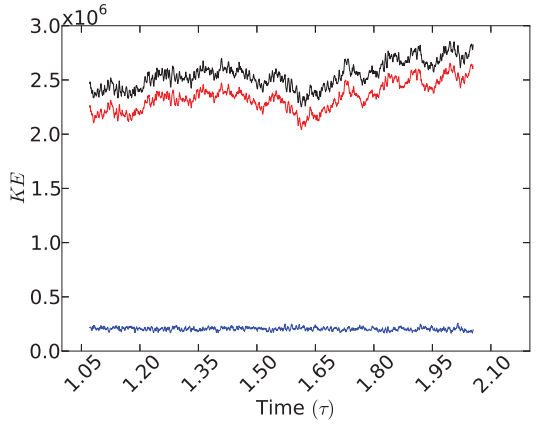

(e) $Ra^* = 113.6Ra_c^* = 0.5000$

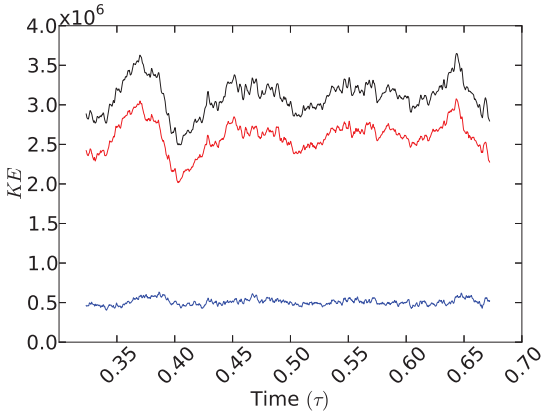

(f) $Ra^* = 227.3Ra_c^* = 1.0000$

Figure 4.9: Kinetic energy time series data for $N_\rho = 10^{-2}$ at $\eta_{nb} = 0.80$. The black line represents the total kinetic energy $KE = KE_\zeta + KE_\gamma$, where KE_ζ is represented by the red line and KE_γ is represented by the blue line.

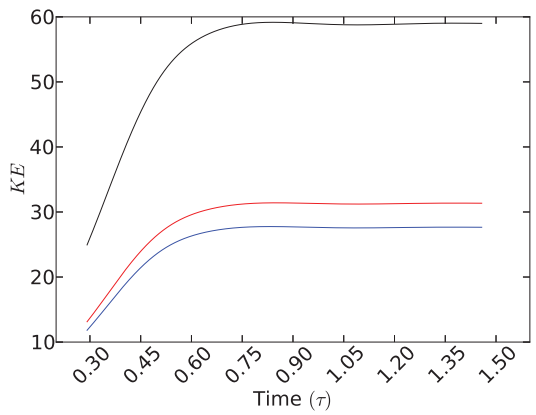

(a) $Ra^* = Ra_c^* = 0.0054$

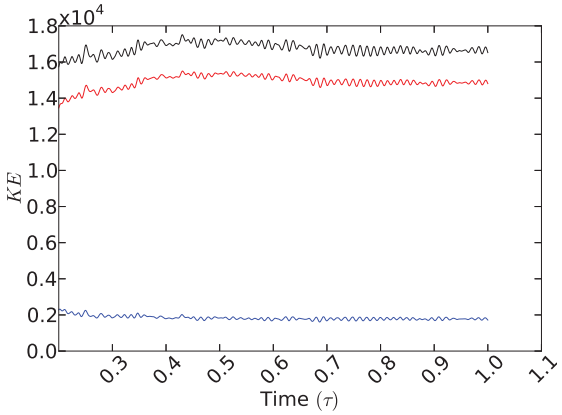

(b) $Ra^* = 1.8Ra_c^* = 0.0100$

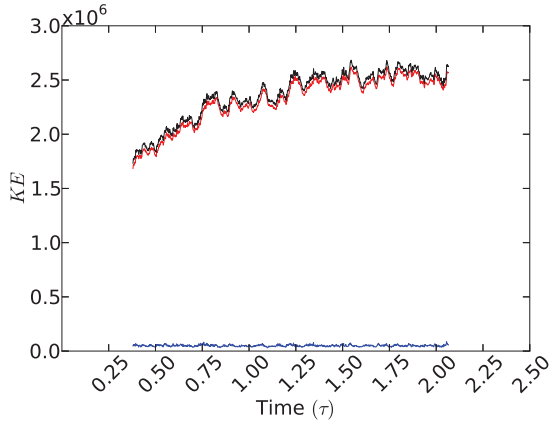

(c) $Ra^* = 9.3Ra_c^* = 0.0500$

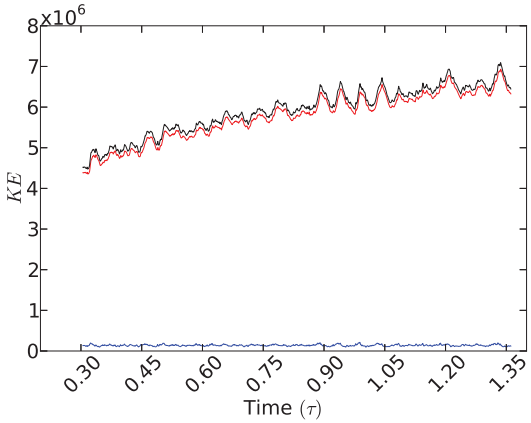

(d) $Ra^* = 18.1Ra_c^* = 0.1000$

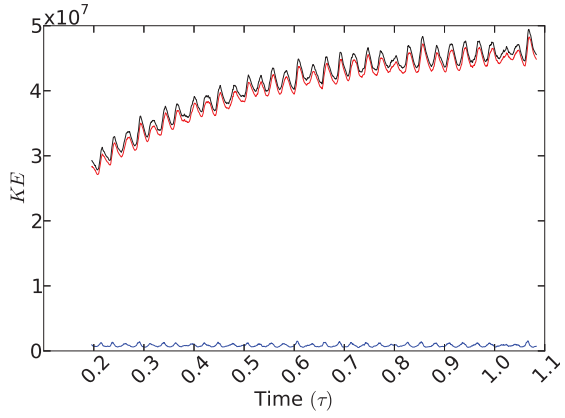

(e) $Ra^* = 92.6Ra_c^* = 0.5000$

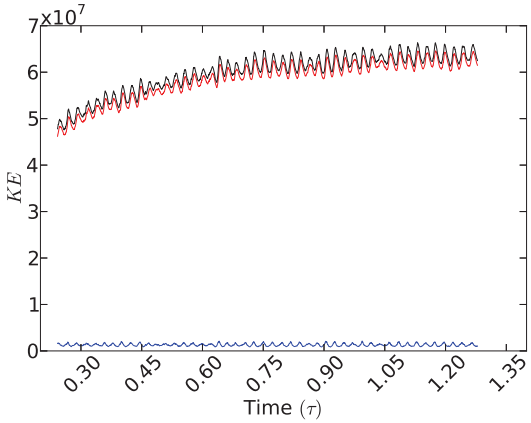

(f) $Ra^* = 138.9Ra_c^* = 0.7500$

Figure 4.10: Kinetic energy time series data for $N_\rho = 1$ at $\eta_{nb} = 1.00$. The black line represents the total kinetic energy $KE = KE_\zeta + KE_\gamma$, where KE_ζ is represented by the red line and KE_γ is represented by the blue line.

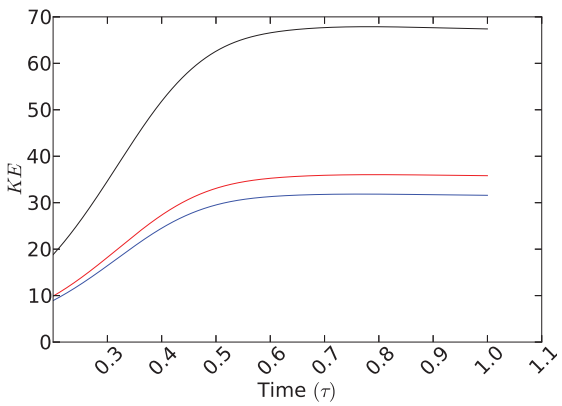

(a) $Ra^* = Ra_c^* = 0.0055$

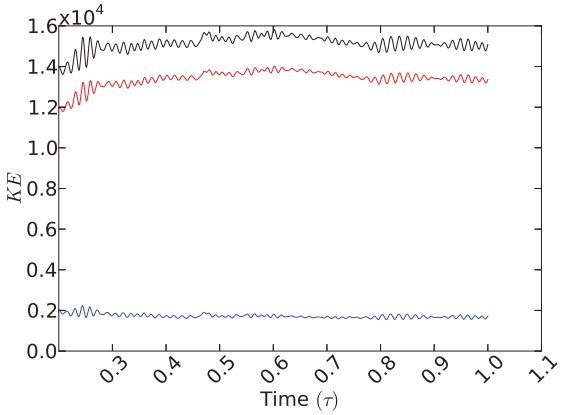

(b) $Ra^* = 1.8Ra_c^* = 0.0100$

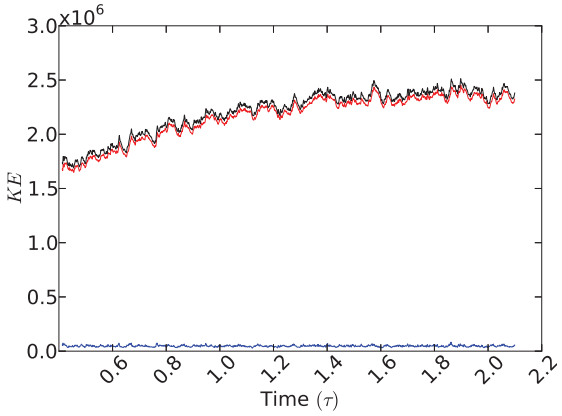

(c) $Ra^* = 9.1Ra_c^* = 0.0500$

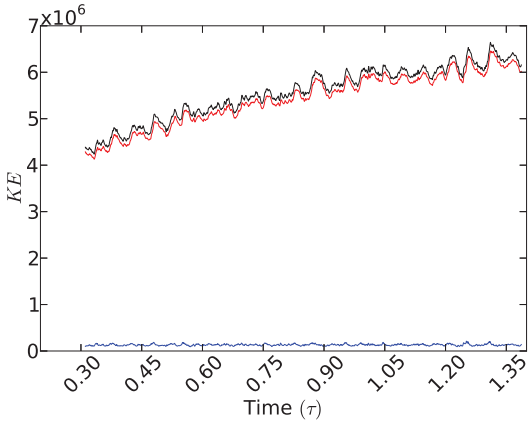

(d) $Ra^* = 18.2Ra_c^* = 0.1000$

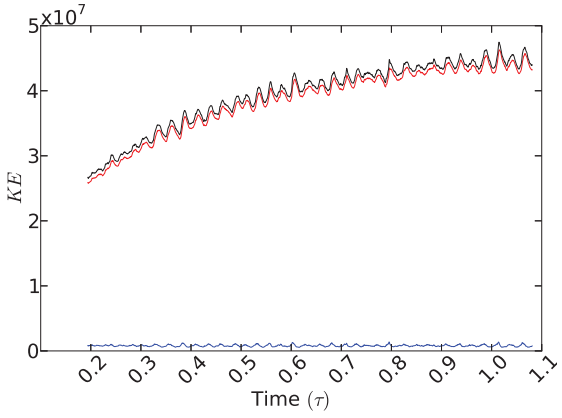

(e) $Ra^* = 90.9Ra_c^* = 0.5000$

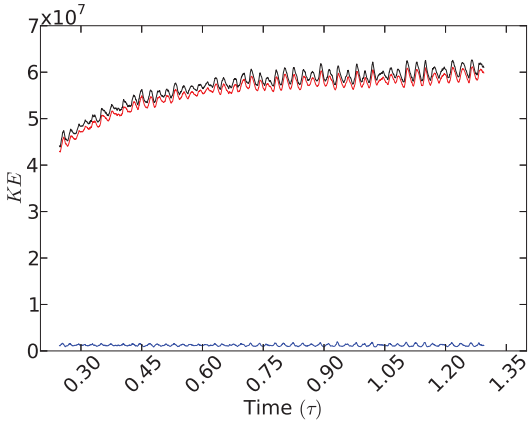

(f) $Ra^* = 136.4Ra_c^* = 0.7500$

Figure 4.11: Kinetic energy time series data for $N_\rho = 1$ at $\eta_{nb} = 0.98$. The black line represents the total kinetic energy $KE = KE_\zeta + KE_\gamma$, where KE_ζ is represented by the red line and KE_γ is represented by the blue line.

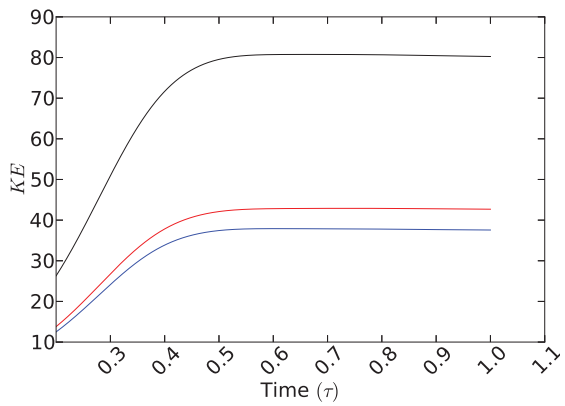

(a) $Ra^* = Ra_c^* = 0.0056$

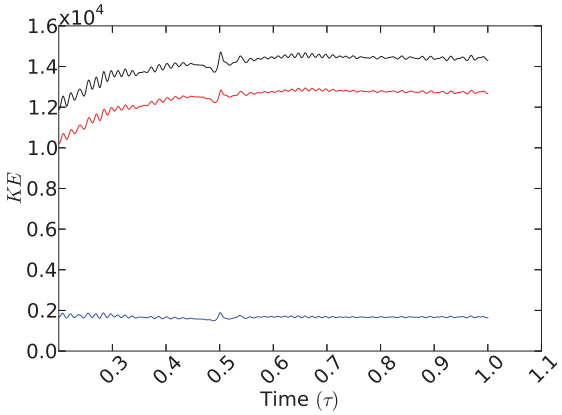

(b) $Ra^* = 1.8Ra_c^* = 0.0100$

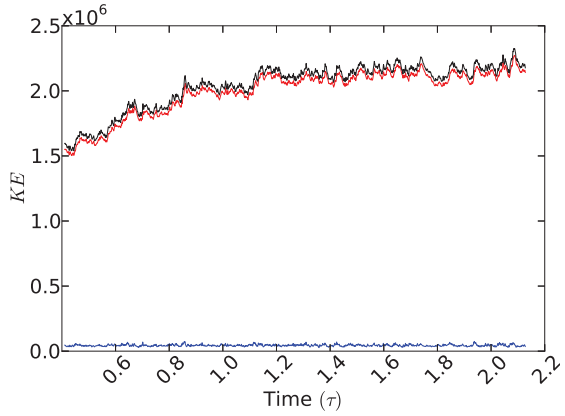

(c) $Ra^* = 8.9Ra_c^* = 0.0500$

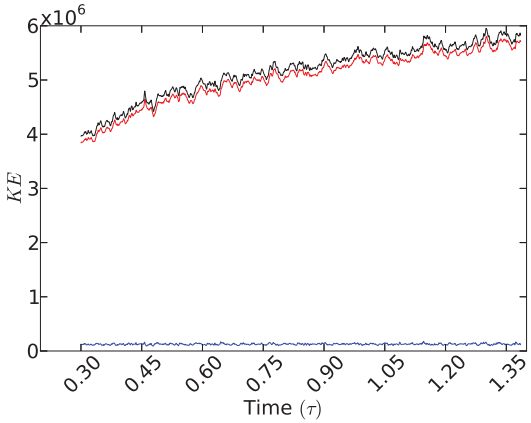

(d) $Ra^* = 17.9Ra_c^* = 0.1000$

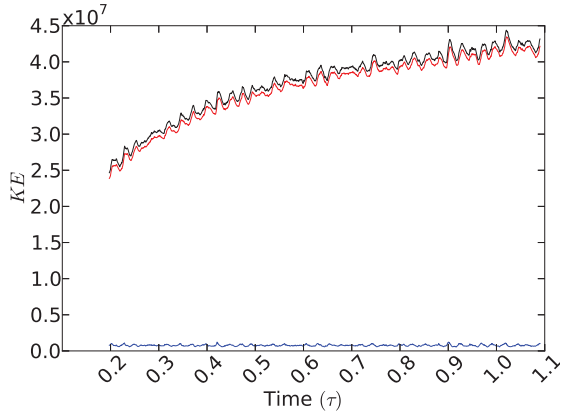

(e) $Ra^* = 89.3Ra_c^* = 0.5000$

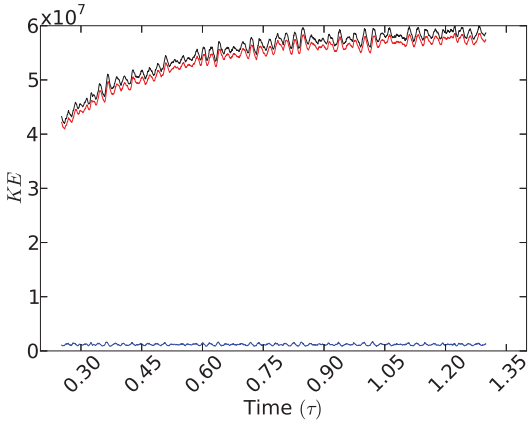

(f) $Ra^* = 133.9Ra_c^* = 0.7500$

Figure 4.12: Kinetic energy time series data for $N_\rho = 1$ at $\eta_{nb} = 0.96$. The black line represents the total kinetic energy $KE = KE_\zeta + KE_\gamma$, where KE_ζ is represented by the red line and KE_γ is represented by the blue line.

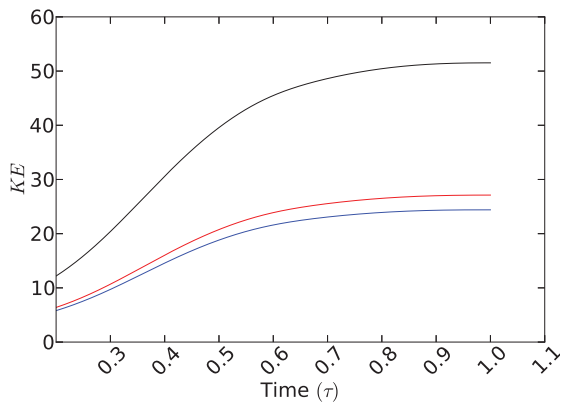

(a) $Ra^* = Ra_c^* = 0.0060$

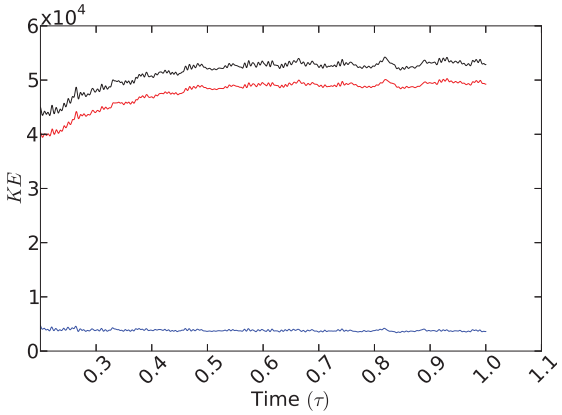

(b) $Ra^* = 2.5Ra_c^* = 0.0150$

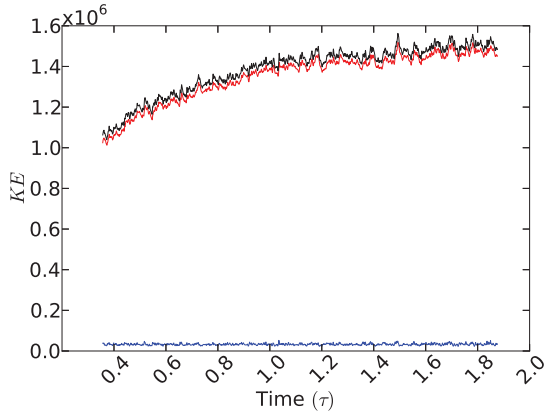

(c) $Ra^* = 8.3Ra_c^* = 0.0500$

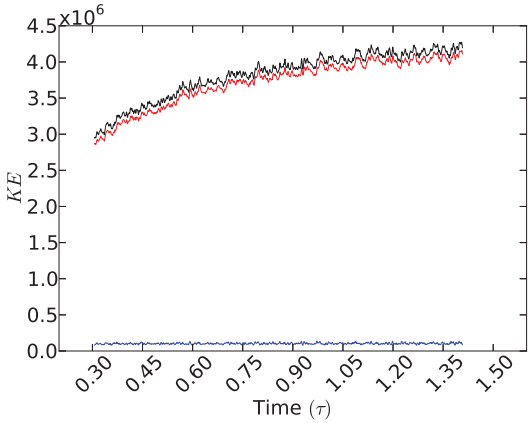

(d) $Ra^* = 16.7Ra_c^* = 0.1000$

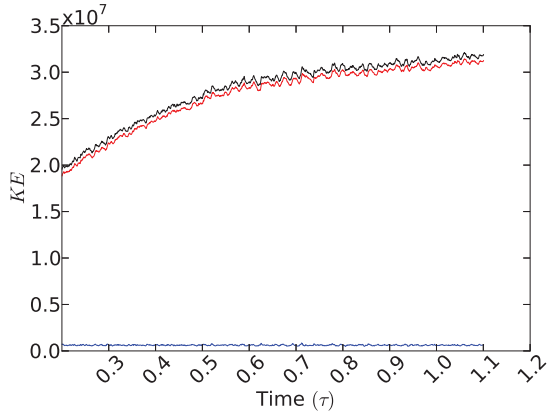

(e) $Ra^* = 83.3Ra_c^* = 0.5000$

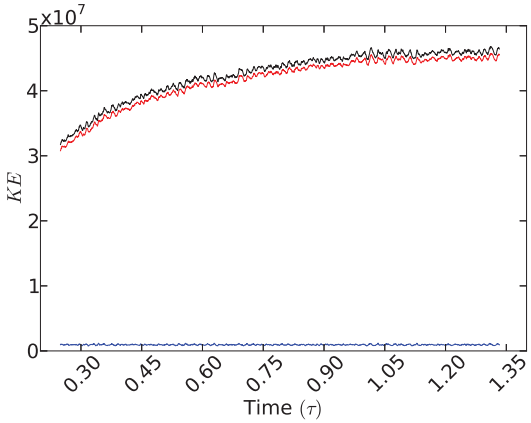

(f) $Ra^* = 125.0Ra_c^* = 0.7500$

Figure 4.13: Kinetic energy time series data for $N_\rho = 1$ at $\eta_{nb} = 0.90$. The black line represents the total kinetic energy $KE = KE_\zeta + KE_\gamma$, where KE_ζ is represented by the red line and KE_γ is represented by the blue line.

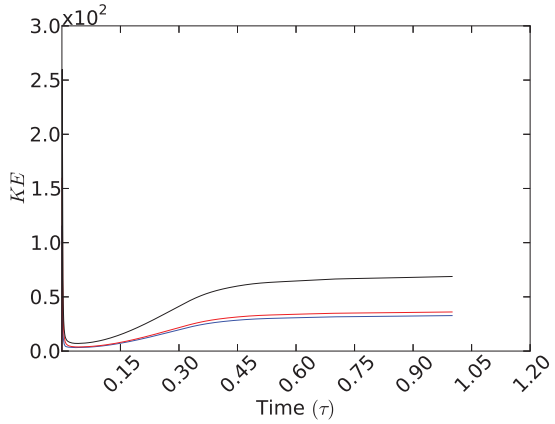

(a) $Ra^* = Ra_c^* = 0.0074$

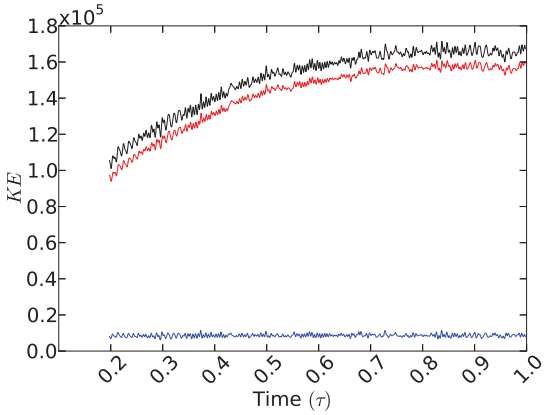

(b) $Ra^* = 4.1Ra_c^* = 0.0300$

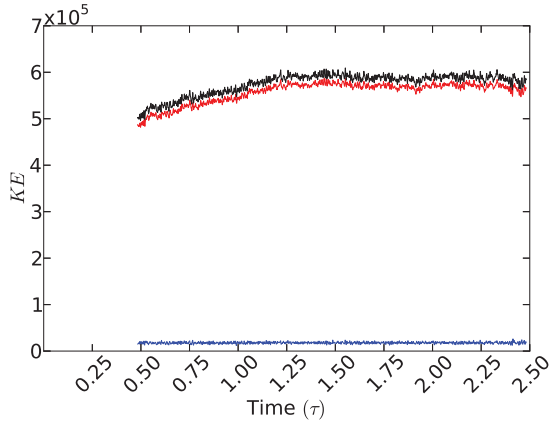

(c) $Ra^* = 6.8Ra_c^* = 0.0500$

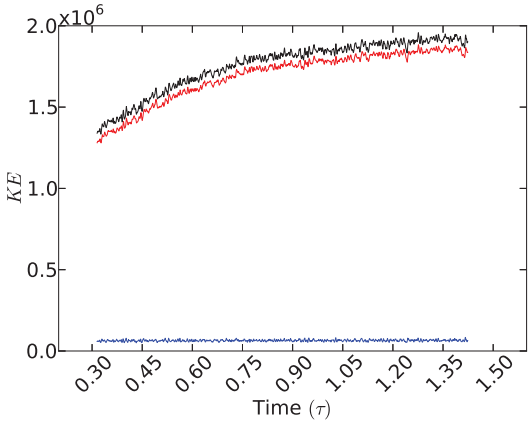

(d) $Ra^* = 13.6Ra_c^* = 0.1000$

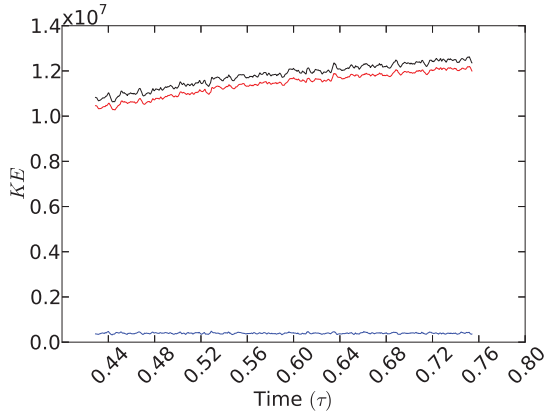

(e) $Ra^* = 67.6Ra_c^* = 0.5000$

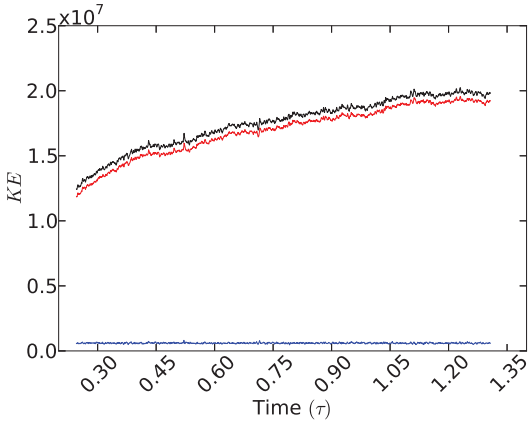

(f) $Ra^* = 101.4Ra_c^* = 0.7500$

Figure 4.14: Kinetic energy time series data for $N_\rho = 1$ at $\eta_{nb} = 0.80$. The black line represents the total kinetic energy $KE = KE_\zeta + KE_\gamma$, where KE_ζ is represented by the red line and KE_γ is represented by the blue line.

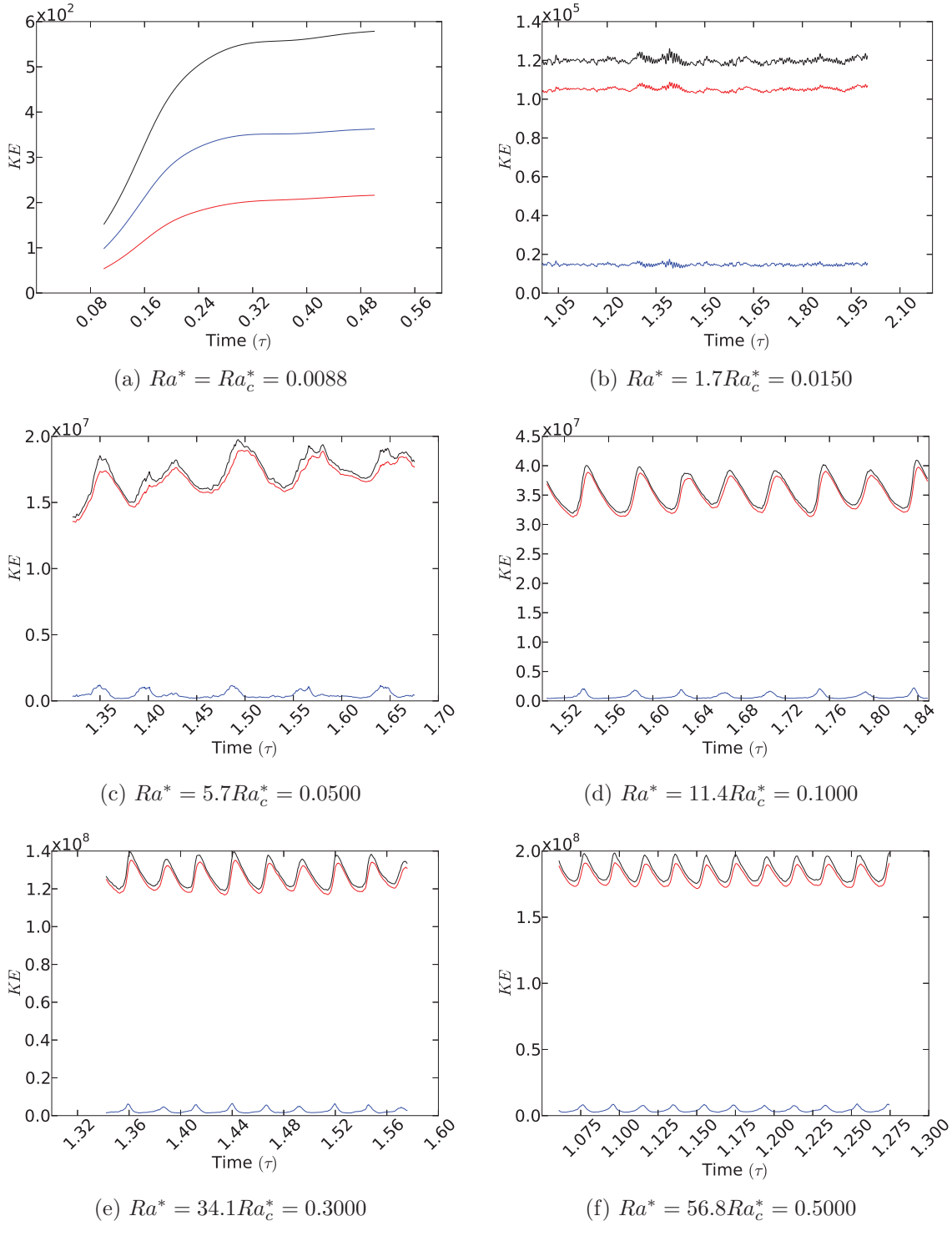

(a) $Ra^* = Ra_c^* = 0.0088$

(b) $Ra^* = 1.7Ra_c^* = 0.0150$

(c) $Ra^* = 5.7Ra_c^* = 0.0500$

(d) $Ra^* = 11.4Ra_c^* = 0.1000$

(e) $Ra^* = 34.1Ra_c^* = 0.3000$

(f) $Ra^* = 56.8Ra_c^* = 0.5000$

Figure 4.15: Kinetic energy time series data for $N_\rho = 3$ at $\eta_{nb} = 1.00$. The black line represents the total kinetic energy $KE = KE_\zeta + KE_\gamma$, where KE_ζ is represented by the red line and KE_γ is represented by the blue line.

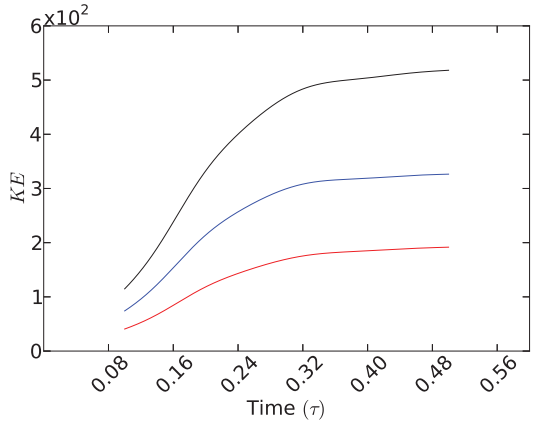

(a) $Ra^* = Ra_c^* = 0.0090$

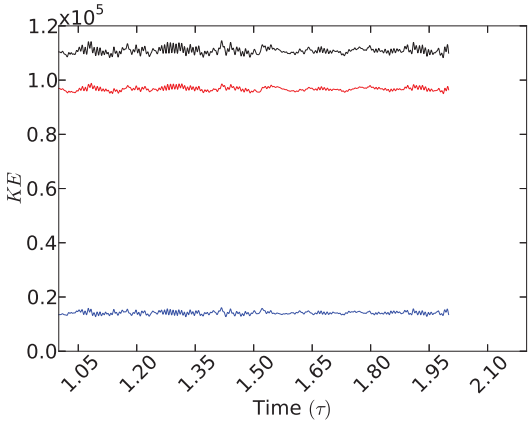

(b) $Ra^* = 1.7Ra_c^* = 0.0150$

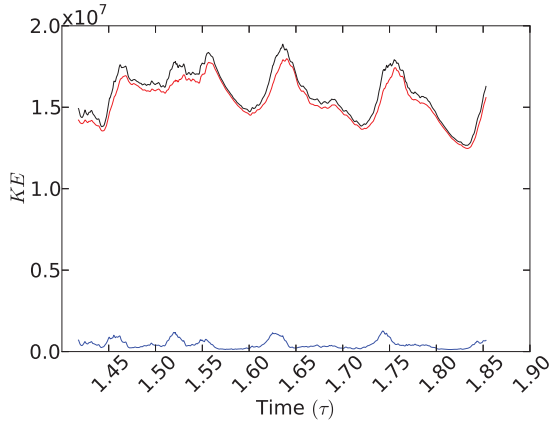

(c) $Ra^* = 5.6Ra_c^* = 0.0500$

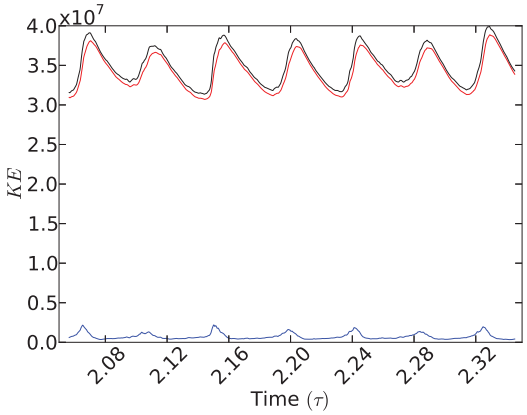

(d) $Ra^* = 11.1Ra_c^* = 0.1000$

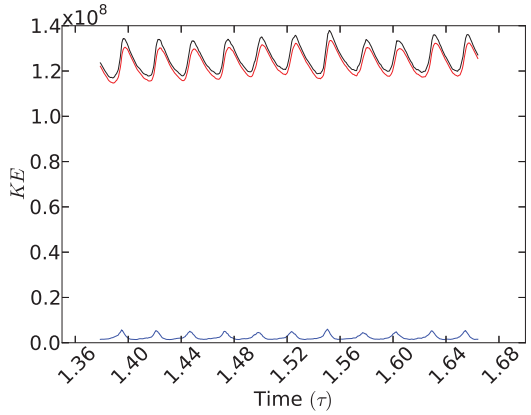

(e) $Ra^* = 33.3Ra_c^* = 0.3000$

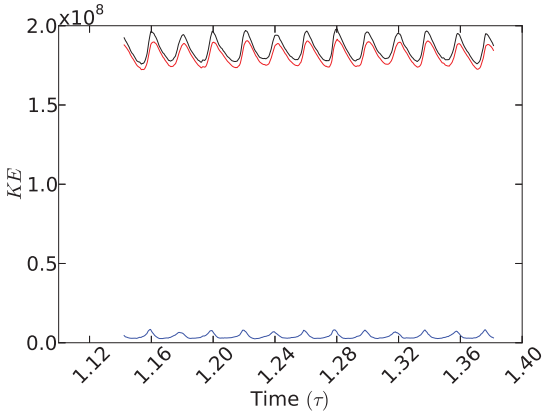

(f) $Ra^* = 55.6Ra_c^* = 0.5000$

Figure 4.16: Kinetic energy time series data for $N_\rho = 3$ at $\eta_{nb} = 0.98$. The black line represents the total kinetic energy $KE = KE_\zeta + KE_\gamma$, where KE_ζ is represented by the red line and KE_γ is represented by the blue line.

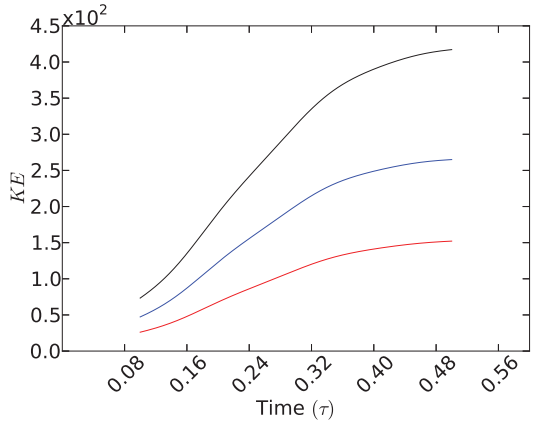

(a) $Ra^* = Ra_c^* = 0.0091$

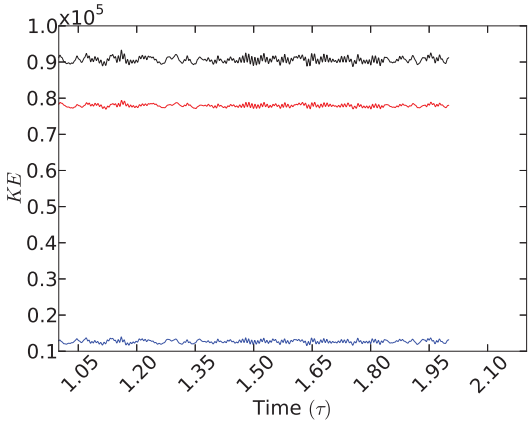

(b) $Ra^* = 1.6Ra_c^* = 0.0150$

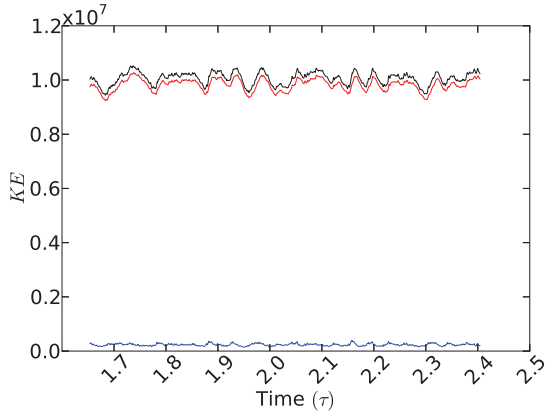

(c) $Ra^* = 5.5Ra_c^* = 0.0500$

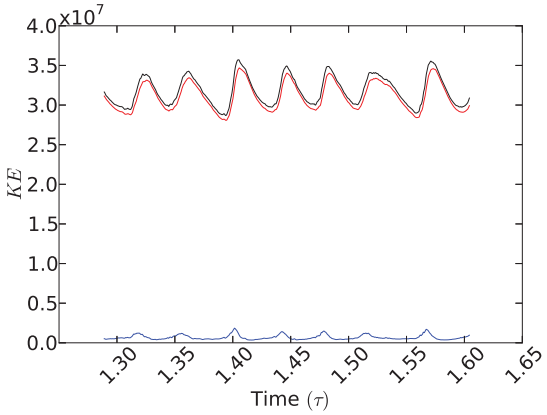

(d) $Ra^* = 11.0Ra_c^* = 0.1000$

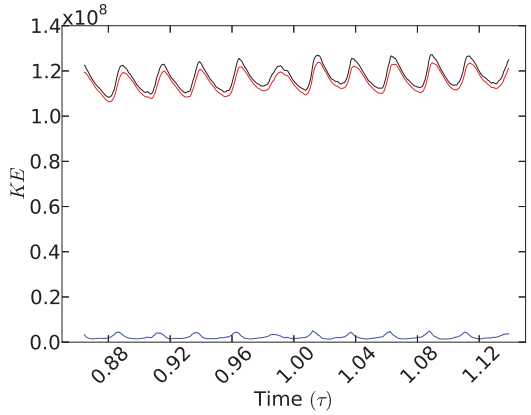

(e) $Ra^* = 33.0Ra_c^* = 0.3000$

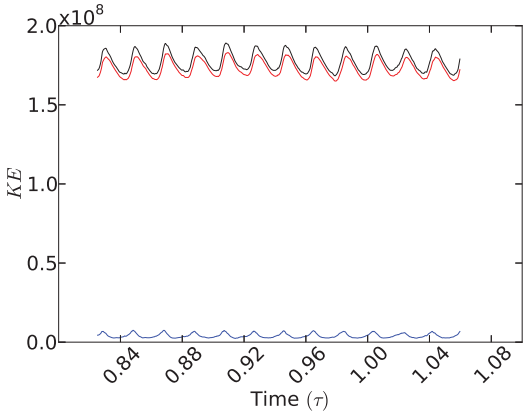

(f) $Ra^* = 54.9Ra_c^* = 0.5000$

Figure 4.17: Kinetic energy time series data for $N_\rho = 3$ at $\eta_{nb} = 0.96$. The black line represents the total kinetic energy $KE = KE_\zeta + KE_\gamma$, where KE_ζ is represented by the red line and KE_γ is represented by the blue line.

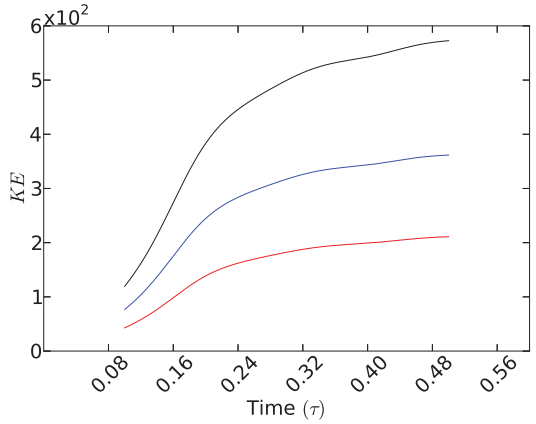

(a) $Ra^* = Ra_c^* = 0.0096$

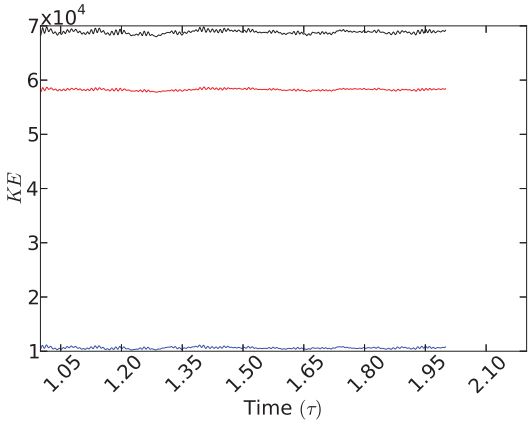

(b) $Ra^* = 1.6Ra_c^* = 0.0150$

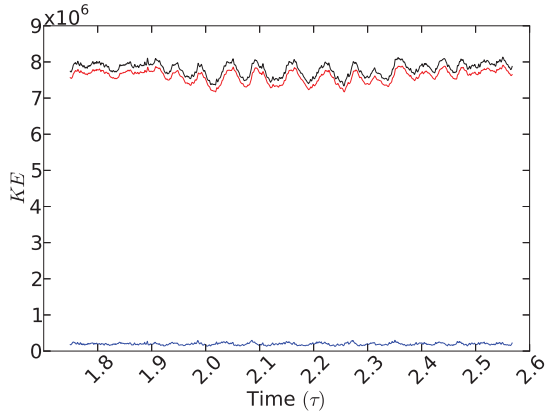

(c) $Ra^* = 5.2Ra_c^* = 0.0500$

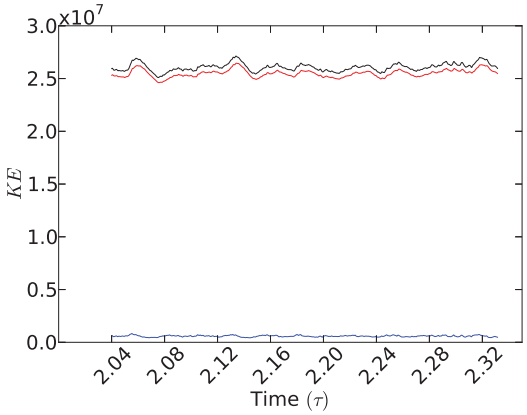

(d) $Ra^* = 10.4Ra_c^* = 0.1000$

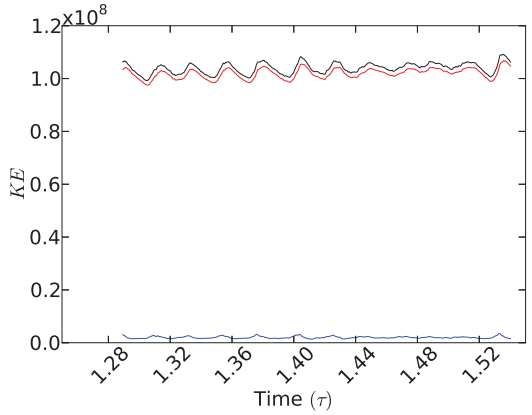

(e) $Ra^* = 31.3Ra_c^* = 0.3000$

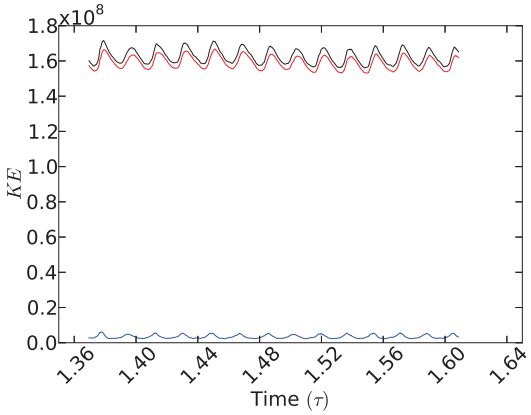

(f) $Ra^* = 52.1Ra_c^* = 0.5000$

Figure 4.18: Kinetic energy time series data for $N_\rho = 3$ at $\eta_{nb} = 0.90$. The black line represents the total kinetic energy $KE = KE_\zeta + KE_\gamma$, where KE_ζ is represented by the red line and KE_γ is represented by the blue line.

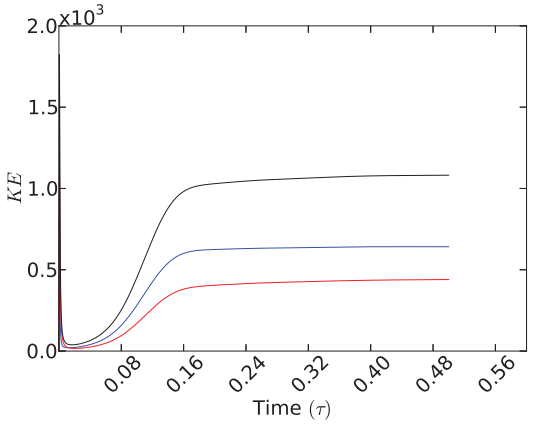

(a) $Ra^* = Ra_c^* = 0.0116$

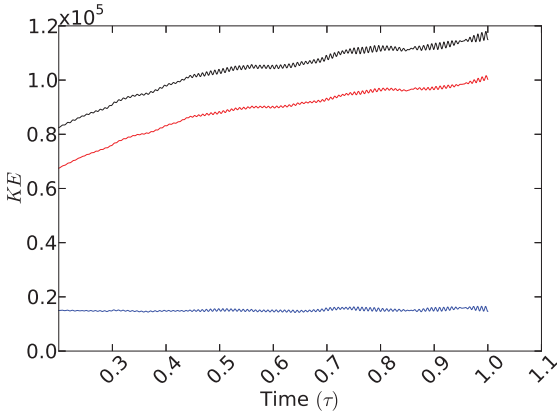

(b) $Ra^* = 1.7Ra_c^* = 0.0200$

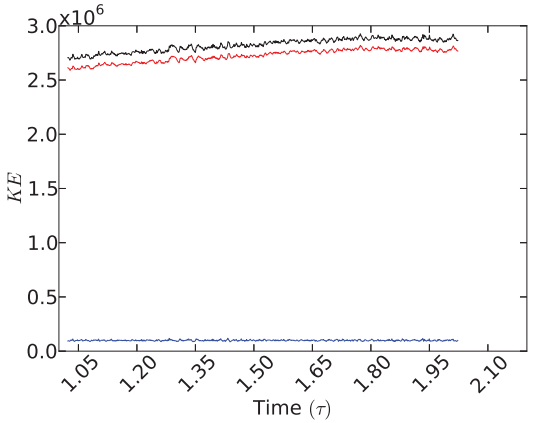

(c) $Ra^* = 4.3Ra_c^* = 0.0500$

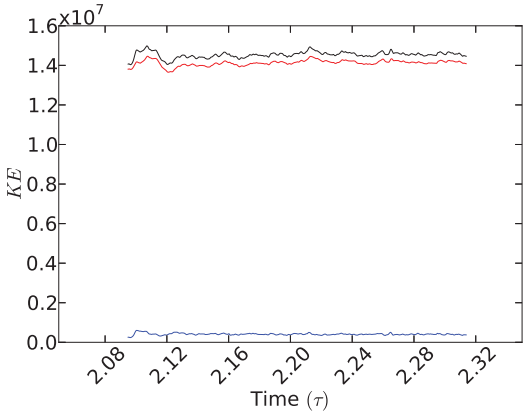

(d) $Ra^* = 8.6Ra_c^* = 0.1000$

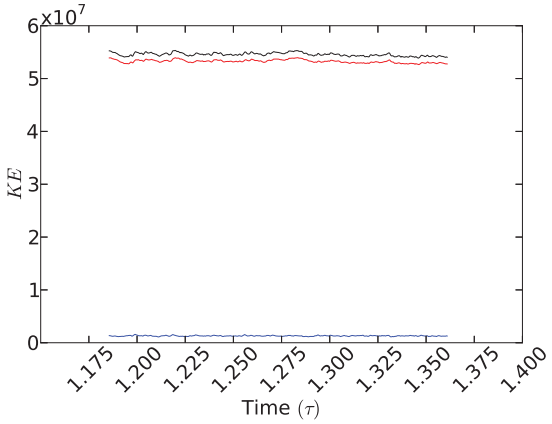

(e) $Ra^* = 25.9Ra_c^* = 0.3000$

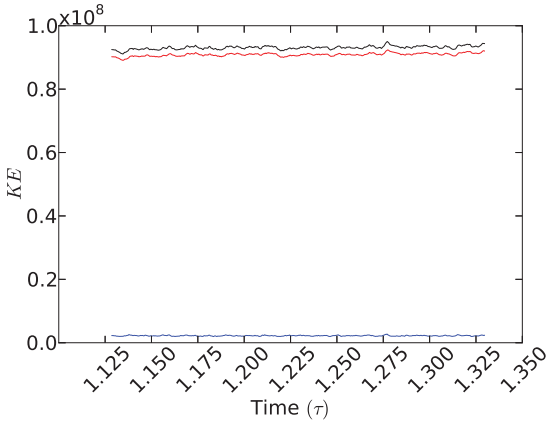

(f) $Ra^* = 43.1Ra_c^* = 0.5000$

Figure 4.19: Kinetic energy time series data for $N_\rho = 3$ at $\eta_{nb} = 0.80$. The black line represents the total kinetic energy $KE = KE_\zeta + KE_\gamma$, where KE_ζ is represented by the red line and KE_γ is represented by the blue line.

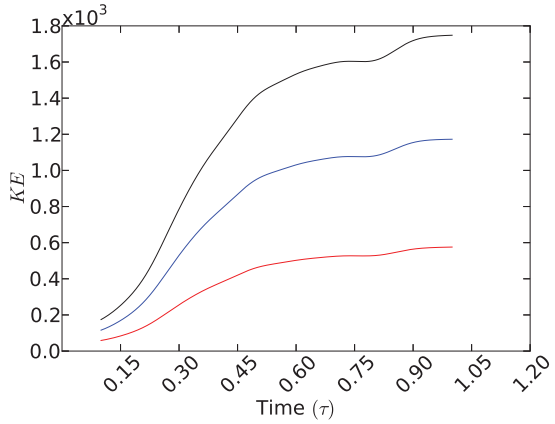

(a) $Ra^* = Ra_c^* = 0.0111$

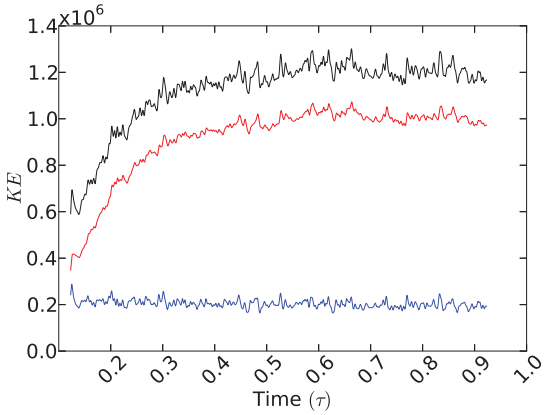

(b) $Ra^* = 1.8Ra_c^* = 0.0200$

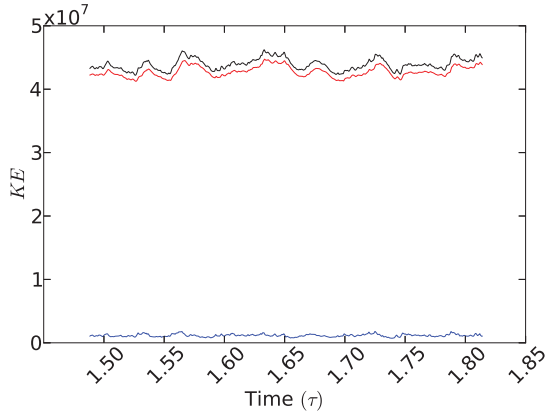

(c) $Ra^* = 4.5Ra_c^* = 0.0500$

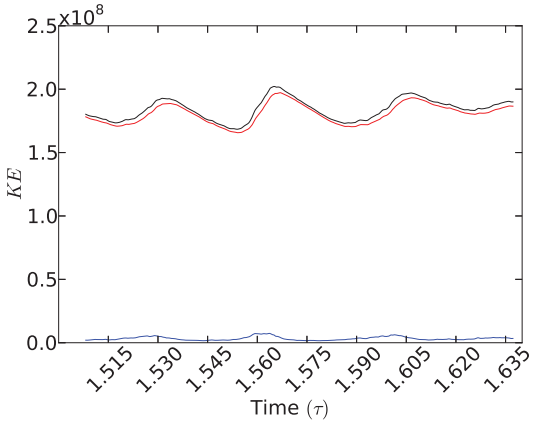

(d) $Ra^* = 9.0Ra_c^* = 0.1000$

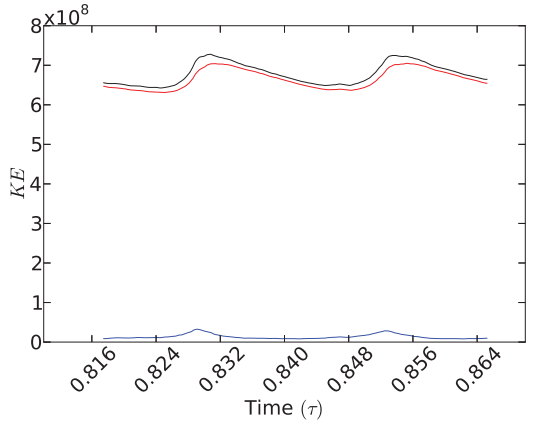

(e) $Ra^* = 27.0Ra_c^* = 0.3000$

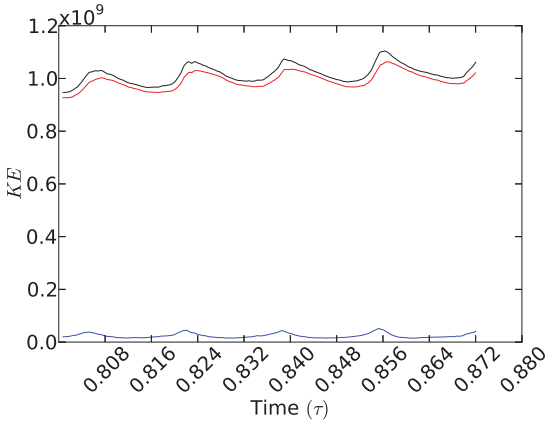

(f) $Ra^* = 45.0Ra_c^* = 0.5000$

Figure 4.20: Kinetic energy time series data for $N_\rho = 5$ at $\eta_{nb} = 1.00$. The black line represents the total kinetic energy $KE = KE_\zeta + KE_\gamma$, where KE_ζ is represented by the red line and KE_γ is represented by the blue line.

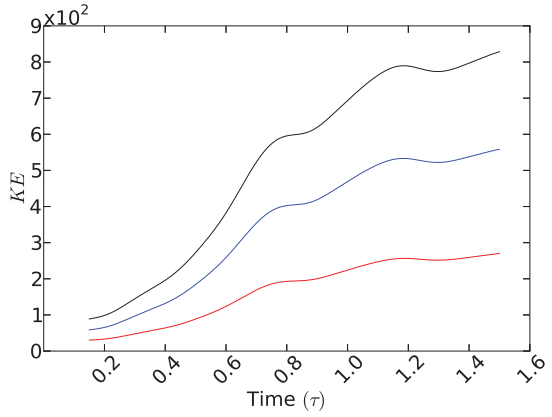

(a) $Ra^* = Ra_c^* = 0.0111$

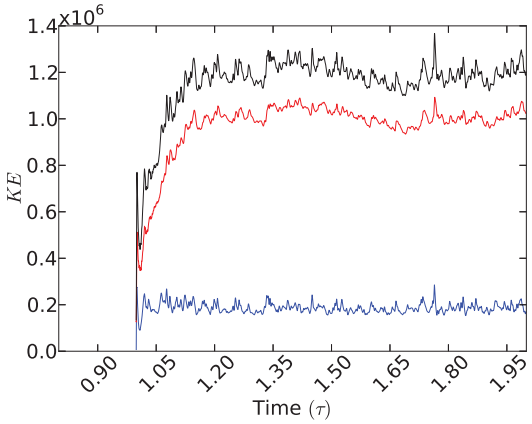

(b) $Ra^* = 1.8Ra_c^* = 0.0200$

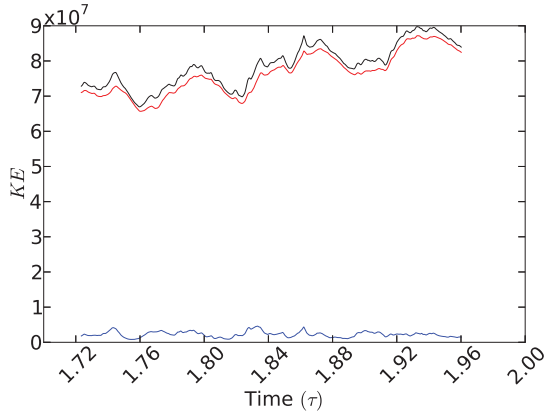

(c) $Ra^* = 4.5Ra_c^* = 0.0500$

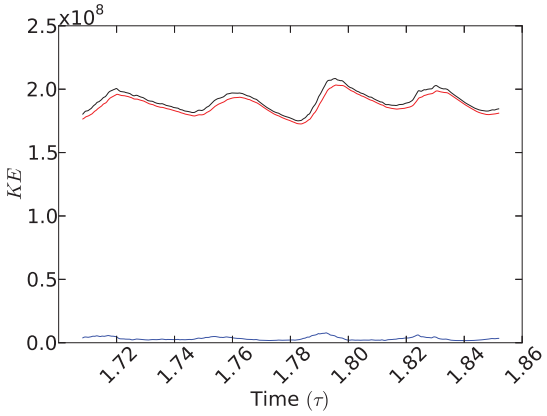

(d) $Ra^* = 9.0Ra_c^* = 0.1000$

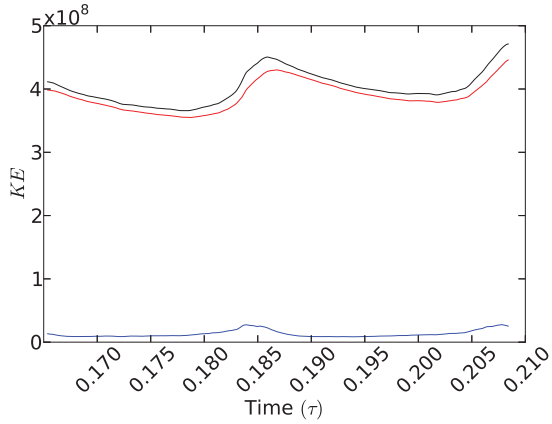

(e) $Ra^* = 27.0Ra_c^* = 0.3000$

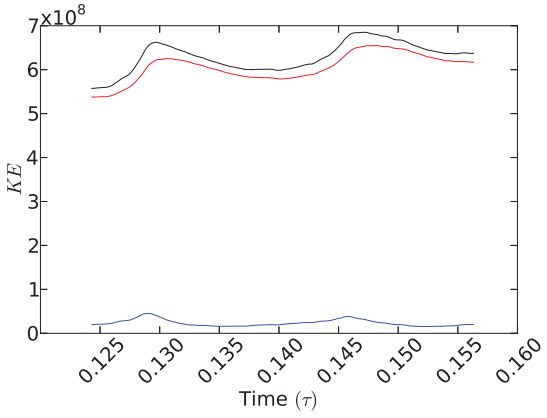

(f) $Ra^* = 45.0Ra_c^* = 0.5000$

Figure 4.21: Kinetic energy time series data for $N_\rho = 5$ at $\eta_{nb} = 0.98$. The black line represents the total kinetic energy $KE = KE_\zeta + KE_\gamma$, where KE_ζ is represented by the red line and KE_γ is represented by the blue line.

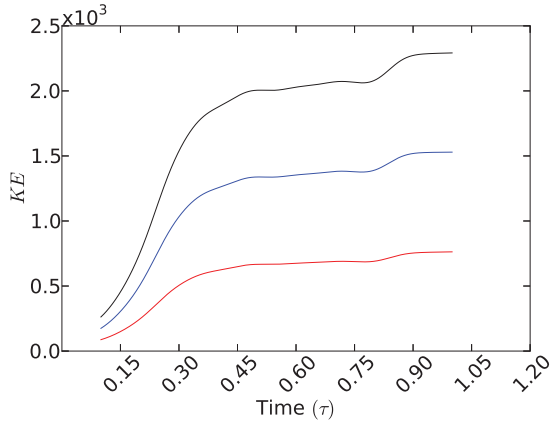

(a) $Ra^* = Ra_c^* = 0.0112$

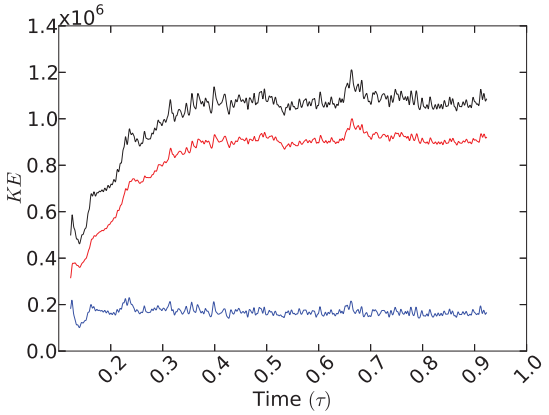

(b) $Ra^* = 1.8Ra_c^* = 0.0200$

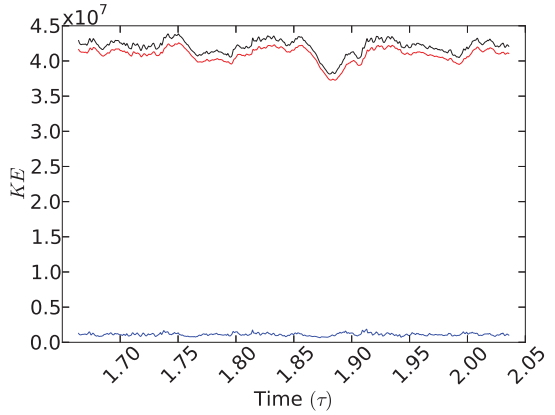

(c) $Ra^* = 4.5Ra_c^* = 0.0500$

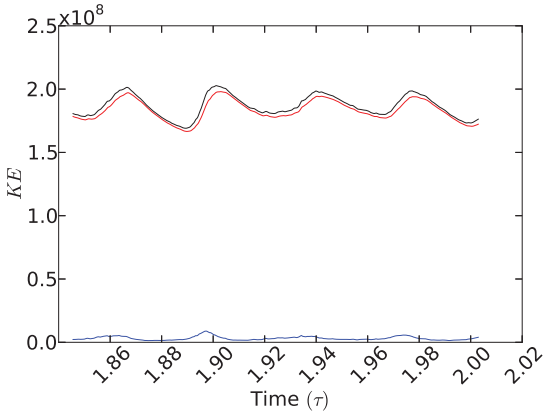

(d) $Ra^* = 8.9Ra_c^* = 0.1000$

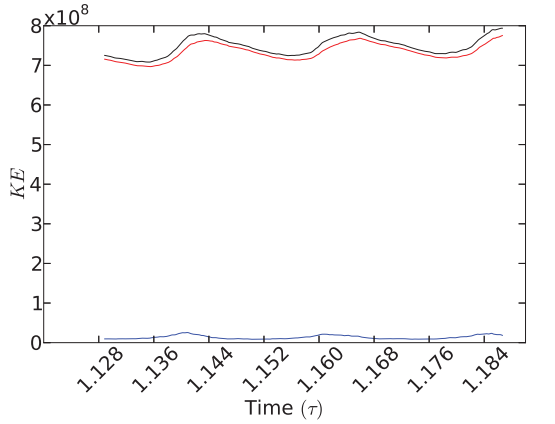

(e) $Ra^* = 26.8Ra_c^* = 0.3000$

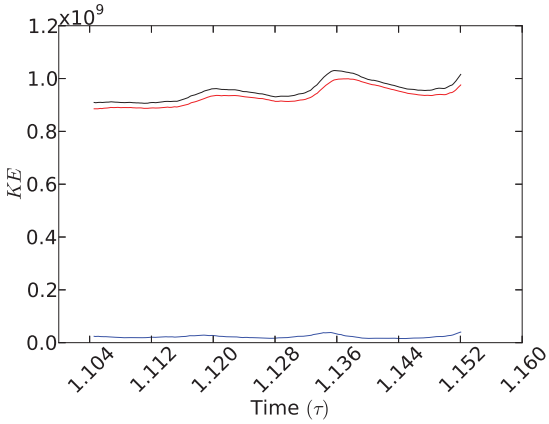

(f) $Ra^* = 44.6Ra_c^* = 0.5000$

Figure 4.22: Kinetic energy time series data for $N_\rho = 5$ at $\eta_{nb} = 0.96$. The black line represents the total kinetic energy $KE = KE_\zeta + KE_\gamma$, where KE_ζ is represented by the red line and KE_γ is represented by the blue line.

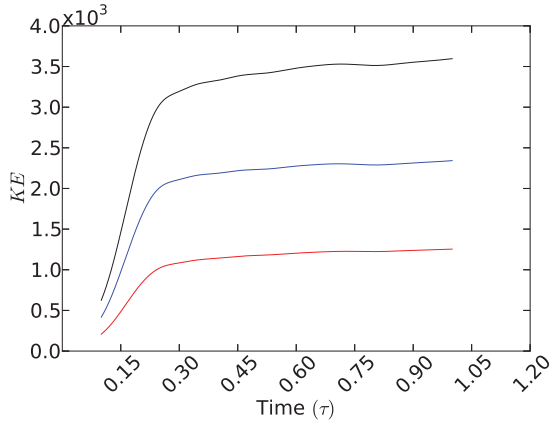

(a) $Ra^* = Ra_c^* = 0.0116$

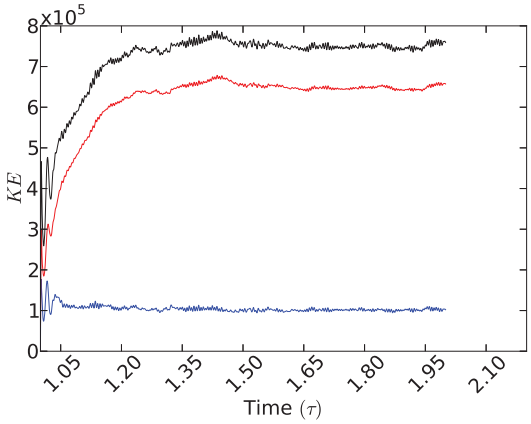

(b) $Ra^* = 1.7Ra_c^* = 0.0200$

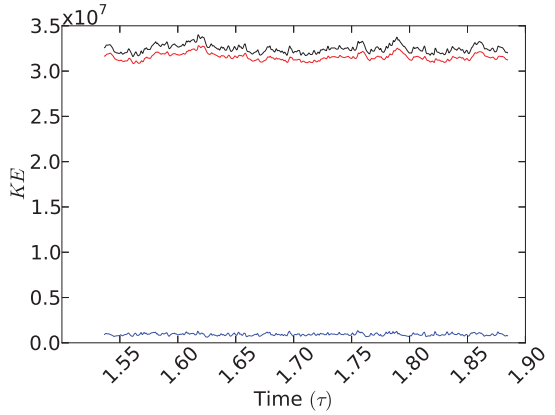

(c) $Ra^* = 4.3Ra_c^* = 0.0500$

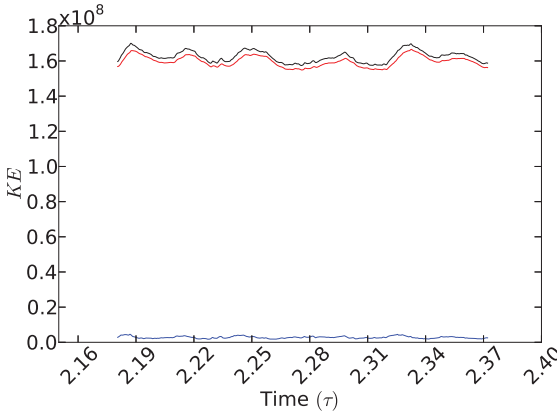

(d) $Ra^* = 8.6Ra_c^* = 0.1000$

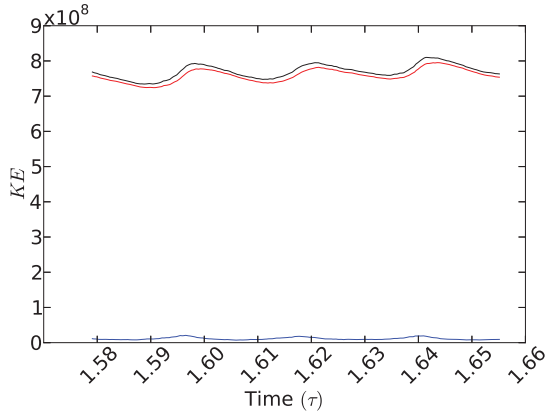

(e) $Ra^* = 25.9Ra_c^* = 0.3000$

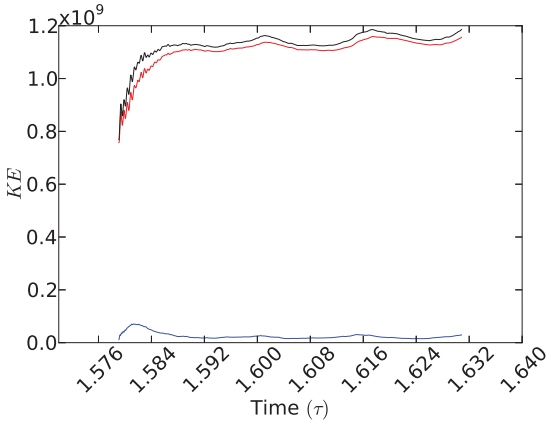

(f) $Ra^* = 43.1Ra_c^* = 0.5000$

Figure 4.23: Kinetic energy time series data for $N_\rho = 5$ at $\eta_{nb} = 0.90$. The black line represents the total kinetic energy $KE = KE_\zeta + KE_\gamma$, where KE_ζ is represented by the red line and KE_γ is represented by the blue line.

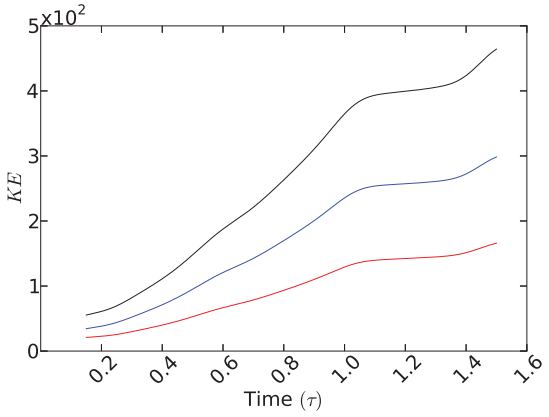

(a) $Ra^* = Ra_c^* = 0.0132$

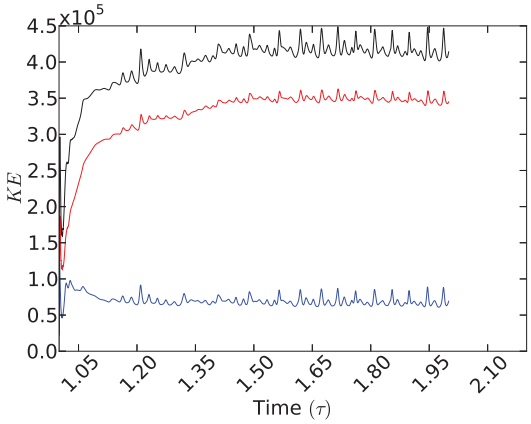

(b) $Ra^* = 1.5Ra_c^* = 0.0200$

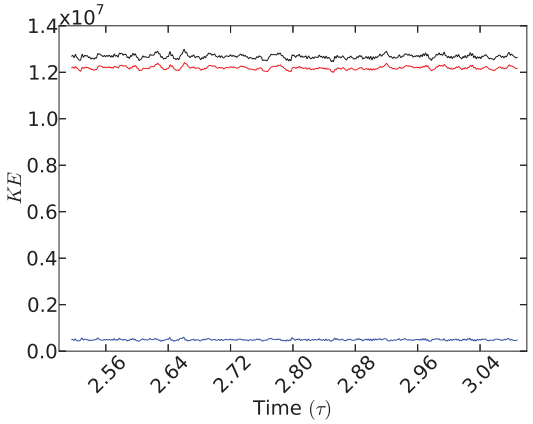

(c) $Ra^* = 3.8Ra_c^* = 0.0500$

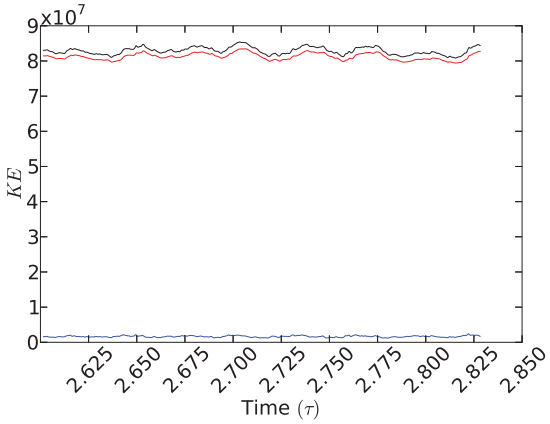

(d) $Ra^* = 7.6Ra_c^* = 0.1000$

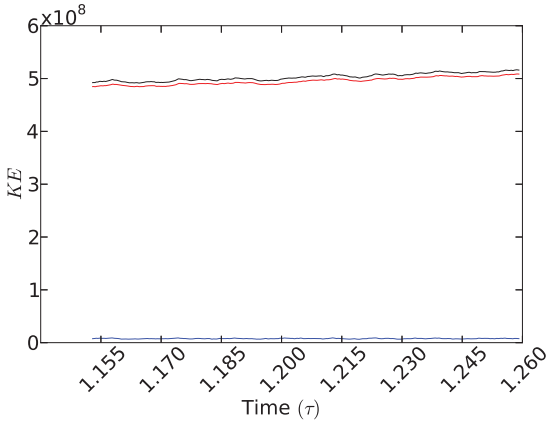

(e) $Ra^* = 22.7Ra_c^* = 0.3000$

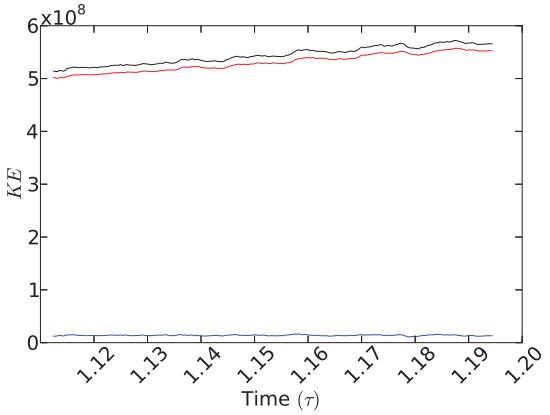

(f) $Ra^* = 37.9Ra_c^* = 0.5000$

Figure 4.24: Kinetic energy time series data for $N_\rho = 5$ at $\eta_{nb} = 0.80$. The black line represents the total kinetic energy $KE = KE_\zeta + KE_\gamma$, where KE_ζ is represented by the red line and KE_γ is represented by the blue line.

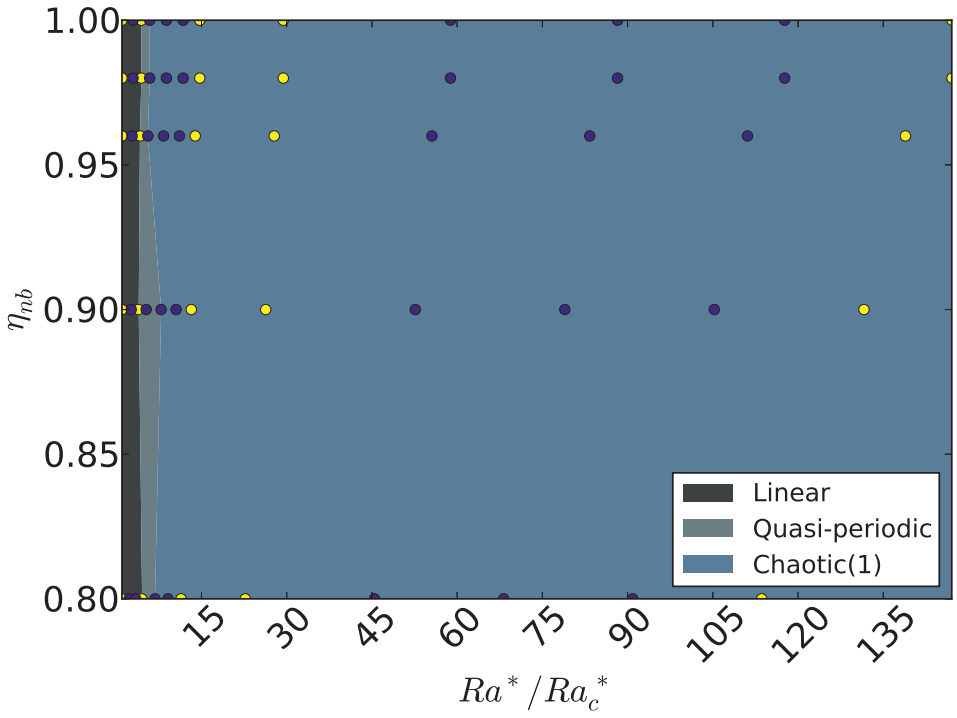

Figure 4.25: The convection regime diagram for $N_\rho = 10^{-2}$ and $E = 10^{-4}$ for various η_{nb} and Ra^*/Ra_c^*. The regimes indicated by the legend in this graph presents the convection regimes the models were exhibiting based on their respective η_{nb} and Ra^*/Ra_c^* values. The range for Ra^*/Ra_c^* goes up to $Ra^* = 0.5000$, where Ra_c^* is dependant on η_{nb}. The yellow dots represents the models presented in this chapter given by Figures 4.5 to 4.9. The purple dots represent the models that were not presented in this chapter.

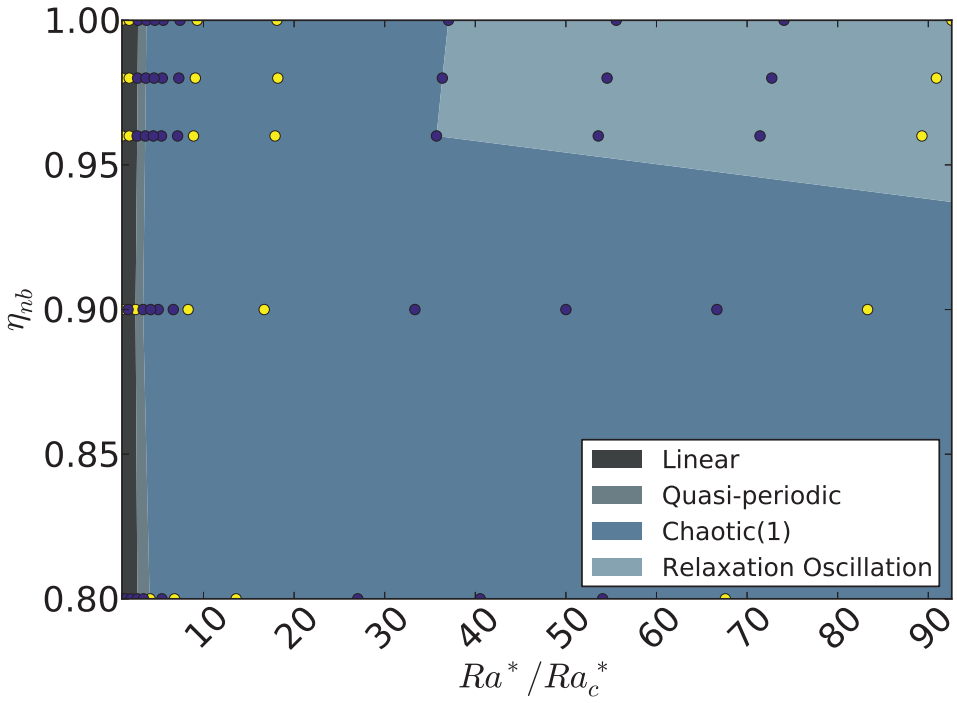

Figure 4.26: The convection regime diagram for $N_\rho = 1$ and $E = 10^{-4}$ for various η_{nb} and Ra^*/Ra_c^*. The regimes indicated by the legend in this graph presents the convection regimes the models were exhibiting based on their respective η_{nb} and Ra^*/Ra_c^* values. The range for Ra^*/Ra_c^* goes up to $Ra^* = 0.5000$, where Ra_c^* is dependant on η_{nb}. The yellow dots represents the models presented in this chapter given by Figures 4.10 to 4.14. The purple dots represent the models that were not presented in this chapter.

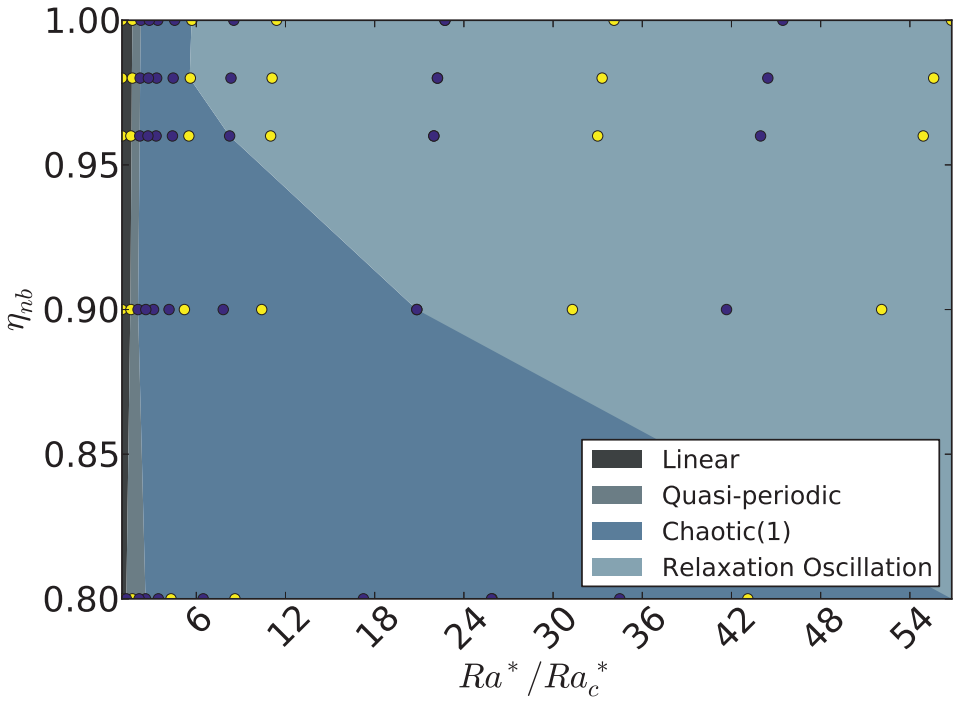

Figure 4.27: The convection regime diagram for $N_\rho = 3$ and $E = 10^{-4}$ for various η_{nb} and Ra^*/Ra_c^*. The regimes indicated by the legend in this graph presents the convection regimes the models were exhibiting based on their respective η_{nb} and Ra^*/Ra_c^* values. The range for Ra^*/Ra_c^* goes up to $Ra^* = 0.5000$, where Ra_c^* is dependant on η_{nb}. The yellow dots represents the models presented in this chapter given by Figures 4.15 to 4.19. The purple dots represent the models that were not presented in this chapter.

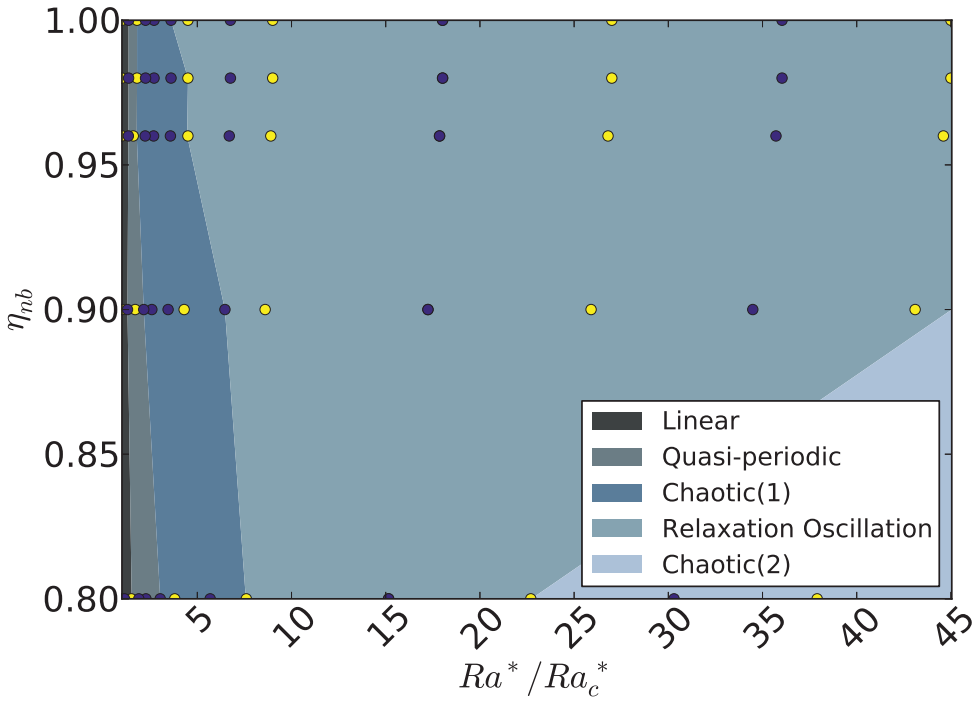

Figure 4.28: The convection regime diagram for $N_\rho = 5$ and $E = 10^{-4}$ for various η_{nb} and Ra^*/Ra_c^*. The regimes indicated by the legend in this graph presents the convection regimes the models were exhibiting based on their respective η_{nb} and Ra^*/Ra_c^* values. The range for Ra^*/Ra_c^* goes up to $Ra^* = 0.5000$, where Ra_c^* is dependant on η_{nb}. The yellow dots represents the models presented in this chapter given by Figures 4.20 to 4.24. The purple dots represent the models that were not presented in this chapter.

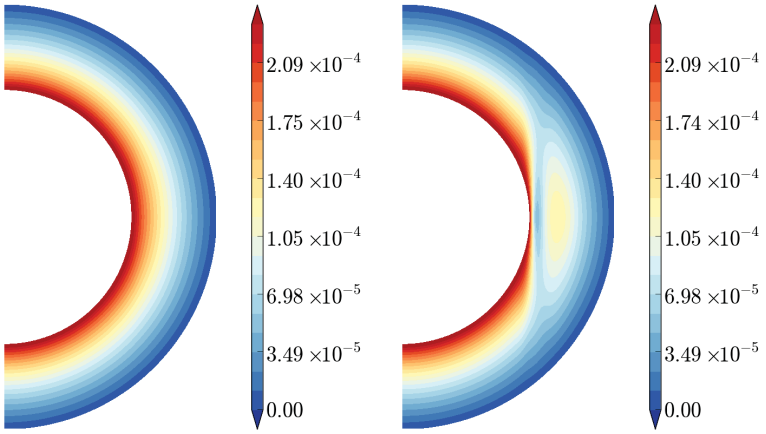

(a) $Ra^* = Ra_c^* = 0.0034$

(b) $Ra^* = 4.4Ra_c^* = 0.0150$

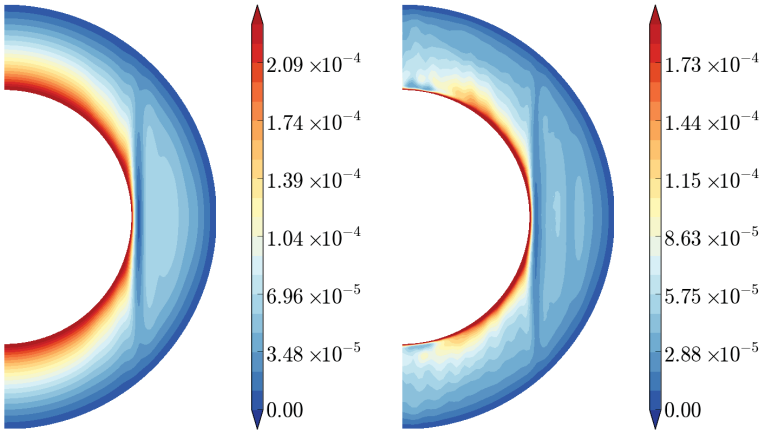

(c) $Ra^* = 14.7Ra_c^* = 0.0500$

(d) $Ra^* = 29.4Ra_c^* = 0.1000$

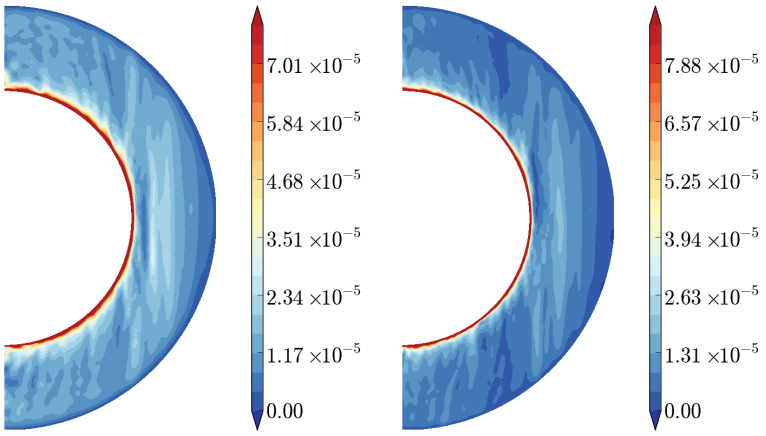

(e) $Ra^* = 147.1Ra_c^* = 0.5000$

(f) $Ra^* = 294.1Ra_c^* = 1.0000$

Figure 4.29: The azimuthally averaged radial entropy gradient profile of the rotating spherical shell with $N_\rho = 10^{-2}$ at $\eta_{nb} = 1.00$. Note the $\partial s/\partial r \geq 0$ implies that the fluid is convectively unstable while $\partial s/\partial r < 0$ implies the fluid is in a stably stratified state.

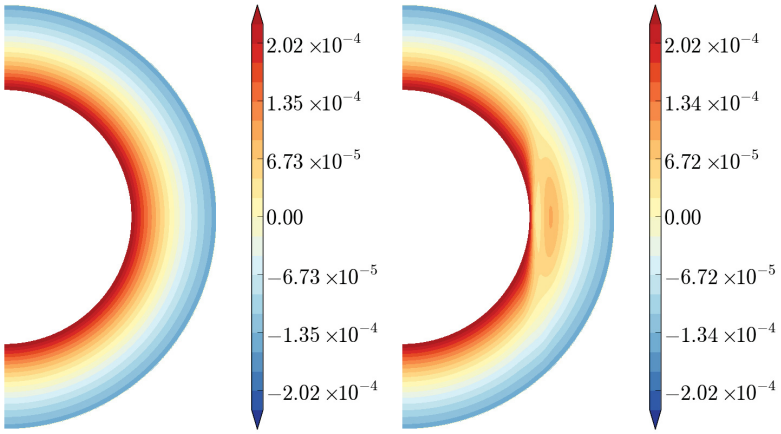

(a) $Ra^* = Ra_c^* = 0.0044$

(b) $Ra^* = 4.5Ra_c^* = 0.0200$

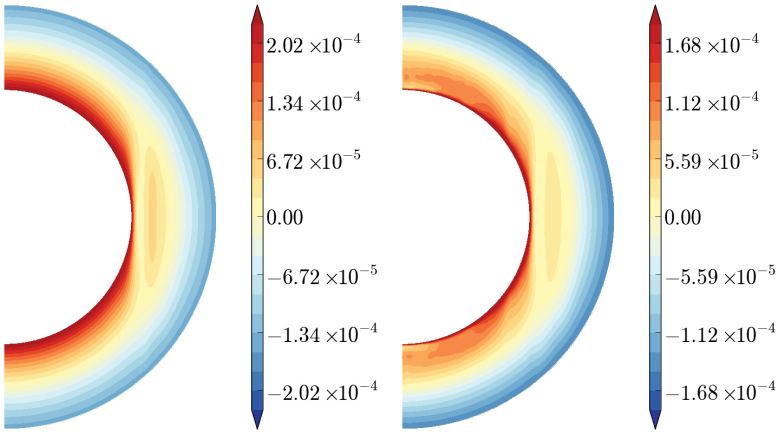

(c) $Ra^* = 11.4Ra_c^* = 0.0500$

(d) $Ra^* = 22.7Ra_c^* = 0.1000$

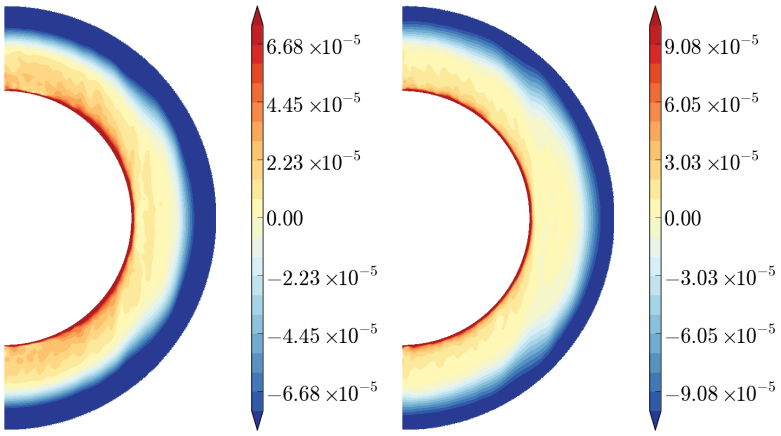

(e) $Ra^* = 113.6Ra_c^* = 0.5000$

(f) $Ra^* = 227.3Ra_c^* = 1.0000$

Figure 4.30: The azimuthally averaged radial entropy gradient profile of the rotating spherical shell with $N_\rho = 10^{-2}$ at $\eta_{nb} = 0.80$. Note the $\partial s/\partial r \geq 0$ implies that the fluid is convectively unstable while $\partial s/\partial r < 0$ implies the fluid is in a stably stratified state.

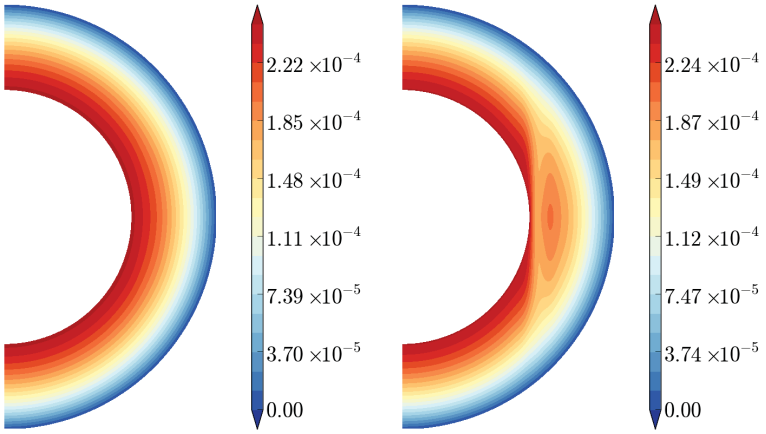

(a) $Ra^* = Ra_c^* = 0.0054$ (b) $Ra^* = 1.8Ra_c^* = 0.0100$

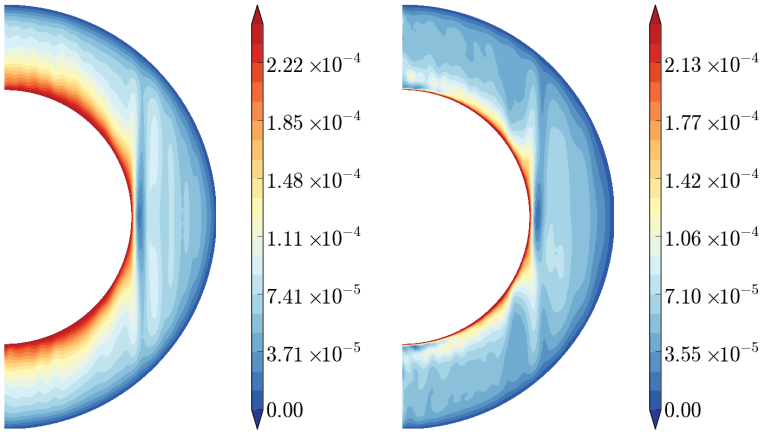

(c) $Ra^* = 9.3Ra_c^* = 0.0500$ (d) $Ra^* = 18.1Ra_c^* = 0.1000$

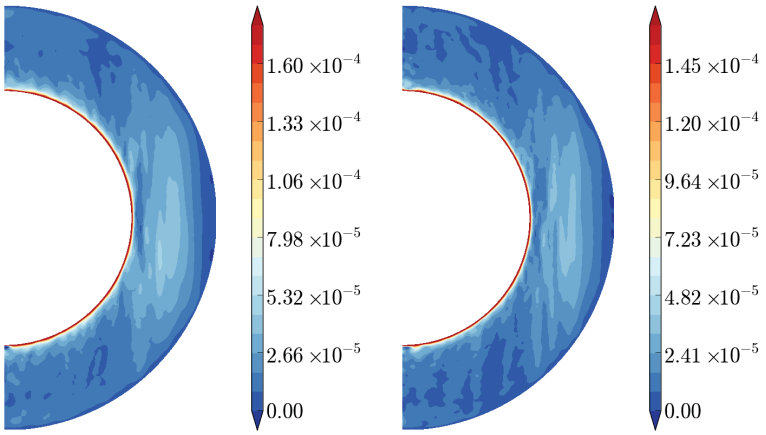

(e) $Ra^* = 92.6Ra_c^* = 0.5000$ (f) $Ra^* = 138.9Ra_c^* = 0.7500$

Figure 4.31: The azimuthally averaged radial entropy gradient profile of the rotating spherical shell with $N_\rho = 1$ at $\eta_{nb} = 1.00$. Note the $\partial s/\partial r \geq 0$ implies that the fluid is convectively unstable while $\partial s/\partial r < 0$ implies the fluid is in a stably stratified state.

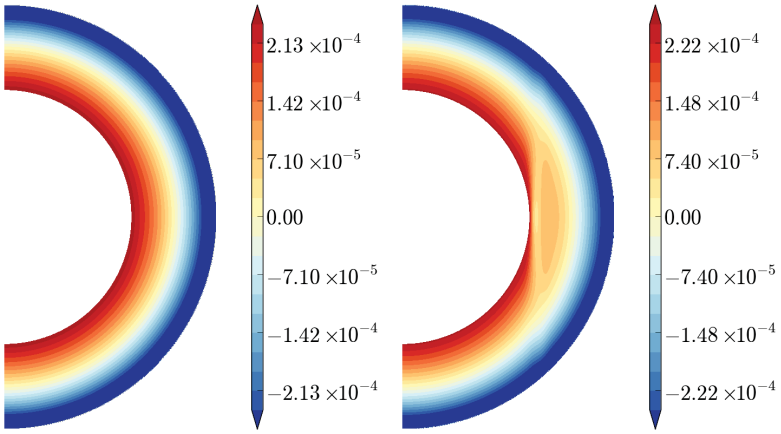

(a) $Ra^* = Ra_c^* = 0.0074$ (b) $Ra^* = 4.1Ra_c^* = 0.0300$

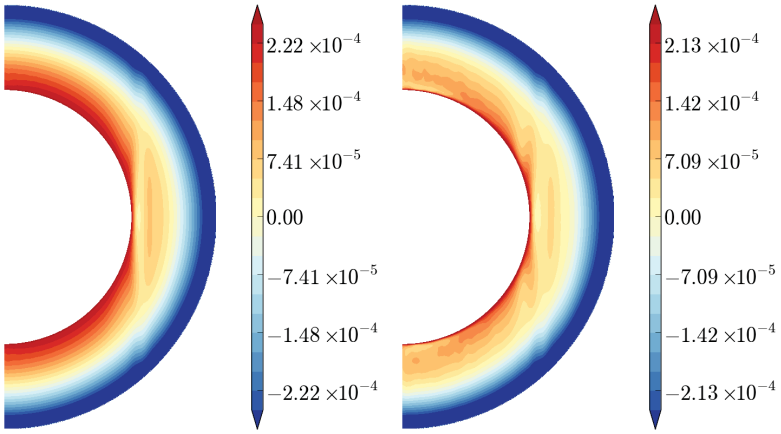

(c) $Ra^* = 6.8Ra_c^* = 0.0500$ (d) $Ra^* = 13.6Ra_c^* = 0.1000$

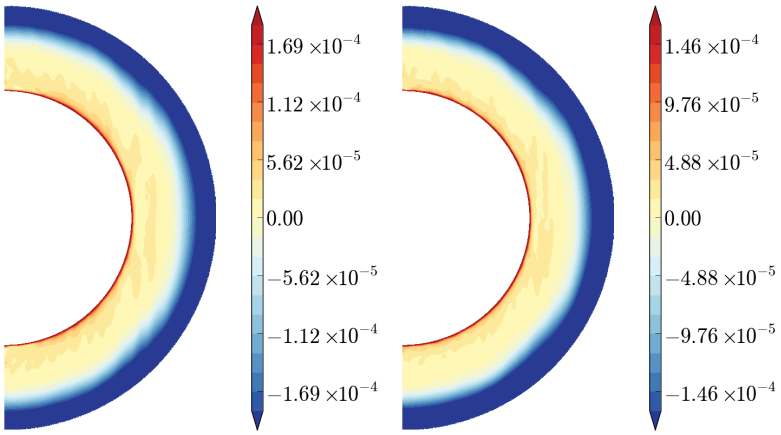

(e) $Ra^* = 67.6Ra_c^* = 0.5000$ (f) $Ra^* = 101.4Ra_c^* = 0.7500$

Figure 4.32: The azimuthally averaged radial entropy gradient profile of the rotating spherical shell with $N_\rho = 1$ at $\eta_{nb} = 0.80$. Note the $\partial s/\partial r \geq 0$ implies that the fluid is convectively unstable while $\partial s/\partial r < 0$ implies the fluid is in a stably stratified state.

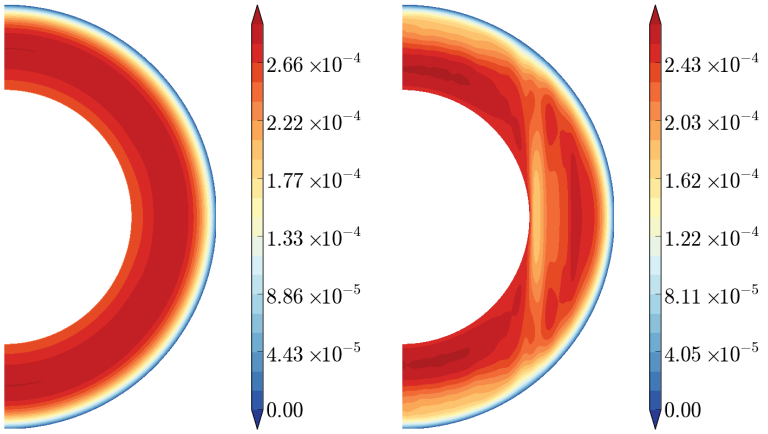

(a) $Ra^* = Ra_c^* = 0.0088$

(b) $Ra^* = 2.8Ra_c^* = 0.0200$

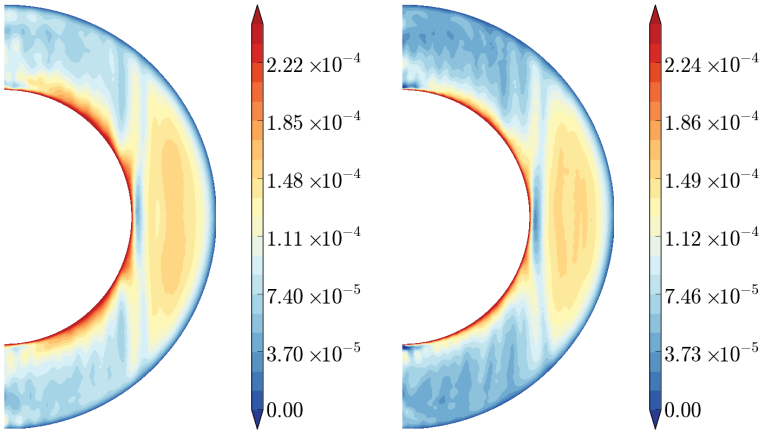

(c) $Ra^* = 8.5Ra_c^* = 0.0750$

(d) $Ra^* = 11.4Ra_c^* = 0.1000$

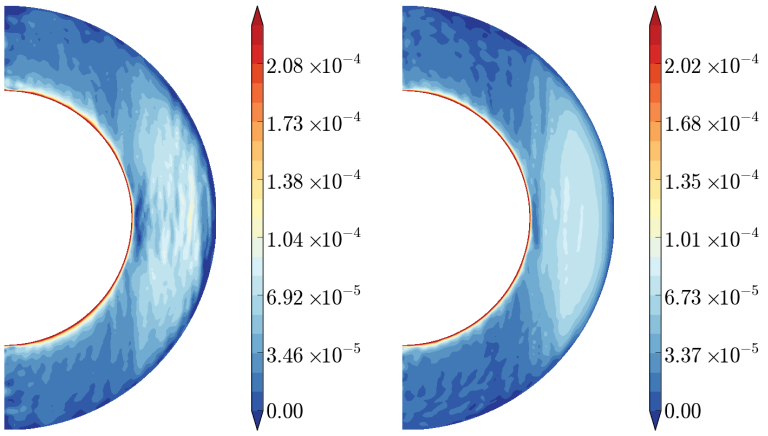

(e) $Ra^* = 34.1Ra_c^* = 0.3000$

(f) $Ra^* = 56.8Ra_c^* = 0.5000$

Figure 4.33: The azimuthally averaged radial entropy gradient profile of the rotating spherical shell with $N_\rho = 3$ at $\eta_{nb} = 1.00$. Note the $\partial s/\partial r \geq 0$ implies that the fluid is convectively unstable while $\partial s/\partial r < 0$ implies the fluid is in a stably stratified state.

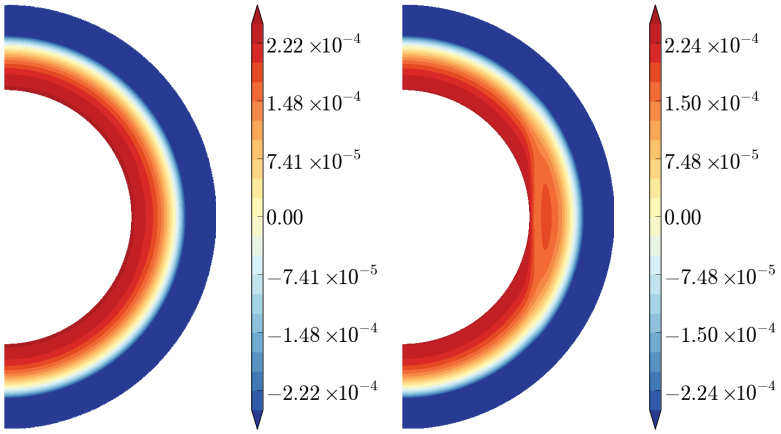

(a) $Ra^* = Ra_c^* = 0.0116$ (b) $Ra^* = 1.7Ra_c^* = 0.0200$

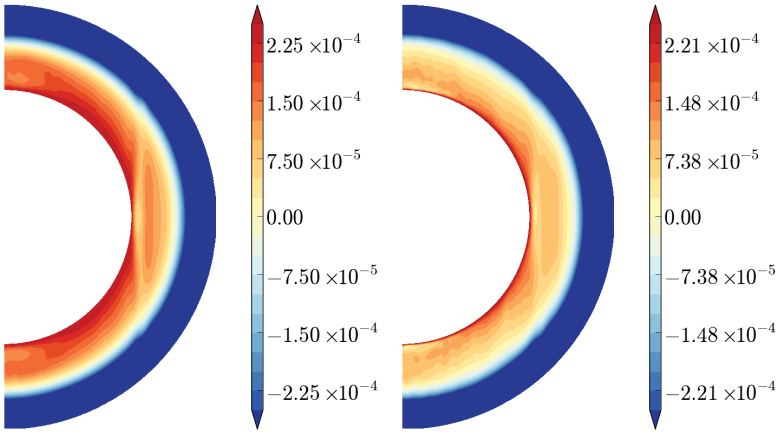

(c) $Ra^* = 4.3Ra_c^* = 0.0500$ (d) $Ra^* = 8.6Ra_c^* = 0.1000$

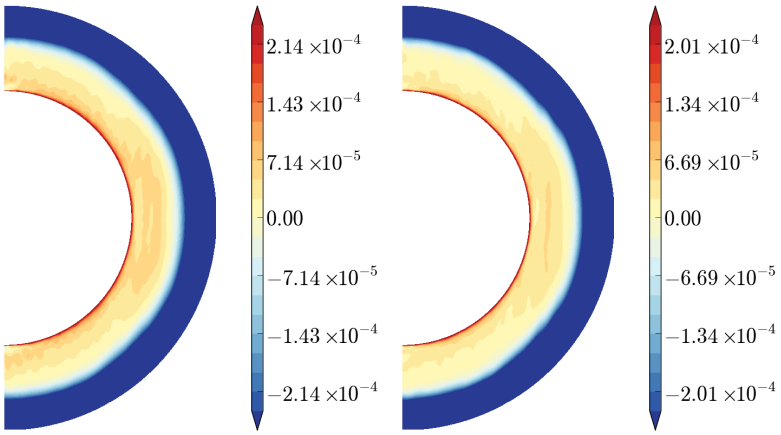

(e) $Ra^* = 25.9Ra_c^* = 0.3000$ (f) $Ra^* = 43.1Ra_c^* = 0.5000$

Figure 4.34: The azimuthally averaged θ entropy gradient profile of the rotating spherical shell with $N_\rho = 3$ at $\eta_{nb} = 0.80$. Note the $\partial s/\partial r \geq 0$ implies that the fluid is convectively unstable while $\partial s/\partial r < 0$ implies the fluid is in a stably stratified state.

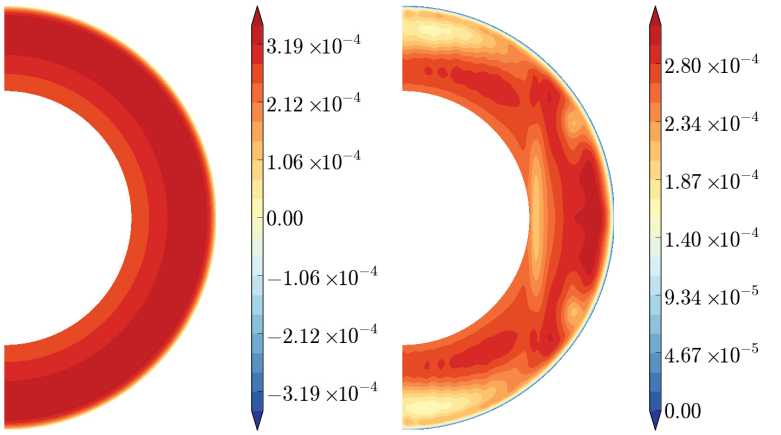

(a) $Ra^* = Ra_c^* = 0.0111$ (b) $Ra^* = 1.8Ra_c^* = 0.0200$

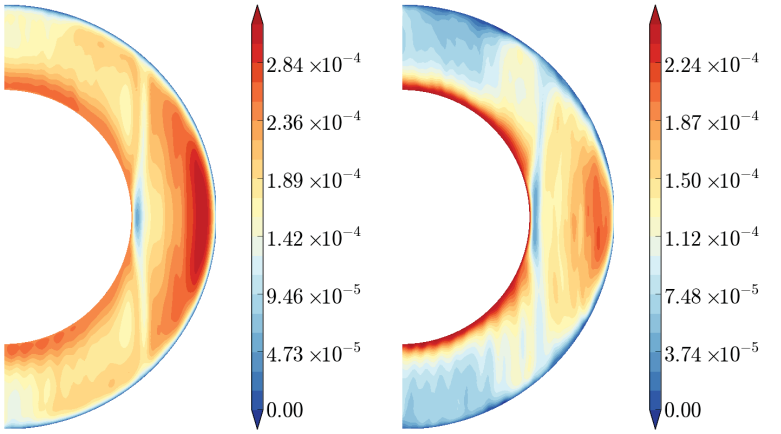

(c) $Ra^* = 4.5Ra_c^* = 0.0500$ (d) $Ra^* = 9.0Ra_c^* = 0.1000$

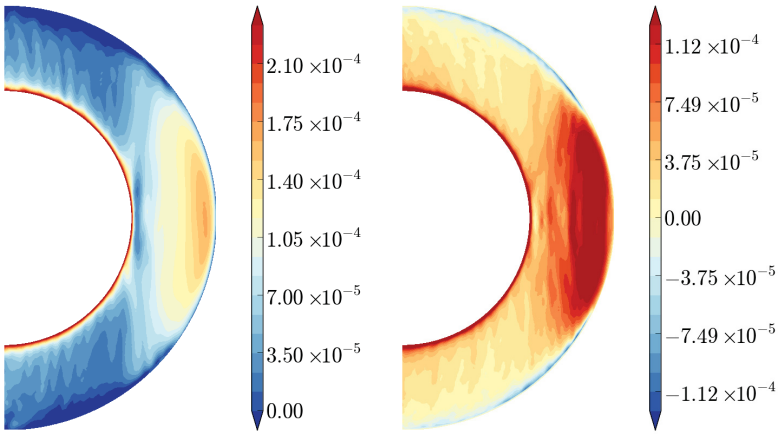

(e) $Ra^* = 27.0Ra_c^* = 0.3000$ (f) $Ra^* = 45.0Ra_c^* = 0.5000$

Figure 4.35: The azimuthally averaged θ entropy gradient profile of the rotating spherical shell with $N_\rho = 5$ at $\eta_{nb} = 1.00$. Note the $\partial s/\partial r \geq 0$ implies that the fluid is convectively unstable while $\partial s/\partial r < 0$ implies the fluid is in a stably stratified state.

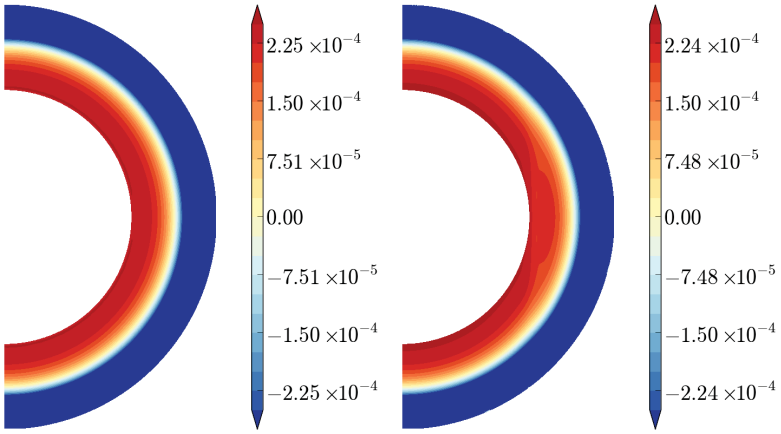

(a) $Ra^* = Ra_c^* = 0.0132$ (b) $Ra^* = 1.5Ra_c^* = 0.0200$

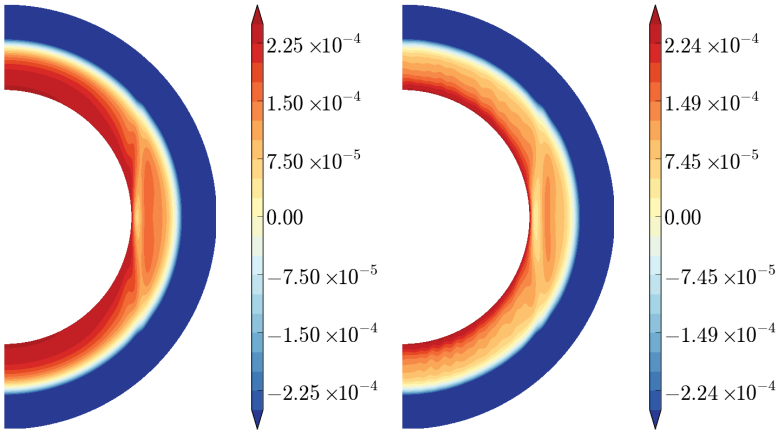

(c) $Ra^* = 3.8Ra_c^* = 0.0500$ (d) $Ra^* = 7.6Ra_c^* = 0.1000$

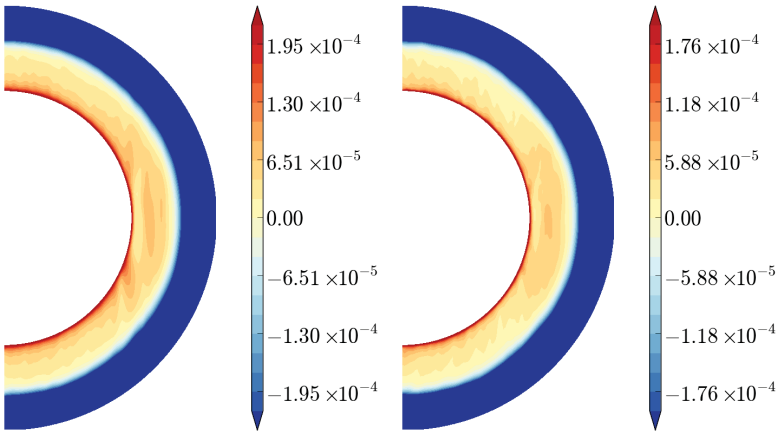

(e) $Ra^* = 22.7Ra_c^* = 0.3000$ (f) $Ra^* = 37.9Ra_c^* = 0.5000$

Figure 4.36: The azimuthally averaged θ entropy gradient profile of the rotating spherical shell with $N_\rho = 5$ at $\eta_{nb} = 0.80$. Note the $\partial s/\partial r \geq 0$ implies that the fluid is convectively unstable while $\partial s/\partial r < 0$ implies the fluid is in a stably stratified state.

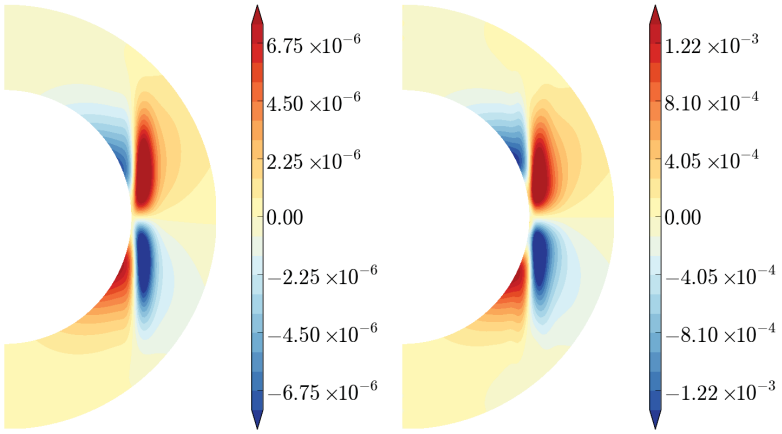

(a) $Ra^* = Ra_c^* = 0.0034$ (b) $Ra^* = 4.4Ra_c^* = 0.0150$

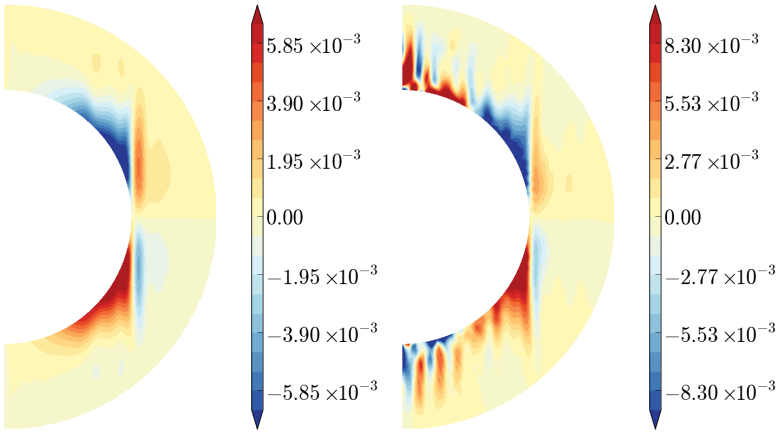

(c) $Ra^* = 14.7Ra_c^* = 0.0500$ (d) $Ra^* = 29.4Ra_c^* = 0.1000$

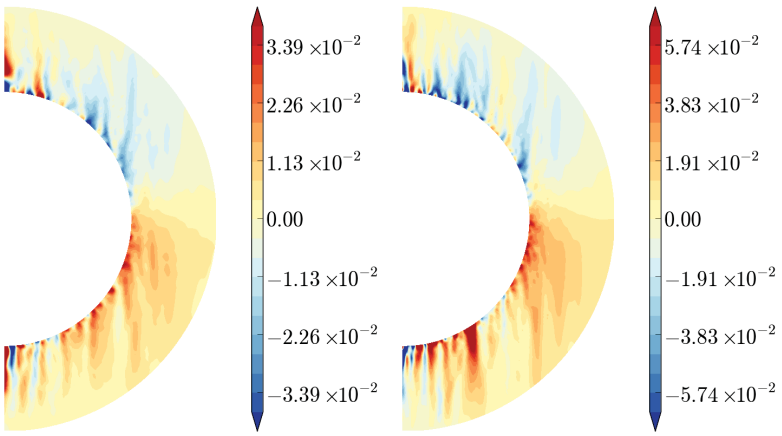

(e) $Ra^* = 147.1Ra_c^* = 0.5000$ (f) $Ra^* = 294.1Ra_c^* = 1.0000$

Figure 4.37: The azimuthally averaged $\partial u_\phi/\partial z$ profile of the rotating spherical shell with $N_\rho = 10^{-2}$ at $\eta_{nb} = 1.00$.

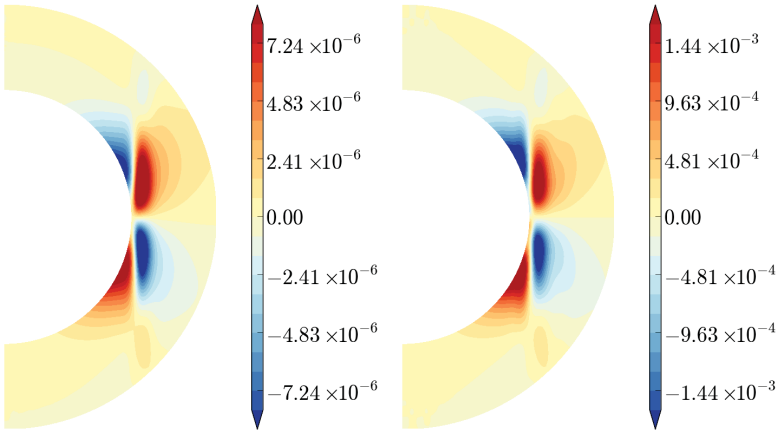

(a) $Ra^* = Ra_c^* = 0.0044$ (b) $Ra^* = 4.5Ra_c^* = 0.0200$

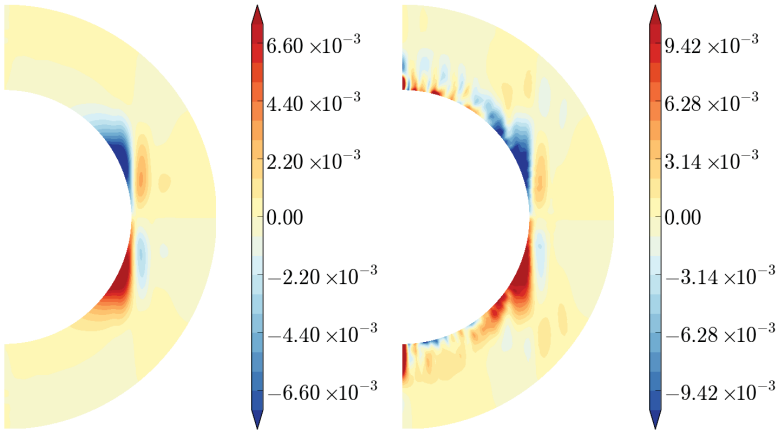

(c) $Ra^* = 11.4Ra_c^* = 0.0500$ (d) $Ra^* = 22.7Ra_c^* = 0.1000$

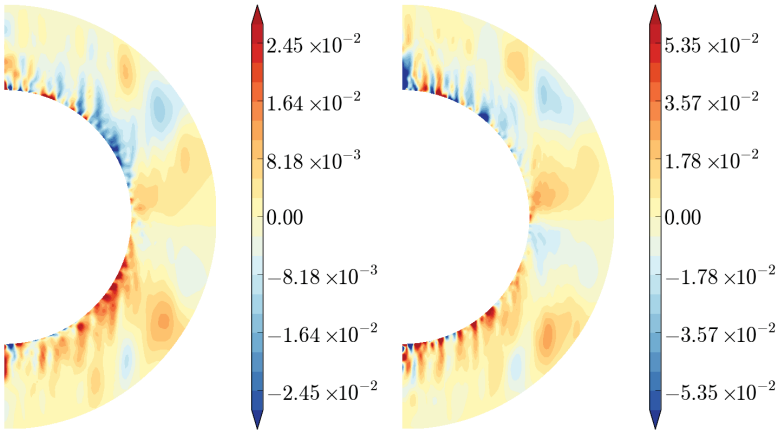

(e) $Ra^* = 113.6Ra_c^* = 0.5000$ (f) $Ra^* = 227.3Ra_c^* = 1.0000$

Figure 4.38: The azimuthally averaged $\partial u_\phi/\partial z$ profile of the rotating spherical shell with $N_\rho = 10^{-2}$ at $\eta_{nb} = 0.80$.

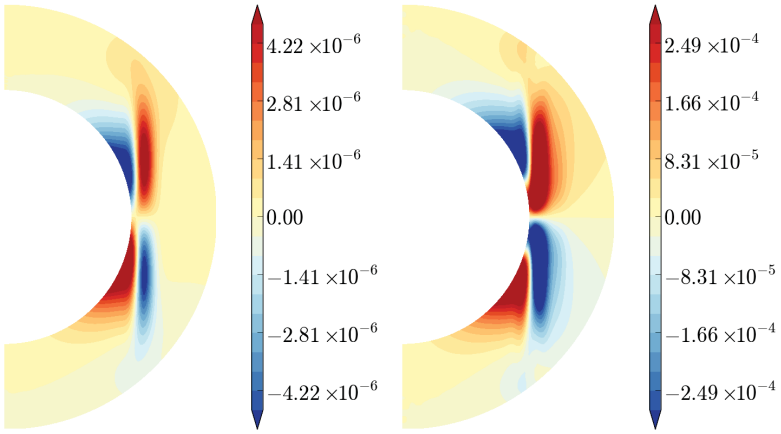

(a) $Ra^* = Ra_c^* = 0.0054$ (b) $Ra^* = 1.8Ra_c^* = 0.0100$

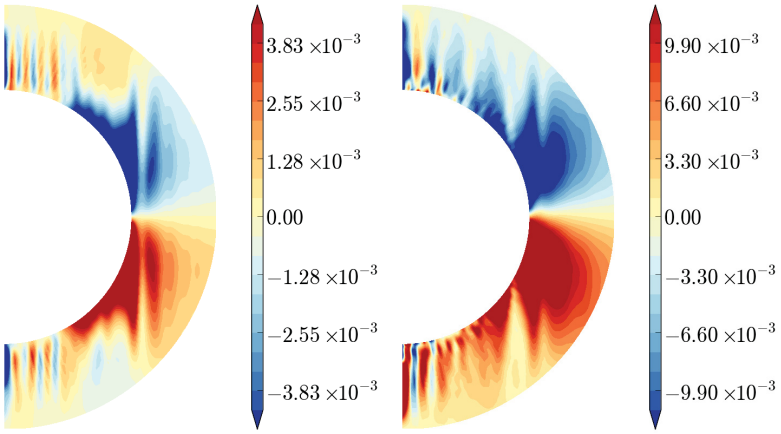

(c) $Ra^* = 9.3Ra_c^* = 0.0500$ (d) $Ra^* = 18.1Ra_c^* = 0.1000$

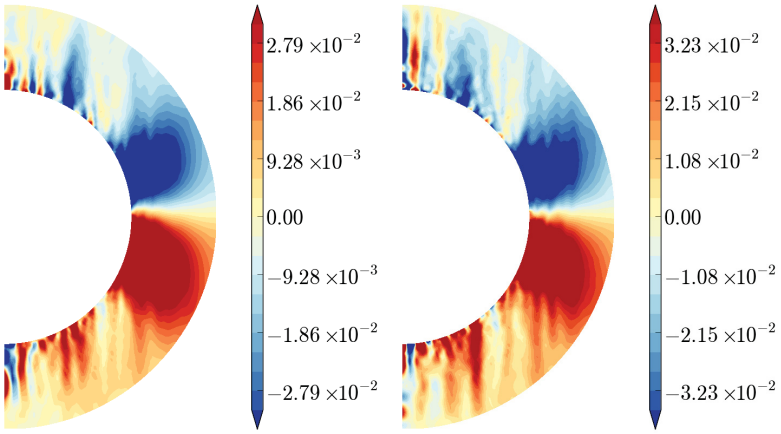

(e) $Ra^* = 92.6Ra_c^* = 0.5000$ (f) $Ra^* = 138.9Ra_c^* = 0.7500$

Figure 4.39: The azimuthally averaged $\partial u_\phi/\partial z$ profile of the rotating spherical shell with $N_\rho = 1$ at $\eta_{nb} = 1.00$.

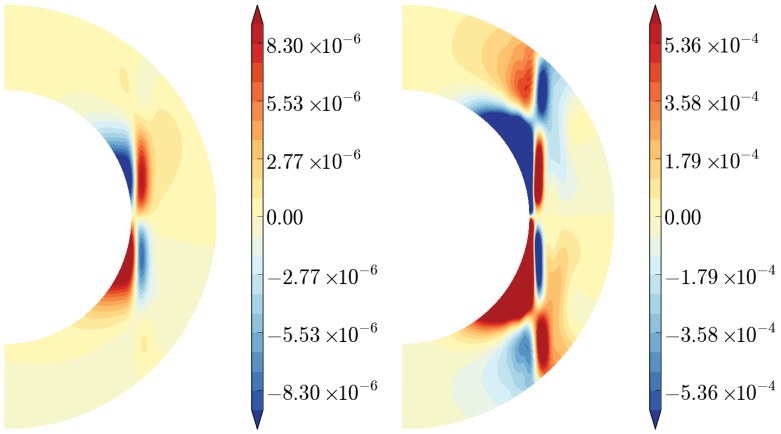

(a) $Ra^* = Ra_c^* = 0.0074$ (b) $Ra^* = 4.1Ra_c^* = 0.0300$

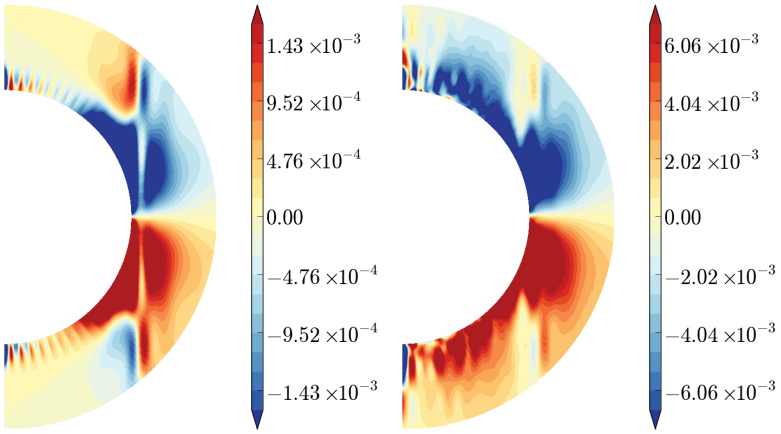

(c) $Ra^* = 6.8Ra_c^* = 0.0500$ (d) $Ra^* = 13.6Ra_c^* = 0.1000$

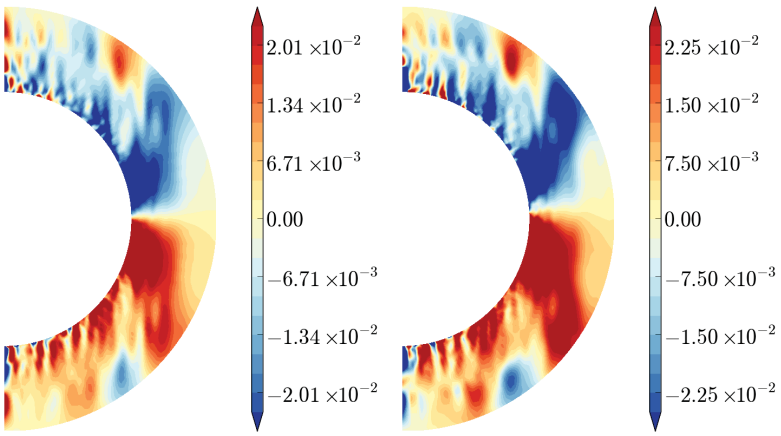

(e) $Ra^* = 67.6Ra_c^* = 0.5000$ (f) $Ra^* = 101.4Ra_c^* = 0.7500$

Figure 4.40: The azimuthally averaged $\partial u_\phi/\partial z$ profile of the rotating spherical shell with $N_\rho = 1$ at $\eta_{nb} = 0.80$.

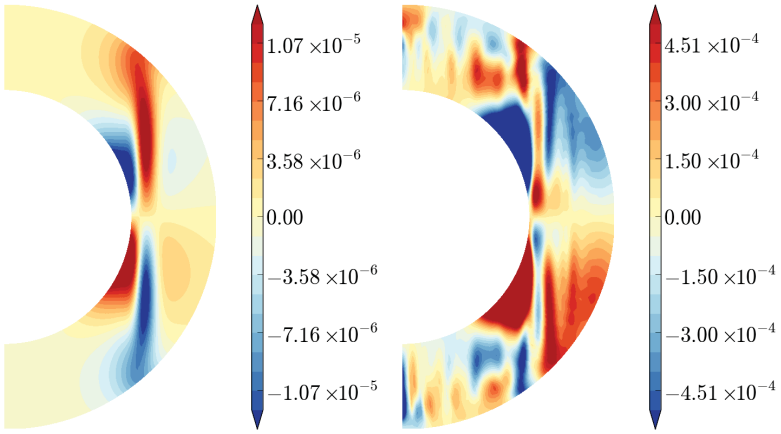

(a) $Ra^* = Ra_c^* = 0.0088$ (b) $Ra^* = 2.8Ra_c^* = 0.0200$

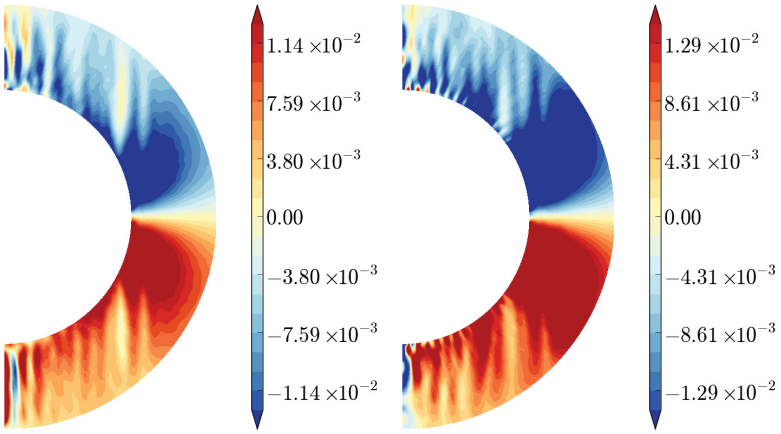

(c) $Ra^* = 8.5Ra_c^* = 0.0750$ (d) $Ra^* = 11.4Ra_c^* = 0.1000$

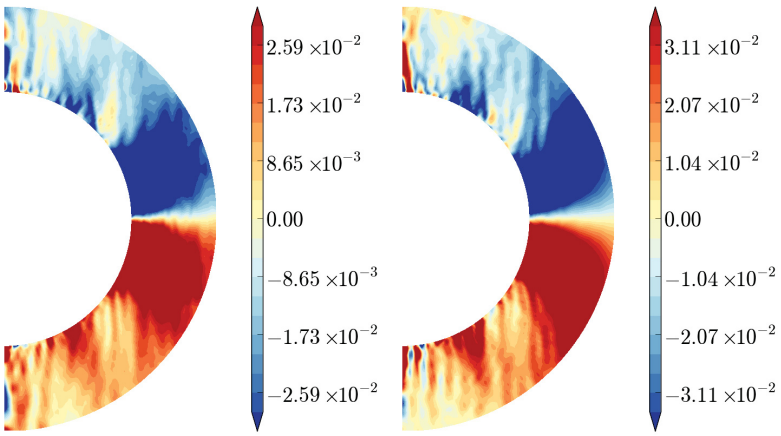

(e) $Ra^* = 34.1Ra_c^* = 0.3000$ (f) $Ra^* = 56.8Ra_c^* = 0.5000$

Figure 4.41: The azimuthally averaged $\partial u_\phi/\partial z$ profile of the rotating spherical shell with $N_\rho = 3$ at $\eta_{nb} = 1.00$.

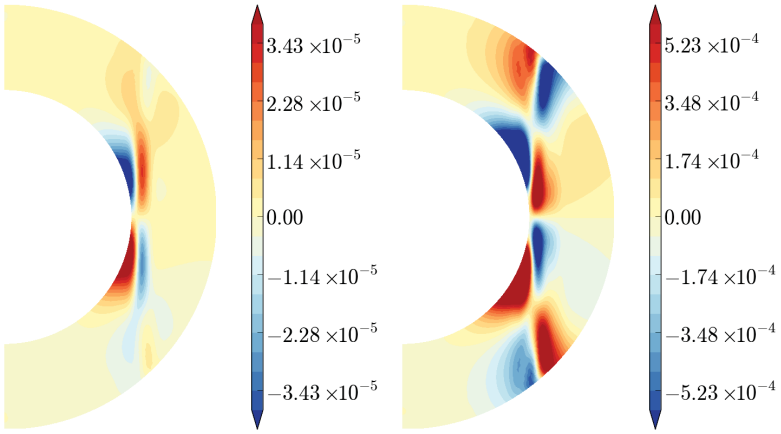

(a) $Ra^* = Ra_c^* = 0.0116$ (b) $Ra^* = 1.7Ra_c^* = 0.0200$

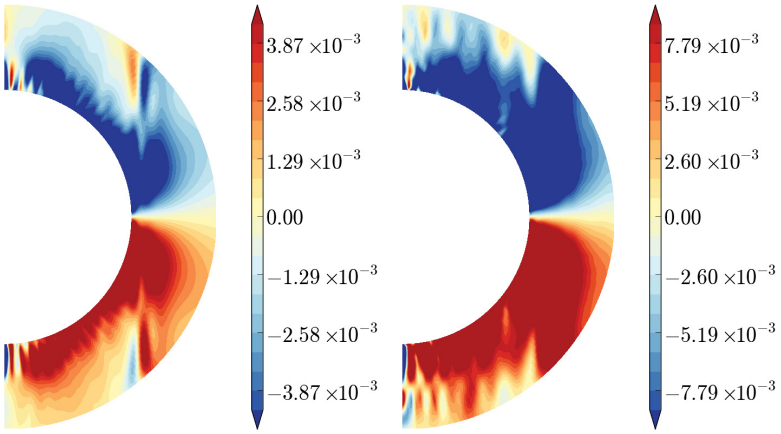

(c) $Ra^* = 4.3Ra_c^* = 0.0500$ (d) $Ra^* = 8.6Ra_c^* = 0.1000$

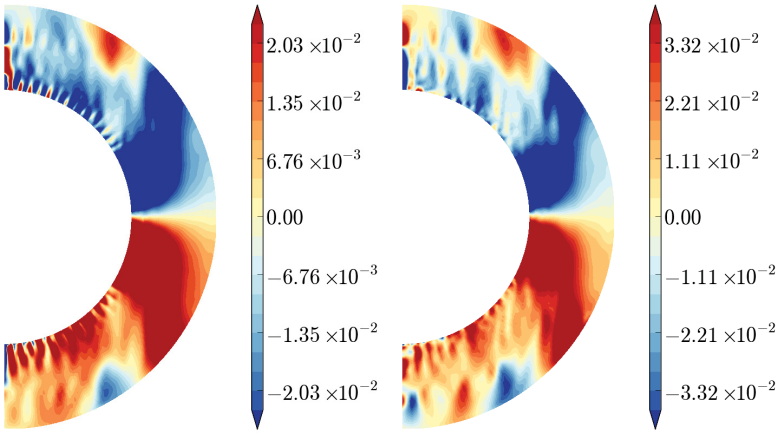

(e) $Ra^* = 25.9Ra_c^* = 0.3000$ (f) $Ra^* = 43.1Ra_c^* = 0.5000$

Figure 4.42: The azimuthally averaged $\partial u_\phi/\partial z$ profile of the rotating spherical shell with $N_\rho = 3$ at $\eta_{nb} = 0.80$.

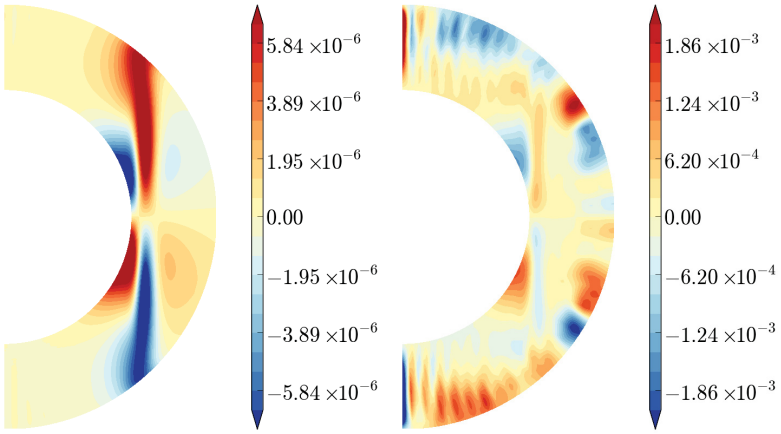

(a) $Ra^* = Ra_c^* = 0.0111$ (b) $Ra^* = 1.8Ra_c^* = 0.0200$

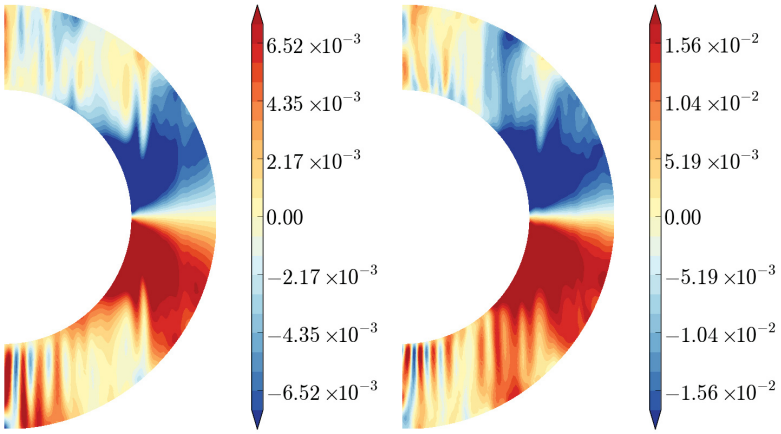

(c) $Ra^* = 4.5Ra_c^* = 0.0500$ (d) $Ra^* = 9.0Ra_c^* = 0.1000$

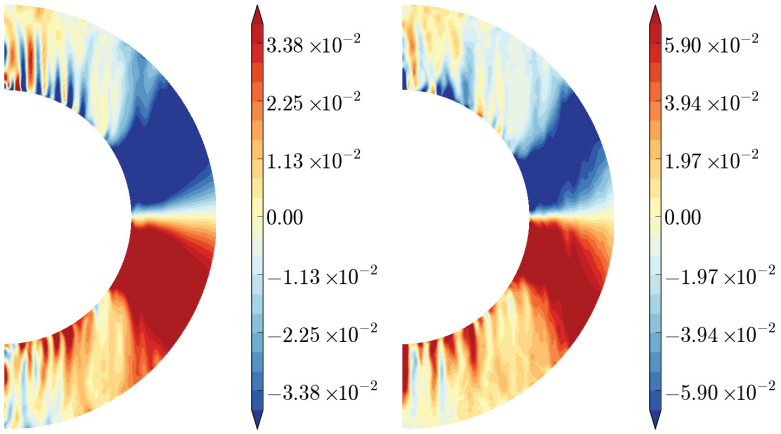

(e) $Ra^* = 27.0Ra_c^* = 0.3000$ (f) $Ra^* = 45.0Ra_c^* = 0.5000$

Figure 4.43: The azimuthally averaged $\partial u_\phi/\partial z$ profile of the rotating spherical shell with $N_\rho = 5$ at $\eta_{nb} = 1.00$.

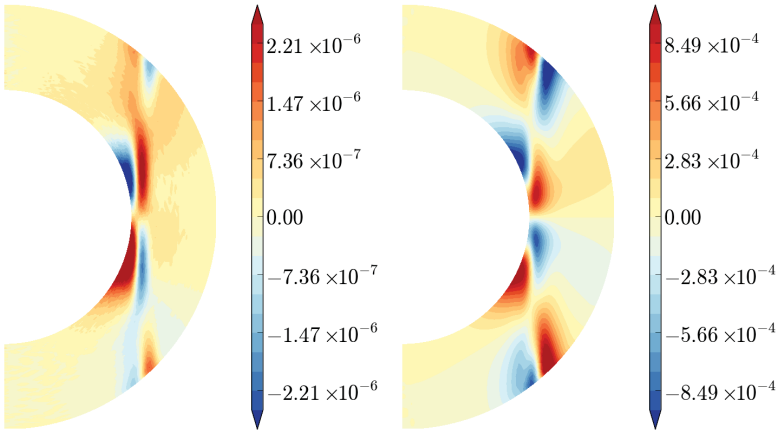

(a) $Ra^* = Ra_c^* = 0.0132$ (b) $Ra^* = 1.5Ra_c^* = 0.0200$

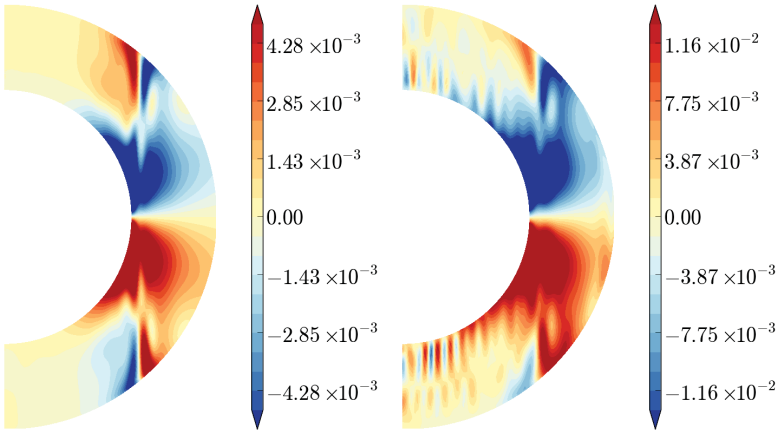

(c) $Ra^* = 3.8Ra_c^* = 0.0500$ (d) $Ra^* = 7.6Ra_c^* = 0.1000$

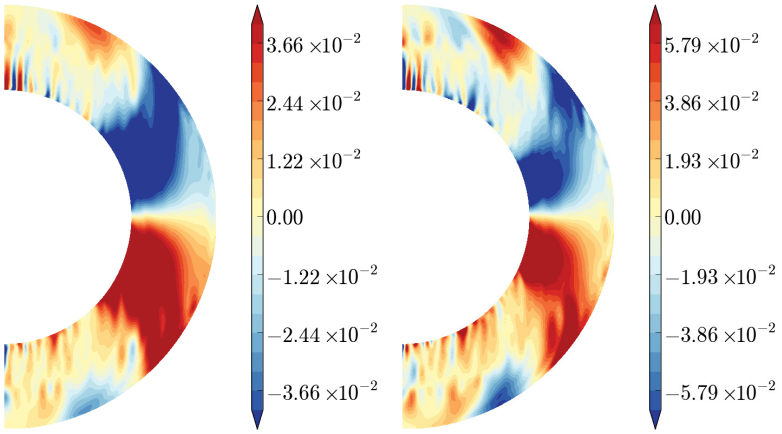

(e) $Ra^* = 22.7Ra_c^* = 0.3000$ (f) $Ra^* = 37.9Ra_c^* = 0.5000$

Figure 4.44: The azimuthally averaged $\partial u_\phi/\partial z$ profile of the rotating spherical shell with $N_\rho = 5$ at $\eta_{nb} = 0.80$.

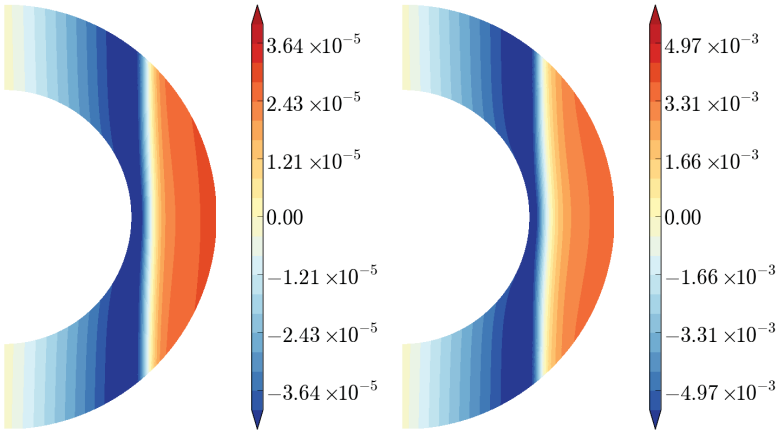

(a) $Ra^* = Ra_c^* = 0.0034$ (b) $Ra^* = 4.4Ra_c^* = 0.0150$

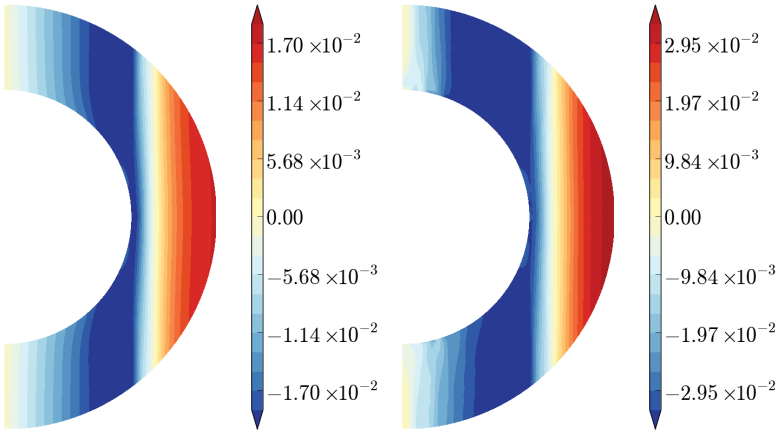

(c) $Ra^* = 14.7Ra_c^* = 0.0500$ (d) $Ra^* = 29.4Ra_c^* = 0.1000$

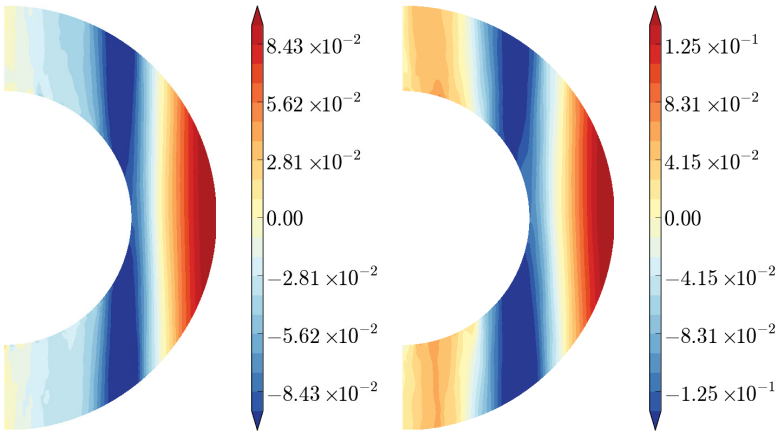

(e) $Ra^* = 147.1Ra_c^* = 0.5000$ (f) $Ra^* = 294.1Ra_c^* = 1.0000$

Figure 4.45: The azimuthally averaged zonal velocity profile of the rotating spherical shell with $N_\rho = 10^{-2}$ at $\eta_{nb} = 1.00$. Note that zonal velocity greater than zero implies a prograde directional flow while the opposite implies the retrograde direction.

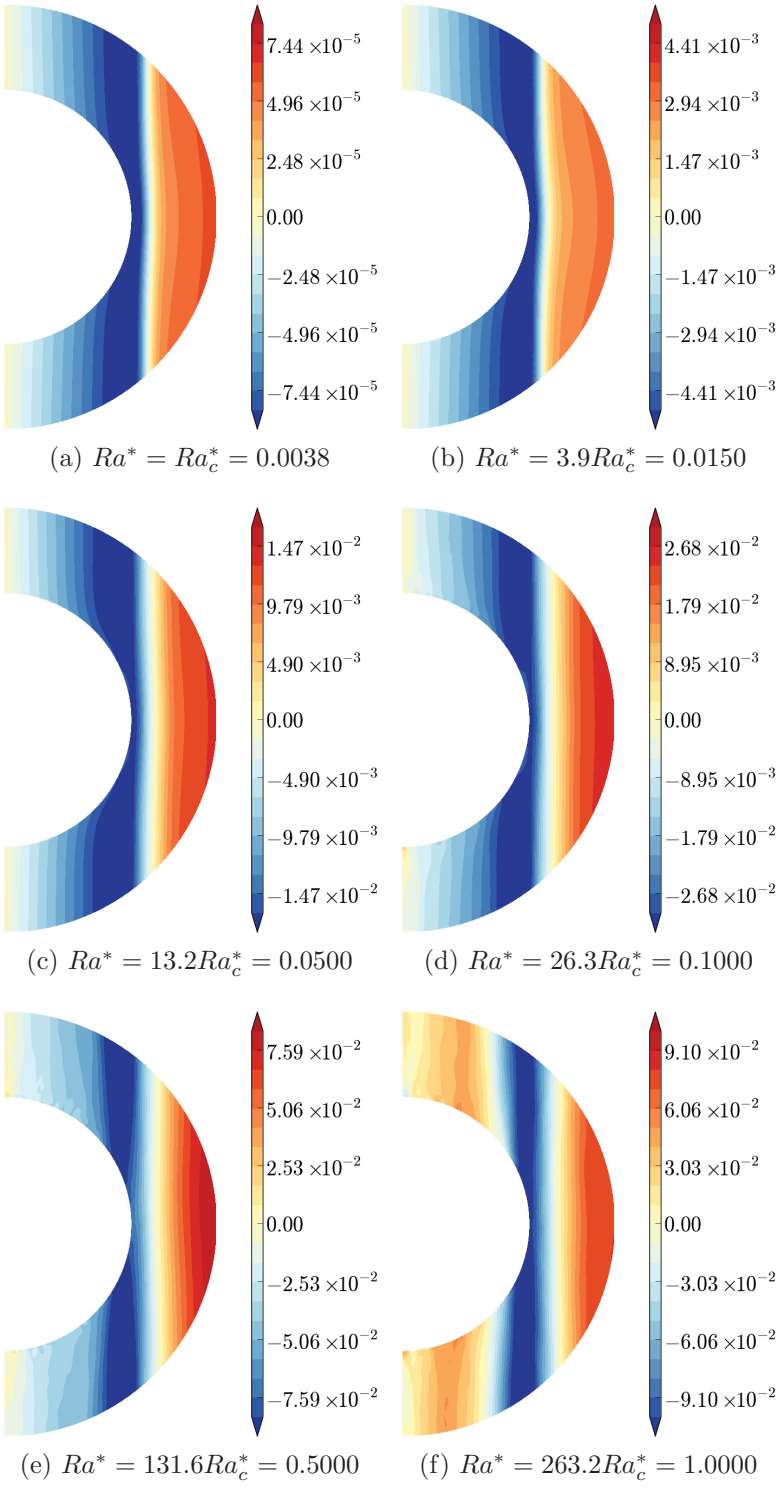

(a) $Ra^* = Ra_c^* = 0.0038$ (b) $Ra^* = 3.9Ra_c^* = 0.0150$

(c) $Ra^* = 13.2Ra_c^* = 0.0500$ (d) $Ra^* = 26.3Ra_c^* = 0.1000$

(e) $Ra^* = 131.6Ra_c^* = 0.5000$ (f) $Ra^* = 263.2Ra_c^* = 1.0000$

Figure 4.46: The azimuthally averaged zonal velocity profile of the rotating spherical shell with $N_\rho = 10^{-2}$ at $\eta_{nb} = 0.90$. Note that zonal velocity greater than zero implies a prograde directional flow while the opposite implies the retrograde direction.

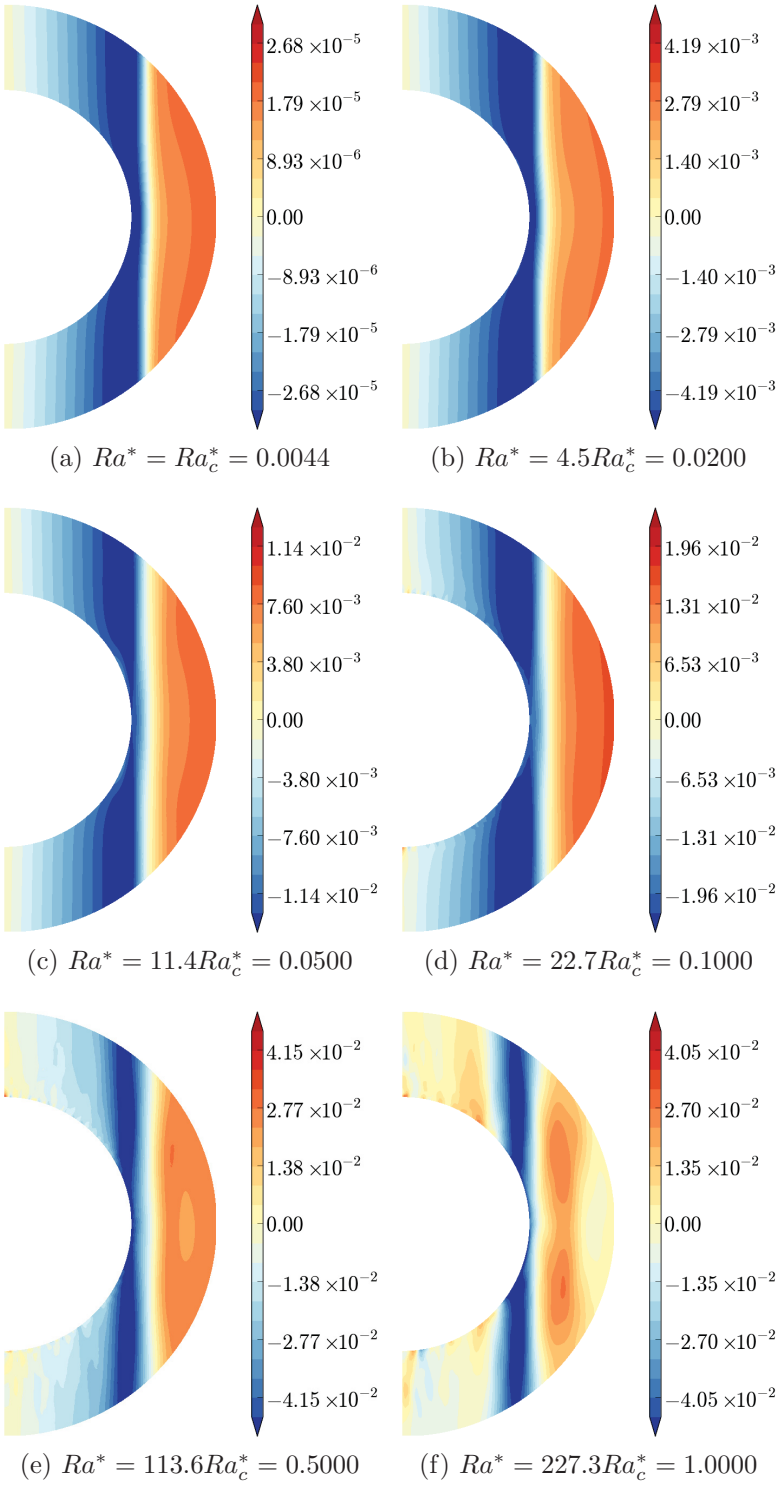

(a) $Ra^* = Ra_c^* = 0.0044$ (b) $Ra^* = 4.5Ra_c^* = 0.0200$

(c) $Ra^* = 11.4Ra_c^* = 0.0500$ (d) $Ra^* = 22.7Ra_c^* = 0.1000$

(e) $Ra^* = 113.6Ra_c^* = 0.5000$ (f) $Ra^* = 227.3Ra_c^* = 1.0000$

Figure 4.47: The azimuthally averaged zonal velocity profile of the rotating spherical shell with $N_\rho = 10^{-2}$ at $\eta_{nb} = 0.80$. Note that zonal velocity greater than zero implies a prograde directional flow while the opposite implies the retrograde direction.

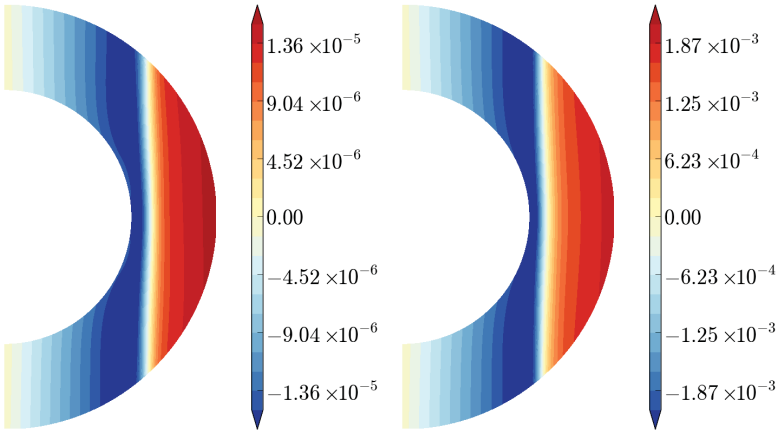

(a) $Ra^* = Ra_c^* = 0.0054$ (b) $Ra^* = 1.8Ra_c^* = 0.0100$

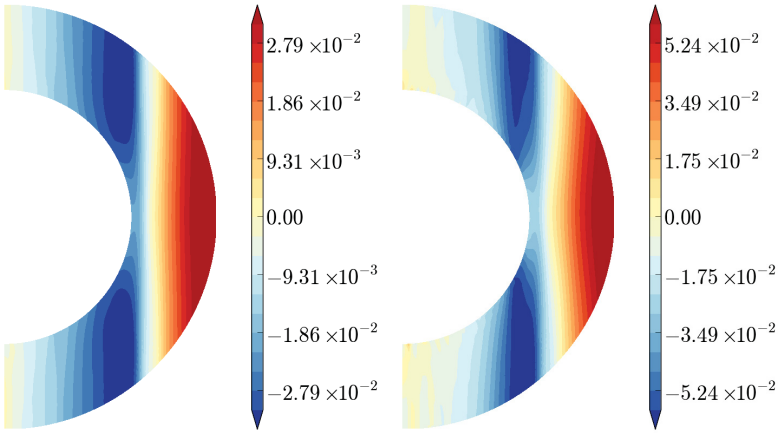

(c) $Ra^* = 9.3Ra_c^* = 0.0500$ (d) $Ra^* = 18.1Ra_c^* = 0.1000$

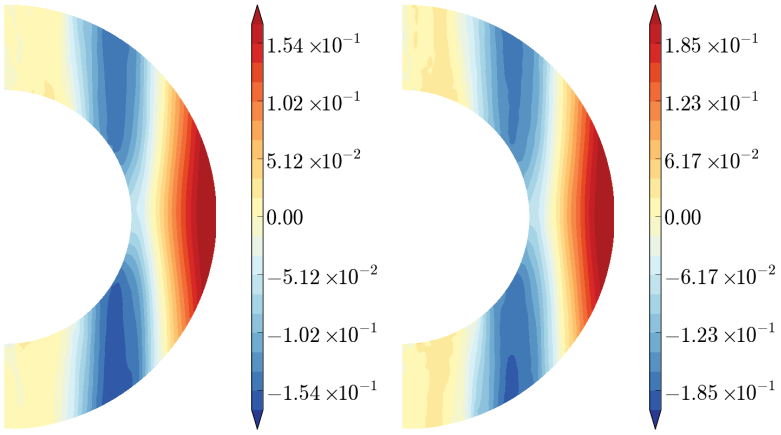

(e) $Ra^* = 92.6Ra_c^* = 0.5000$ (f) $Ra^* = 138.9Ra_c^* = 0.7500$

Figure 4.48: The azimuthally averaged zonal velocity profile of the rotating spherical shell with $N_\rho = 1$ at $\eta_{nb} = 1.00$. Note that zonal velocity greater than zero implies a prograde directional flow while the opposite implies the retrograde direction.

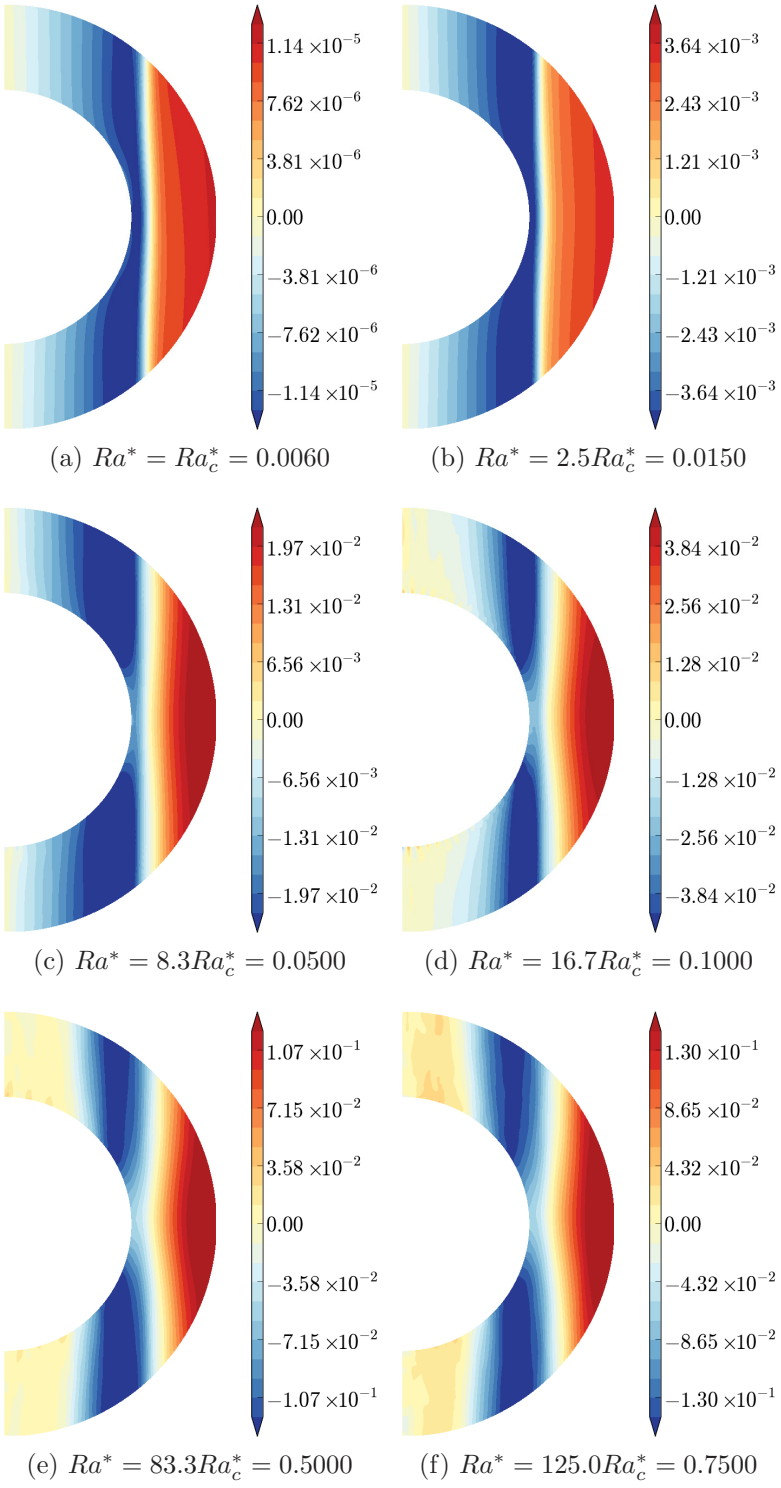

(a) $Ra^* = Ra_c^* = 0.0060$ (b) $Ra^* = 2.5Ra_c^* = 0.0150$

(c) $Ra^* = 8.3Ra_c^* = 0.0500$ (d) $Ra^* = 16.7Ra_c^* = 0.1000$

(e) $Ra^* = 83.3Ra_c^* = 0.5000$ (f) $Ra^* = 125.0Ra_c^* = 0.7500$

Figure 4.49: The azimuthally averaged zonal velocity profile of the rotating spherical shell with $N_\rho = 1$ at $\eta_{nb} = 0.90$. Note that zonal velocity greater than zero implies a prograde directional flow while the opposite implies the retrograde direction.

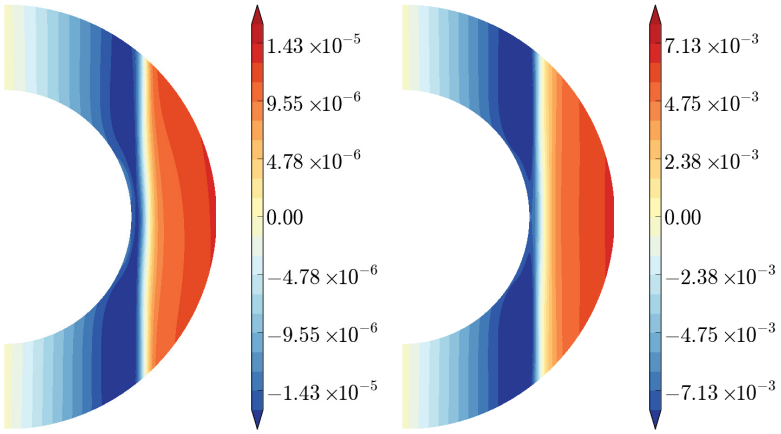

(a) $Ra^* = Ra_c^* = 0.0074$ (b) $Ra^* = 4.1Ra_c^* = 0.0300$

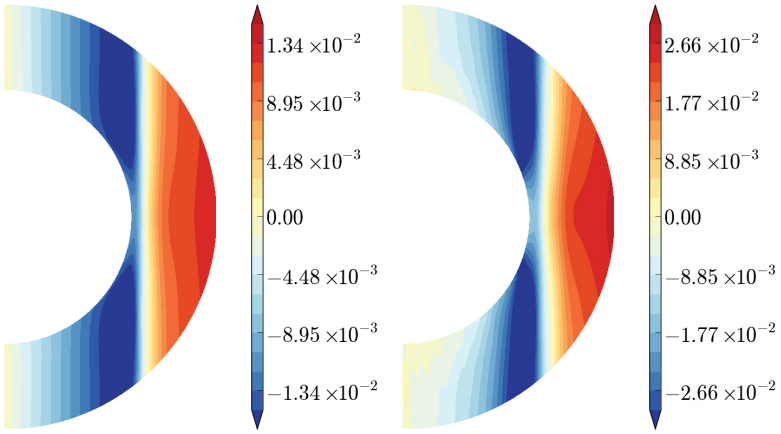

(c) $Ra^* = 6.8Ra_c^* = 0.0500$ (d) $Ra^* = 13.6Ra_c^* = 0.1000$

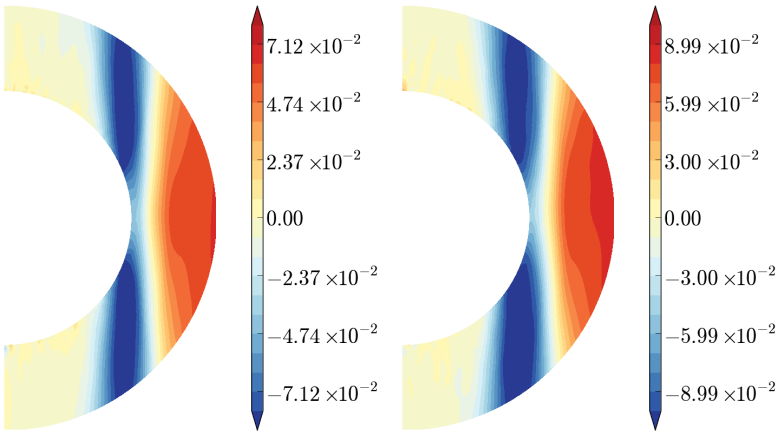

(e) $Ra^* = 67.6Ra_c^* = 0.5000$ (f) $Ra^* = 101.4Ra_c^* = 0.7500$

Figure 4.50: The azimuthally averaged zonal velocity profile of the rotating spherical shell with $N_\rho = 1$ at $\eta_{nb} = 0.80$. Note that zonal velocity greater than zero implies a prograde directional flow while the opposite implies the retrograde direction.

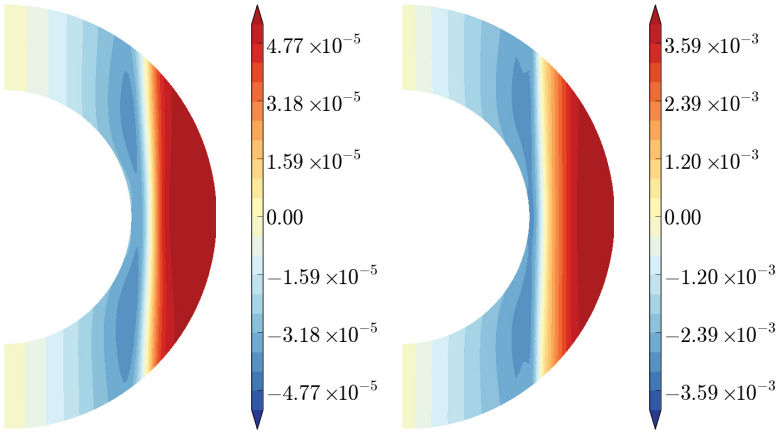

(a) $Ra^* = Ra_c^* = 0.0088$ (b) $Ra^* = 1.7Ra_c^* = 0.0150$

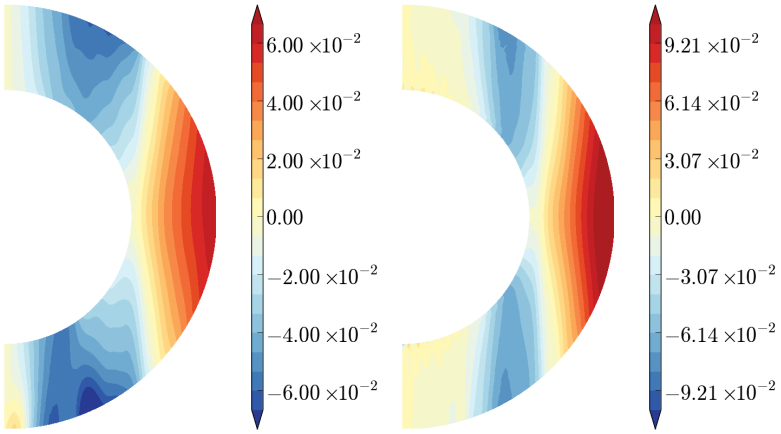

(c) $Ra^* = 5.7Ra_c^* = 0.0500$ (d) $Ra^* = 11.4Ra_c^* = 0.1000$

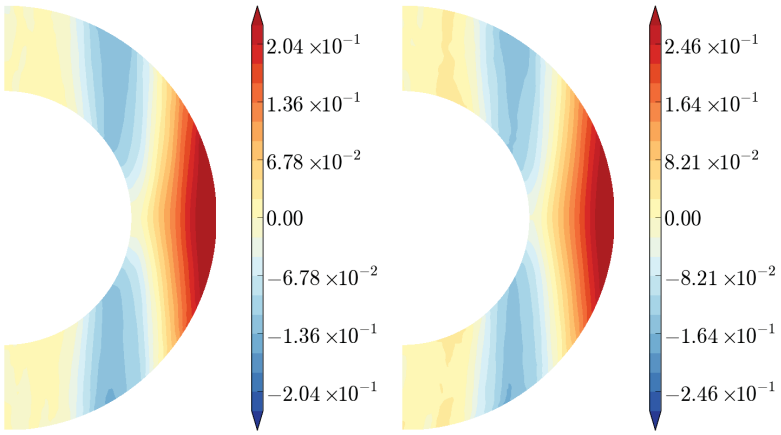

(e) $Ra^* = 34.1Ra_c^* = 0.3000$ (f) $Ra^* = 56.8Ra_c^* = 0.5000$

Figure 4.51: The azimuthally averaged zonal velocity profile of the rotating spherical shell with $N_\rho = 3$ at $\eta_{nb} = 1.00$. Note that zonal velocity greater than zero implies a prograde directional flow while the opposite implies the retrograde direction.

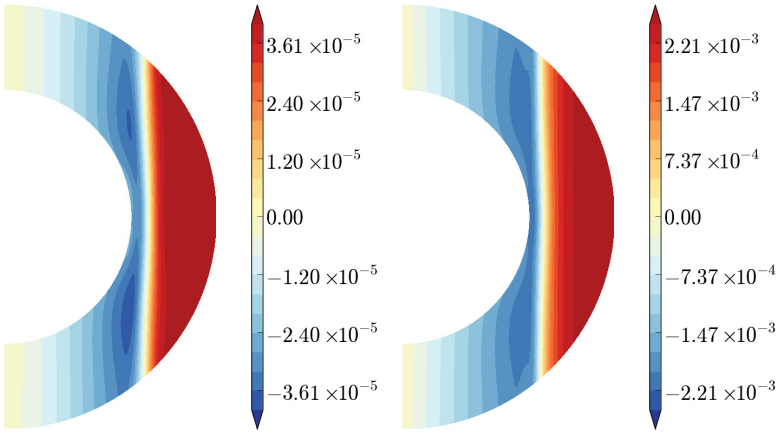

(a) $Ra^* = Ra_c^* = 0.0096$ (b) $Ra^* = 1.6Ra_c^* = 0.0150$

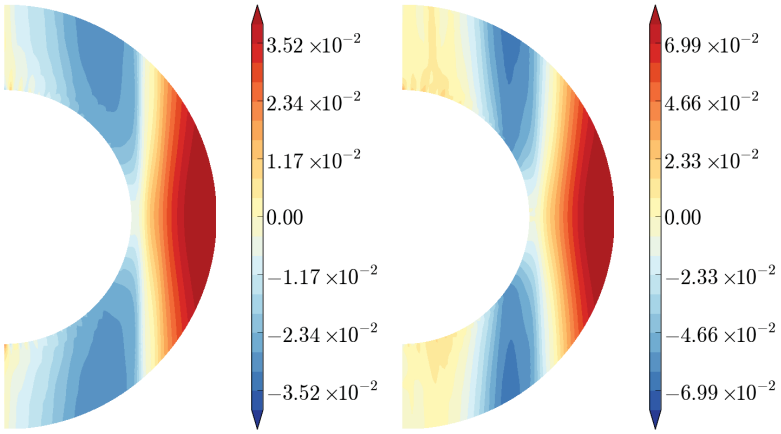

(c) $Ra^* = 5.2Ra_c^* = 0.0500$ (d) $Ra^* = 10.4Ra_c^* = 0.1000$

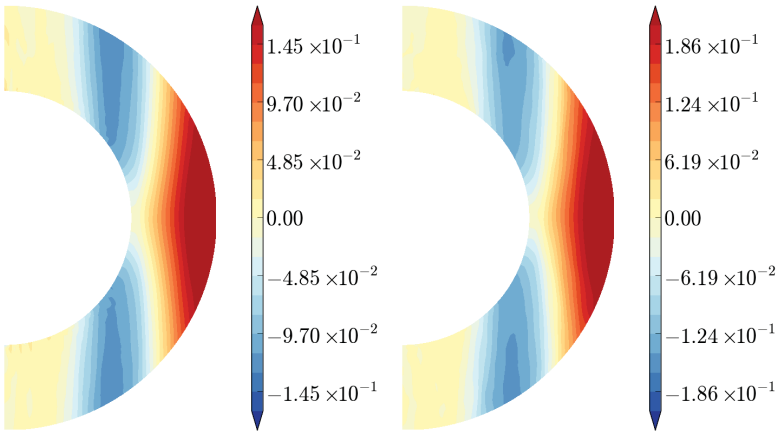

(e) $Ra^* = 31.3Ra_c^* = 0.3000$ (f) $Ra^* = 52.1Ra_c^* = 0.5000$

Figure 4.52: The azimuthally averaged zonal velocity profile of the rotating spherical shell with $N_\rho = 3$ at $\eta_{nb} = 0.90$. Note that zonal velocity greater than zero implies a prograde directional flow while the opposite implies the retrograde direction.

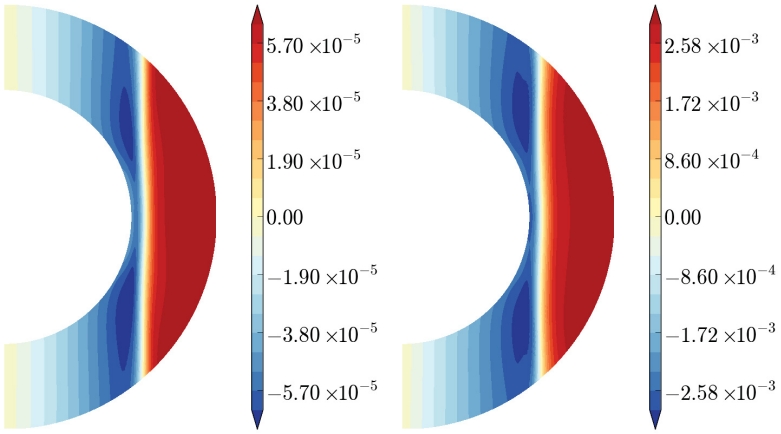

(a) $Ra^* = Ra_c^* = 0.0116$ (b) $Ra^* = 1.7Ra_c^* = 0.0200$

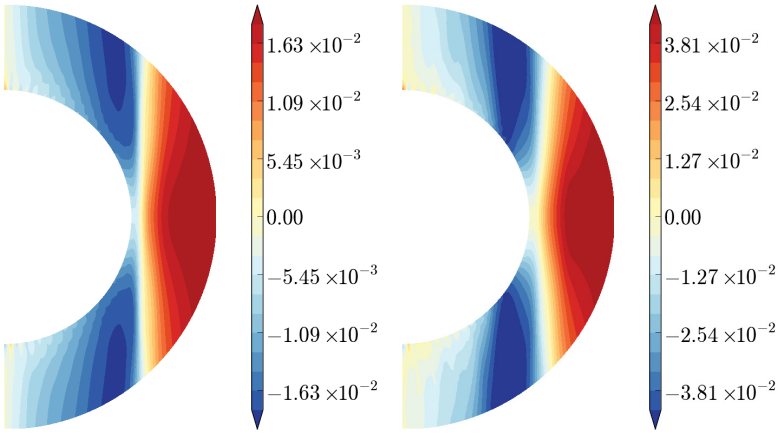

(c) $Ra^* = 4.3Ra_c^* = 0.0500$ (d) $Ra^* = 8.6Ra_c^* = 0.1000$

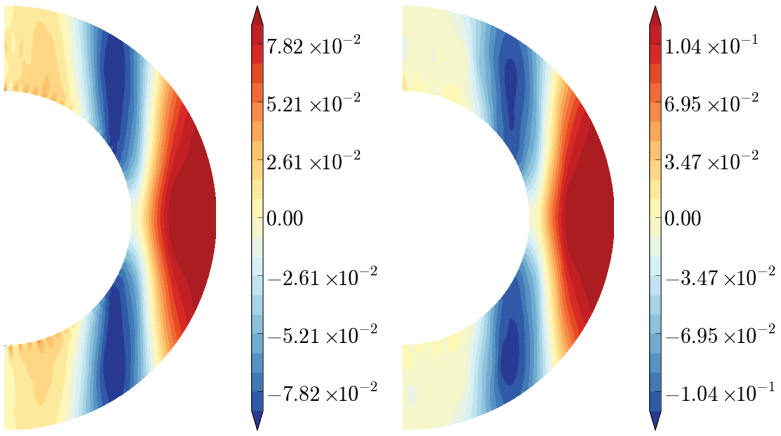

(e) $Ra^* = 25.9Ra_c^* = 0.3000$ (f) $Ra^* = 43.1Ra_c^* = 0.5000$

Figure 4.53: The azimuthally averaged zonal velocity profile of the rotating spherical shell with $N_\rho = 3$ at $\eta_{nb} = 0.80$. Note that zonal velocity greater than zero implies a prograde directional flow while the opposite implies the retrograde direction.

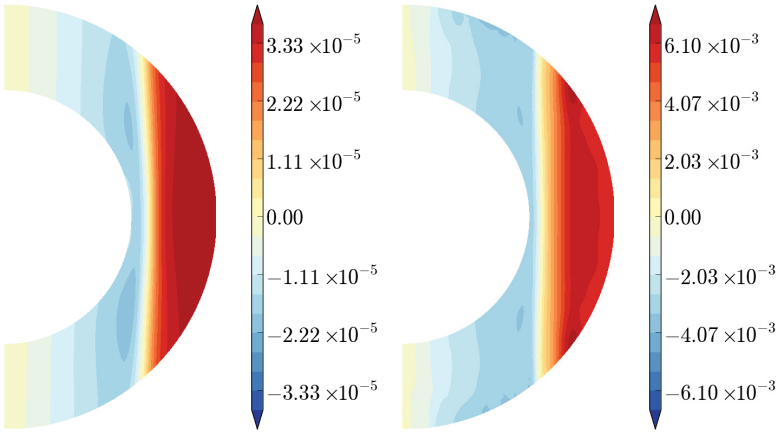

(a) $Ra^* = Ra_c^* = 0.0111$ (b) $Ra^* = 1.8Ra_c^* = 0.0200$

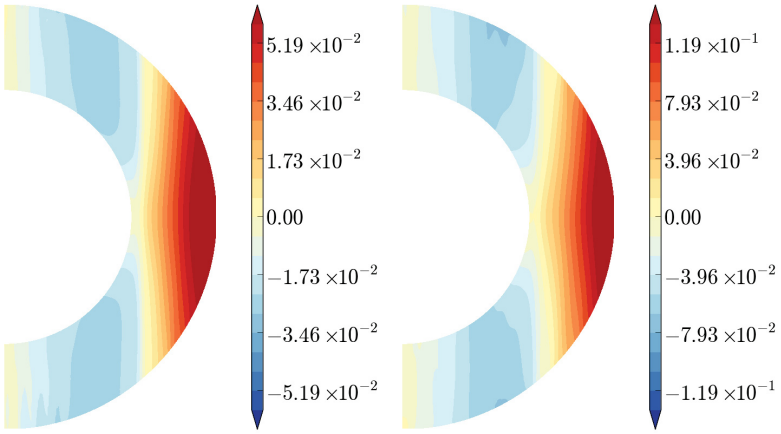

(c) $Ra^* = 4.5Ra_c^* = 0.0500$ (d) $Ra^* = 9.0Ra_c^* = 0.1000$

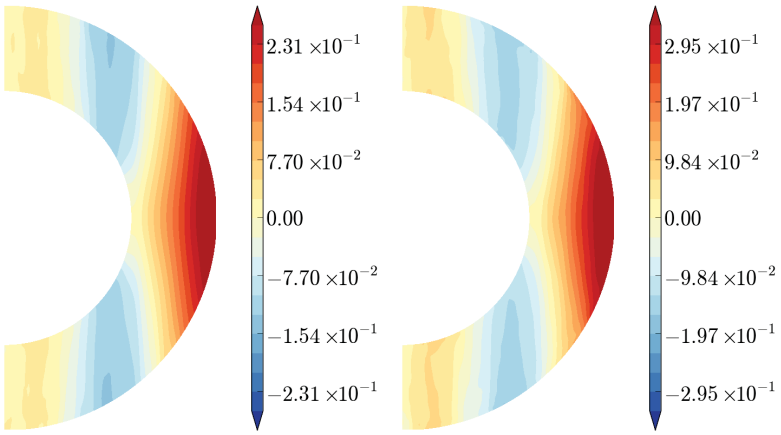

(e) $Ra^* = 27.0Ra_c^* = 0.3000$ (f) $Ra^* = 45.0Ra_c^* = 0.5000$

Figure 4.54: The azimuthally averaged zonal velocity profile of the rotating spherical shell with $N_\rho = 5$ at $\eta_{nb} = 1.00$. Note that zonal velocity greater than zero implies a prograde directional flow while the opposite implies the retrograde direction.

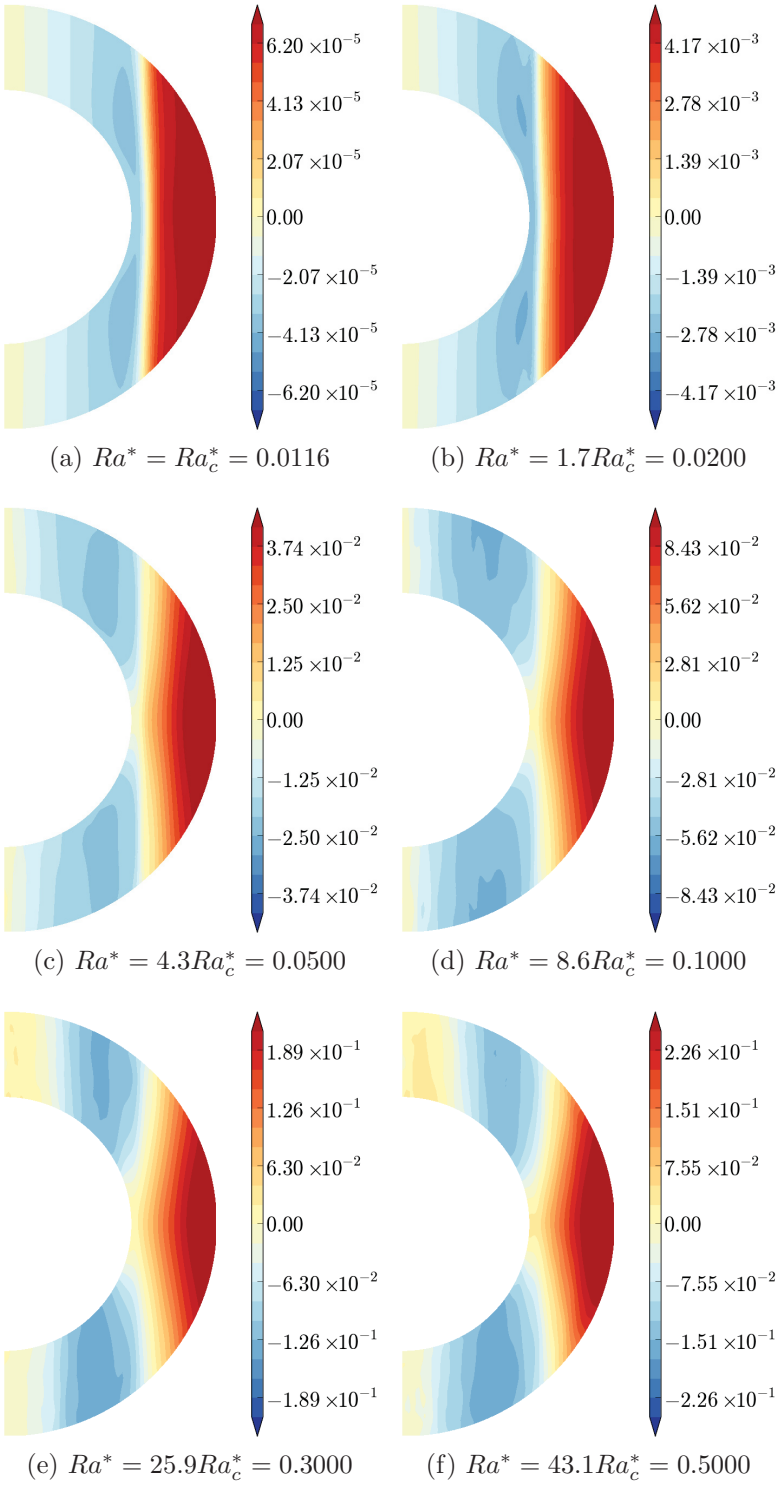

(a) $Ra^* = Ra_c^* = 0.0116$ (b) $Ra^* = 1.7Ra_c^* = 0.0200$

(c) $Ra^* = 4.3Ra_c^* = 0.0500$ (d) $Ra^* = 8.6Ra_c^* = 0.1000$

(e) $Ra^* = 25.9Ra_c^* = 0.3000$ (f) $Ra^* = 43.1Ra_c^* = 0.5000$

Figure 4.55: The azimuthally averaged zonal velocity profile of the rotating spherical shell with $N_\rho = 5$ at $\eta_{nb} = 0.90$. Note that zonal velocity greater than zero implies a prograde directional flow while the opposite implies the retrograde direction.

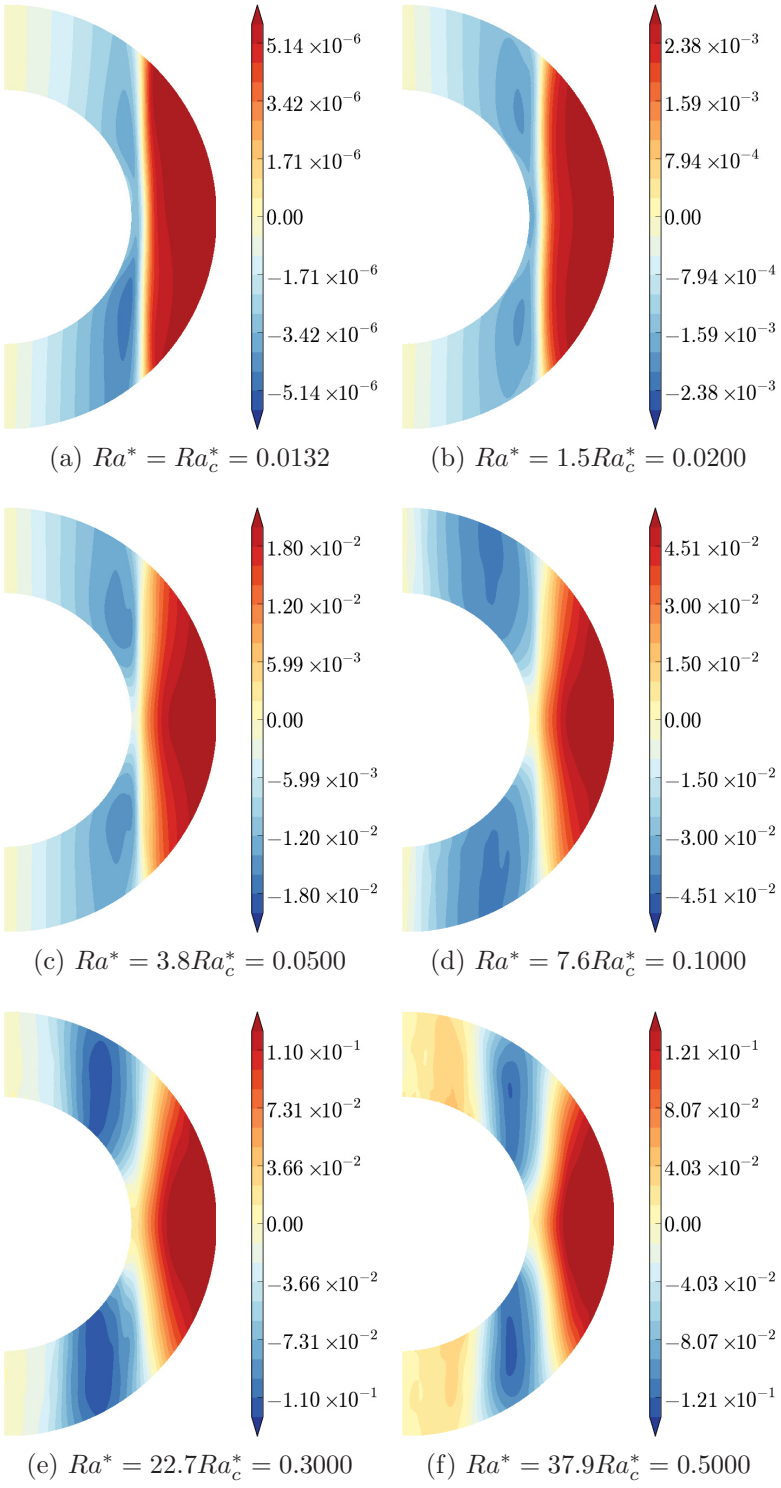

(a) $Ra^* = Ra_c^* = 0.0132$ (b) $Ra^* = 1.5Ra_c^* = 0.0200$

(c) $Ra^* = 3.8Ra_c^* = 0.0500$ (d) $Ra^* = 7.6Ra_c^* = 0.1000$

(e) $Ra^* = 22.7Ra_c^* = 0.3000$ (f) $Ra^* = 37.9Ra_c^* = 0.5000$

Figure 4.56: The azimuthally averaged zonal velocity profile of the rotating spherical shell with $N_\rho = 5$ at $\eta_{nb} = 0.80$. Note that zonal velocity greater than zero implies a prograde directional flow while the opposite implies the retrograde direction.

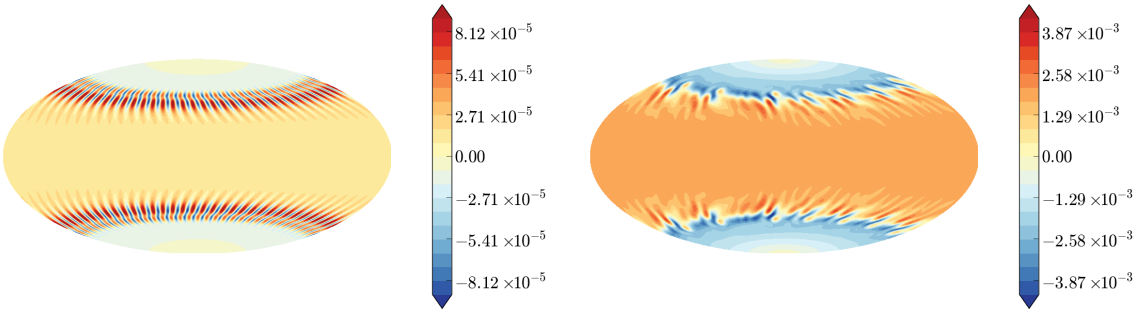

(a) $Ra^* = Ra_c^* = 0.0054$

(b) $Ra^* = 1.8Ra_c^* = 0.0100$

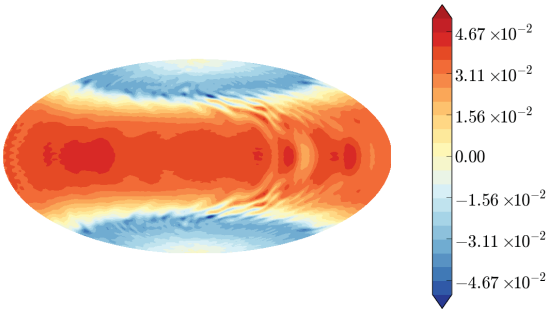

(c) $Ra^* = 9.3Ra_c^* = 0.0500$

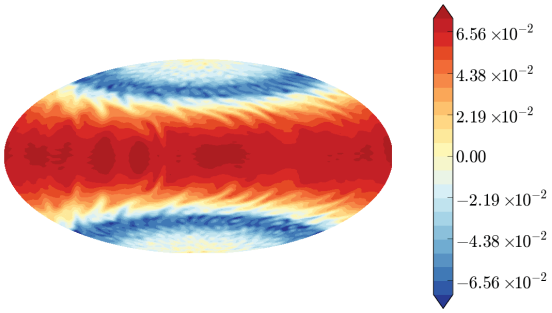

(d) $Ra^* = 18.1Ra_c^* = 0.1000$

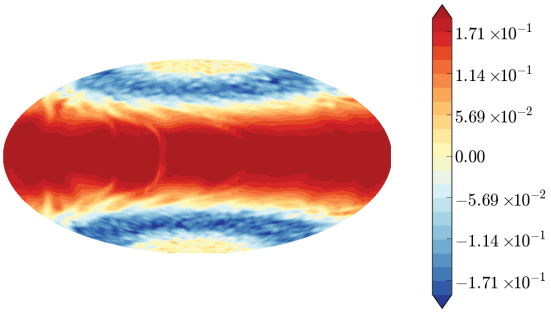

(e) $Ra^* = 92.6Ra_c^* = 0.5000$

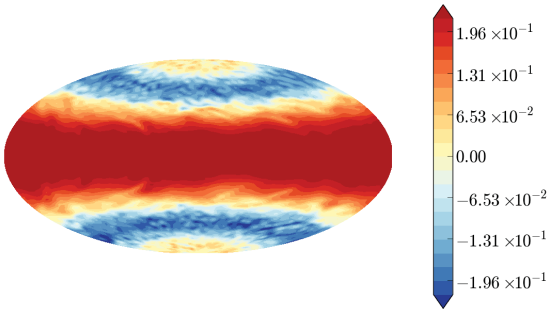

(f) $Ra^* = 138.9Ra_c^* = 0.7500$

Figure 4.57: A hammer projection of the zonal velocity of the rotating spherical shell with $N_\rho = 1$ at $\eta_{nb} = 1.00$ at the outer boundary. Note that zonal velocity greater than zero implies a prograde directional flow while the opposite implies the retrograde direction.

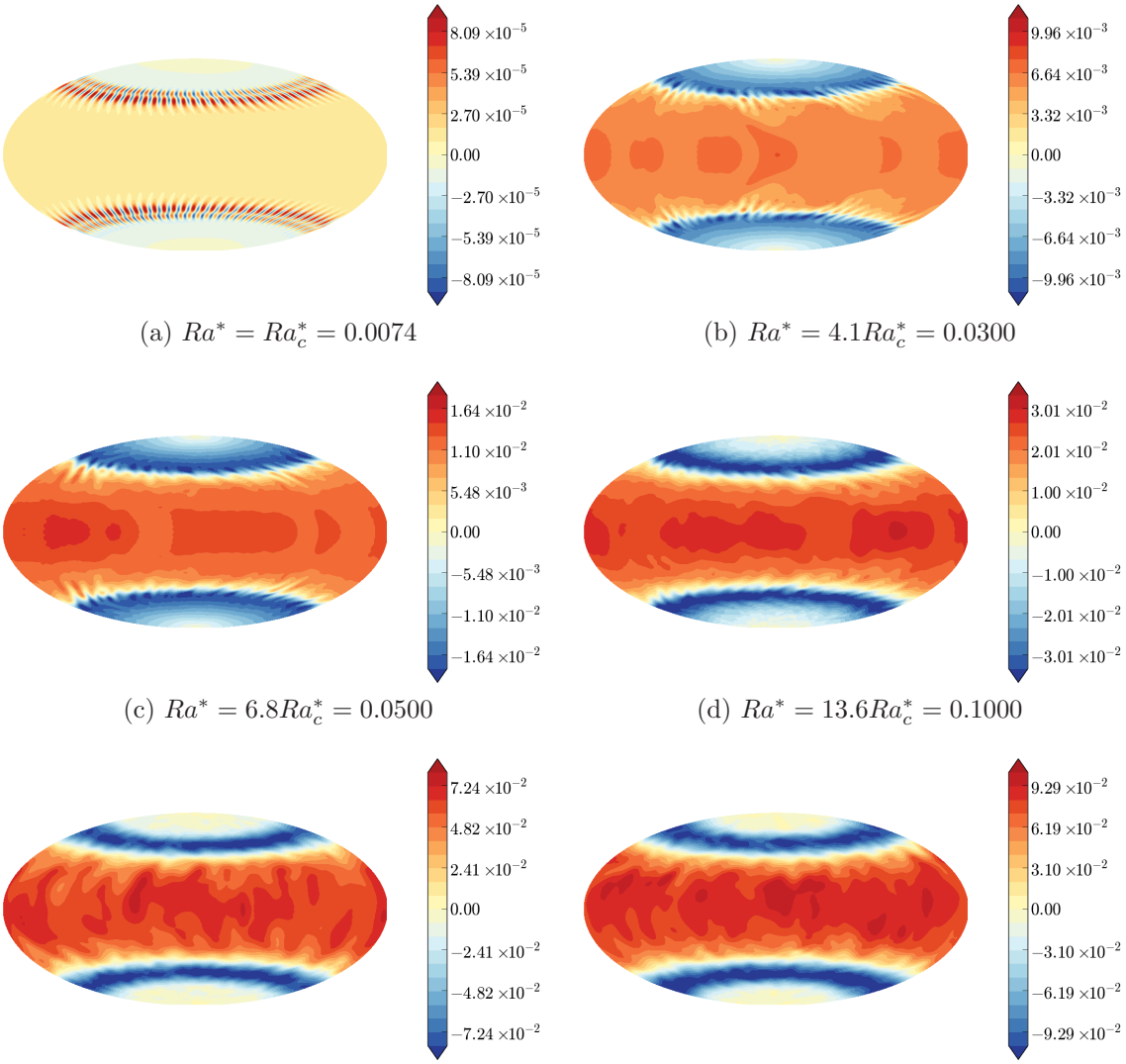

(a) $Ra^* = Ra_c^* = 0.0074$

(b) $Ra^* = 4.1Ra_c^* = 0.0300$

(c) $Ra^* = 6.8Ra_c^* = 0.0500$

(d) $Ra^* = 13.6Ra_c^* = 0.1000$

(e) $Ra^* = 67.6Ra_c^* = 0.5000$

(f) $Ra^* = 101.4Ra_c^* = 0.7500$

Figure 4.58: A hammer projection of the zonal velocity of the rotating spherical shell with $N_\rho = 1$ at $\eta_{nb} = 0.80$ at the outer boundary. Note that zonal velocity greater than zero implies a prograde directional flow while the opposite implies the retrograde direction.

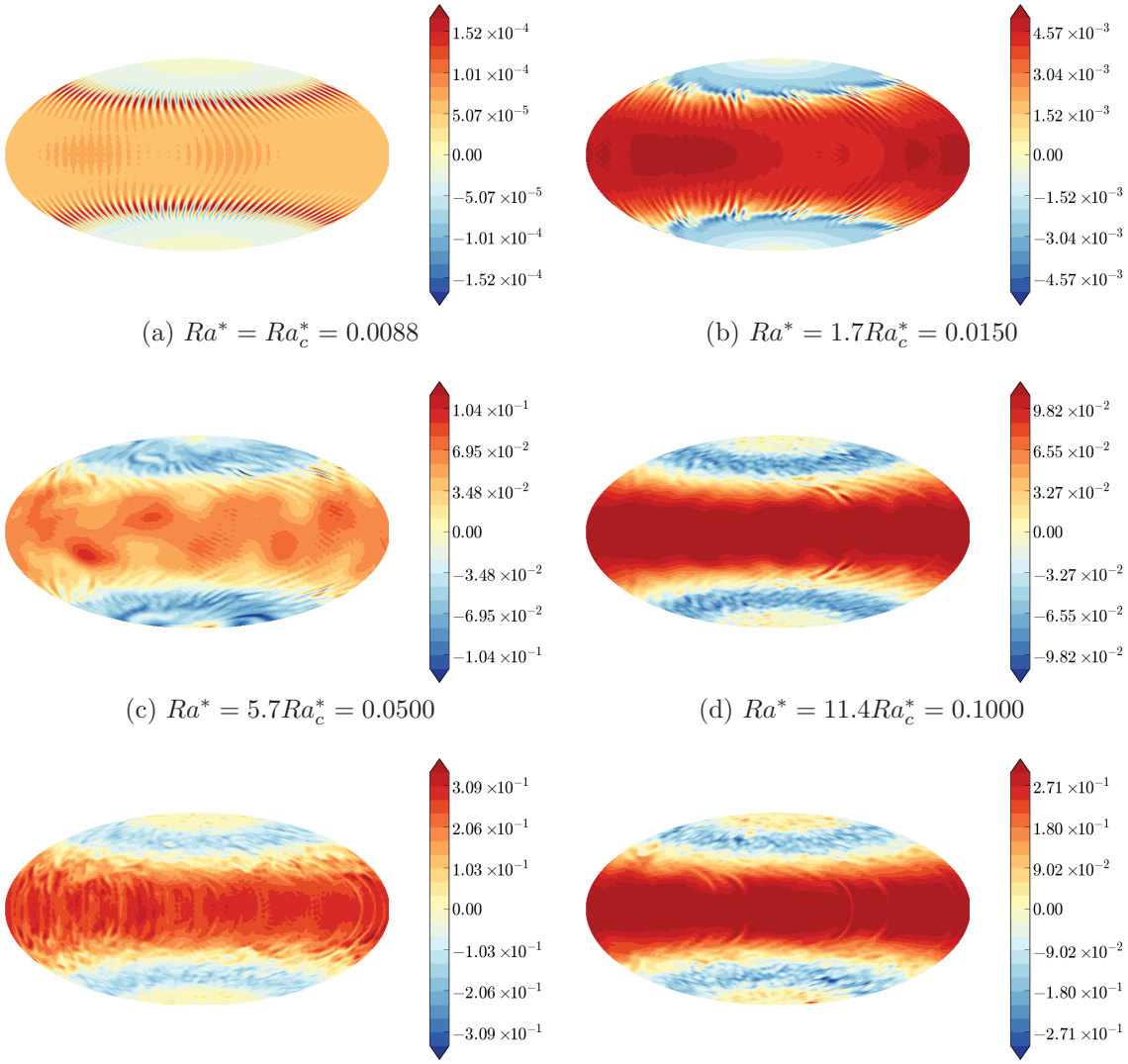

(a) $Ra^* = Ra_c^* = 0.0088$ (b) $Ra^* = 1.7Ra_c^* = 0.0150$

(c) $Ra^* = 5.7Ra_c^* = 0.0500$ (d) $Ra^* = 11.4Ra_c^* = 0.1000$

(e) $Ra^* = 34.1Ra_c^* = 0.3000$ (f) $Ra^* = 56.8Ra_c^* = 0.5000$

Figure 4.59: A hammer projection of the zonal velocity of the rotating spherical shell with $N_\rho = 3$ at $\eta_{nb} = 1.00$ at the outer boundary. Note that zonal velocity greater than zero implies a prograde directional flow while the opposite implies the retrograde direction.

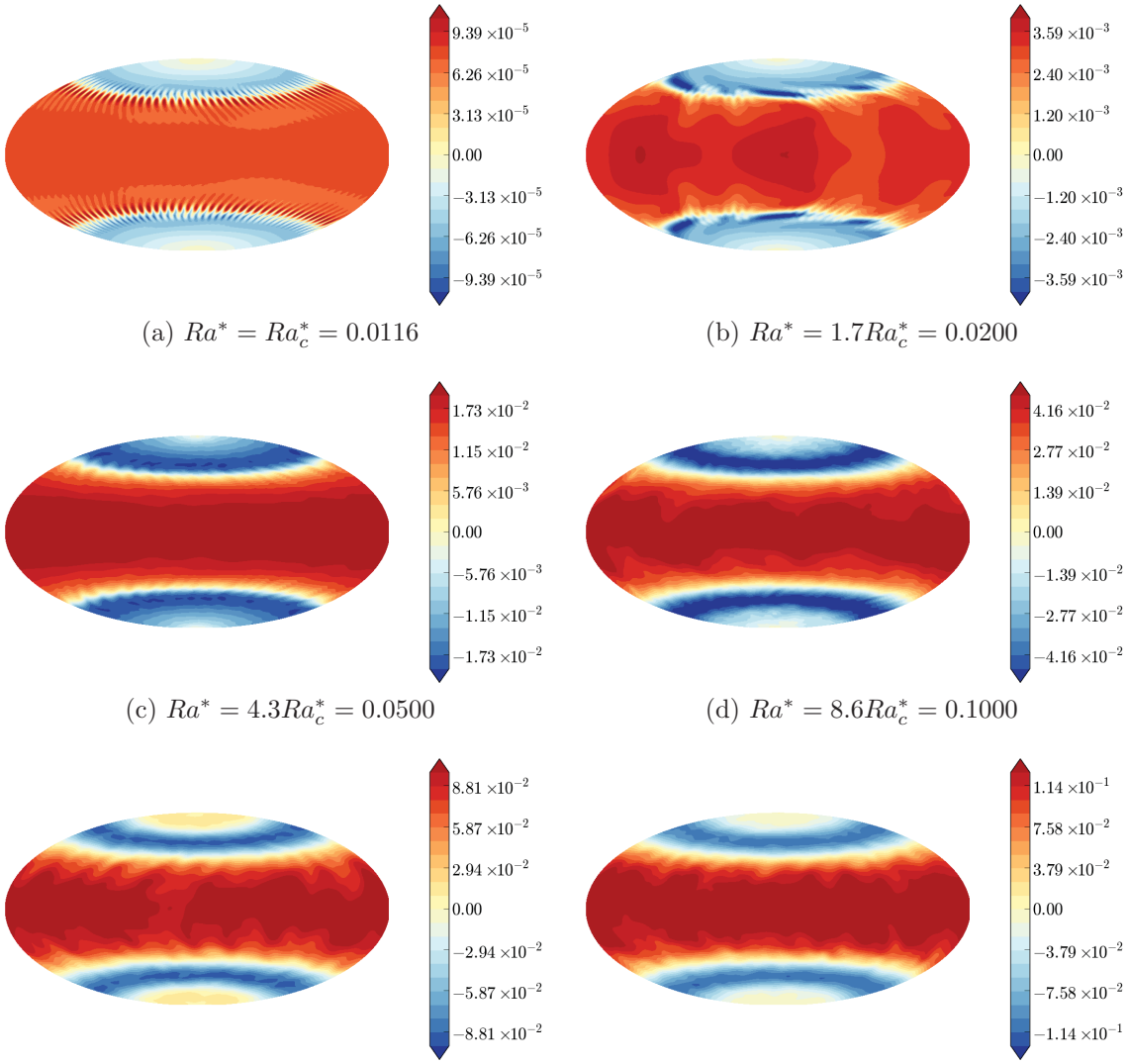

(a) $Ra^* = Ra_c^* = 0.0116$

(b) $Ra^* = 1.7Ra_c^* = 0.0200$

(c) $Ra^* = 4.3Ra_c^* = 0.0500$

(d) $Ra^* = 8.6Ra_c^* = 0.1000$

(e) $Ra^* = 25.9Ra_c^* = 0.3000$

(f) $Ra^* = 43.1Ra_c^* = 0.5000$

Figure 4.60: A hammer projection of the zonal velocity of the rotating spherical shell with $N_\rho = 3$ at $\eta_{nb} = 0.80$ at the outer boundary. Note that zonal velocity greater than zero implies a prograde directional flow while the opposite implies the retrograde direction.

Chapter 5

Vorticity Formation near the Tangent Cylinder

Based on the previous chapter, implementing the stably stratified fluid layer near the outer boundary using the constant conductive entropy radial gradient boundary conditions can change the fluid dynamics of a rotating anelastic convective spherical shell. For one, the stably stratified fluid layer has a tendency to force the fluid motion to be two dimensional, which is along the azimuthal and cylindrical radial directions. This can be seen in rotating anelastic spherical shell models with high density stratification in the previous chapter, where the strong retrograde jets near the outer boundary start to become smoother when the stably stratified fluid layer thickness increases. However, a special set of models exist where they generate long-lived eddies near the tangent cylinder. These are the near-Boussinesq models with a thick, stably stratified fluid layer. They also exhibit great eddies near the tangent cylinder that are somewhat comparable to the Great Red Spot observed on Jupiter.

5.1 Two-Dimensional Eddy Formation

For two-dimensional turbulence to evolve freely, a coherent vorticity is needed (Carnevale, McWilliams, Pomeau, Weiss, & Young, 1991). Consider the vorticity $\boldsymbol{\omega}$ defined by

$$\boldsymbol{\omega} = \nabla \times \boldsymbol{u}, \tag{5.1}$$

where the fluid velocity field is denoted as $\boldsymbol{u}$. Two-dimensional turbulence can form if one of the components of $\boldsymbol{\omega}$ is coherent, which means that it remains consistent in magnitude and shape over time. Based on a numerical study conducted by Riley, Metcalfe, and Weiss-

man (1981) analyzing the effects of vertical density stratification on turbulence of a non-rotating Boussinesq fluid, the implementation of the stably stratified fluid layer along the outer boundary has a tendency to inhibit the vortex line stretching. However, the horizontal components of the vortex line is larger than the vertical component. This correlates to the stably stratified fluid layer inhibiting the vertical growth of the fluid motion while enhancing the horizontal growth within this layer. This enhancement could lead to the development of two-dimensional eddies.

Two-dimensional eddies are constrained by the Rossby deformation radius L_d, which is defined by

$$L_d = H_\rho \sqrt{|\mathscr{R}(r)|} \tag{5.2}$$

(Heimpel et al., 2016). The density scale height H_ρ is defined as

$$H_\rho = -\frac{1}{\frac{d \ln \bar{\rho}}{dr}}, \tag{5.3}$$

where background density is denoted as $\bar{\rho}$. The depth dependant Rayleigh number, $\mathscr{R}(r)$, is represented by

$$\mathscr{R}(r) = \frac{g(r)\beta(r)}{g_o \beta_i} Ra^*, \tag{5.4}$$

where gravity is represented by $g(r)$ with $g_o = g(r_o)$, radial entropy gradient is represented by $\beta(r) = \mathrm{d}s_c(r)/\mathrm{d}r$ with $\beta_i = \beta(r_i)$ and modified Rayleigh number is represented by $Ra^* = RaE^2/Pr$. The Rossby deformation radius, L_d, represents the length scale that result from the balance between the gravitational forces that want to keep the surface at constant r flat and the Coriolis forces that want to deform it (e.g., Pedlosky, 1987). The value of L_d roughly determines the length scale of the eddies.

5.2 Near-Boussinesq Model

One set of models that exhibit eddies near the tangent cylinder are the near-Boussinesq ($N_\rho = 10^{-2}$) models with $\eta_{nb} = 0.80$, Prandtl number $Pr = 1$, Ekman number $E = 10^{-4}$, and radius ratio $\eta = 0.60$, where the stably stratified fluid layer thickness is defined as $r_o(1-\eta_{nb})$. At $Ra^* \geq 91.5Ra_c^* = 0.4000$ with critical modified Rayleigh number $Ra_c^* = 0.0044$, eddies start forming near the tangent cylinder near the outer boundary of the rotating spherical shell. The kinetic energy time series for $Ra^* = 0.4000$, 0.5000, 1.0000, 2.0000, and 3.0000

are presented in Figure 5.1, which all exhibit low frequency oscillations. The axisymmetric (azimuthally averaged) radial entropy gradient profile ($\partial s/\partial r$) presented in Figure 5.2 of the same models all exhibit perturbations in the weakly convective fluid layer ($\partial s/\partial r \approx 0$) near the tangent cylinder. These perturbations increase in area for the stably stratified region as Ra^* increases. However, the axisymmetric $\partial u_\phi/\partial z$ profile for $N_\rho = 10^{-2}$ models (which can be seen in Figure 5.3) are different compared with the $N_\rho = 1$ and 3 models with $\eta_{nb} = 0.80$, which are shown in Figures 4.40 and 4.42, respectively. While the $N_\rho \geq 1$ models exhibit $\partial u_\phi/\partial z > 0$ dominance in the Northern hemisphere and $\partial u_\phi/\partial z < 0$ in the Southern hemisphere, the near-Boussinesq models with $Ra^* \geq 0.400$ experiences a mix of the two in both hemispheres with the high magnitude areas constrained near the inner boundary and near the tangent cylinder.

For $Ra^* = 0.4000$, this model exhibit long-lived eddies near the tangent cylinder at both the Northern and Southern hemispheres. Figure 5.4 shows a series of hammer projection images at the outer boundary of the zonal velocity u_ϕ between times $t = 0.6805\tau$ and $t = 0.7113\tau$. This figure shows six eddies rotating around the tangent cylinder of the spherical shell indicated by a pair of maximum and minimum areas between the strong prograde and retrograde jets at both hemispheres. However, each eddy in the Northern hemisphere has a counterpart centred at the same longitude at the Southern hemisphere, where each pair of eddies rotate around the tangent cylinder in the prograde direction at the same speed. Each eddy in the Northern hemisphere appears to travel at different speeds. They also appear to maintain their zonal velocity (u_ϕ) magnitude while keeping their geometry time dependent.

The radial vorticity ω_r at $r = r_o$ of the the model is presented in Figure 5.5 between $t = 0.6805\tau$ and $t = 0.7113\tau$. This figure indicates that much of the radial vorticity action occur near the tangent cylinder at both hemispheres. The maximum and minimum areas in Figure 5.5 can be associated with the eddies observed with in Figure 5.4.

The observations of the eddies in $Ra^* = 0.4000$ are very similar to models with $Ra^* = 0.5000$. However, the nature of these eddies changes drastically for increasing Ra^* ($Ra^* \geq 1.0000$). They merge to form great eddies at both hemispheres. Since increasing Ra^* increases the overall fluid speed and turbulent motion in the system, either a large fluid speed, turbulent motion, or both are needed to generate these great eddies.

5.2.1 Generation of Great Eddies

Increasing the thermal forcing to $Ra^* = 1.0000$ leads the formation of great eddies rotating around the tangent cylinder for $N_\rho = 10^{-2}$ with $\eta_{nb} = 0.80$ at both hemispheres. For both great eddies to form, the long-lived eddies (similar to the ones observed in $Ra^* = 0.4000$)

need to merge together. This can be seen in Figure 5.6, which shows the zonal flow velocity of the $Ra^* = 1.0000$ model in hammer projection form between $t = 0.2047\tau$ and $t = 0.2223\tau$ at $r = r_o$. Between $t = 0.2117\tau$ and $t = 0.2187\tau$, which is associated with Figures 5.6(c) to 5.6(e), the $Ra^* = 1.0000$ model shows the merging of two eddies at both hemispheres, which is absent in the $Ra^* = 0.4000$ model. This results in an eddy with a much larger zonal flow magnitude with respect to the other eddies, which is shown in Figure 5.6(e). These merged eddies maintain a time dependent geometry and zonal velocity magnitude. However, the prograde part of these eddies appear to interact with the strong prograde jet via diagonal trailing features.

These great eddies form when more of the long-lived eddies rotating around the tangent cylinder begin to merge. This can be seen in Figure 5.7, which shows the zonal velocity between $t = 0.2258\tau$ and $t = 0.2433\tau$ at the outer boundary. This figure shows that the merging of two long-lived eddies leads the formation of a larger long-lived eddy, which is shown in Figures 5.7(a) to 5.7(e). Finally, the remaining two large long-lived eddies at both hemispheres merge together to form great eddies, which can be seen at Figure 5.7(f). The resulting eddies do not have a diagonal prograde trailing features but rather a head and a trailing feature along the tangent cylinder with prograde and retrograde components.

For the rest of the model, these great eddies remain relatively stable. Figure 5.8 shows the final state of the great eddies between $t = 0.3011\tau$ and $t = 0.3178\tau$. These great eddies exhibit a head and tail feature travelling in the retrograde direction around the tangent cylinder. They also have a faint retrograde zonal flow that surrounds the front of the eddies' head. A strong prograde area or equatorial spot in between the eddies at the equator is surrounded by retrograde flow and travels at the same speed as the great eddies. The equatorial spot's geometry and zonal flow magnitude is also time dependent. However, the radial vorticity shown in Figure 5.9 between $t = 0.3011\tau$ and $t = 0.3178\tau$ also shows that the great eddies at both hemispheres is anticyclonic.

The azimuthal slice of u_ϕ and u_θ at $t = 0.2231\tau$ of the great eddies can be seen in Figure 5.10 where the azimuthal slices are taken at the centres of both the minimum u_θ and u_ϕ of the Northern great storm. Based on the azimuthal slices, these great eddies extend from $r = r_o$ to the equator near the tangent cylinder. The u_ϕ azimuthal slice of the great eddies also indicates that the motion of the storm is in columnar form, implying that they are driven by convection. This is presented in Figures 5.10(d) and 5.10(f). This is further supported by images of the equatorial slice of the radial velocity between $t = 0.3011\tau$ and $t = 0.3178\tau$ presented in Figure 5.11. The radial velocity of the model exhibits non-linear convection cells but with a gap between large magnitude convection cells and the low magnitude convection cells. The high magnitude convection cells at the counterclockwise

side of the gap is associated with the great eddies of the model and drifts clockwise around the inner boundary.

5.2.2 Increasing Rotational Constraint

While maintaining $Ra^* = 1.0000$ for $N_\rho = 10^{-2}$ with $\eta_{nb} = 0.80$, the model with decreasing E from $E = 10^{-4}$ to $E = 3.0 \cdot 10^{-5}$ still maintains great eddies at both hemispheres. The time series data for this model shown in Figure 5.12(a) exhibits low frequency oscillations similar to the $E = 10^{-4}$ models. The axisymmetric $\partial s/\partial z$ profile shown in Figure 5.12(b) for the $E = 3 \cdot 10^{-5}$ model is also similar to the $E = 10^{-4}$ models, which is shown in Figure 5.2. However, the $\partial u_\phi/\partial z$ profile shown in Figure 5.12(c) exhibits a greater number of constrained $\partial u_\phi/\partial z > 0$ and $\partial u_\phi/\partial z < 0$ areas near the outer boundary and near the poles compared to the $E = 10^{-4}$ models.

The great eddies for the $N_\rho = 10^{-2}$ with $\eta_{nb} = 0.80$, $Ra^* = 1.0000$, and $E = 3.0 \cdot 10^{-5}$ are generated similarly to the $E = 10^{-4}$ counterpart such that they are generated by the merging of several long-lived eddies. This can be seen in Figure 5.13, where it shows the hammer projection of the zonal velocity of the rotating convecting fluid at the outer boundary between $t = 0.6805\tau$ and $t = 0.7113\tau$. In this figure, the long-lived eddies all merge together to form a pair of strong long-lived eddies, where the resulting eddy can be seen in Figure 5.13(f). This pair roughly maintains their magnitude and geometry, which can be seen in Figure 5.14 between $t = 0.1053\tau$ and $t = 0.1228\tau$. Figure 5.14 also shows that these eddies eventually gain energy from the zonal flow until they transform into the great eddies as seen in Figure 5.15, where it drifts westward between $t = 0.1351\tau$ and $t = 0.1504\tau$. These great eddies remain relatively stable for the duration of the model, while they still have the head and the trailing feature similar to the great eddies from the $E = 10^{-4}$ model. The radial vorticity at the outer boundary presented in Figure 5.16 between $t = 0.1351\tau$ and $t = 0.1504\tau$ shows that the great eddies are anticyclonic in nature, which is consistent with the great eddies from the $E = 10^{-4}$ model. Azimuthal slices of both u_ϕ and u_θ presented in Figure 5.17 at $t = 0.3569\tau$ are also similar to the $E = 10^{-4}$ counterpart, showing that the great eddies are driven by convection.

Another interesting feature for decreasing E is the generation of a high latitude prograde jets adjacent to the retrograde jets. These high latitude prograde jets appear to be unaffected by the strong long-lived eddies, nor do they affect the great eddies. The high latitude jets begin to broaden and increase in zonal velocity magnitude as time progresses, which can be seen in Figure 5.18, which represents the zonal velocity at $r = r_o$ between $t = 1.342\tau$ and $t = 1.371\tau$. The magnitude of the great eddies' zonal velocity also increases with time.

5.3 Discussion

Based on observations from the great eddies on $N_\rho = 10^{-2}$, $Ra^* = 1.0000$, and $\eta_{nb} = 0.80$ models with $E = 10^{-4}$ and $E = 3 \cdot 10^{-5}$, they share some characteristics similar to that of the Great Red Spot on Jupiter. The Great Red Spot on Jupiter is an anticyclonic storm that drifts westward at a planetographic latitude of 22^oS (Hide, 1961). The great eddies exhibit by the $N_\rho = 10^{-2}$ and $Ra^* = 1.0000$ models are anticyclonic in nature that drift westward near the tangent cylinder with latitude $\cos^{-1}(\eta) \approx 53^o$N and S. Assuming that the radius ratio for Jupiter is 0.90, the latitude associated with the tangent cylinder is roughly 26^o (Gastine & Wicht, 2012). This latitude is close to where the Great Red Spot of Jupiter resides in. Another feature shared between both the great eddies and the Great Red Spot is that they drift westward. However, one of the more trivial differences is that these models produce a great eddy at each hemisphere, while there only exists one great eddy called the Great Red Spot at the Southern Hemisphere for Jupiter (Vasavada et al., 1998).

Based on these models, the convective nature of the near-Boussinesq fluid is what drives the generation of the great eddies. The azimuthal slices from both the $E = 10^4$ and $E = 3 \cdot 10^{-5}$ models, which can be seen in Figures 5.10 and 5.17, respectively, both show that these great eddies extend in columnar form from the outer boundary to the equator. However, the thermal winds generated at the outer boundary based on Figures 5.3 and 5.12 also conflict with the zonal jets typically generated from rotating convection. The constrained $\partial u_\phi / \partial z < 0$ and $\partial u_\phi / \partial z > 0$ areas near the outer boundary and near the tangent cylinder want to force the fluid to travel in the retrograde direction. However, the constrained $\partial u_\phi / \partial z > 0$ and $\partial u_\phi / \partial z < 0$ areas at the Northern and Southern hemispheres, respectively, near the tangent cylinder and near the equator want to force the zonal flow in the prograde direction. The directionality of these areas conflict with each other, which could be associated with the generation of the two-dimensional turbulence within the the strong equatorial prograde jet. This could explain why the rotating convective models with $N_\rho \geq 1$ from the fourth chapter did not exhibit long-lived eddies at the outer boundary, in which these models show a dominance in $\partial u_\phi / \partial z > 0$ at the Southern hemisphere and $\partial u_\phi / \partial z < 0$ at the Northern hemisphere, but not a mixture of the two.

From Tritton (1988), the formation of both the long-lived and great eddies depend on both on the mean velocity gradient and the density stratification of the fluid. To describe the generation of turbulence, the Richardson number can be used. This number is represented

by

$$Ri = -\frac{g(\mathrm{d}\bar{\rho}/\mathrm{d}r)}{\bar{\rho}(\mathrm{d}<u>/\mathrm{d}r)^2}, \tag{5.5}$$

where $<u>$ is the mean velocity (e.g., Tritton, 1988). Equation (5.6) can be rewritten as

$$Ri = -\frac{gdE^2(\mathrm{d}\bar{\rho}/\mathrm{d}r)}{\nu\bar{\rho}(\mathrm{d}<Ro>/\mathrm{d}r)^2}, \tag{5.6}$$

where Ro is the Rossby number. Notice that the sign of the background density gradient is important in defining Ri, whereas the sign of the mean velocity gradient does not matter. If the density increases towards the top boundary (i.e., $\mathrm{d}\bar{\rho}/\mathrm{d}r > 0$), then $Ri < 0$, implying that both the shear and the buoyancy leads to the generation of turbulence. For a small negative Ri, shear is dominant in the flow, leading to the generation of eddies. However, if negative Ri is large, then buoyancy is dominant, which leads to turbulent motion similar to that of free convection. If the density increases towards the bottom boundary, then $Ri > 0$ and thus turbulence cannot be sustained for large Ri (Tritton, 1988).

The $N_\rho = 10^{-2}$ models with $\eta_{nb} = 1.00$, 0.98, 0.96, and 0.90 do not exhibit any long-lived eddies, nor do any of the $N_\rho \geq 1$ models with $\eta_{nb} = 1.00$, 0.98, 0.96, 0.90, and 0.80. This implies that a combination of both N_ρ and η_{nb} play a role in the Richardson number. However, there is an uncertainty in whether or not to increase or decrease η_{nb} from $\eta_{nb} = 0.80$ when N_ρ increases from $N_\rho = 10^{-2}$ in order to replicate the great eddies. Decreasing Ek also leads to a smaller Ri, which could result in the generation of eddies. Replicating the great eddies for higher N_ρ is needed to further understand the how stably stratified fluid layer leads to the generation of long-lived eddies.

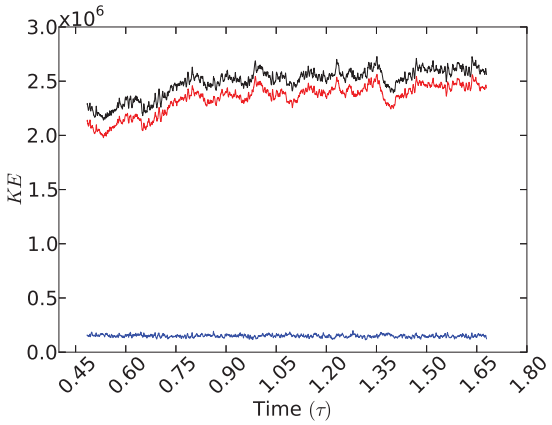

(a) $Ra^* = 92.5 Ra_c^* = 0.4000$

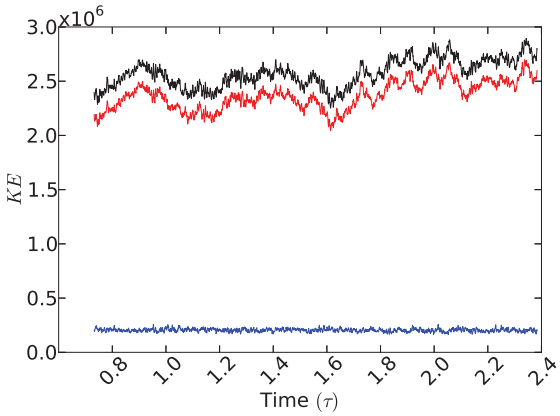

(b) $Ra^* = 114.4 Ra_c^* = 0.5000$

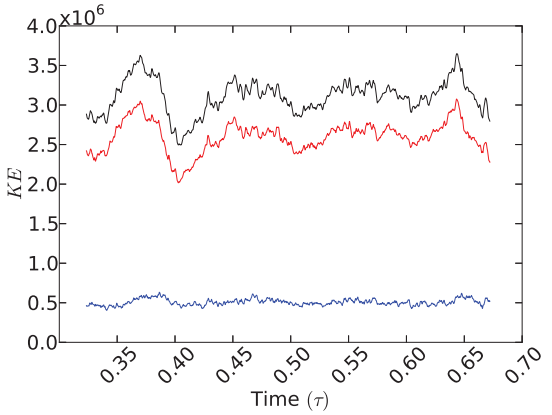

(c) $Ra^* = 228.8 Ra_c^* = 1.0000$

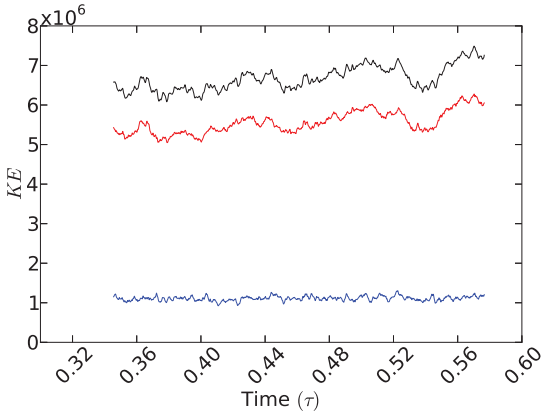

(d) $Ra^* = 457.5 Ra_c^* = 2.0000$

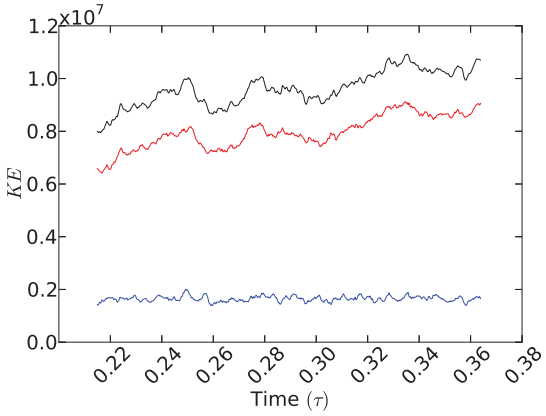

(e) $Ra^* = 686.3 Ra_c^* = 3.0000$

Figure 5.1: Kinetic energy time series data for $N_\rho = 10^{-2}$ at $\eta_{nb} = 0.80$ for $E = 10^{-4}$. The black line represents the total kinetic energy $KE = KE_\zeta + KE_\gamma$ where KE_ζ is the toroidal component of the kinetic energy and KE_γ is the poloidal component. Note that KE_ζ is represented by the red line and KE_γ is represented by the blue line.

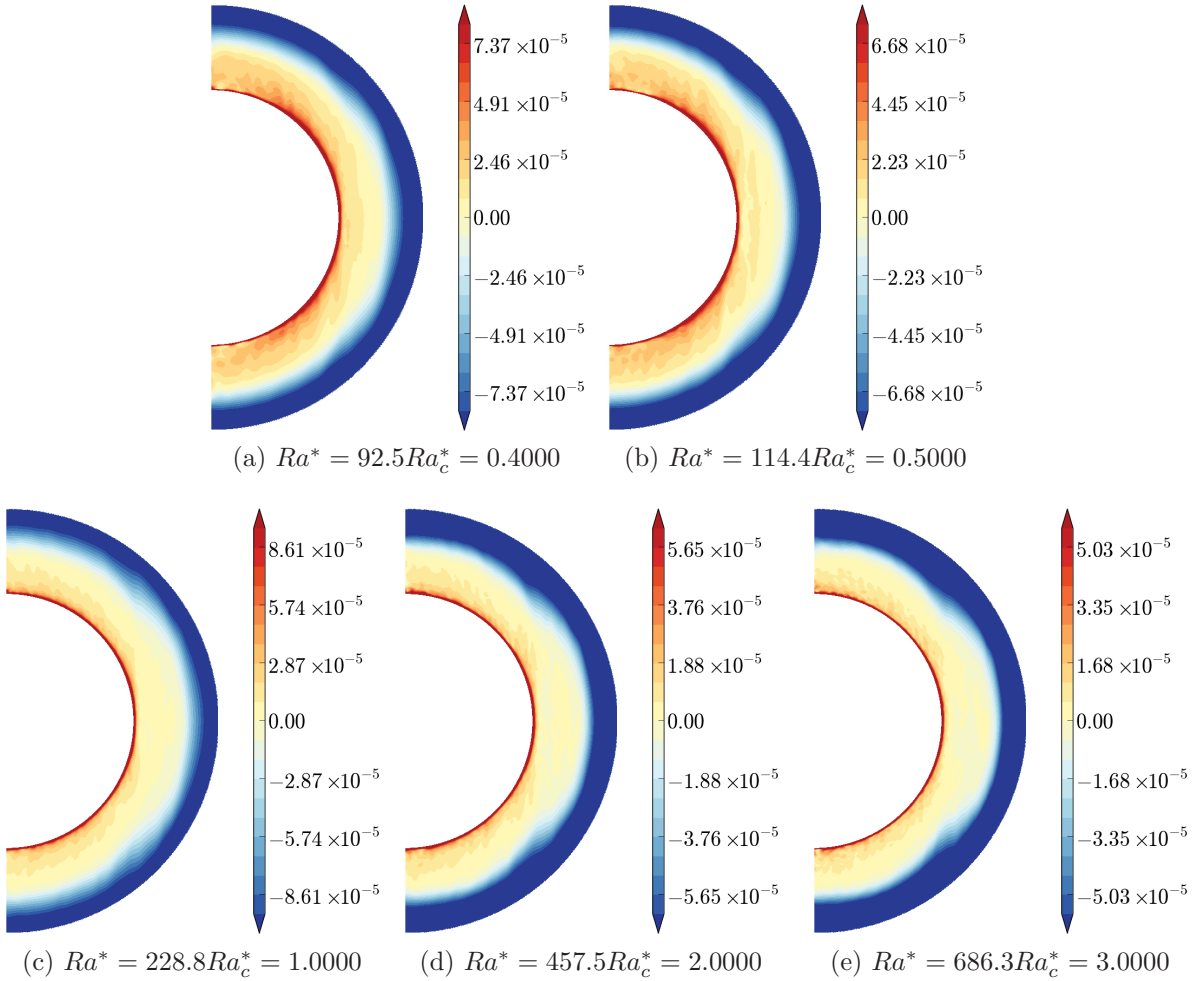

(a) $Ra^* = 92.5Ra_c^* = 0.4000$ (b) $Ra^* = 114.4Ra_c^* = 0.5000$

(c) $Ra^* = 228.8Ra_c^* = 1.0000$ (d) $Ra^* = 457.5Ra_c^* = 2.0000$ (e) $Ra^* = 686.3Ra_c^* = 3.0000$

Figure 5.2: The azimuthally averaged radial entropy gradient $(\partial s/\partial r)$ profile of the rotating spherical shell with $N_\rho = 10^{-2}$ at $\eta_{nb} = 0.80$ for $E = 10^{-4}$.

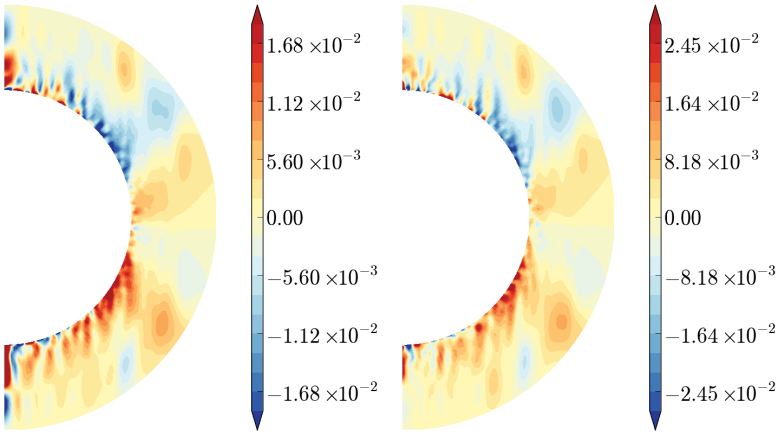

(a) $Ra^* = 92.5Ra_c^* = 0.4000$ (b) $Ra^* = 114.4Ra_c^* = 0.5000$

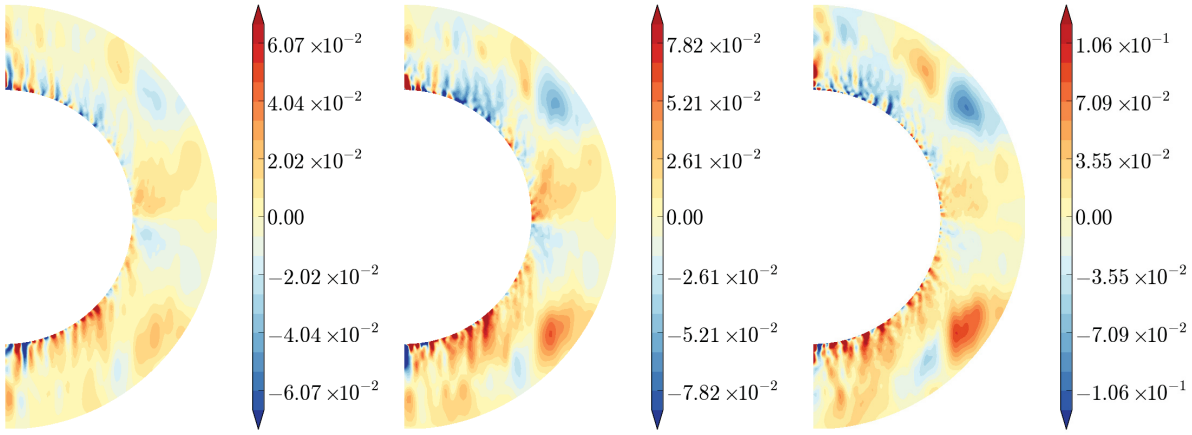

(c) $Ra^* = 228.8Ra_c^* = 1.0000$ (d) $Ra^* = 457.5Ra_c^* = 2.0000$ (e) $Ra^* = 686.3Ra_c^* = 3.0000$

Figure 5.3: The azimuthally averaged $\partial u_\phi/\partial z$ profile of the rotating spherical shell with $N_\rho = 10^{-2}$ at $\eta_{nb} = 0.80$ for $E = 10^{-4}$.

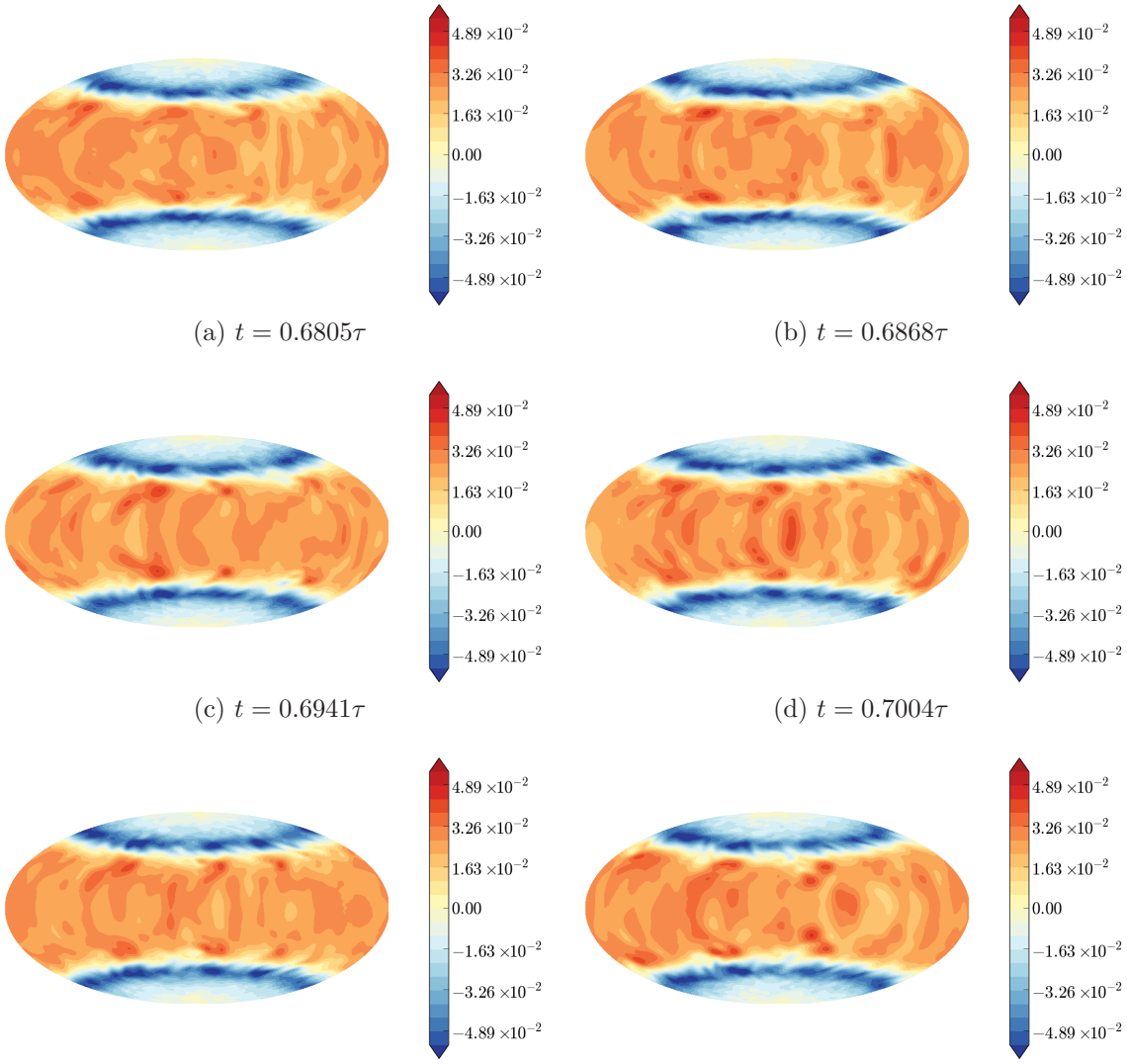

(a) $t = 0.6805\tau$ (b) $t = 0.6868\tau$

(c) $t = 0.6941\tau$ (d) $t = 0.7004\tau$

(e) $t = 0.7070\tau$ (f) $t = 0.7113\tau$

Figure 5.4: A series of images between $t = 0.6805\tau$ and $t = 0.7113\tau$ for time t representing the zonal velocity at the outer boundary of $N_\rho = 10^{-2}$, $\eta_{nb} = 0.80$, $E = 10^{-4}$, and $Ra^* = 0.4000$ model. These images shows the progression of the eddies indicated by a pair of maximum and minimum areas near the tangent cylinder with $u_\phi > 0$ representing the prograde flow.

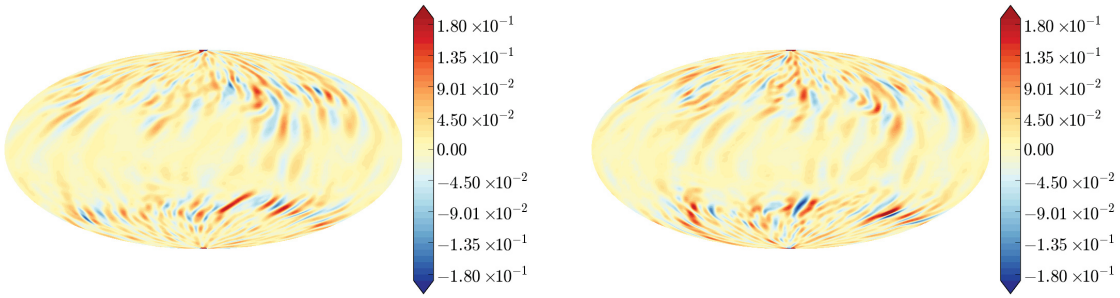

(a) $t = 0.6805\tau$ (b) $t = 0.6868\tau$

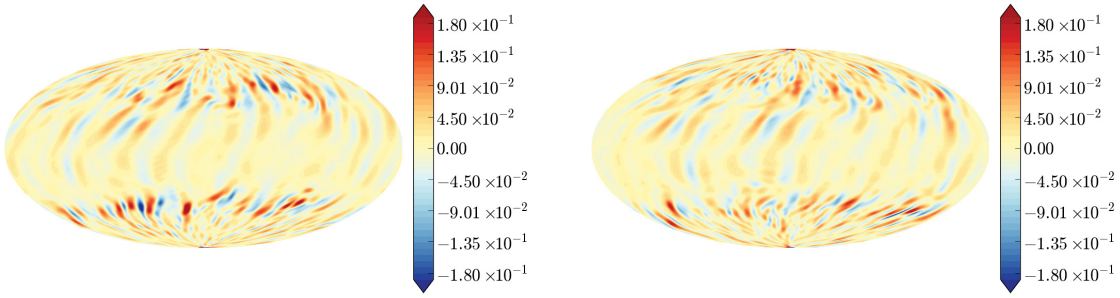

(c) $t = 0.6941\tau$ (d) $t = 0.7004\tau$

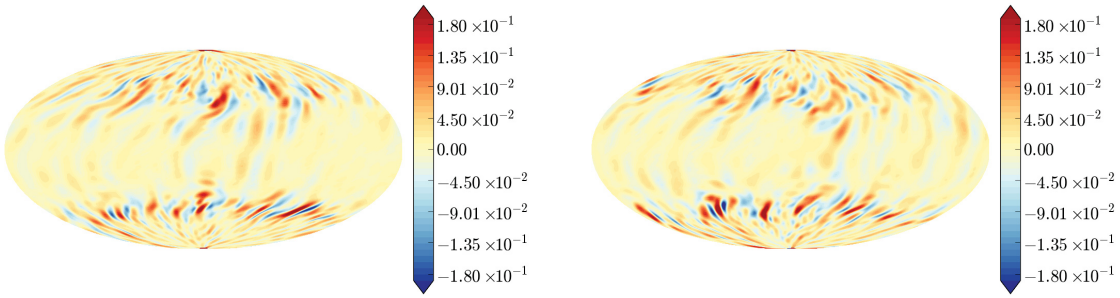

(e) $t = 0.7070\tau$ (f) $t = 0.7113\tau$

Figure 5.5: A series of images representing the radial vorticity of the fluid flow at the outer boundary of $N_\rho = 10^{-2}$, $\eta_{nb} = 0.80$, $E = 10^{-4}$ and $Ra^* = 0.4000$ model. These images shows the progression of the eddies indicated by a pair of maximum and minimum areas near the tangent cylinder.

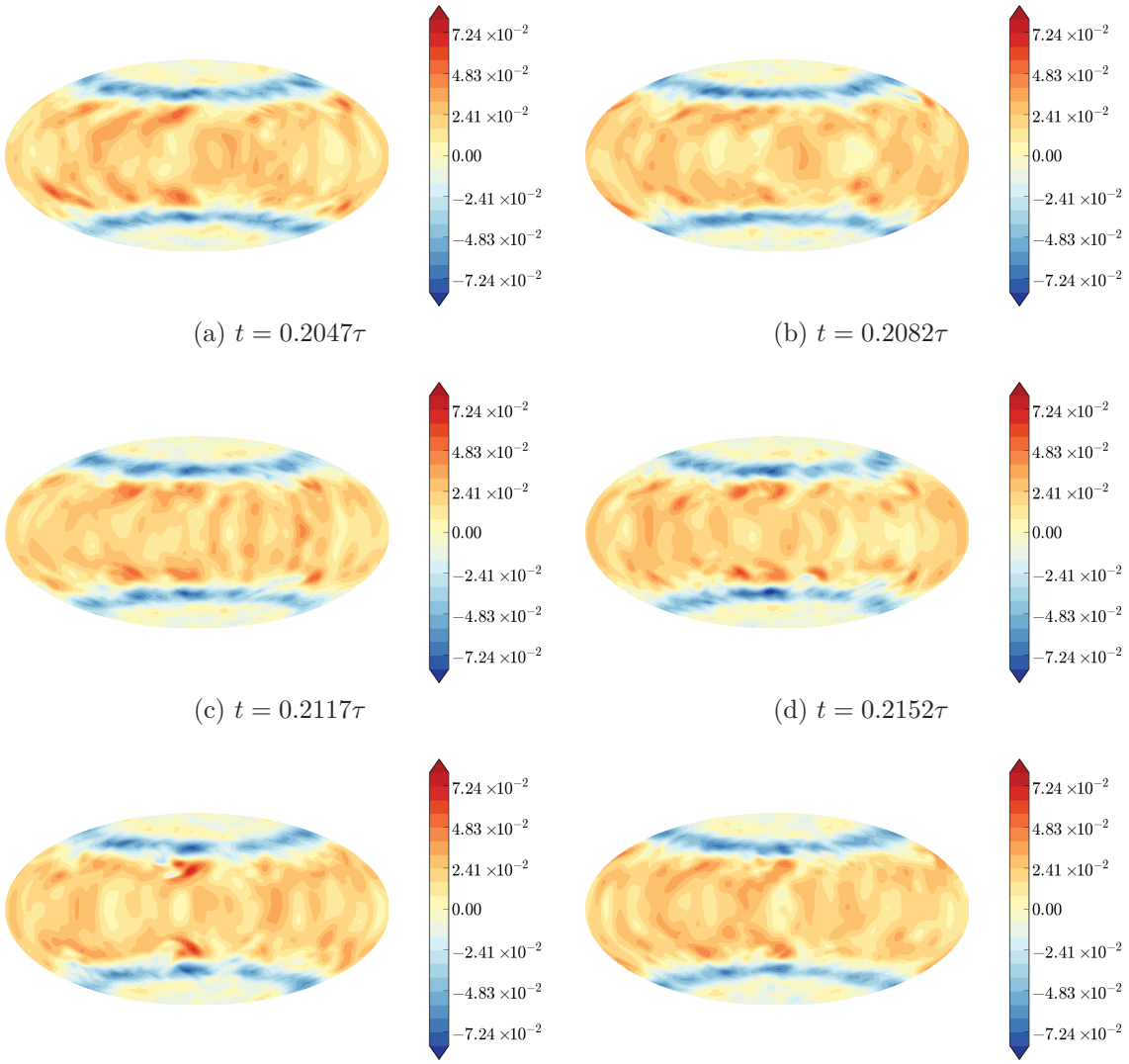

(a) $t = 0.2047\tau$ (b) $t = 0.2082\tau$

(c) $t = 0.2117\tau$ (d) $t = 0.2152\tau$

(e) $t = 0.2187\tau$ (f) $t = 0.2223\tau$

Figure 5.6: A series of images between $t = 0.2047\tau$ and $t = 0.2223\tau$ for time t representing the zonal velocity at the outer boundary of $N_\rho = 10^{-2}$, $\eta_{nb} = 0.80$, $E = 10^{-4}$, and $Ra^* = 1.0000$ model. These images shows the progression of the eddies indicated by a pair of maximum and minimum areas near the tangent cylinder with $u_\phi > 0$ representing the prograde flow. Two eddies can be seen merging at (c) to (e).

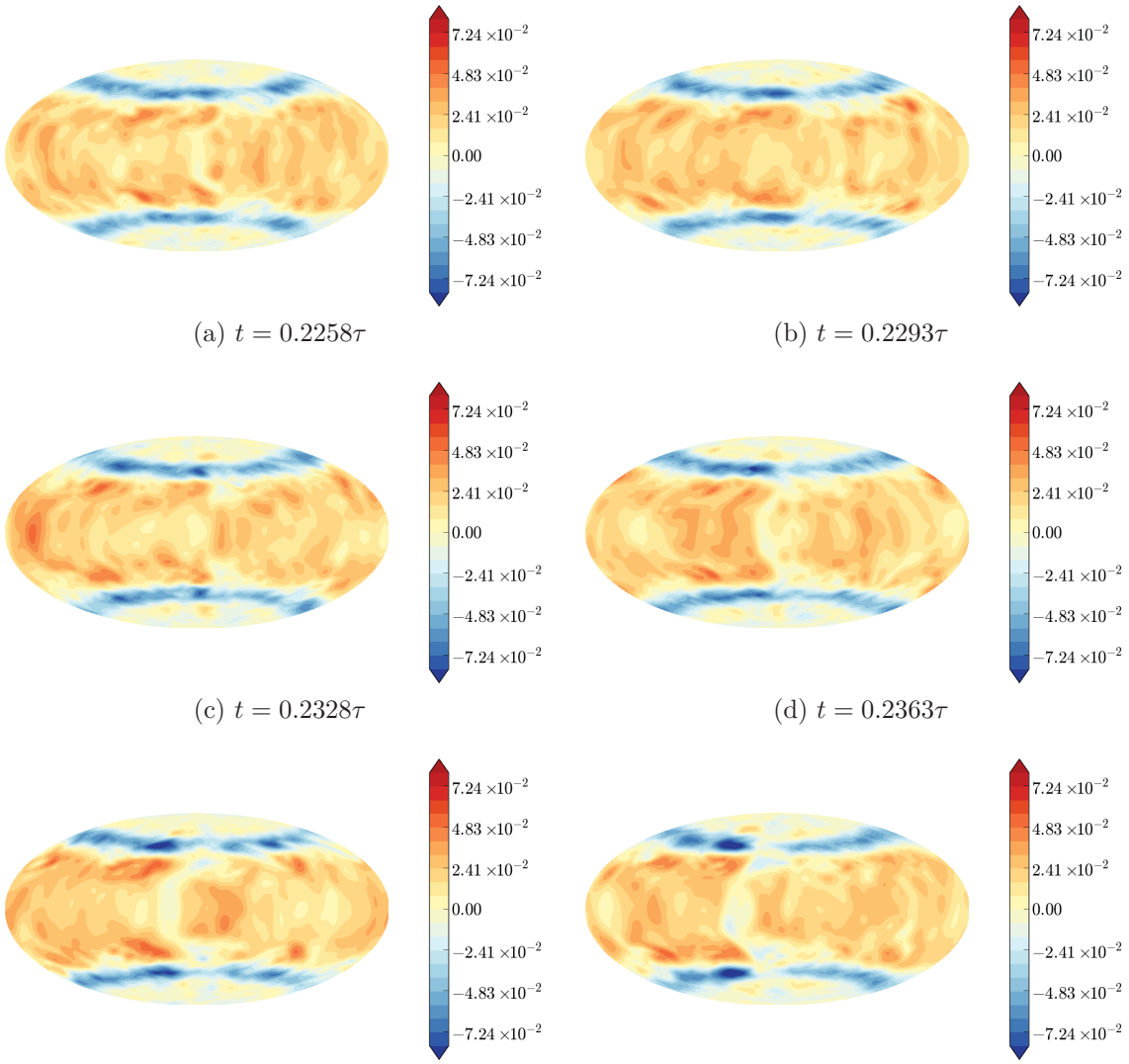

(a) $t = 0.2258\tau$ (b) $t = 0.2293\tau$

(c) $t = 0.2328\tau$ (d) $t = 0.2363\tau$

(e) $t = 0.2398\tau$ (f) $t = 0.2433\tau$

Figure 5.7: A series of images between $t = 0.6805\tau$ and $t = 0.7113\tau$ for time t representing the zonal velocity at the outer boundary of $N_\rho = 10^{-2}$, $\eta_{nb} = 0.80$, $E = 10^{-4}$, and $Ra^* = 1.0000$ model. These images show the formation of the great storm via merging of eddies indicated by a pair of maximum and minimum areas near the tangent cylinder with $u_\phi > 0$ representing the prograde flow.

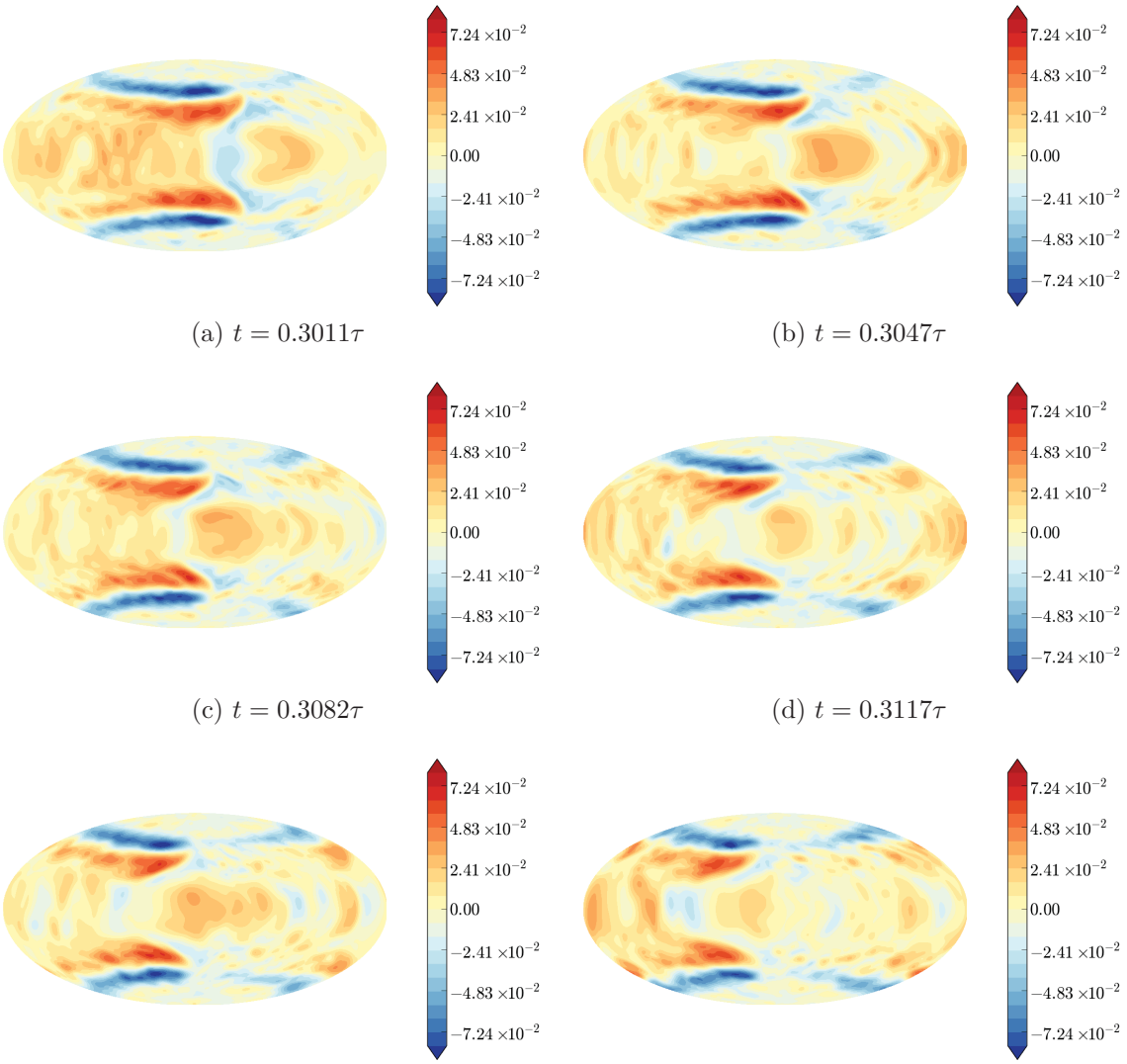

(a) $t = 0.3011\tau$ (b) $t = 0.3047\tau$

(c) $t = 0.3082\tau$ (d) $t = 0.3117\tau$

(e) $t = 0.3152\tau$ (f) $t = 0.3187\tau$

Figure 5.8: A series of images between $t = 0.6805\tau$ and $t = 0.7113\tau$ for time t representing the zonal velocity at the outer boundary of $N_\rho = 10^{-2}$, $\eta_{nb} = 0.80$, $E = 10^{-4}$, and $Ra^* = 1.0000$ model. These images shows the progression of the great eddies indicated by a pair of maximum and minimum areas near the tangent cylinder with $u_\phi > 0$ representing the prograde flow. Each storm exhibits a trailing feature.

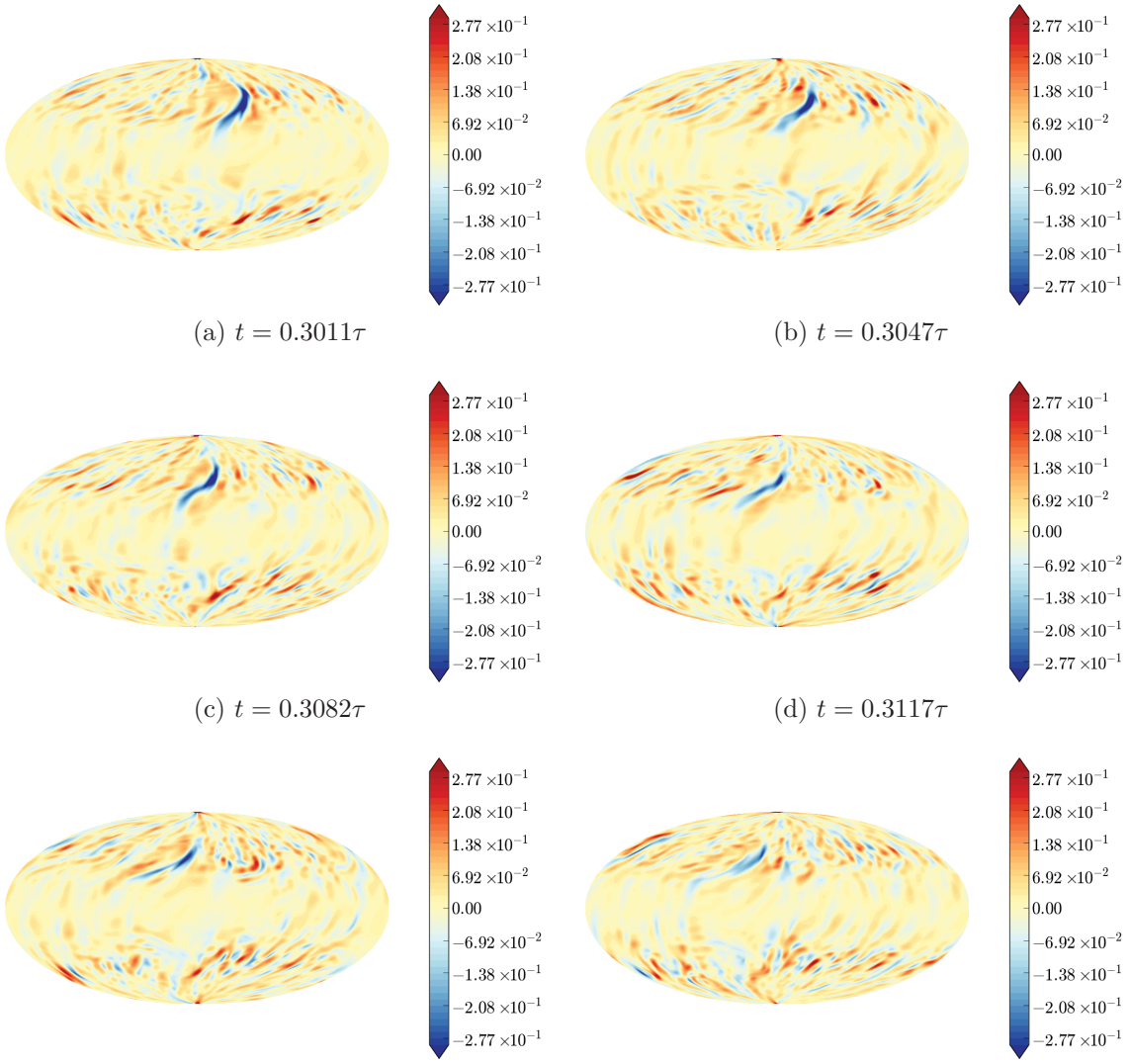

(a) $t = 0.3011\tau$ (b) $t = 0.3047\tau$

(c) $t = 0.3082\tau$ (d) $t = 0.3117\tau$

(e) $t = 0.3152\tau$ (f) $t = 0.3187\tau$

Figure 5.9: A series of images between $t = 0.6805\tau$ and $t = 0.7113\tau$ for time t representing the radial vorticity at the outer boundary of $N_\rho = 10^{-2}$, $\eta_{nb} = 0.80$, $E = 10^{-4}$, and $Ra^* = 1.0000$ model. The great eddies are indicated by the minimum area in the Northern hemisphere followed by the maximum area in the Southern hemisphere within the same line of longitude.

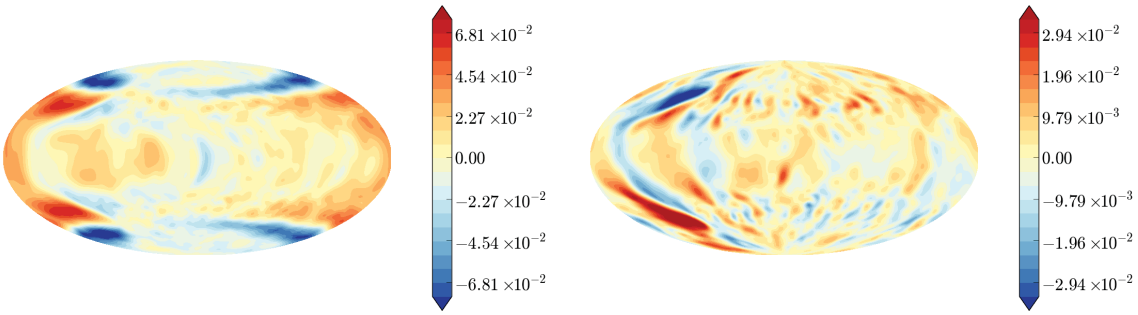

(a) u_ϕ at $r = r_o$ (b) u_θ at $r = r_o$

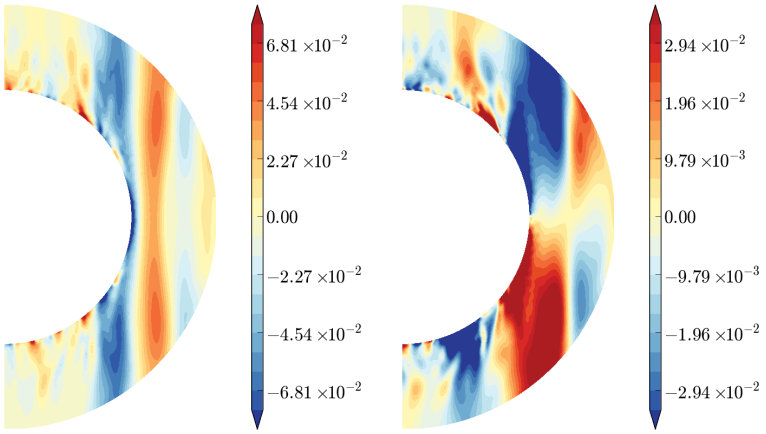

(c) u_ϕ at centre of $\min(u_\theta)$ (d) u_θ at centre of $\min(u_\theta)$

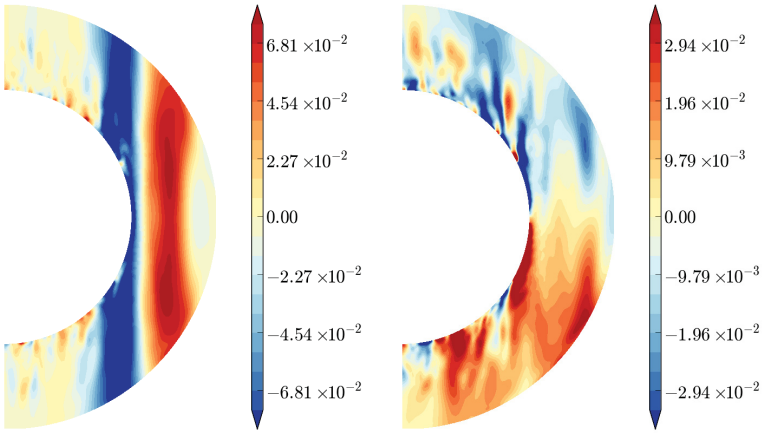

(e) u_ϕ at centre of $\min(u_\phi)$ (f) u_θ at centre of $\min(u_\phi)$

Figure 5.10: The azimuthal slices of u_ϕ and u_θ of the $N_\rho = 10^{-2}$, $\eta_{nb} = 0.80$, $E = 10^{-4}$, and $Ra^* = 1.0000$ model centred at the Northern great storm's $\min(u_\theta)$ and $\min(u_\phi)$ based on (a) and (b). Note that $u_\theta > 0$ implies that the fluid flows in the Northern direction. Note that (a) and (b) show u_ϕ and u_θ at $r = r_o$ at $t = 0.2231\tau$.

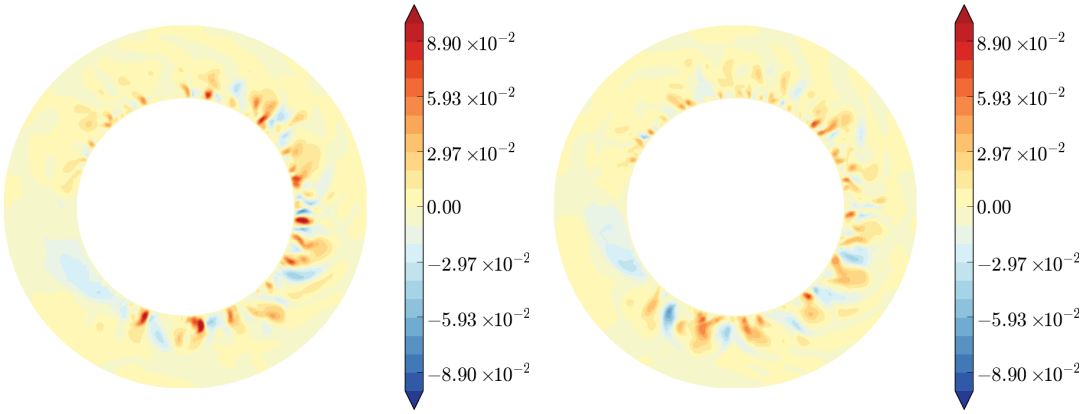

(a) $t = 0.3011\tau$ (b) $t = 0.3047\tau$

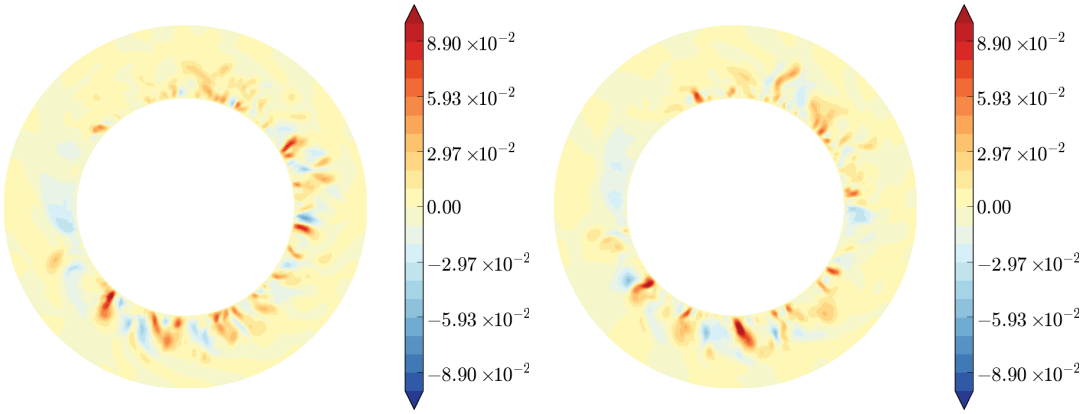

(c) $t = 0.3082\tau$ (d) $t = 0.3117\tau$

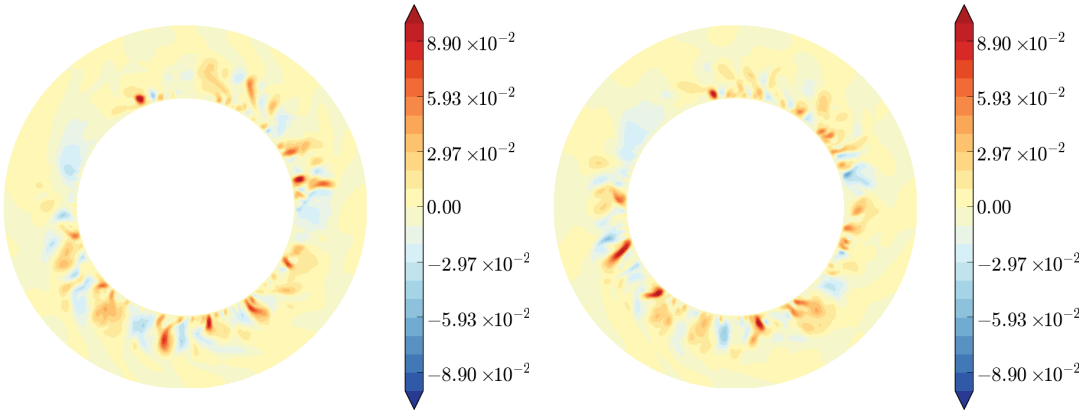

(e) $t = 0.3152\tau$ (f) $t = 0.3187\tau$

Figure 5.11: A series of images between $t = 0.6805\tau$ and $t = 0.7113\tau$ for time t representing the equatorial slice of the radial velocity u_r of $N_\rho = 10^{-2}$, $\eta_{nb} = 0.80$, $E = 10^{-4}$, and $Ra^* = 1.0000$ model. The great eddies are indicated by the global minimum area in the Northern hemisphere followed by the global maximum area in the Southern hemisphere within the same line of longitude. Note that $u_r > 0$ implies the fluid flows towards $r = r_o$.

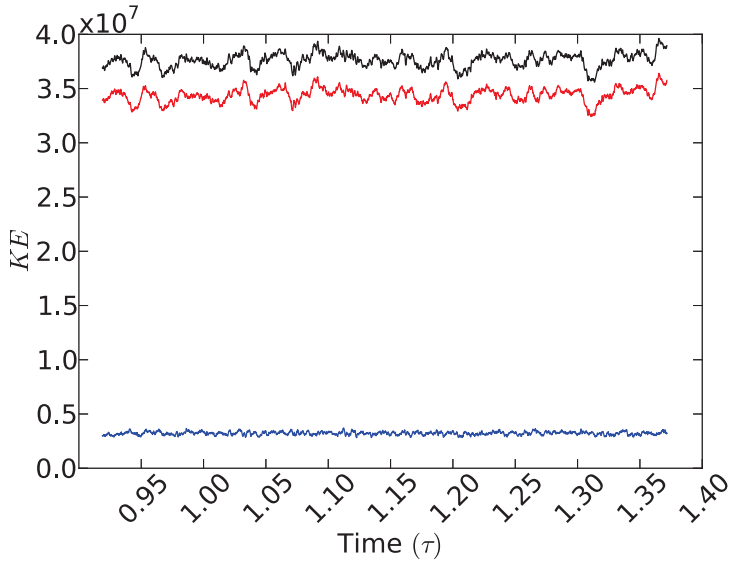

(a) KE Time Series

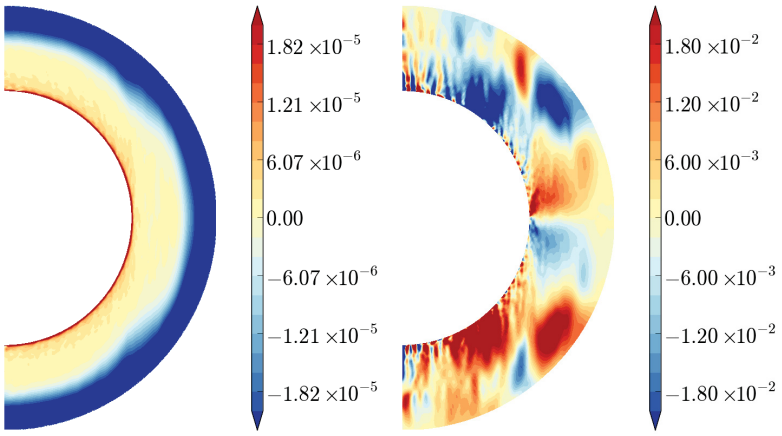

(b) $\partial s/\partial r$ (c) $\partial u_\phi/\partial z$

Figure 5.12: Time series data of $N_\rho = 10^{-2}$, $\eta_{nb} = 0.80$, $E = 3.0 \cdot 10^{-5}$, and $Ra^* = 1.0000$ model represented by (a). The black line represents the total kinetic energy $KE = KE_\zeta + KE_\gamma$ where KE_ζ (Red Line) is the toroidal component of the kinetic energy and KE_γ (Blue Line) is the poloidal component. Azimuthal slice of the axisymmetric $\partial s/\partial r$ profile is represented by (b). The azimuthally averaged $\partial u_\phi/\partial z$ profile is represented by (c).

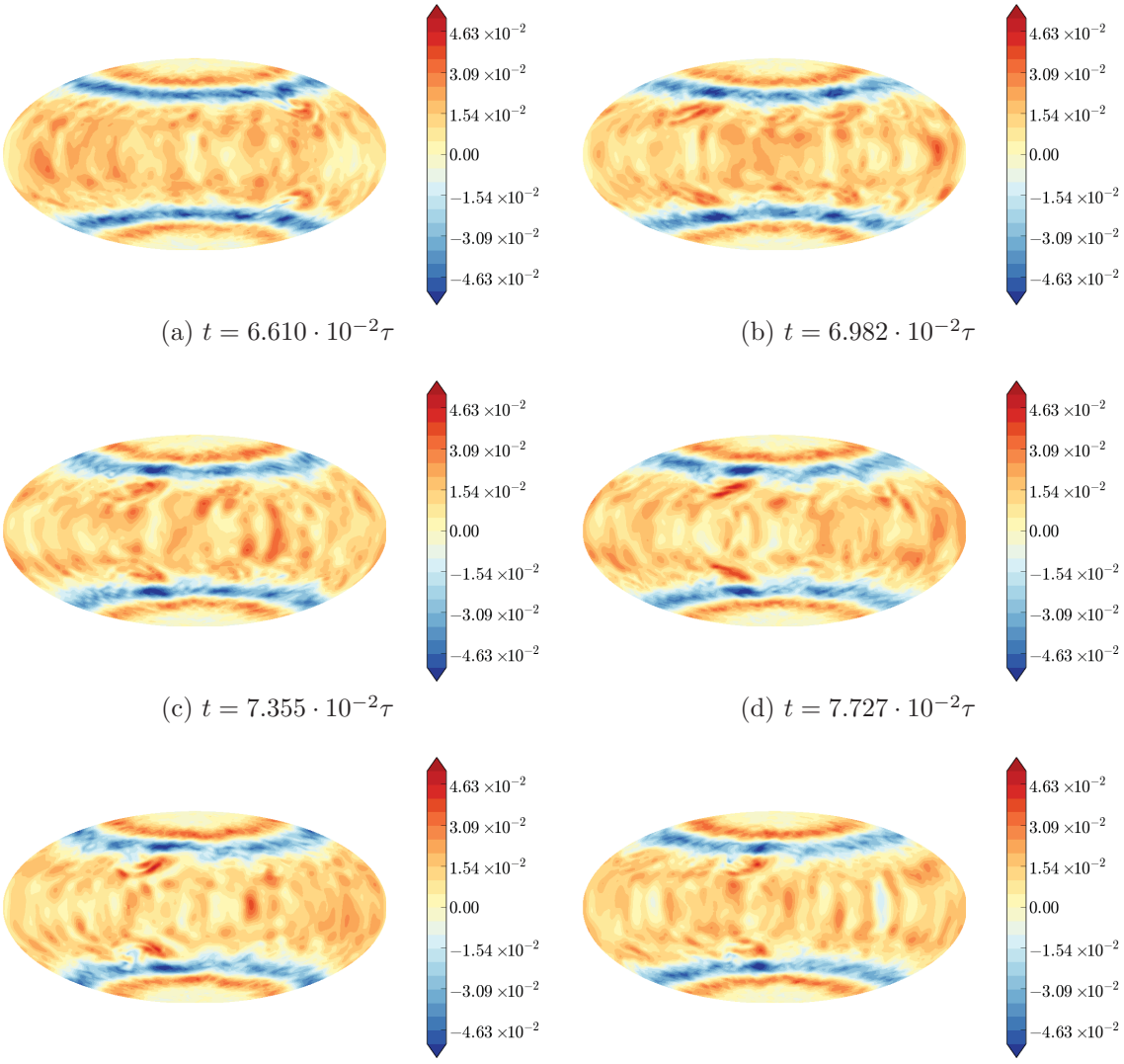

(a) $t = 6.610 \cdot 10^{-2}\tau$ (b) $t = 6.982 \cdot 10^{-2}\tau$

(c) $t = 7.355 \cdot 10^{-2}\tau$ (d) $t = 7.727 \cdot 10^{-2}\tau$

(e) $t = 8.100 \cdot 10^{-2}\tau$ (f) $t = 8.473 \cdot 10^{-2}\tau$

Figure 5.13: A series of images between $t = 6.518 \cdot 10^{-2}\tau$ and $t = 8.379 \cdot 10^{-2}\tau$ for time t representing the zonal velocity at the outer boundary of $N_\rho = 10^{-2}$, $\eta_{nb} = 0.80$, $E = 3.0{\cdot}10^{-5}$, and $Ra^* = 1.0000$ model. These images shows the progression of the eddies indicated by a pair of maximum and minimum areas near the tangent cylinder with $u_\phi > 0$ representing the prograde flow. Eddies start forming at (a) to (b) and then two eddies can be seen merging at (c) to (e).

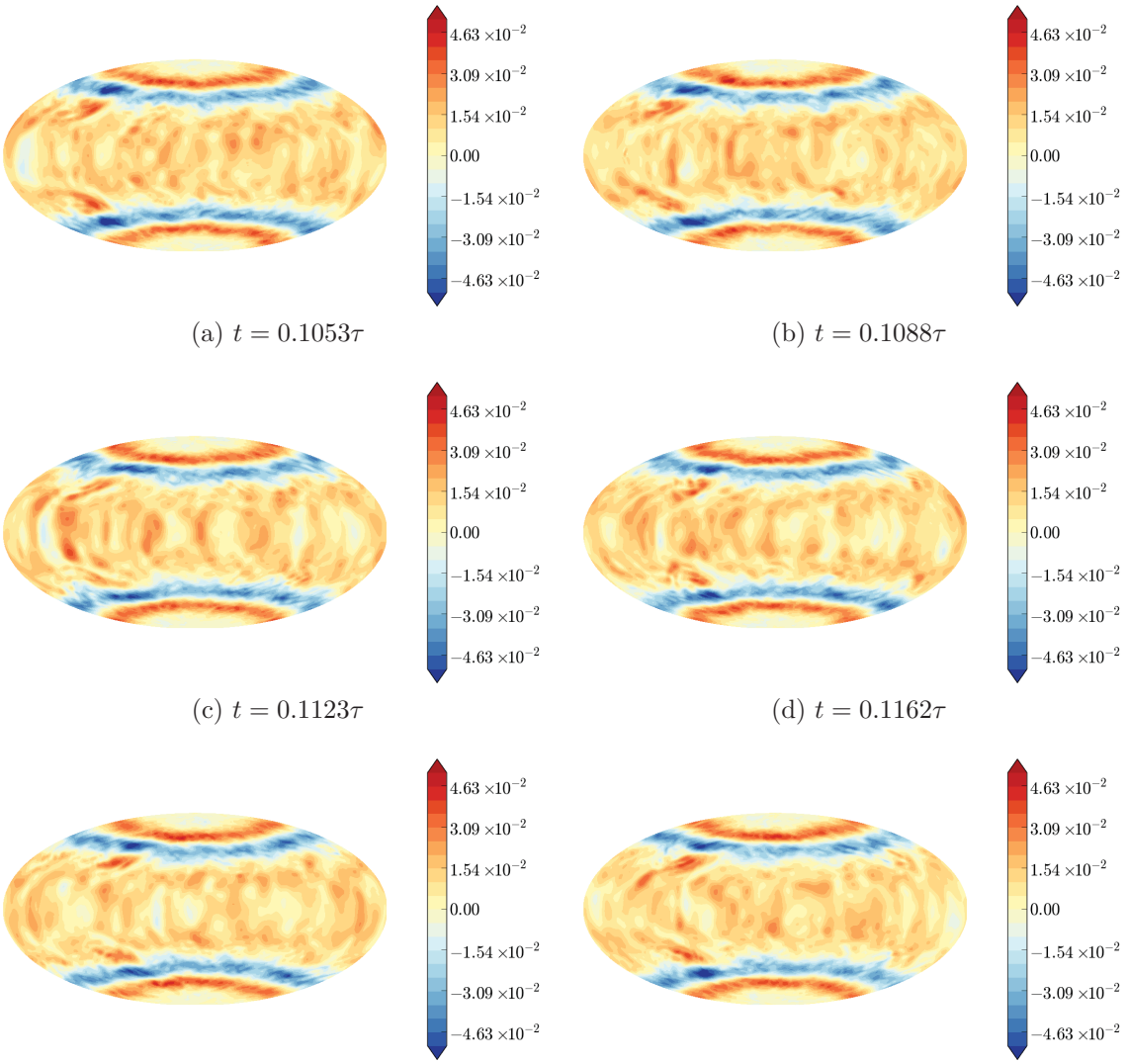

(a) $t = 0.1053\tau$ (b) $t = 0.1088\tau$

(c) $t = 0.1123\tau$ (d) $t = 0.1162\tau$

(e) $t = 0.1196\tau$ (f) $t = 0.1228\tau$

Figure 5.14: A series of images between $t = 0.1053\tau$ and $t = 0.1228\tau$ for time t representing the zonal velocity at the outer boundary of $N_\rho = 10^{-2}$, $\eta_{nb} = 0.80$, $E = 3.0 \cdot 10^{-5}$, and $Ra^* = 1.0000$ model. These images show the formation of a strong long-lived eddies via merging of eddies indicated by a pair of maximum and minimum areas near the tangent cylinder with $u_\phi > 0$ representing the prograde flow.

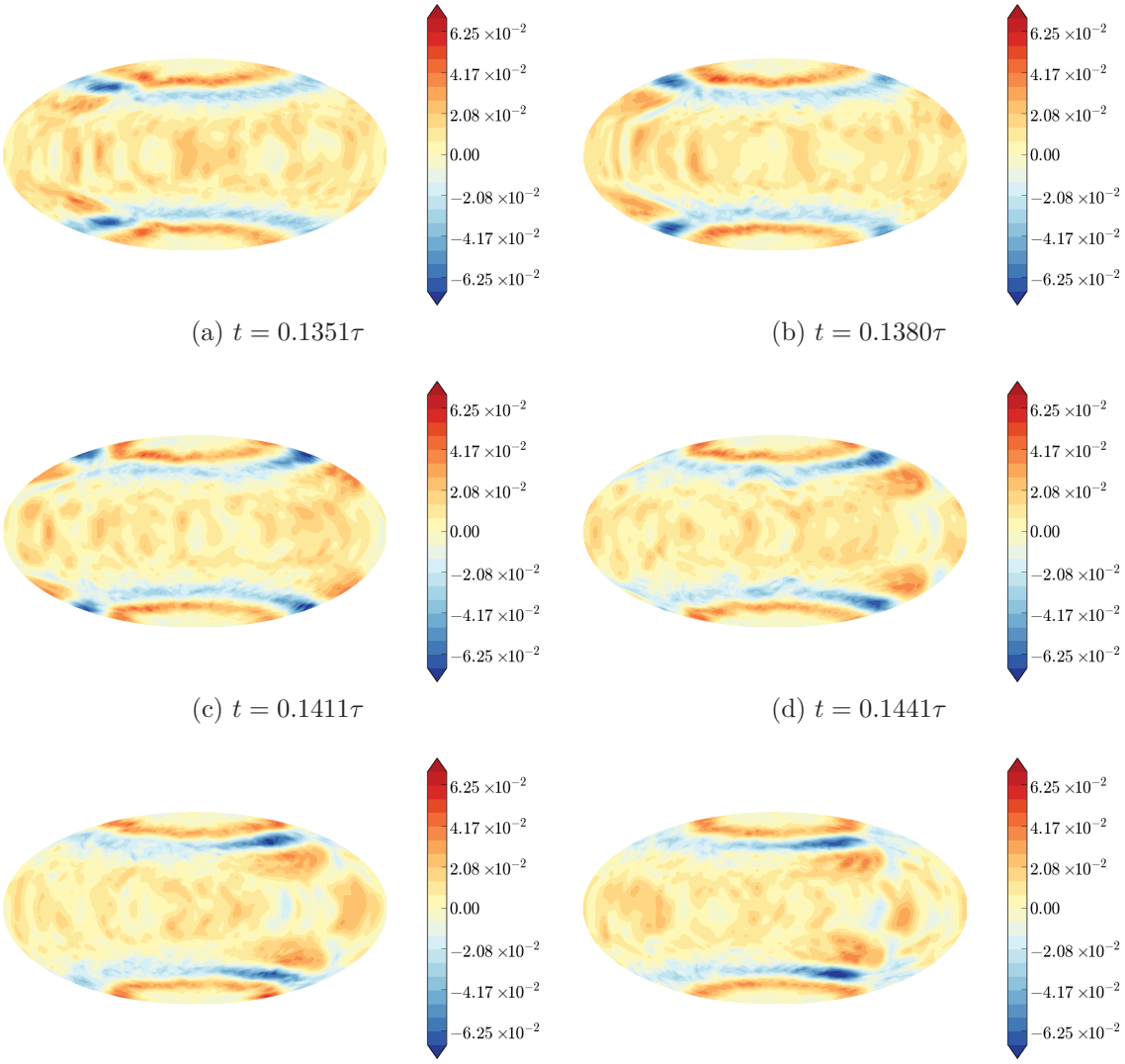

(a) $t = 0.1351\tau$ (b) $t = 0.1380\tau$

(c) $t = 0.1411\tau$ (d) $t = 0.1441\tau$

(e) $t = 0.1472\tau$ (f) $t = 0.1504\tau$

Figure 5.15: A series of images between $t = 0.1351\tau$and $t = 0.1504\tau$ for time t representing the zonal velocity at the outer boundary of $N_\rho = 10^{-2}$, $\eta_{nb} = 0.80$, $E = 3.0 \cdot 10^{-5}$, and $Ra^* = 1.0000$ model. These images shows the formation of the great eddies via strong retrograde and prograde jets feeding energy into the strong long-lived eddies.

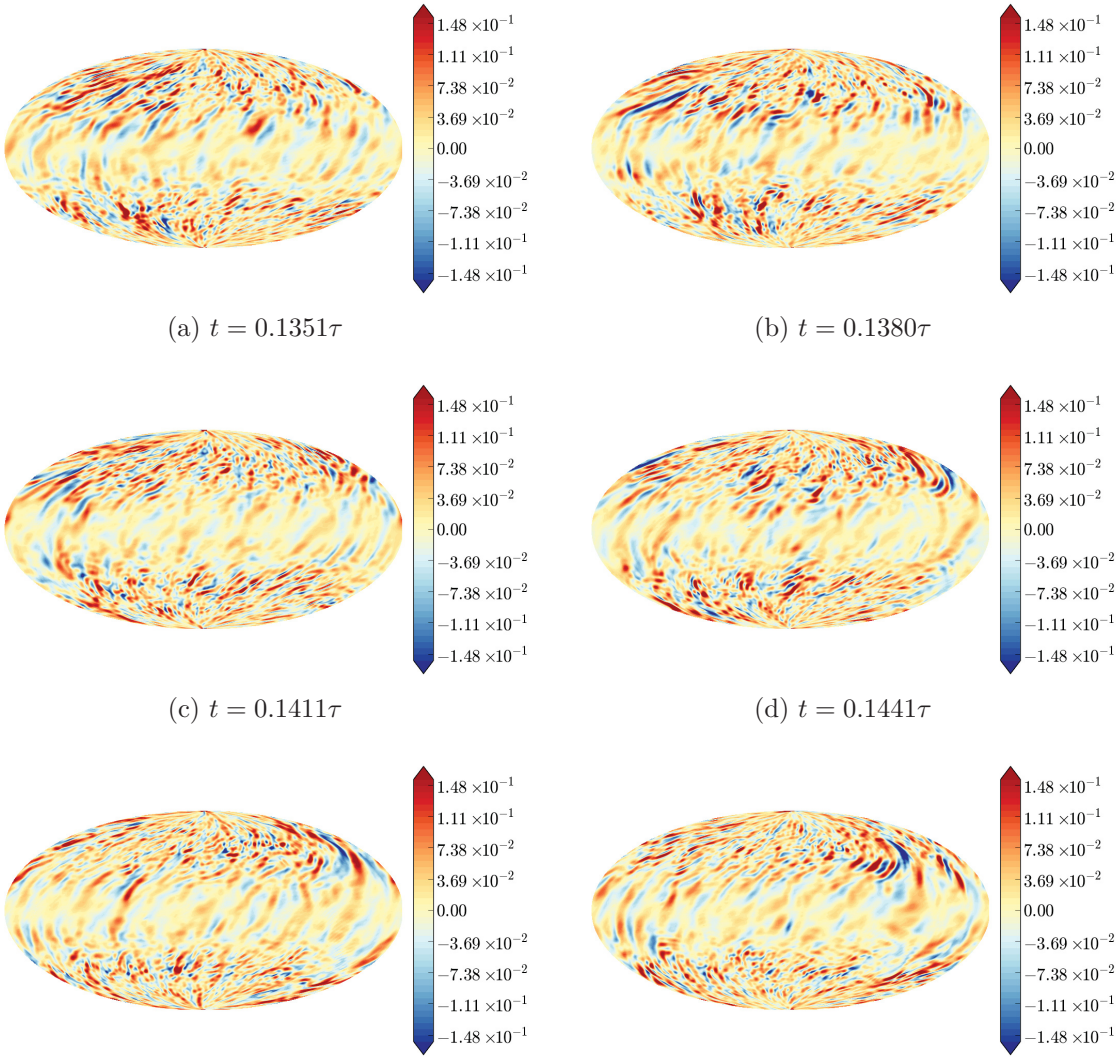

(a) $t = 0.1351\tau$ (b) $t = 0.1380\tau$

(c) $t = 0.1411\tau$ (d) $t = 0.1441\tau$

(e) $t = 0.1472\tau$ (f) $t = 0.1504\tau$

Figure 5.16: A series of images between $t = 0.1351\tau$ and $t = 0.1504\tau$ for time t representing the radial vorticity at the outer boundary of $N_\rho = 10^{-2}$, $\eta_{nb} = 0.80$, $E = 3.0 \cdot 10^{-5}$, and $Ra^* = 1.0000$ model.

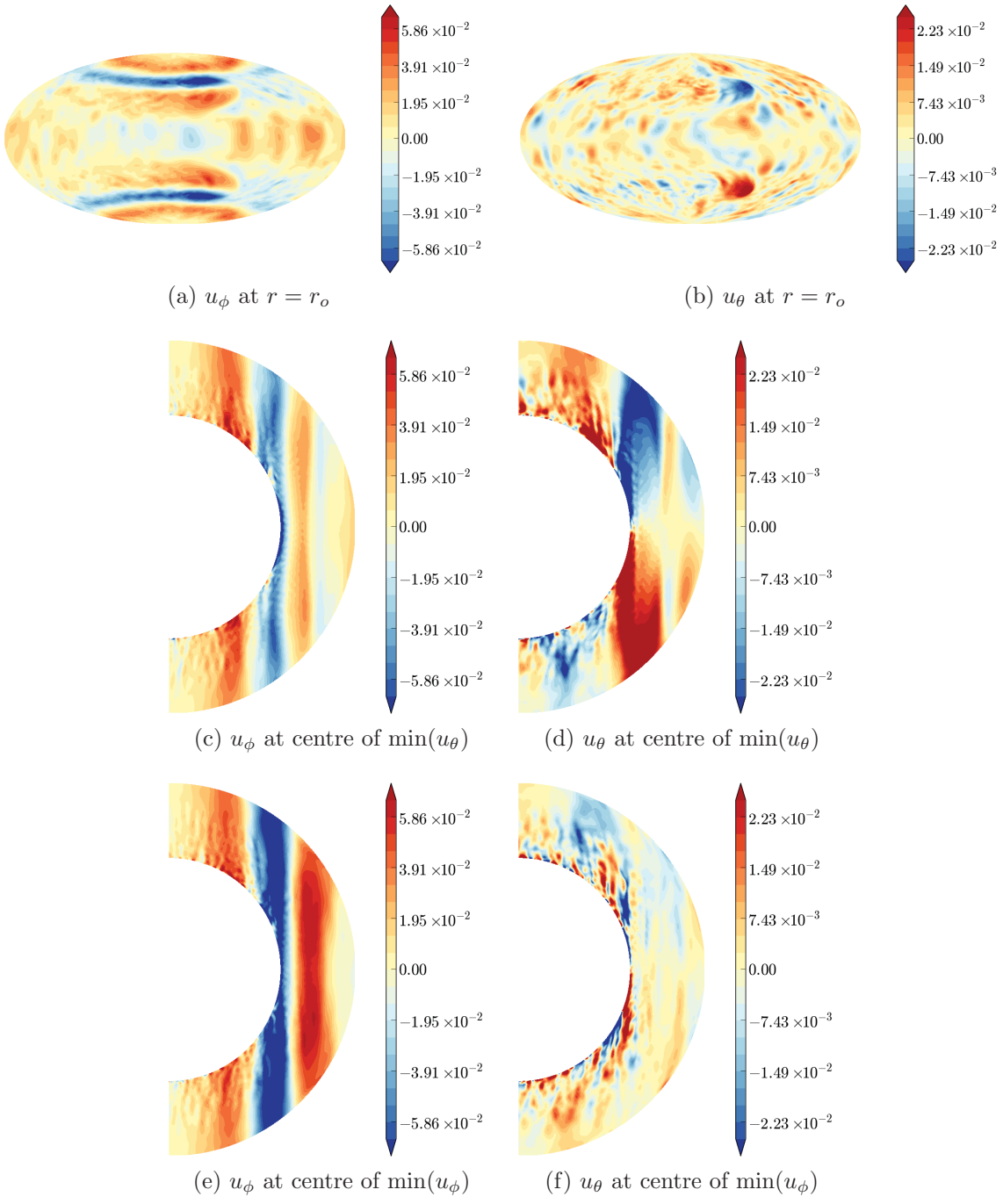

(a) u_ϕ at $r = r_o$

(b) u_θ at $r = r_o$

(c) u_ϕ at centre of $\min(u_\theta)$

(d) u_θ at centre of $\min(u_\theta)$

(e) u_ϕ at centre of $\min(u_\phi)$

(f) u_θ at centre of $\min(u_\phi)$

Figure 5.17: The azimuthal slices of u_ϕ and u_θ of the $N_\rho = 10^{-2}$, $\eta_{nb} = 0.80$, $E = 10^{-4}$, and $Ra^* = 1.0000$ model centred at the Northern great storm's $\min(u_\theta)$ and $\min(u_\phi)$ based on (a) and (b). Note that $u_\theta > 0$ implies that the fluid flows in the Northern direction. Note that (a) and (b) show u_ϕ and u_θ at $r = r_o$ at $t = 0.3569\tau$.

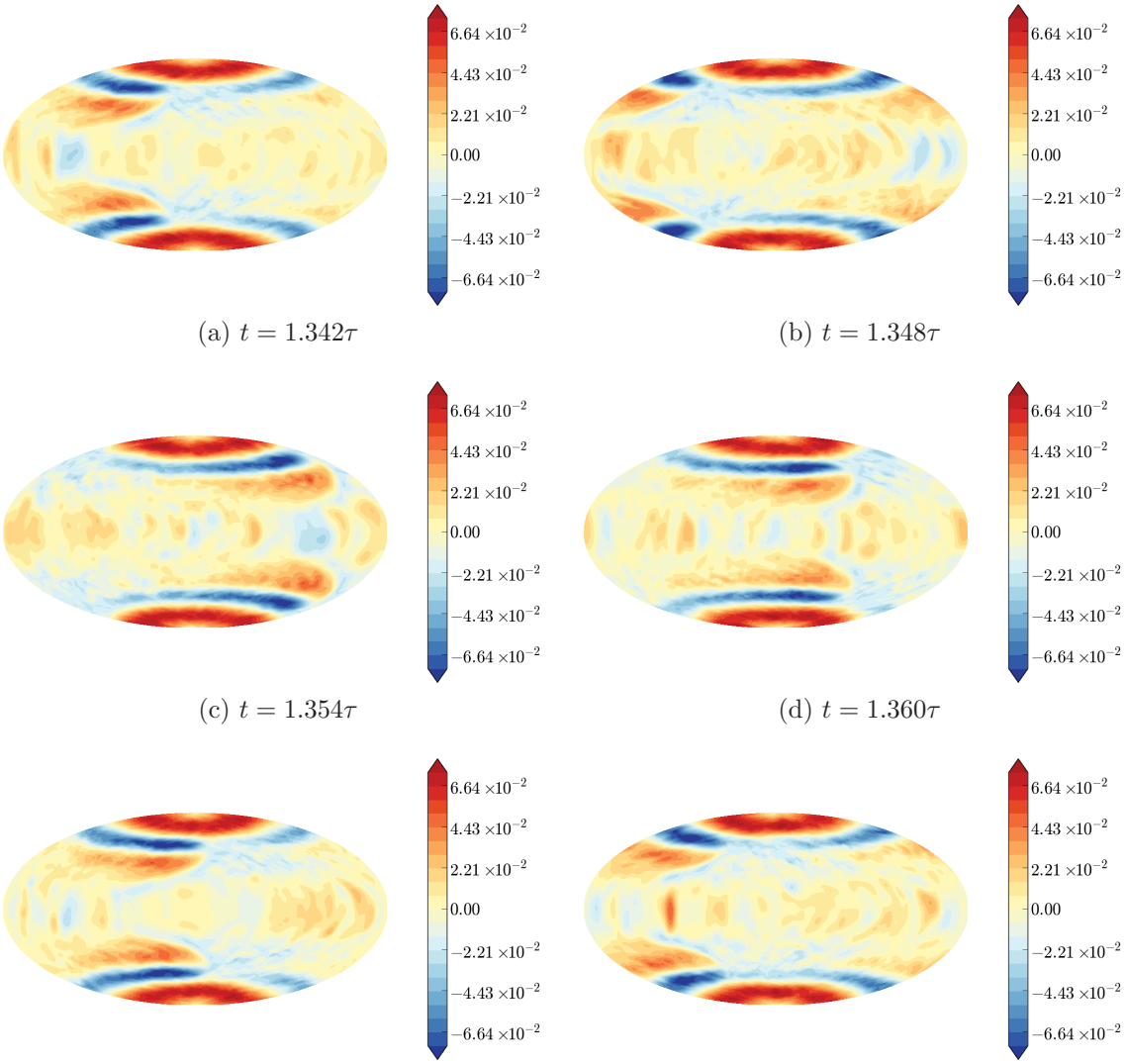

(a) $t = 1.342\tau$ (b) $t = 1.348\tau$

(c) $t = 1.354\tau$ (d) $t = 1.360\tau$

(e) $t = 1.365\tau$ (f) $t = 1.371\tau$

Figure 5.18: A series of images between $t = 1.342\tau$ and $t = 1.371\tau$ for time t representing the zonal velocity at the outer boundary of $N_\rho = 10^{-2}$, $\eta_{nb} = 0.80$, $E = 3.0 \cdot 10^{-5}$, and $Ra^* = 1.0000$ model.

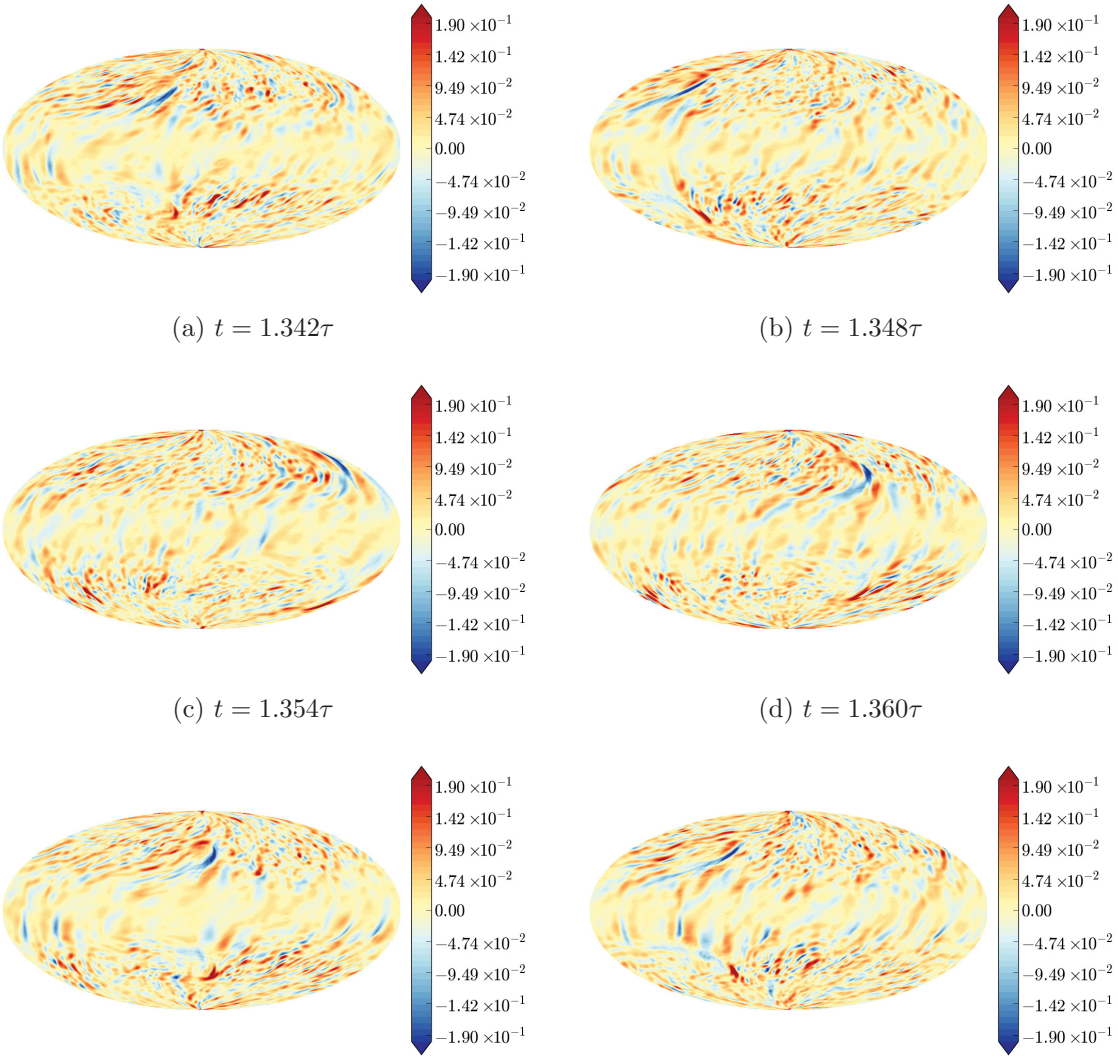

(a) $t = 1.342\tau$ (b) $t = 1.348\tau$

(c) $t = 1.354\tau$ (d) $t = 1.360\tau$

(e) $t = 1.365\tau$ (f) $t = 1.371\tau$

Figure 5.19: A series of images between $t = 1.342\tau$ and $t = 1.371\tau$ for time t representing the radial vorticity at the outer boundary of $N_\rho = 10^{-2}$, $\eta_{nb} = 0.80$, $E = 3.0 \cdot 10^{-5}$, and $Ra^* = 1.0000$ model.

Chapter 6

Conclusions

For the majority of this thesis, we focus on modelling the fluid dynamics of rotating anelastic spherical shells with convection, which is based on previous studies that have generated zonal jets with properties equivalent to Jovian zonal jets (e.g., Cuff, 2016; Gastine & Wicht, 2012). Measurements from the Galileo space probe imply that Jupiter has a stably stratified fluid layer between roughly 0 and 9 bars (Magalhaes et al., 2002). This layer could have an effect on the fluid dynamics of a rotating convective anelastic spherical shell. Thus, we use the constant conductive radial entropy gradient boundary conditions to include a stably stratified fluid layer near the outer boundary. Parameters such as the number of density scale heights (or density stratification denoted as N_ρ), the stably stratified fluid layer thickness, and the modified Rayleigh number Ra^* are varied to understand the interaction between convection and the stably stratified fluid layer

In chapter three, we simulate the fluid dynamics of polar regional models on a rapidly rotating Boussinesq spherical shell with convection. Regional modelling should provide more emphasis on the fluid dynamics at the selected area of the spherical shell. Due to the presence of polar singularities associated with using the spherical coordinate system, the cubed-sphere curvilinear grid coordinate system is used instead, where it projects a sphere onto a cube with a local cartesian coordinate system on each face. However, using conventional horizontal periodic boundary conditions would unlikely provide realistic results of the model. Thus, two different horizontal open boundary conditions (sponge and Orlanski) were implemented onto the rotating convective regional model. The end result is that all models output either unrealistic results or experience numerical problems. This is likely due to the strong fluid motion associated with a rotating convective system. Future models that want to focus on the polar region of rotating convection spherical shell models must either adjust the sponge or Orlanski conditions, or use different open boundary conditions to account for the strong

fluid motion associated with rotating convection.

One noticeable effect that the stably stratified fluid layer has on the fluid dynamics of the rotating anelastic spherical shell models with convection is that it has a tendency to suppress zonal flow oscillations. Based on the kinetic energy time series data for each model, we can deduce that a model can reach one of five regimes. For increasing Ra^*, they are the linear, quasi-periodic, first chaotic, relaxation oscillation, and second chaotic states. The zonal flow oscillations can be observed with models in the relaxation oscillation state. Based on our results, the models that reach this state typically have a high density stratification such that $N_\rho \geq 1$. As the stably stratified fluid layer thickness increases, the amplitude of these oscillations decreases until they are fully suppressed. Examples of this behaviour can be seen in the kinetic energy time series data for $N_\rho = 1$, 3, and 5 models. Models that exhibit full suppression of the zonal flow oscillations (i.e. high stratification models that remain in the first chaotic state) can be seen with $N_\rho = 1$ and $\eta_{nb} = 0.94$, 0.90, and 0.80, and $N_\rho = 3$ with $\eta_{nb} = 0.80$.

Another noticeable effect is that the stably stratified fluid layer has a tendency to restrict the fluid flow to two dimensions. This can be seen by a comparison between the $\eta_{nb} = 1.00$ models and the $\eta_{nb} = 0.80$ models for $N_\rho = 1$ and 3. As η_{nb} decreases, the rough retrograde jets observed on η_{nb} models become smoother.

However, we also noticed that the stability in the stably stratified fluid layer increases as Ra^* increases. This can be inferred from the $N_\rho = 5$ models with $\eta_{nb} = 0.80$. These models with $7.5 \leq Ra^*/Ra_c^* \leq 22.5$ exhibit the relaxation oscillation regime, where Ra_c^* represents the critical Rayleigh number or the minimum Ra^* needed for force the model into a convective state. For $Ra^*/Ra_c^* > 22.5$, these models exhibit the second chaotic state. This implies that as Ra^* increases, the stability in the stably stratified fluid layer also increases. This can also be inferred from the azimuthally averaged radial entropy gradient ($\partial s/\partial r$) profiles of each model. From these profiles, as Ra^* increases, the stability throughout the shell increases, which is denoted as a decrease in $\partial s/\partial r$. This could imply that for any $\eta_{nb} \neq 1.00$ models that exhibit the relaxation oscillation regime, the model could be forced into the second chaotic state for a large enough Ra^*.

For a set of rotating convective near-Boussinesq ($N_\rho = 10^{-2}$) spherical shell models with half of the shell from the outer boundary set as the stably stratified fluid layer ($\eta_{nb} = 0.80$), they exhibit long-lived and great eddies near the tangent cylinder. The generation of long-lived eddies requires a sufficiently large thermal forcing of at least $Ra^* = 0.4000$. For each long-lived eddy at the Northern hemisphere, there would be a long-lived eddy at the Southern hemisphere, which is centred at the same longitude as its Northern counterpart. Further increasing the thermal forcing to $Ra^* = 1.0000$ leads to the merging of these long-lived

eddies, leading to the formation of great eddies, which are seen near the tangent cylinder at both hemispheres. Based on the azimuthal slices of the zonal velocity centred near the great eddies, they show that the fluid motion is in columnar form, implying that the great eddies are driven by convection. The characteristics of these eddies are somewhat similar to the Great Red Spot observed in Jupiter such that they both have the same westward drift direction, same anticyclonic nature, and similar latitudinal locations associated with the tangent cylinder. This could also explain how the Great Red Spot is formed and how it is driven.

To further investigate the effects of the stably stratified fluid layer, another parameter study could be done by varying the Ekman number. By lowering the Ekman number, high latitudinal jets could be formed. This can be seen for the $N_\rho = 10^{-2}$ model with $\eta_{nb} = 0.80$, $Ra^* = 1.0000$, and $E = 3 \cdot 10^{-5}$, where the typical value of $E = 10^{-4}$ is used for the other models. Decreasing the Ekman number could also lead to the generation of long-lived eddies for $N_\rho \geq 1$ models. This can be inferred from the Richardson number, which indicates that decreasing the Ekman number could lead to shear dominant flow, possibly resulting in the generation of eddies.

Bibliography

Adcroft, A., Campin, J. M., Hill, C., & Marshall, J. (2004). Implementation of an atmosphere-ocean general circulation model on the expanded spherical cube. *Monthly Weather Review*, *132*(12), 2845-2863. doi: 10.1175/MWR2823.1

Adcroft, A., Hill, C., & Marshall, J. (1997). Representation of topography by shaved cells in a height coordinate ocean model. *American Meteorological Society*, *125*(9), 2293-2315. doi: 10.1175/1520-0493(1997)125⟨2293:ROTBSC⟩2.0.CO;2

Anderson, J. D., Laing, P. A., Lau, E. L., Liu, A. S., Nieto, M. M., & Turyshev, S. G. (2002). Study of the anomalous acceleration of pioneer 10 and 11. *Physical Review D*, *65*(8), 082004/1-50. doi: 10.1103/PhysRevD.65.082004

Atkinson, D. H., Pollack, J. B., & Seiff, A. (1998). The galileo probe doppler wind experiment: Measurement of the deep zonal winds on jupiter. *Journal of Geophysical Research: Planets*, *103*(E10), 22911–22928. doi: 10.1029/98JE00060

Breuer, M., Manglik, A., Wicht, J., Trümper, T., Harder, H., & Hansen, U. (2010). Thermochemically driven convection in a rotating spherical shell. *Geophysical Journal International*, *183*(1), 150-162. doi: 10.1111/j.1365-246X.2010.04722.x

Busse, F. H. (1976). A simple model of convection in the jovian atmosphere. *Icarus*, *29*(2), 255-260. doi: 10.1016/0019-1035(76)90053-1

Camerlengo, A. L., & O'Brien, J. J. (1980). Open boundary conditions in rotating fluids. *Journal of Computational Physics*, *35*(1), 12-35. doi: 10.1016/0021-9991(80)90031-5

Carnevale, G. F., McWilliams, J. C., Pomeau, Y., Weiss, J. B., & Young, W. R. (1991, May). Evolution of vortex statistics in two-dimensional turbulence. *Phys. Rev. Lett.*, *66*(21), 2735–2737. doi: 10.1103/PhysRevLett.66.2735

Chandrasekhar, S. (1981). *Hydrodynamic and hydromagnetic stability*. New York, NY: Dover Publications.

Christensen, U., Olson, P., & Glatzmaier, G. A. (1999). Numerical modelling of the geodynamo: a systematic parameter study. *Geophysical Journal International*, *138*(2), 393-409. doi: 10.1046/j.1365-246X.1999.00886.x

Christensen, U. R., Aubert, J., Cardin, P., Gibbons, E. D. S., Glatzmaier, G. A., Grote,

E., ... Zhang, K. (2001). A numerical dynamo benchmark. *Physics of the Earth and Planetary Interiors*, *128*(1-4), 25-34. doi: 10.1016/S0031-9201(01)00275-8

Cuff, K. (2016). *Simulations of rotating anelastic convection: Entropy boundary conditions* (Master's Thesis). University of Alberta.

D'Amario, L. A., Bright, L. E., & Wolf, A. A. (1992, 01). Galileo trajectory design. *Space Science Reviews*, *60*(1), 23–78. doi: 10.1007/BF00216849

Dowling, T. E., Fischer, A. S., Gierasch, P., Harrington, J., R. P., L., Jr., & Santora, C. M. (1998). The explicit planetary isentropic-coordinate (epic) atmospheric model. *Icarus*, *132*(2), 221-238. doi: 10.1006/icar.1998.5917

Fischer, D. (2001). *Mission jupiter: The spectacular journey of the galileo spacecraft.* New York, NY: Copernicus Books.

French, M., Becker, A., Lorenzen, W., Nettelmann, N., Bethkenhagen, M., Wicht, J., & Redmer, R. (2012). Ab initio simulations for material properties along the jupiter adiabat. *The Astrophysical Journal Supplement Series*, *202*(1), 1-11. doi: 10.1088/0067-0049/202/1/5

Gallacher, P. C., Hebert, D. A., & Schaferkotter, M. R. (2011). Nesting a nonhydrostatic model in a hydrostatic model: The boundary interface. *Ocean Modelling*, *40*(2), 190-198. doi: 10.1016/j.ocemod.2011.08.006

Garcia-Melendo, E., Perez-Hoyos, S., Sanchez-Lavega, A., & Hueso, R. (2011). Saturn's zonal wind profile in 2004-2009 from cassini iss images and its long-term variability. *Icarus*, *215*(1), 62-74. doi: 10.1016/j.icarus.2011.07.005

Gastine, T., Heimpel, M., & Wicht, J. (2014). Zonal flow scaling in rapidly-rotating compressible convection. *Physics of the Earth and Planetary Interiors*, *232*, 36-50. doi: 10.1016/j.pepi.2014.03.011

Gastine, T., & Wicht, J. (2012). Effects of compressibility on driving zonal flow in gas giants. *Icarus*, *219*(1), 428-442. doi: 10.1016/j.icarus.2012.03.018

Gastine, T., Wicht, J., Duarte, L. D. V., Heimpel, M., & Becker, A. (2014). Explaining jupiter's magnetic field and equatorial jet dynamics. *Geophysical Research Letters*, *41*(15), 5410–5419. doi: 10.1002/2014GL060814

GFDL. (2016). *Fv3: Finite-volume cubed-sphere dynamical core.* Retrieved from `https://www.gfdl.noaa.gov/fv3/fv3-grids/`

Glatzmaier, G. A. (1984). Numerical simulations of stellar convective dynamos. i. the model and method. *Journal of Computational Physics*, *55*(3), 461-484. doi: 10.1016/0021-9991(84)90033-0

Glatzmaier, G. A. (2014). *Introduction to modelling convection in planets and stars: Magnetic field, density stratification, rotation.* Princeton, NJ: Princeton University Press.

Glatzmaier, G. A., & Roberts, P. H. (1995). A three-dimensional convective dynamo solution with rotating and finitely conducting inner core and mantle. *Physics of the Earth and Planetary Interiors*, *91*(1-3), 63-75. doi: 10.1016/0031-9201(95)03049-3

Gopalakrishnan, G., Cornuelle, B. D., Hoteit, I., Rudnick, D. L., & Owens, W. B. (2013). State estimates and forecasts of the loop current in the gulf of mexico using the mitgcm and its adjoint. *Journal of Geophysical Research: Oceans*, *118*(7), 3292-3314. doi: 10.1002/jgrc.20240

Griffies, S. M., & Hallberg, R. W. (2000). Biharmonic friction with a smagorinsky-like viscosity for use in large-scale eddy-permitting ocean models. *Monthly Weather Review*, *128*(8), 2935-2946. doi: 10.1175/1520-0493(2000)128⟨2935:BFWASL⟩2.0.CO;2

Griffiths, D. J. (1999). *Introduction to electrodynamics* (3rd ed.). Upper Saddle River, NJ: Prentice Hall.

Griffiths, D. J. (2005). *Introduction to quantum mechanics* (2nd ed.). Upper Saddle River, NJ: Prentice Hall.

Guillot, T. (1999). Interiors of giant planets inside and outside the solar system. *Science*, *286*(5437), 72-77. doi: 10.1126/science.286.5437.72

Heimbach, P., Hill, C., & Giering, R. (2002). Automatic generation of efficient adjoint code for a parallel navier-stokes solver. In P. M. A. Sloot, A. G. Hoekstra, C. J. K. Tan, & J. J. Dongarra (Eds.), *Computational science — iccs 2002: International conference amsterdam, the netherlands, april 21–24, 2002 proceedings, part ii* (p. 1019-1028). Berlin, Heidelberg: Springer Berlin Heidelberg. doi: 10.1007/3-540-46080-2_107

Heimpel, M., Aurnou, J., & Wicht, J. (2005). Simulation of equatorial and high-latitude jets on jupiter in a deep convection model. *Nature*, *438*(7065), 193-196. Retrieved from `http://login.ezproxy.library.ualberta.ca/login?url=https://search.proquest.com/docview/204569583?accountid=14474`

Heimpel, M., Gastine, T., & Wicht, J. (2016). Simulations of deep-seated zonal jets and shallow vortices in gas giant atmospheres. *Nature Geoscience*, *9*(1), 19-24. doi: 10.1038/ngeo2601

Held, I. M., & Suarez, M. J. (1994). A proposal for the intercomparison of the dynamical cores of atmospheric general circulation models. *Bulletin of the American Meteorological Society*, *75*(10), 1825-1830. doi: 10.1175/1520-0477(1994)075⟨1825:APFTIO⟩2.0.CO;2

Hide, R. (1961). Origin of jupiter's great red spot. *Nature*, *190*(4779), 895-896. doi: 10.1038/190895a0

Hide, R. (1968). Jupiter's great red spot. *Scientific American*, *218*(2), 74-83. doi: 10.1038/scientificamerican0268-74

Hill, C., Adcroft, A., Jamous, D., & Marshall, J. (1999). A strategy for terascale climate modeling. In W. Walter & N. Kreitz (Eds.), *Towards teracomputing : proceedings of the eighth ecmwf workshop on the use of parallel processors in meteorology, reading, uk, november 16-20, 1998* (p. 406-425). River Edge, New Jersey: World Scientific.

Hill, C., & Marshall, J. (1996). Application of a parallel navier-stokes model to ocean circulation. In A. Ecer (Ed.), *Parallel computational fluid dynamics: Implementations and results using parallel computers : Proceedings of the parallel cfd '95 conference, pasadena, ca, u.s.a., 26-29 june, 1995* (p. 545-552). Amsterdam, New York: Elsevier.

Irwin, P. G. J., Weir, A. L., Taylor, S. B. F. W., Calcutt, S. B., & Carlson, R. W. (2001). The origin of belt/zone contrasts in the atmosphere of jupiter and their correlation with 5-μm opacity. *Icarus*, *149*(2), 397-415. doi: 10.1006/icar.2000.6542

Jones, C. A., Boronski, P., Brun, A. S., Glatzmaier, G. A., Gastine, T., Miesch, M. S., & Wicht, J. (2011). Anelastic convection-driven dynamo benchmarks. *Icarus*, *216*(1), 120-135. doi: 10.1016/j.icarus.2011.08.014

Jones, C. A., & Kuzanyan, K. M. (2009). Compressible convection in the deep atmospheres of giant planets. *Icarus*, *204*(1), 227-238. doi: 10.1016/j.icarus.2009.05.022

Kataria, T., Sing, D. K., Lewis, N. K., Visscher, C., Showman, A. P., Fortney, J. J., ... Marley, M. S. (2016). The atmospheric circulation of a nine-hot-jupiter sample: Probing circulation and chemistry over a wide phase space. *The Astrophysical Journal*, *821*(1), 1–16. doi: 10.3847/0004-637X/821/1/9

Kwok, R., Hunke, E. C., Maslowski, W., Menemenlis, D., & Zhang, J. (2008). Variability of sea ice simulations assessed with rgps kinematics. *Journal of Geophysical Research: Oceans*, *113*(C11), 1–20. (C11012) doi: 10.1029/2008JC004783

Liu, J., Goldreich, P. M., & Stevenson, D. J. (2008). Constraints on deep-seated zonal winds inside jupiter and saturn. *Icarus*, *196*(2), 653-664. doi: 10.1016/j.icarus.2007.11.036

Magalhaes, J. A., Seiff, A., & Young, R. E. (2002). The stratification of jupiter's troposphere at the galileo probe entry site. *Icarus*, *158*(2), 410-433. doi: 10.1006/icar.2002.6891

Marshall, J., Adcroft, A., Hill, C., Perelman, L., & Heisey, C. (1997). A finite-volume, incompressible navier stokes model for studies of the ocean on parallel computers. *Journal of Geophysical Research*, *102*(C3), 5753-5766. doi: 10.1029/96JC02775

Marshall, J., Hill, C., Perelman, L., & Adcroft, A. (1997). Hydrostatic, quasi-hydrostatic, and nonhydrostatic ocean modeling. *Journal of Geophysical Research*, *102*(C3), 5733-5752. doi: 10.1029/96JC02776

Morales-Juberias, R., & Dowling, T. E. (2013). Jupiter's great red spot: Fine-scale matches of model vorticity patterns to prevailing cloud patterns. *Icarus*, *225*(1), 216-227. doi: 10.1016/j.icarus.2013.03.026

Nair, R. D., Thomas, S. J., & Loft, R. D. (2005). A discontinuous galerkin transport scheme on the cubed sphere. *Monthly Weather Review*, *133*(4), 814-828. doi: 10.1175/MWR2890.1

NASA. (2009). *Jupiter globe.* Retrieved from `https://solarsystem.nasa.gov/galleries/jupiter-globe`

NASA. (2016a). *Over saturn's turbulent north.* Retrieved from `https://saturn.jpl.nasa.gov/resources/7565/?category=images`

NASA. (2016b). *Pia11214: Saturn's south polar region revealed.* Retrieved from `https://photojournal.jpl.nasa.gov/catalog/PIA11214`

NASA. (2016c). *Pia21031: Close-up views of jupiter's north pole.* Retrieved from `https://photojournal.jpl.nasa.gov/catalog/PIA21031`

NASA. (2016d). *Saturn, approaching northern summer.* Retrieved from `https://saturn.jpl.nasa.gov/resources/7504/?category=images`

NASA. (2017). *Pia21641: Southern storms.* Retrieved from `https://photojournal.jpl.nasa.gov/catalog/PIA21641`

Nellis, W., Weir, S., & Mitchell, A. (1996). Metallization and electrical conductivity of hydrogen in jupiter. *SCIENCE*, 936–937. Retrieved from `https://www.jstor.org/stable/pdf/2891523.pdf`

Nybakken, R. (2011, March). The juno mission to jupiter - a pre-launch update. In *2011 aerospace conference* (p. 1-8). doi: 10.1109/AERO.2011.5747272

Orlanski, I. (1976). A simple boundary condition for unbounded hyperbolic flows. *Journal of Computational Physics*, *21*(3). doi: 10.1002/qj.49712253209

Pedlosky, J. (1987). *Geophysical fluid dynamics* (2nd ed.). New York, NY: Springer-Verlag.

Porco, C. C., West, R. A., McEwen, A., Del Genio, A. D., Ingersoll, A. P., Thomas, P., ... Vasavada, A. R. (2003). Cassini imaging of jupiter's atmosphere, satellites and rings. *Science*, *299*(5612), 1541-1547. doi: 10.1126/science.1079462

Press, W. H., Teukolsky, S. A., Vetterling, W. T., & Flannery, B. P. (2007). *Numerical recipes: The art of scientific computing* (3rd ed.). New York, NY: Cambridge University Press.

Rancic, M., Purser, R. J., & Mesinger, F. (1996). A global shallow-water model using an expanded spherical cube: Gnomonic versus conformal coordinates. *Quarterly Journal of the Royal Meteorological Society*, *122*(532), 959-982.

Rhines, P. B. (1975). Waves and turbulence on a beta-plane. *Journal of Fluid Mechanics*, *69*(3), 417-443. doi: 10.1017/S0022112075001504

Riley, J. J., Metcalfe, R. W., & Weissman, M. A. (1981). Direct numerical simulations of homogeneous turbulence in density-stratified fluids. *AIP Conference Proceedings*,

76(1), 79-112. doi: 10.1063/1.33198

Rivier, L., Loft, R., & Polvani, L. M. (2002). An efficient spectral dynamical core for distributed memory computers. *Monthly Weather Review*, *130*(5), 1384-1396. doi: 10.1175/1520-0493(2002)130⟨1384:AESDCF⟩2.0.CO;2

Roullet, G., & Madec, G. (2000). Salt conservation, free surface, and varying levels: A new formulation for ocean general circulation models. *Journal of Geophysical Research: Oceans*, *105*(C10), 23927–23942. doi: 10.1029/2000JC900089

Schaeffer, N. (2013). Efficient spherical harmonic transforms aimed at pseudospectral numerical simulations. *Geochemistry, Geophysics, Geosystems*, *14*(3), 751-758. doi: 10.1002/ggge.20071

Scott, R. K., & Polvani, L. M. (2007). Forced-dissipative shallow-water turbulence on the sphere and the atmospheric circulation of the giant planets. *Journal of the Atmospheric Sciences*, *64*(9), 3158-3176. doi: 10.1175/JAS4003.1

Simon, A. A., Wong, M. H., & Orton, G. S. (2015). First results from the hubble opal program: Jupiter in 2015. *The Astrophysical Journal*, *812*(1), 55. doi: 10.1088/0004-637X/812/1/55

Smagorinsky, J. (1963). General circulation experiments with the primitive equations. i. the basic experiment. *Monthly Weather Review*, *91*(3), 99-164. doi: 10.1175/1520-0493(1963)091⟨0099:GCEWTP⟩2.3.CO;2

Smith, B. A., & Hunt, G. E. (1976). Motions and morphology of clouds in the atmosphere of Jupiter. In T. Gehrels (Ed.), *Iau colloq. 30: Jupiter: Studies of the interior, atmosp here, magnetosphere and satellites* (p. 564-585).

Smith, B. A., & Hunt, G. E. (2004). Dynamics of jupiter's atmosphere. In F. Bagenal, T. Dowling, & W. Mckinnon (Eds.), *Jupiter: The planet, satellites and magnetosphere* (p. 105-127). Cambridge: Cambridge University Press.

Smith, B. A., Soderblom, L., Beebe, R., Boyce, J., Briggs, G., Bunker, A., ... Suomi, V. E. (1981). Encounter with saturn: Voyager 1 imaging science results. *Science*, *212*(4491), 163-191. doi: 10.1126/science.212.4491.163

Takehiro, S., & Lister, J. R. (2001). Penetration of columnar convection into an outer stably stratified layer in rapidly rotating spherical fluid shells. *Earth and Planetary Science Letters*, *187*(3), 357 - 366. doi: 10.1016/S0012-821X(01)00283-7

Tritton, D. J. (1988). *Physical fluid dynamics* (2nd ed.). New York, NY: Oxford Science Publications.

Vallis, G. K. (2006). *Atmospheric and oceanic fluid dynamics: Fundamentals and large-scale circulation*. Cambridge, U.K.: Cambridge University Press.

Vasavada, A. R., Ingersoll, A. P., Banfield, D., Bell, M., Gierasch, P. J., Belton, M. J., ...

Senske, D. A. (1998). Galileo imaging of jupiter's atmosphere: The great red spot, equatorial region, and white ovals. *Icarus*, *135*(1), 265-275. doi: 10.1006/icar.1998.5984

Vasavada, A. R., & Showman, A. P. (2005). Jovian atmospheric dynamics: an update after galileo and cassini. *Reports on Progress in Physics*, *68*(8), 1935. Retrieved from http://stacks.iop.org/0034-4885/68/i=8/a=R06

Wicht, J. (2002). Inner-core conductivity in numerical dynamo simulations. *Physics of the Earth and Planetary Interiors*, *132*(4), 281-302. doi: 10.1016/S0031-9201(02)00078-X

Williams, G. P. (1978). Planetary circulations: 1. barotropic representation of jovian and terrestrial turbulence. *Journal of the Atmospheric Sciences*, *35*(8), 1399-1326. doi: 10.1175/1520-0469(1978)035⟨1399:PCBROJ⟩2.0.CO;2

Zang, Y., Street, R. L., & Koseff, J. R. (1994). A non-staggered grid, fractional step method for time-dependent incompressible navier-stokes equations in curvilinear coordinates. *Journal of Computational Physics*, *114*(1), 18-33. doi: 10.1006/jcph.1994.1146

Zhang, K. (1992). Spiralling columnar convection in a rapidly rotating spherical fluid shells. *Journal of Fluid Mechanics*, *236*, 535-556. doi: 10.1017/S0022112092001526

Zhang, K., & Schubert, G. (2000). Magnetohydrodynamics in rapidly rotating spherical systems. *Annual Review of Fluid Mechanics*, *32*(1), 409-443. doi: 10.1146/annurev.fluid.32.1.409